Investigation of the contribution of redox stress to the therapy resistance of cells experiencing hypoxia



Sophie Alice Twigger

St Peter's College, University of Oxford

Thesis submitted to the University of Oxford in accordance with the requirements for the degree of Doctor of Philosophy

Supervisor: **Professor Ester M. Hammond**

Michaelmas Term 2024

Abstract

There is a well-established relationship between hypoxia (low oxygen) and poor patient prognosis. Hypoxia has been described as a major mechanism of resistance to all standard therapies. Despite this, our tools to measure and exploit hypoxia have not been translated into wide-spread clinical use. Moreover, hypoxia is often considered as a static state, whereas tumour cells actually experience dynamic changes in oxygen level which then have significant impact on the biological response. Here, we set out to make a reversible fluorescent probe capable of measuring changes in oxygenation. Our goal was to design a probe which would fluoresce in response to hypoxia but then return to a non-fluorescent state once oxygen levels increased. The probe generated was chemically validated but unfortunately did not have properties suitable for use in cells.

There has been some controversy as to how falling oxygen levels impact redox homeostasis with some reports describing an increase in reactive oxygen species and others suggesting a decrease. Here we took multiple approaches to investigate changes in redox in hypoxia and found that the levels of reactive oxygen species rapidly increase and are followed by a slower elevation of glutathione levels, a major cellular antioxidant. The increases in reactive oxygen species in hypoxia suggested that these cells could be sensitive to agents with a redox-dependent mechanism of action. We investigated the response to the therapeutic molecular cluster, Ag5, which is known to kill cancer cells through targeting both glutathione and thioredoxin. Contrary to our hypothesis, we found that the hypoxic cells were less sensitive to Ag5 than the normoxic comparators. Although importantly, hypoxic cancer cells are significantly more sensitive to Ag5 than

non-transformed cells. We found that the hypoxia-mediated resistance to Ag5 could be reversed using approaches which increase mitochondrial reactive oxygen species. The efficacy of Ag5 in combination with radiation is also described. Overall, we provide valuable insight into the redox landscape of hypoxic cells and highlight the importance of mimicking physiological oxygen levels in all pre-clinical testing.

Dedicated to all the people whose lives have been impacted by cancer.

I hope to contribute to the efforts of curing cancer and
strive towards a future free from this disease.

Acknowledgements

Where to start, this really has been the best four years of my life. I never expected to be here, and it has been better than I could have imagined, and a massive part of that is thanks to my amazing supervisor. Ester, you have been a grounding force throughout my time here, and even though I spent my first two years in chemistry, I can't remember a time you weren't there for me! There are so many things I could say about how amazing this woman is and what an influence she has had in my life, but I think she knows how I feel about her! You once said that a supervisor is for life and not just for Christmas and honestly you have been there for everything, giving me the confidence and opportunity to thrive. I don't think I could thank you enough and I am excited and looking forward to the years to come, with your advice and guidance in them! Love and hugs always xxx

To my parents, I honestly could not ask for better people to have on my side through everything. I love you guys so much and I wouldn't change you for the world. You have always supported me and believed in me in every stage of my life, especially when I'm worrying and overthinking, which is most of the time. I would not have been able to do this without my main supporters behind me every step of the way. I remember applying to PhD projects and thinking it wasn't worth wasting £70 on the Oxford application because there's no chance I would get it, but you guys paid knowing I could do it, and I am so glad you did. The three of us driving down to Oxford, in a van with all my stuff in, to this little flat began the journey of a lifetime. Jeune street has been a safe space for me and honestly, I cannot imagine leaving this cosy little spot I call home!

To everyone else that has helped me get to where I am today, I am forever grateful. From the person that helped me organise the process that is PhD applications and drove me to the interview that led to all of this, to all the people that I've met along the way, it has been an amazing journey filled with happiness and great memories that I will never forget. Starting in the chemistry lab, having never done a column, I learnt so much from some amazing scientists. From dancing to the good energy playlist in the lab to cruising along in a canal boat, some great times were had! Moving to the biology lab allowed my love for the hypoxia field to begin. A special shout out to my favourite hypoxia chamber, Donna, always reliable, speedy and maybe a little too warm during stressful experiments! I have met so many funny, intelligent, kind people in the lab and the department as a whole which has enriched my experience in the green building. Some memorable times being endlessly changing the gas cylinders, chats with KitKats in Esters office and competing over the daily wordle! And of course, being made fun of for my absolute lack of geographical knowledge and non-existent sense of direction! My best friend moving to Oxford just added to my time here. It really does feel like home, and I will cherish everyone I've had the opportunity to meet and get to know whilst here.

I have grown so much in these four years and experienced opportunities I never thought possible. Some of my fondest memories here include exploring this beautiful city that I have been able to call home, with my favourite place being down by the river. Training for the Oxford half marathon really made me appreciate how lovely Oxford is, as I ran up and down the toe-path more times than I can count, and running the Half with my dad was a core memory I will always cherish. Being part of St Peter's college boat club has been a highlight of my time here, allowing me to meet so many amazing people whilst trying out a new sport that I have fallen in love with.

Receiving Ag5 from Arjuna to test in hypoxia has really shaped my work and I am so glad that Ester gave me this project. Being able to go to Santiago and work in the lab where it was produced was such a great experience for my first solo travelling. And having a first author paper from this work is honestly something I never saw in my future, and it still doesn't feel real!

One thing I do want to talk about here is mental health. The phrase I have heard most in my life is to have more confidence in myself. My confidence has soared whilst here, from talking at conferences, to exploring my own ideas and getting support from the people around me, and I am so happy with the person I've grown into. I have always been an anxious and stressy person and whilst at Oxford, it was suggested to me that I might have OCD. This is something I don't really speak about freely as I've always seen it as something bad and something that makes me weak. But it doesn't, it makes me strong, coping with the compulsions and overthinking that come along with this whilst completing a thesis has been extremely hard at times, and I am so proud of myself that I did it and I don't think I let myself feel that enough! I hope that me talking about this, encourages more people to feel comfortable in themselves, as it is something that needs to be spoken about more and I wish I had the courage earlier.

A little tribute to my four-legged, furry bestest friend in the whole wide world, Ellie, you were such a huge part of our family, and I will always miss you!

Overall, thank you to everyone that has helped me get to the place I am today and been a part of my journey, with particular recognition to my amazing supervisor and wonderful parents. I can't wait to see where the next chapter takes me!

Table of Contents

Abstract ..... **II**

Acknowledgements ..... **V**

Table of Contents ..... **VII**

List of Figures ..... **X**

List of Tables ..... **XII**

List of Schemes ..... **XIII**

Abbreviations ..... **XIV**

Chapter 1: Introduction **1**

1.1 Cancer *2*
1.1.1 The origin of cancer 2
1.1.2 Cancer prevalence 2
1.1.3 The hallmarks of cancer 3
1.1.4 The tumour microenvironment 4

1.2 Hypoxia *6*
1.2.1 Defining hypoxia 6
1.2.2 Hypoxia and cancer 8
1.2.3 Hypoxia-mediated resistance to therapy 10
1.2.4 Measuring hypoxia 14
1.2.5 Targeting tumour hypoxia 19
1.2.6 The biological response to hypoxia 22
1.2.7 Hypoxia-inducible factors (HIFs) 23

1.3 Redox *30*
1.3.1 Defining redox 30
1.3.2 Reactive Oxygen Species (ROS) 30
1.3.3 Consequences of ROS 33
1.3.4 ROS-mediated biological response 34
1.3.5 Antioxidants 37

1.4 Oxidative stress *42*
1.4.1 Defining oxidative stress 42
1.4.2 The role of NRF2 in oxidative stress 42
1.4.3 Outcome of oxidative stress 44
1.4.4 Oxidative stress mediated mechanisms of cell death 46

1.5 Cancer and Redox *49*
1.5.1 ROS in cancer 49
1.5.2 Effects of elevated ROS on cancer cells 49
1.5.3 Therapeutically targeting redox homeostasis 50
1.5.4 Targeting the GSH and Trx systems 52
1.5.5 Therapeutic molecular cluster, Ag5 54

1.6 Hypoxia and Redox *56*
1.6.1 ROS in hypoxia 56
1.6.2 Functions of ROS in hypoxia 57
1.6.3 Antioxidant targets of HIF-1 59
1.6.4 HIF upregulates glycolysis and supresses oxidative phosphorylation 60

1.7 Aims of this study *66*

Chapter 2: Materials and Methods **67**

2.1 Chemistry materials and methods *68*
2.1.1 Chemicals 68
2.1.2 Thin layer chromatography 68
2.1.3 Normal phase silica gel flash column chromatography 68
2.1.4 Semi-preparative HPLC 69
2.1.5 Melting point determination 69
2.1.6 Infrared spectroscopy 69
2.1.7 NMR 69
2.1.8 Electrospray ionisation mass spectrometry 71
2.1.9 Analytical high performance liquid chromatography 71
2.1.10 Liquid chromatography-mass spectrometry (LCMS) 71
2.1.11 Electrochemistry 72
2.1.12 UV/Vis spectroscopy 73
2.1.13 Fluorolog 74
2.1.14 Hypoxia chamber 74
2.1.15 Enzyme assay 75

2.2 Biology materials and methods *77*
2.2.1 Materials 77
2.2.2 Tissue culture 79
2.2.3 Mycoplasma testing 80
2.2.4 Cryopreservation of cells 80
2.2.5 Thawing of cells 80
2.2.6 Hypoxia treatment 80
2.2.7 Ag5 treatment 81
2.2.8 MTT assay 81
2.2.9 Radiation treatment 82
2.2.10 Colony survival assay 82
2.2.11 Protein lysate preparation 83
2.2.12 Immunoblotting 83
2.2.13 Immunofluorescence 84
2.2.14 Lipid peroxidation assay 84
2.2.15 GSH-Glo assay 85
2.2.16 FL-1 GSH assay 85
2.2.17 TrxR assay 85
2.2.18 Mitochondrial ROS assay 86
2.2.19 Total ROS assay 86
2.2.20 PRDX3 assay 86
2.2.21 Statistical analysis 87

Chapter 3: Design, synthesis, and validation of a reversible, fluorescent probe for measuring real time hypoxia **88**

3.1 Introduction *89*
3.1.1 Current hypoxia sensing probes 89
3.1.2 Probe design 90

3.2 Results *92*
3.2.1 Probe synthesis 92
3.2.2 Electrochemistry 96
3.2.3 Chemistry characterisation 99
3.2.4 UV/Vis and Fluorescence studies 103
3.2.5 Cytochrome P450 assay 105
3.2.6 Theories for why the probe was not emitting fluorescence 107
3.2.7 Fluorophore variation 108

3.2.8 Locked form synthesis 109
3.2.9 UV/Vis and Fluorescence studies 113
3.2.10 Cellular testing of HCIQ and locked probe 114

3.3 Discussion *117*

Chapter 4: Hypoxia-mediated changes in redox 120

4.1 Introduction *121*

4.2 Results *121*
4.2.1 Hypoxia and redox-dependent therapy 121
4.2.2 ROS levels in hypoxia 122
4.2.3 Antioxidant levels in hypoxia 124
4.2.4 Redox changes over time in hypoxia 131
4.2.5 Impact of HIF-1 signalling on redox 134

4.3 Discussion *138*

Chapter 5: The activity of therapeutic molecular cluster Ag5 is dependent on oxygen level and HIF-1 mediated signalling 141

5.1 Introduction *142*

5.2 Results *142*
5.2.1 Ag5 leads to loss of viability in cancer but not normal cells 142
5.2.2 Ag5 mechanism of cell death 146
5.2.3 Hypoxic cells are less sensitive to Ag5 148
5.2.4 Ag5 shows reduced activity in hypoxia 152
5.2.5 Cells are sensitive to Ag5 upon immediate hypoxic exposure 155
5.2.6 Sensitivity to Ag5 in hypoxia is rescued by loss of HIF-1α 156
5.2.7 Sensitivity to Ag5 is restored in hypoxia by loss of PDK1/3 159
5.2.8 Ag5 increases the radiosensitivity of hypoxic cells 163

5.3 Discussion *165*

Chapter 6: Discussion 167

Chapter 7: References 173

Chapter 8: Appendix 210

8.1 Supplementary information *211*

8.2 Experimental *214*
8.2.1 Indolequinone synthesis 214
8.2.2 Hemicyanine synthesis: 219
8.2.3 PEG derivative synthesis: 222
8.2.4 Other Knoevenagel condensation syntheses: 223
8.2.5 Initial probe synthesis: 226
8.2.6 Fluorophore variation probe synthesis: 228
8.2.7 Locked form probe synthesis: 230

8.3 NMR Spectra *244*

8.4 Presentations, awards and manuscripts from this thesis *252*
8.4.1 Poster and oral presentations 252
8.4.2 Prizes/Awards 253
8.3.3 Manuscripts 253

List of Figures

Figure 1.1: The hallmarks of cancer. 4
Figure 1.2: Key components of the tumour microenvironment (TME). 5
Figure 1.3: Chronic and acute hypoxia. 9
Figure 1.4: Radiolysis of water creating DNA damage. 11
Figure 1.5: Mechanism for reduction of nitroimidazole compounds. 15
Figure 1.6: Regulation of hypoxia-inducible factor (HIF). 27
Figure 1.7: Redox balance. 30
Figure 1.8: Redox elements in the cell. 33
Figure 1.9: Concentration dependent ROS signalling. 35
Figure 1.10: Reactions of GSH with GPx and GST and regeneration of GSH via GR. 40
Figure 1.11: Main components of the cellular antioxidant response. 41
Figure 1.12: NRF2 regulation. 43
Figure 1.13: Mechanism of ferroptosis. 47
Figure 1.14: Mechanism of apoptosis. 48
Figure 1.15: The 'Achilles heel' of cancer cells. 51
Figure 1.16: Therapeutics targeting the GSH and Trx systems. 53
Figure 1.17: Ag5 mechanism of action. 55
Figure 1.18: Proposed DFT mechanism of Ag5 interaction with R-SH. 56
Figure 1.19: Overview of HIF-1α mediated regulation of tumour cell metabolism. 61
Figure 3.1: Reversibility seen for HCIQ electrochemically via cyclic voltammetry. 98
Figure 3.2: Reversibility seen for NA-HCIQ electrochemically via cyclic voltammetry. 99
Figure 3.3: Chemical characterisation of oxidised and reduced HCIQ. 100
Figure 3.4: Colour change displaying the reversibility of HCIQ. 100
Figure 3.5: Comparison of oxidised, reduced and re-oxidised HCIQ. 101
Figure 3.6: LCMS analysis of HCIQ chemical reduction. 102
Figure 3.7: Absorption spectrum of oxidised and chemically reduced HCIQ. 103
Figure 3.8: Cuvette containing a reduced sample of HCIQ. 104
Figure 3.9: Emission spectrum of chemically reduced HCIQ. 105
Figure 3.10: Enzyme assay samples of HCIQ with and without enzyme addition. 106
Figure 3.11: Structure of target locked probe. 110
Figure 3.12: Absorption spectrum of locked probe. 113
Figure 3.13: Emission spectrum of locked probe. 114
Figure 3.14: OE21 cells treated with locked probe. 115
Figure 3.15: Ex/Em wavelength range of locked probe. 115
Figure 3.16: The atmospherically controlled plate reader can be maintained at 0.2 % O_2. 116
Figure 3.17: Fluorescence intensity of HCIQ and locked probe in A549 cells over time in both normoxia and hypoxia. 117
Figure 4.1: Radiosensitivity significantly decreases with decreasing O_2 concentration. 122
Figure 4.2: Total ROS levels increase significantly in hypoxia. 123
Figure 4.3: Mitochondrial ROS levels increase significantly in hypoxia. 124
Figure 4.4: GSH assay outline. 125
Figure 4.5: GSH levels increase significantly in hypoxic conditions. 125
Figure 4.6: Total GSH levels increase significantly in hypoxic conditions. 126

Figure 4.7: In solution validation of novel GSH probe (FL-1)..... 127
Figure 4.8: Cellular validation of novel GSH probe (FL-1). 128
Figure 4.9: GSH levels increase significantly in hypoxia. 129
Figure 4.10: Comparison of fixed and non-fixed cells treated with FL-1..... 130
Figure 4.11: TrxR assay outline. 131
Figure 4.12: TrxR activity does not significantly change in hypoxia. 131
Figure 4.13: Mitochondrial ROS and GSH changes over time in hypoxia (2 % O_2). 133
Figure 4.14: Mitochondrial ROS increases in hypoxia..... 133
Figure 4.15: Redox changes over time in hypoxia (2 % O_2). 134
Figure 4.16: Total ROS levels increase significantly in hypoxia in a HIF-independent manner. 135
Figure 4.17: Mitochondrial ROS levels increase significantly in hypoxia in a HIF-dependent manner. 136
Figure 4.18: Comparison of CellROX and MitoSOX localisation. 137
Figure 4.19: GSH levels increase significantly in hypoxia in a HIF-independent manner. 138
Figure 5.1: Ag5 is toxic to cancer cells but not non-transformed cells..... 143
Figure 5.2: IC50 curves for Ag5 in A549 and MRC5 cell lines..... 144
Figure 5.3: Ag5 effect is independent of silver ion toxicity..... 144
Figure 5.4: ROS levels are higher in cancer cells than non-transformed cells. 145
Figure 5.5: Toxicity of Ag5 is not cancer cell line dependent. 146
Figure 5.6: Ag5 induces cell death via apoptosis. 147
Figure 5.7: Ag5 did not result in increased lipid peroxidation. 148
Figure 5.8: Hypoxic cells are less sensitive to Ag5. 149
Figure 5.9: <0.1 % O_2 shows a different biological response to milder hypoxia (2, 0.5 % O_2). 150
Figure 5.10: Reduced sensitivity to Ag5 in hypoxia is independent of cancer cell line. 150
Figure 5.11: Mechanism of MTT reduction in the cell. 151
Figure 5.12: Hypoxic cells are less sensitive to Ag5 in clonogenic studies. 152
Figure 5.13: Ag5 leads to a ROS increase in normoxia but not hypoxia. 153
Figure 5.14: Ag5-induced PRDX3 oxidation increases in a dose-dependent manner in normoxia, but not hypoxia..... 154
Figure 5.15: PRDX3 oxidation changes due to Ag5 are not cell line specific. 154
Figure 5.16: Cells are sensitive to Ag5 upon immediate exposure to Ag5. 155
Figure 5.17: Sensitivity to Ag5 upon immediate hypoxia exposure is independent of cell line. 156
Figure 5.18: HIF-1α is stabilised in RKO$^{HIF\text{-}1\alpha+/+}$ cells at 2 % O_2, but not in RKO$^{HIF\text{-}1\alpha-/-}$ cells. 157
Figure 5.19: Sensitivity to Ag5 is HIF-1α dependent. 157
Figure 5.20: RKO cells are less sensitive to Ag5 in hypoxia (2 % O_2)..... 158
Figure 5.21: Cells with stabilised HIF-1α are less sensitive to Ag5. 159
Figure 5.22: Increasing mitochondrial ROS, increases sensitivity to Ag5. 160
Figure 5.23: OxPhos is repressed in hypoxia by the action of PDK1/3. 161
Figure 5.24: Depletion of PDK1 and PDK3 results in increased mitochondrial ROS in hypoxia. 162
Figure 5.25: Sensitivity to Ag5 in hypoxia can be rescued by loss of PDK1/3. 163
Figure 5.26: Ag5 increases the radiosensitivity of hypoxic (<0.1 % O_2) cells. 159

List of Tables

Table 1.1: Average pO_2 and oxygen percentages for healthy tissue in the body. 7
Table 1.2: ROS species in the cell. 31
Table 1.3: ROS producing components in the cell. 32
Table 1.4: Components of the antioxidant response. 38
Table 1.5: Redox homeostasis associated genes regulated by members of the antioxidant transcription factor network. 45
Table 2.1: Enzyme assay variants. 76
Table 2.2: Cell lines used in this study. 77
Table 2.3: Chemicals and reagents used in this study. 77
Table 2.4: Commercially available and in-house synthesised compounds used in this study. 78
Table 2.5: Commercially available detection kits used in this study. 78
Table 2.6: Primary antibodies used in this study. 78
Table 2.7: Secondary antibodies used in this study. 79
Table 2.8: Seeding numbers for MTT assay. 81
Table 3.1: Common Knoevenagel reaction conditions. 96
Table 3.2: Enzyme assays trialled. 106
Table 3.3: Conditions trialled for reduction and methylation to give the locked indolequinone. 110
Table 8.1: Redox targeting strategies. 211
Table 8.2: Mutational status of the cell lines used in this study. 213

List of Schemes

Scheme 3.1: Chemical structure and proposed mechanism of action for initial target probe. 90
Scheme 3.2: Synthesis of 5-Methoxy-1,2-dimethyl-4,7-dioxo-4,7-dihydro-1*H*-indole-3-carbaldehyde. 93
Scheme 3.3: Synthesis of 2,3,3-Trimethoxy-3*H*-indole. 93
Scheme 3.4: Synthesis of 1-Ethyl-2,3,3-trimethyl-3*H*-indol-1-ium. 93
Scheme 3.5: Initial probe synthesis route. 94
Scheme 3.6: Problem solving for Knoevenagel condensation. 95
Scheme 3.7: Synthesis route to produce target probe. 96
Scheme 3.8: Reversible electrochemical reduction of benzoquinone to hydroquinone. 99
Scheme 3.9: Synthesis route for (*E*)-1-ethyl-2-(2-(5-methoxy-1,2-dimethyl-4,7-dioxo-4,7-dihydro-1*H*-indol-3-yl)vinyl)-3,3-dimethyl-3*H*-benzo[*g*]indol-1-ium. 109
Scheme 3.10: Initial proposed synthesis to obtain the locked indolequinone. 110
Scheme 3.11: Bartoli indole synthesis route proposed to produce locked quinone. .. 111
Scheme 3.12: Literature mechanism for Bartoli indole synthesis. 111
Scheme 3.13: Synthesis of (*E*)-3-(2-(3,3-dimethyl-3*H*-indol-2-yl)vinyl)-1,2,4,7-tetramethyl-1*H*-indole. 112
Scheme 3.14: Synthesis of (*E*)-2-(2-(4,7-dimethoxy-1-methyl-1*H*-indol-3-yl)vinyl)-1-ethyl-3,3-dimethyl-3*H*-indol-1-ium. 113

Abbreviations

•OH- Hydroxyl radical
1CM- One carbon metabolism
$^1O_2$- Singlet oxygen
2D- Two dimensional
3D- Three dimensional
7-AAD- 7-amino-actinomycin D
AcOH- Acetic acid
ACU- Atmospherically controlled unit
AHR- Aryl hydrocarbon receptor
ATCC- American type culture collection
ATM- Ataxia telangiectasia mutated
ATP- Adenosine triphosphate
ATR- Ataxia telangiectasia and rad3-related
BNIP3- Bcl-2 adenovirus E1B 19kDa-interacting protein 3
BNIP3L Bcl-2 adenovirus E1B 19kDa-interacting protein 3-like
BODIPY- Boron-dipyrromethene
BOLD-MRI- Blood oxygen level-dependent-magnetic resonance imaging
BSA- Bovine serum albumin
BSO- Buthionine sulfoximine
CAC- Colorectal adenocarcinoma
CAT- Catalase
CCC- Clear cell carcinoma
$CDCl_3$- Deuterated chloroform
CNC- Cap'n'collar
CO_2- Carbon dioxide
COSY- Homonuclear correlation spectroscopy
COX- Cytochrome *c* oxidase
Cs- Caesium
CUL3- Cullin-3
Cys- Cysteine
D_2O- Deuterated water
DCE-MRI- Dynamic contrast enhanced-magnetic resonance imaging
DDR- DNA damage response
DEPC- Diethyl pyrocarbonate
DFT- Density functional theory
DMEM- Dulbecco's modified eagle medium
DMSO- Dimethyl sulfoxide
DNA- Deoxyribonucleic acid
dNTP- Deoxynucleotide triphosphate
DSB- Double strand break
DTNB- 5,5'-Dithiobis(2-nitrobenzoic) acid
ECL- Electrochemiluminescence
ED50- Median effective dose
elf2α- Eukaryotic initiation factor 2α
Em- Emission
EPO- Erythropoietin
eq.- Equivalents
ER- Endoplasmic reticulum
ESI- Electrospray ionisation
ESI-MS- Electrospray ionisation mass spectrometry
ETC- Electron transport chain
EtI- Ethyl iodide
EtOAc- Ethyl acetate
EtOH-Ethanol
Ex- Excitation
FACs- Fluorescence-activated cell sorting
FAZA- Fluoroazomycinarabinoside
FBS- Foetal bovine serum
FCCP- Carbonyl cyanide p-(trifluoromethoxy) phenylhydrazone
Fe-S- Iron-sulphur
FIH- Factor-inhibiting HIF
FMISO- Fluoromisonidazole
FRET- Fluorescence resonance energy transfer
G6PD- Glucose-6-phosphate dehydrogenase
GAPDH- Glyceraldehyde 3-phosphate dehydrogenase
GCL- γ-glutamyl-cysteine ligase
GCLM- Glutamate-cysteine ligase
GLUT- Glucose transporter
GPx- Glutathione peroxidase
GPX4- Glutathione peroxidase four
GR- Glutathione reductase
GSH- Glutathione
GSS- Glutathione synthetase
GSSG- Oxidised glutathione
GST- Glutathione S-transferase

h- Hours
H_2O- Water
H_2O_2- Hydrogen peroxide
HAP- Hypoxia activated prodrug
HCIQ- Hemicyanine indolequinone
HCl- Hydrochloric acid
HIF- Hypoxia inducible factor
HMBC- Heteronuclear multiple bond correlation
HMOX- Heme oxygenase
HNO_3- Nitric acid
HOCl- Hypochlorous acid
HOMO- Highest occupied molecular orbital
HPLC- High performance liquid chromatography
HRE- Hypoxia-response element
HRMS- High-resolution mass spectrometry
HSQC- Heteronuclear single quantum coherence spectroscopy
IC50- Half-maximal inhibitory concentration
ICG- Indocyanine green
IMS- Intermembrane space
IR- Irradiation
KEAP1- Kelch-like ECH-associated protein 1
LCFA- Long chain fatty acid
LCMS- Liquid chromatography-mass spectrometry
LOOH- Lipid peroxide
LUMO- Lowest unoccupied molecular orbital
MCT4- Monocarboxylate transporter four
MeCN- Acetonitrile
MEF- Mouse embryo fibroblast
MeI- Methyl iodide
MeOD- Deuterated methanol
MeOH- Methanol
Met- Methionine
Min- Minute
MMTS- Methyl methanethiosulfonate
MPTP- Mitochondrial permeability transition pore
MRI- Magnetic resonance imaging
mRNA- Messenger ribonucleic acid
MS- Mass spectrometry
mTORC1- Mammalian target of rapamycin complex 1
MTT- 3-(4,5-Dimethyl-2-yl)-2,5-diphenyltetrazolium bromide
MXI1- MAX-interacting protein 1
NA-HCIQ- Non-alkylated hemicyanine indolequinone
$Na_2S_2O_4$- Sodium dithionite
NAC- *N*-acetylcysteine
NAD^+- Nicotinamide adenine dinucleotide
NADH-Nicotinamide adenine dinucleotide phosphate
NADPH- Nicotinamide adenine dinucleotide phosphate hydrogen
NaH- Sodium hydride
NCI- National cancer institute
NEM- *N*-ethylmaleimide
NIR- Near infrared
NIR- Near-infrared
NMR- Nuclear magnetic resonance
NO•- Nitric oxide
NOX- NAPDH oxidase
NQO1- NAD(P)H quinone dehydrogenase 1
NRF2- Nuclear factor erythroid 2-related factor 2
ns- Not significant
NSCLC- Non-small cell lung cancer
O_2- Oxygen
$O_2^{\bullet-}$- Superoxide
O_3- Ozone
OAC- Oesophageal adenocarcinoma
OCR- Oxygen consumption rate
ODDD- Oxygen-dependent degradation domain
OE-MRI- Oxygen enhanced-magnetic resonance imaging
OER- Oxygen enhancement ratio
$ONOO^-$- Peroxynitrite
$ONOOCO_2^-$- Nitrosoperoxycarbonate
OSCC- Oesophageal squamous cell carcinoma
OxPhos- Oxidative phosphorylation
PAS- Per-Arnt-Sim

PBS- Phosphate-buffered saline
PDH- Pyruvate dehydrogenase
PDK- Pyruvate dehydrogenase kinase
PEG- Polyethylene glycol
PERK- Protein kinase RNA (PKR)-like ER kinase
PET- Positron emission tomography
PFA- Paraformaldehyde
PHD- Prolyl hydroxylase domain
PI3K/Akt- Phosphatidylinositol 3-kinase/ protein kinase B
PIMO- Pimonidazole
pO_2- Partial pressure of oxygen
PPP- Pentose phosphate pathway
PRDX/Prx- Peroxiredoxin
PRDX3- Thioredoxin-dependent peroxide reductase
PTEN- Phosphatase and TENsin homolog deleted on chromosome 10
PUFA- Polyunsaturated fatty acid
PVDF- Polyvinylidene fluoride
PX-12- 1-methylpropyl-2-imidazole disulfide
RCC- Renal clear cell carcinoma
RIPA- Radioimmunoprecipitation assay
RNA- Ribonucleic acid
RO•- Alkoxyl radical
ROO•- Peroxyl radical
ROS- Reactive oxygen species
RP- Reverse phase
RPMI- Roswell Park memorial institute
SDS- Sodium dodecyl sulphate
sec- Seconds
SEM- Standard error of the mean
SESN- Sestrin
SIRT- Sirtuin
SOD- Superoxide dismutase
SPECT- Single-photon emission computed tomography
Srx- Sulfaredoxin
TAD- Transactivation domain
TBS- Tris-buffered saline
TC- Tissue culture
TCA- Tricarboxylic acid
TCEP- Tris(2-carboxyethyl)phosphine
TLC- Thin layer chromatography
TMC- Therapeutic molecular cluster
TME- Tumour microenvironment
TMS- Tetramethylsilane
TNB^{2-}- 5-Thio-2-nitrobenzoic acid
TNT- Trinitrotoluene
Trx- Thioredoxin
TrxR- Thioredoxin reductase
Tyr- Tyrosine
UK- United Kingdom
UPR- unfolded protein response
UV- Ultraviolet
VEGF- Vascular endothelial growth factor
VHL- von Hippel-Lindau
Vis- Visible
WHO- World health organisation
WT- Wild type
xCT- Cysteine/glutamate antiporter

Chapter 1: Introduction

1.1 Cancer

1.1.1 The origin of cancer

The word cancer was coined by, the father of medicine, Hippocrates (460-370 B.C.) who referred to the disease as 'Karakinos' named after the moveable crab that grips its surroundings with its claws (Afify and Seno, 2023). The Roman encyclopaedist, Aulus Cornelius Celsus, later translated 'Karakinos' to cancer in his book De Medicina, as cancer means crab in Latin (Afify and Seno, 2023). Today, organisations such as NCI and WHO, define cancer as a disease in which abnormal cells grow uncontrollably and spread to other parts of the body (NCI; WHO).

1.1.2 Cancer prevalence

Cancer is a leading cause of death worldwide and it is estimated that 1 in 2 people born in the UK after 1961 will be diagnosed with some form of cancer in their lifetime (Cancer Research UK). In February 2024, the International Agency for Research on Cancer (WHO's cancer agency) released the latest estimated worldwide statistics. In 2022, 20 million new cancer cases were estimated, with 9.7 million deaths. As examples, lung cancer was shown to be the most commonly occurring cancer worldwide, with 2.5 million new cases, female breast cancer ranked second, with colorectal cancer at third. These data show that even though our understanding of how to diagnose and treat cancer has advanced, with 35 million new cases estimated for 2050 (WHO), increased effort is required.

1.1.3 The hallmarks of cancer

The process by which normal cells transform into malignant cancer cells was first characterised in 2000 (Hanahan and Weinberg, 2000). Originally, six biological traits were proposed, that had the potential to encompass almost all of the biology of all types of tumours (Weinberg, 2014). These 'hallmarks' were self-sufficiency in growth signals, insensitivity to growth-inhibitory (antigrowth) signals, evasion of programmed cell death (apoptosis), limitless replicative potential, sustained angiogenesis, and tissue invasion and metastasis (Hanahan and Weinberg, 2000). They postulated that these six factors were acquired by cells in order to breach a hardwired anticancer defence mechanism (Hanahan and Weinberg, 2000).

The concept of cancer hallmarks was furthered in 2011 with the addition of two factors, reprogramming of energy metabolism and evading immune destruction (***Figure 1.1***) (Hanahan and Weinberg, 2011). Here, Hanahan and Weinberg elaborated that tumours are more than insular masses of proliferating cancer cells and went on to describe how the tumour microenvironment impacts the majority of the hallmarks (Hanahan and Weinberg, 2011).

Hanahan added to this model again in 2022 with four enabling characteristics, unlocking phenotypic plasticity, nonmutational epigenetic reprogramming, polymorphic microbiomes and senescent cells (Hanahan, 2022).

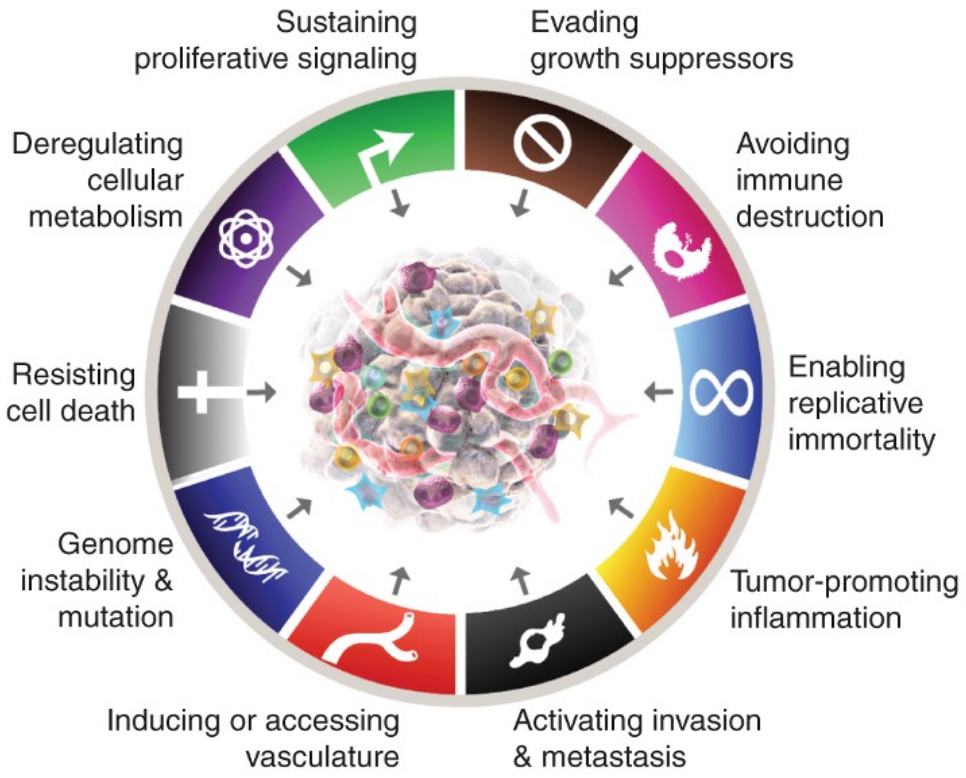


Figure 1.1: **The hallmarks of cancer.** The eight hallmark capabilities (and two enabling characteristics) needed for normal cells to overcome an anticancer threshold and become a malignant tumour. The ten traits shown include the original six hallmarks proposed in 2000 and the additional two added in 2011, with their respective enabling characteristic (Hanahan and Weinberg, 2000, 2011). Reproduced from (Hanahan, 2022), with permission (license number: 5873010046466).

1.1.4 The tumour microenvironment

A tumour is formed from cancer cells in close proximity with other cells such as immune cells, stromal cells, blood vessels and extracellular matrix which, together, make up the tumour microenvironment (TME). The TME is unique to the tumour and organ type (***Figure 1.2***) (Baghban et al., 2020). In 1863, Rudolph Virchow documented one of the first observations of tumour and microenvironment interacting, showing leukocyte infiltration is a characteristic of solid tumours (Maman and Witz, 2018; Schmidt and Weber, 2006). Further to this, in 1889, Paget, concluded metastatic colonisation depended on the properties of the organ (Paget, 1889). This principle was found to underlie the relationship

between primary tumours and their microenvironment, thereby affecting tumour evolution (Witz and Levy-Nissenbaum, 2006).

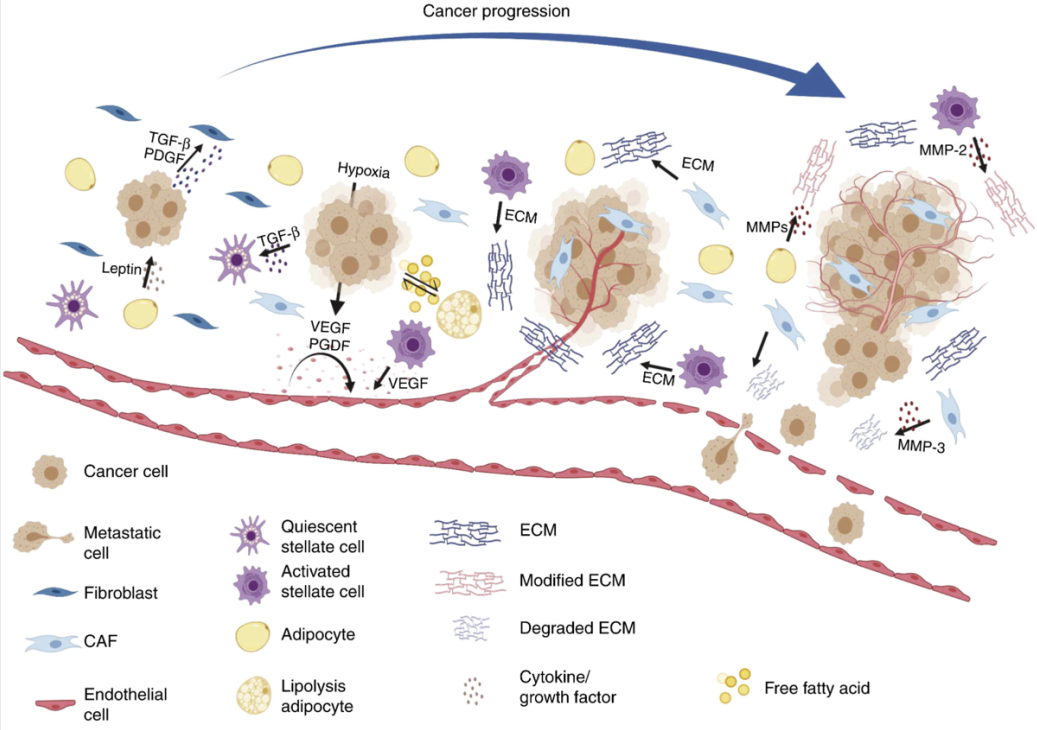


Figure 1.2: **Key components of the tumour microenvironment (TME).** During tumorigenesis cancer cells recruit stromal cells such as endothelial cells, fibroblasts, adipocytes and stellate cells. The composition of the TME can vary depending on the tumour type and organ of tumour residence. Reprinted from (Anderson and Simon, 2020), with permission (license number: 5873001000662).

The TME is now considered essential in cancer growth and progression, with tumour cells stimulating significant molecular, cellular and physical changes within their host tissues (Anderson and Simon, 2020). All components of the TME are needed for the cancer to thrive. For example, endothelial cells form the vascular endothelium allowing transport of water, nutrients and immune cells. Endothelial cells also orchestrate the formation of new blood vessels when the tumour reaches a point where there is insufficient oxygen and increased metabolic waste build-up, creating a hypoxic and acidic microenvironment. To overcome this, the tumour must provide its own blood supply. One way it does this is by activating the hypoxia-inducible factors, leading to a range of

downstream responses such as instructing endothelial cells to secrete vascular endothelial growth factor (VEGF) stimulating them to form new blood vessel lumens (Anderson and Simon, 2020).

1.2 Hypoxia

1.2.1 Defining hypoxia

Hypoxia is defined as a state of insufficient oxygen (O_2), that can be present in normal tissues and wounds, as well as in pathological states such as tumours (Hammond et al., 2014). In the body, cells depend on a constant supply of oxygen for the maintenance of bioenergetic homeostasis and cell survival (Taylor and Scholz, 2022). Oxygen is the terminal acceptor in the electron transport chain (ETC) producing energy for the cell, in the form of ATP (Kaelin and Ratcliffe, 2008). The normal level of oxygen required by tissues can vary dependent on the organ type, with some tissues sustained by partial pressures of oxygen (pO_2) that would be considered hypoxic for other tissues. Examples of healthy tissues pO_2's below show averaged values, measured via electrodes, the single value given is an average of several measurements and does not reflect the dynamic changes in oxygen concentration seen in the body over time (***Table 1.1***) (Hammond et al., 2014). For example, the kidneys can experience stable but steep oxygen gradients due to high oxygen consumption and limited perfusion (Schödel and Ratcliffe, 2019; Scholz et al., 2021; Nolan and Wenger, 2018).

Table 1.1: **Average pO_2 and oxygen percentages for healthy tissue in the body.** 1 mmHg = 0.13 % O_2 and 1 % O_2 = 7.6 mmHg.

Tissue	pO_2/ mmHg	% O_2
Brain	35	4.6 (Dings et al., 1998)
Lung	42.8	5.6 (Le et al., 2006)
Liver	31	4.08 (Brooks et al., 2004)
Kidney	72	9.5 (Müller et al., 1998)
Muscle	25	3.25 (Boekstegers et al., 1990)
Bone marrow	54.9	7.14 (Harrison et al., 2002)
Skin	8-35	1.05-4.61 (Wang et al., 2003)
Intestine	61	8.03 (Thermann et al., 1985)

The majority of scientific research is carried out in atmospheric conditions (21 % O_2), coined 'normoxia'. However, this is not representative of the oxygen level that cells see inside the body, potentially contributing to the failure of clinical trials, as novel therapies are not tested at physiological O_2 levels or 'physoxia'. Hypoxia can be divided further into mild hypoxic levels which are considered to be between 2-0.5 % O_2 (depending on tissue type), in which hypoxia-inducible factors (HIFs) are stabilised, and severe or radiobiological hypoxia which is considered to be <0.13 % O_2 (Carreau et al., 2011; Singleton et al., 2021; Hall and Giaccia, 2018).

In our body, a gradient of oxygen exists around every blood vessel, decreasing in oxygen with increasing distance from vessels (Wenger et al., 2015). Cellular hypoxia occurs when the demand for sufficient O_2 needed for energy production outweighs available O_2 from the existing vasculature, disrupting cellular homeostasis. Examples of hypoxia within normal tissue include the foetal growth plate which is both avascular and hypoxic, and skeletal muscle during exercise when O_2 consumption is elevated (Provot and Schipani, 2007; Lindholm and Rundqvist, 2016).

Pathophysiological hypoxia is a characteristic of the majority of ischaemic diseases, including stroke, myocardial infarction and kidney injury and results in the necrotic cell

death seen in these instances (Semenza, 2014b; a). Hypoxia is also a feature of inflammation, cardiovascular defects and cancer (Lee et al., 2020b). The appearance of hypoxia in tumours was identified over 60 years ago and has become a primary determinant of patient outcome due to the associated therapy resistance (Thomlinson and Gray, 1955; Worth et al., 2022).

1.2.2 Hypoxia and cancer

Most solid tumours have some degree of hypoxia, due to abnormal vasculature and high metabolic demand (Denko, 2008; Hammond et al., 2014). Developing tumours require elevated amounts of nutrients and oxygen from the blood supply for rapid cell proliferation and growth. However, once the diameter of the tumour exceeds 1 mm, the cancer cells outgrow the existing vasculature of the body and O_2 demand outweighs supply (Vaupel et al., 1989). The tumour overcomes this setback by creating its own vascular network, using preexisting vessels or forming new ones via angiogenesis (Folkman, 1990). However, the network of vessels produced is chaotic and abnormal (Siemann and Horsman, 2015; Horsman and Vaupel, 2016). The structural and functional abnormalities of the vessels can include incomplete or absent endothelial linings and basement membranes, leakiness and lack of contractile wall components and physiological receptors (Vaupel et al., 1989). Consequently, the supply of blood to the tumour is often disrupted, not meeting the demand of the cancer cells. An insufficient vasculature system within the tumour network leads to distinct heterogeneity within the TME, including regions of altered metabolism, O_2 tensions, pH and genomic stability (Bristow and Hill, 2008). Two broad forms of hypoxia arise from the poorly formed vasculature, acute and chronic (***Figure 1.3***). Chronic or diffusion-limited hypoxia was first

identified by Thomlinson and Gray who found necrosis at the centre of large tumours, surrounded by rings of intact tumour cells (Thomlinson and Gray, 1955). The distance between a functional blood vessel and the start of necrotic cells did not exceed 180 μm, with the size of the necrotic core increasing as the tumour grew (Thomlinson and Gray, 1955). This distance is similar to that of the diffusion distance of oxygen from a capillary to cells before it is fully metabolised (Chaplin et al., 1987a). This limit in oxygen diffusion throughout the tumour resulted in what was termed chronic or diffusion-limited hypoxia. Acute or transient hypoxia, was later identified (Brown, 1979; Chaplin et al., 1987b) and described as a form of hypoxia arising from the poor construction of the tumour vasculature, resulting in shutdown of vessels, temporary blockages, reversal of flow and periodic fluctuations in flow (Brown and Giaccia, 1998; Kimura et al., 1996).

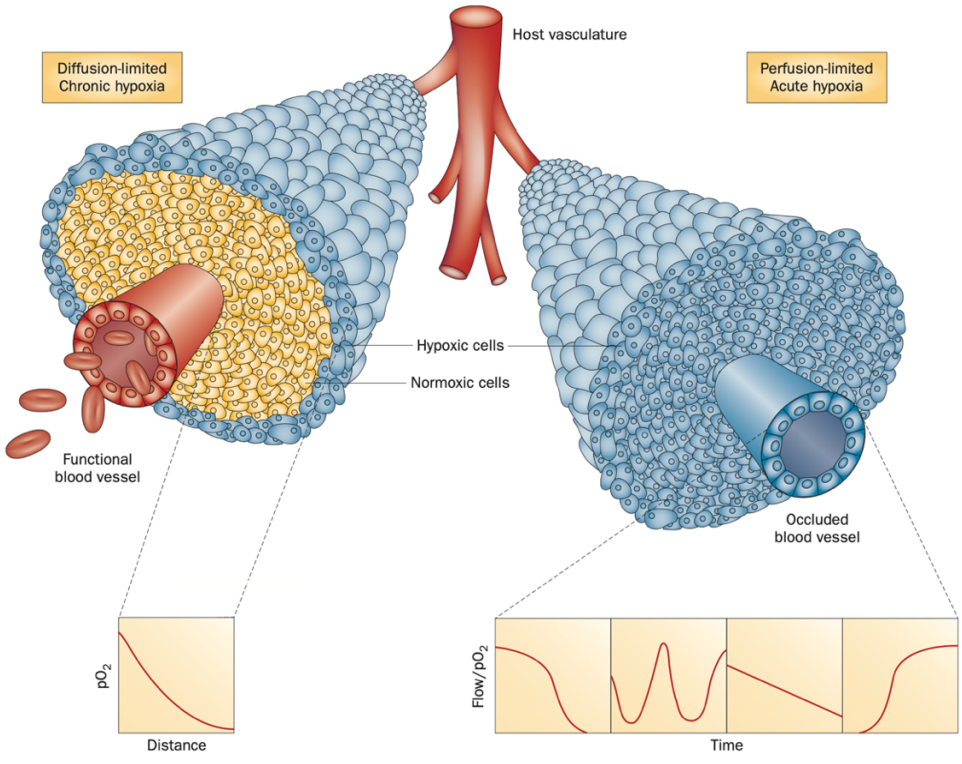


Figure 1.3: **Chronic and acute hypoxia.** Within a tumour there is acute hypoxia due to temporary closure of a vessel for example and chronic hypoxia arising from prolonged restriction to oxygen and nutrients. Reprinted from (Horsman et al., 2012), with permission (license number: 5873011146289).

Periods of reduced oxygen followed by reoxygenation, occurring because of rapid changes in red cell flux, are known as cyclic or intermittent hypoxia (Bader et al., 2020). The periods of hypoxia these tumour cells are exposed to can vary in the range of minutes to hours (Bristow and Hill, 2008). This phenomenon has been known to lead to increases in free radical species in the cell, tissue damage and activation of stress response genes (Prabhakar, 2001; Bader et al., 2021).

1.2.3 Hypoxia-mediated resistance to therapy

Hypoxic tumour cells are resistant to standard therapies including chemotherapy, radiotherapy, immunotherapy and surgery (Brown and Giaccia, 1998; Nordsmark et al., 2005; Vaupel and Harrison, 2004). The most aggressive manifestation of tumour progression is metastasis, a state that is more common if a patient presents with a hypoxic primary tumour, regardless of whether initial treatment includes radiotherapy or surgery (Bristow and Hill, 2008).

Radioresistance

First discovered by Röntgen, x-rays are a common treatment for cancer (Perry, 1896). Today, approximately 50 % of all cancer patients receive radiotherapy, either alone or in combination with other agents (Baskar et al., 2012; Delaney et al., 2005). However, hypoxic tumour cells are radioresistant (Bristow and Hill, 2008). This was demonstrated by Thomlinson and Gray, who reported that the diffusion-limited hypoxia they saw indicated central tumour cells would be more radioresistant due to the absence of molecular oxygen at the time of irradiation (Gray et al., 1953; Thomlinson and Gray, 1955). During radiotherapy, x-ray photons interact with surrounding water molecules in biological matter (water radiolysis), producing highly reactive hydroxyl radicals that can

interact with DNA to create DNA radicals (Hall and Giaccia, 2018; Robert Grimes and Partridge, 2015). The DNA radicals can react with molecular oxygen to produce a permanent DNA peroxyl radical that can be impossible to repair, so the damage is fixed into the DNA (***Figure 1.4***). In contrast, in the absence of oxygen the DNA radicals created can be repaired by donation of hydrogen ions from cellular thiols, so there is decreased fixation of DNA damage, and the DNA can be returned to its original form (Robert Grimes and Partridge, 2015; Hall and Giaccia, 2018; Bristow and Hill, 2008).

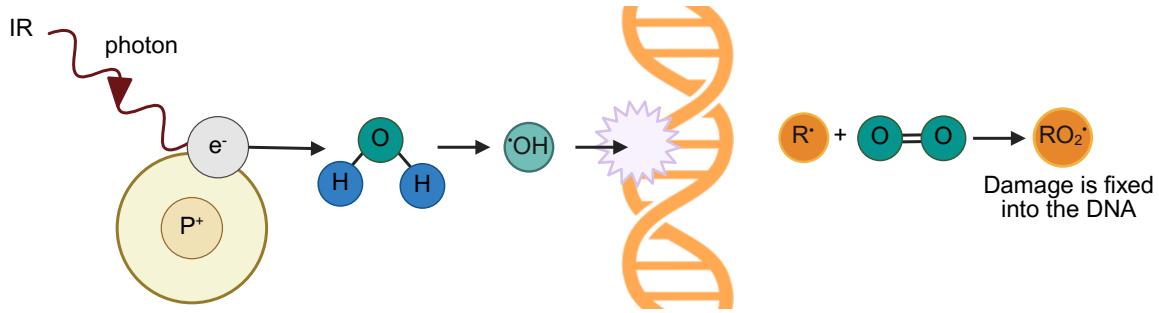


Figure 1.4: **Radiolysis of water creating DNA damage.** X-ray photons interact with water molecules in the body producing hydroxyl radicals, that react with DNA producing fixed DNA peroxyl radicals in the presence of oxygen (Ogawa, 2016). Created with BioRender.com.

An oxygen enhancement ratio (OER) is used to calculate the dose needed to achieve the same killing in hypoxia as would be seen in normoxia (Gray et al., 1953; Hall and Giaccia, 2018). Overall, cells in severe hypoxia are shown to be 2.5-3 times more resistant to radiation than cells in normoxia. Pre-clinical and clinical studies have shown the number of DNA double strand breaks (DSBs) that form in severe hypoxia are also decreased by 2-3-fold (Olive and Banáth, 2004; Frankenberg-Schwager et al., 1991; Terris et al., 2002; Wang et al., 1992; Martin Brown et al., 1992). In comparison, the quantity of DNA-protein crosslinks, that can activate additional DNA repair pathways, show a large relative increase in hypoxia (Zhang et al., 1995).

Additionally, Thomlinson and Gray showed that if the oxygenated, radiosensitive cells are killed following radiation treatment then the inner/hypoxic cells will have an increased oxygen/nutrient supply. This means that the previously hypoxic tumour cells can proliferate, if they retain the ability to replicate, resulting in aggressive tumour growth (Thomlinson and Gray, 1955). Another factor of radiation outcome depends on the nature of the hypoxia. During the radiation treatment it does not matter whether the hypoxia is acute or chronic. However, cells exposed to chronic hypoxia are nutrient deprived, but nutrients can be restored to acutely hypoxic cells therefore, acutely hypoxic cells could repair DNA damage following nutrient restoration, making acute hypoxic cells more resistant than chronic hypoxic cells (Chaplin, 1991; Sørensen and Horsman, 2020).

Surgery resistance

Hypoxic tumours can lead to poor surgical outcome, due to the occurrence of metastasis (Brown and Wilson, 2004). The development of metastases is an aggressive progression of tumour development, and it is more common for hypoxic tumours to develop local reoccurrence and metastatic states than non-hypoxic tumours (Bristow and Hill, 2008). Indicating that hypoxic tumours would fail to be removed under surgical intervention and therefore are resistant to this form of therapy. This has been reported in numerous studies, for example in soft tissue sarcoma patients the median pO_2 for metastasising tumours after treatment was 7.5 mmHg compared to 20 mmHg for non-metastasising tumours and in tumours of the uterine cervix upon histopathological examination patients with low pO_2 tumours exhibited large tumour extensions, more frequent parametrial spread and lymph-vascular space involvement (Brizel et al., 1996; Höckel et al., 1996a).

Chemoresistance

The term chemotherapy was coined by chemist Paul Ehrlich in the 1900s who defined it as the use of chemicals to treat disease (DeVita and Chu, 2008). Cancer treatment via surgery or radiotherapy dominated in the 1960s until cure rates plateaued at approximately 33 %. The strategy of therapy combinations then developed and the tailoring of the three modalities to maximise their anti-tumour effect and reduce normal tissue toxicity became standard practice (Breasted, 1930; Papac, 2001; DeVita, 1978; Osler, 1893).

Even with the success of chemotherapy treatment over the decades, hypoxic tumour cells have shown resistance to this form of cancer therapy. Resistance of hypoxic cells to chemotherapy is due to several factors. For chemical agents to act on cancer cells, they need to be able to access the cells. As already mentioned, the vasculature of tumours is extremely disordered, and vessels do not reach the entirety of the tumour. Therefore, chemotherapeutic agents often do not work on hypoxic regions as the delivery and diffusion are both limited in these areas (Tannock, 1998; Durand, 1994). Hypoxic cells also have low proliferation rates, meaning the effect of chemical agents is less pronounced in hypoxic fractions (Tannock, 1968). Other factors include decreased drug action in the absence of O_2 as seen with the agent bleomycin and etoposide, hypoxia upregulating genes involved in drug resistance, altered pH gradients and selection pressure for the loss of p53-dependent apoptosis (Comerford, 2002; Wartenberg et al., 2003; Teicher et al., 1981; Batchelder et al., 1996).

Even though hypoxia has been widely reported to induce therapy resistance and poor patient outcome, methods to both image and target hypoxic tumour cells are still not adopted in standard clinical practice. Pre-clinical studies of novel cancer therapies are

often not conducted in physiologically relevant conditions and patients in clinical trials are not stratified to determine if their tumour contains hypoxic cells.

1.2.4 Measuring hypoxia

The need for biomarkers to aid clinical development of hypoxia-targeted therapies has been stressed repeatedly over many years (Bhandari et al., 2019; Hunter et al., 2016; Brown and Slim, 1996; Spiegelberg et al., 2019; Meaney et al., 2019). However, after more than three decades there has not been a prospective randomised trial in which hypoxia has been routinely assessed, aside from a small subset of patients (Singleton et al., 2021). Imaging biomarkers that would allow for numerous measurements across the whole tumour, without being invasive would improve patient outcome.

pO_2 electrode

The use of O_2 electrodes was invaluable to demonstrating the link between hypoxia and treatment response and is still the only direct way to measure *p*O_2 in a tissue (Peters et al., 2010; Brizel et al., 1997; Höckel et al., 1996b; Okunieff et al., 1993; Gatenby et al., 1988; Fyles et al., 1998; Nordsmark and Overgaard, 2000). The use of polarographic O_2 electrode measurements showed that patients with more hypoxic tumours had poorer outcomes, partly due to the development of metastases (Brizel et al., 1996; Höckel et al., 1996b). Measurements using these electrodes are considered the 'gold standard' for measuring tumour hypoxia. However, the clinical use of these probes is limited because they are extremely invasive and can often overestimate hypoxic fractions as they cannot distinguish between viable hypoxic tissue and necrotic tissue (Lyng et al., 1997; Vaupel et al., 2007). Additionally, this measurement is a snapshot of what is happening inside of the tumour and not representative of the heterogeneity present in the TME and the

dynamic changes that can take place, so cannot be incorporated in routine clinical practice (Cline et al., 1997).

Positron emission tomography (PET)

PET-based imaging is the most widely used method for evaluating hypoxia in tumours, due to its high specificity and sensitivity to probe physiological processes *in vivo* (Huang et al., 2021). PET works by detecting photons that are emitted by a radionuclide within an organ or tissue (Berger, 2003). The radionuclides used are produced by attaching a radioactive atom to chemical substances that are used naturally by the organ/tissue during its metabolic processes. If perfusion or blood flow is being monitored then the radionuclide can be a type of radioactive oxygen, carbogen, nitrogen or gallium. Radionuclide detection of hypoxia in tumours was first reported in 1981, via the use of ^{14}C labelled misonidazole (Chapman, 1979). Subsequently, two main tracer classes have been developed to specifically study hypoxia with PET: ^{18}F labelled nitroimidazoles and Cu-labelled diacetyl-bis(N^4-methylthiosemicarbozone) analogues (Fleming et al., 2014). Compounds in both of these categories undergo futile cycling in oxygenated conditions but are enzymatically reduced resulting in cellular retention in the absence of oxygen (***Figure 1.5***).

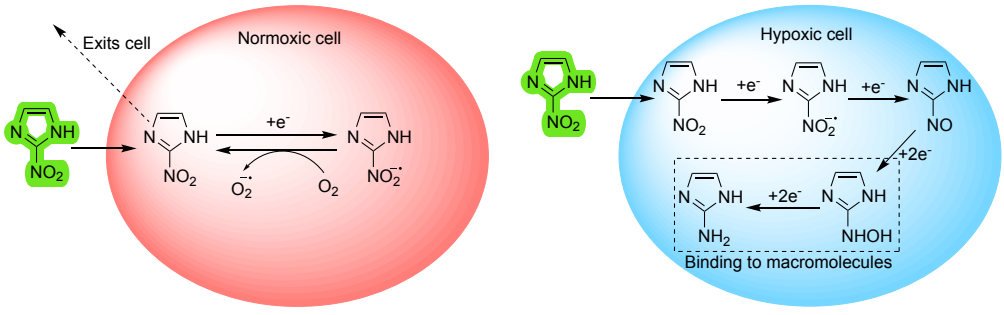


Figure 1.5: **Mechanism for reduction of nitroimidazole compounds.** In well oxygenated conditions a futile cycle of reduction is in place but in hypoxic conditions further reduction takes place, giving the active compound that can bind to macromolecules in the cell (Huang et al., 2021).

Hypoxic biomarkers for PET need to be able to enter cells non-specifically, sample the intracellular contents and leave cells only in the presence of oxygen. Currently, FMISO and FAZA are the most established tracers, with others at various stages of validation and evaluation (Huang et al., 2021). Comparison between different tracers can be complicated due to tumour model and type that can alter the hypoxic conditions and radiotracer uptake. Quantification of hypoxic areas is carried out by using the tumour to background ratio at a given time and needs an approximation of tumour uptake and background uptake (Hammond et al., 2014).

Other compounds containing 2-nitroimidazole functional groups, such as pimonidazole (PIMO) and EF5, can report on low oxygen levels (specifically <1.3 % O_2) (Sun et al., 2011; Gross et al., 1995; Tosun et al., 2023). Under hypoxic conditions these compounds undergo bioreduction to the corresponding 2-aminoimidazole species, covalently bind to macromolecules and accumulate in hypoxic cells (*Figure 1.5*). Pre-clinically these probes can be visualised by immunohistochemical staining which requires biopsies (Bussink et al., 2010). Clinically, radiolabelled versions of the probes can be imaged through PET/SPECT (Chapman et al., 1998). However, once the probe has been reduced, it cannot go back to its original form so cannot report on reoxygenation cycles.

PET imaging of hypoxia can be used to find patients with hypoxic tumours that could then go on to benefit from hypoxia-targeted therapy, such as increased radiation dose or hypoxia-modifying drugs (Horsman et al., 2012). Studies in multiple cancer types have shown that FMISO can predict poor treatment response and prognosis (Lee and Scott, 2007). However, PET imaging has its challenges for example, cost and availability of tracers. Additionally, effective delivery of the tracer can be restricted due to the poor

vasculature present, resulting in accumulation of the tracer in normal tissue or normoxic tumour tissue confusing the results (Fleming et al., 2014).

Magnetic resonance imaging (MRI)

Even though PET-based techniques have dominated the hypoxia imaging field, the emergence of MRI is being established as a more practical and readily translational alternative (O'Connor et al., 2019). MRI uses the natural magnetic properties of the body to produce detailed images (Berger, 2002). The MRI machine produces a strong magnetic field around the patient causing the protons in the body to align with that field. When a radiofrequency current is then pulsed through the patient, the protons are stimulated, and spin out of the equilibrium, straining against the pull of the magnetic field. When the radiofrequency current is stopped, the MRI detector records the energy released as the protons realign with the magnetic field, this energy varies depending on the chemical nature of the molecules.

Recently, the concept of oxygen-enhanced MRI (OE-MRI) has come to the forefront of hypoxic imaging, where it has been validated to quantify the spatial variation of hypoxia (O'Connor et al., 2016). Dynamic contrast enhanced MRI (DCE-MRI) was included to account for tumours that exhibit extensive necrosis, in which a gadolinium-based contrast agent bolus is injected into the vein and passage of the agent is monitored through the tumour microvasculature giving an estimate of perfusion (O'Connor et al., 2012). Advantages of OE-MRI include its ability to allow for repeated measurements. Also, in comparison to PET imaging, MRI has better spatial resolution and is less expensive. Additionally, OE-MRI has been reported to allow the detection of changes in tumour hypoxia during radiotherapy for non-small-cell lung cancer (NSCLC) xenografts and in cancer patients (Salem et al., 2019). OE-MRI has also been suggested as a superior

method to blood oxygen level-dependent (BOLD) imaging, which exploits differences in magnetic resonance transverse relaxation induced by regional differences in deoxygenated haemoglobin levels (Ogawa et al., 1993). BOLD-MRI can cause respiratory distress due to inhalation of the carbogen mixture needed to make the measurements (Taylor et al., 2001). In addition, the vasoactive effects can change tumour perfusion and haematocrit (the ratio of the volume of red blood cells to the total volume of blood), independently altering the BOLD signal (Neeman et al., 2001). Whereas OE-MRI is not dependent on haemoglobin saturation so does not suffer the same limitations as BOLD-MRI (Dewhirst and Birer, 2016).

Numerous pre-clinical fluorescent probes to sense hypoxic environments have been developed, which can then underpin the development of more advanced systems (Elmes, 2016; Luo et al., 2011a; Li et al., 2015; Rtishchev et al., 2001; Yuan et al., 2014; Lee et al., 2012; Cai et al., 2015; Guisán-Ceinos et al., 2022; Sandhu et al., 2017; Wang et al., 2020b; Kiyose et al., 2010; Wang et al., 2023; Uchiyama et al., 2023). For example, the development of clinically useful MRI probes has been informed by pre-clinical fluorescent imaging tools, as these are more easily developed and tested before advancing to MRI probes for use in people (Elmes, 2016). Often the fluorophores used in these probes emit in the near-infrared region (NIR) of the electromagnetic spectrum to allow for improved light penetrability through tissue and remove artefacts associated with auto-fluorescence (Ntziachristos, 2010; Vahrmeijer et al., 2013; Iqbal and Pan, 2016). For example, the NIR cyanine dye indocyanine green (ICG) has been used widely to highlight tumours and guide surgery (Liu et al., 2015; Keating et al., 2016). The mode of action of these probes is fluorescent turn on in hypoxia, creating a significant increase in fluorescence, reducing signal to noise ratio (Grammel and Hang, 2013; Chan et al., 2012).

Chemically, there is a trigger built into the probe structure that will undergo a selective reaction in the reductive environment achieved by hypoxia, releasing the fluorophore. However, if an increase in oxygen concentration occurs after the probe has been activated, no further change will occur to the output. Chemically, the probe fractures to release the fluorophore moiety in hypoxia, and the fluorophore can therefore not be re-caged, highlighting that the use of a reversible system would be key in assessing the spatial and temporal aspect of hypoxia.

1.2.5 Targeting tumour hypoxia

Hypoxia is a key difference between tumour tissue and normal tissue, creating a therapeutic window for hypoxia targeting therapies (Begg et al., 2011). However today there is still not an effective and widely used treatment that eliminates or exploits hypoxia (Wilson and Hay, 2011; Singleton et al., 2021). There have however been several attempts and steps forward in this area, although disappointing clinical trial results have occurred, due to failure in patient selection and stratification and the poor accessibility for systemic agents due to the aberrant vasculature in hypoxic tumours (Le and Courter, 2008; Overgaard, 2011; Dewhirst and Secomb, 2017).

The importance of integrating measures of tumour hypoxia into clinical trials is best exemplified by the phase III trial of tirapazamine (Rischin et al., 2010). The phase II trial showed that patients with more hypoxic tumours were more likely to show local regional failure after chemoradiotherapy but this was improved by including tirapazamine in the treatment regime (Rischin et al., 2006). However, in the phase III trial no measure of hypoxia was taken and subsequently the overall patient population outcome was not improved by the addition of tirapazamine (Rischin et al., 2010; Peters et al., 2010). Today,

it is generally recognised that biomarkers of hypoxia are critical for the testing of hypoxia-targeted therapies. Strategies to treat hypoxic tumours include the following.

Hyperbaric treatment and dose painting

Hyperbaric oxygen (100 % O_2) was trialled but showed toxicity, oxygen seizures and was a cumbersome technique (Fernández et al., 2021). The Dutch ARCON trial combined radiation treatment with carbogen (95 % O_2, 5 % CO_2) and nicotinamide (radiosensitiser) and showed that patients with more hypoxic tumours had significantly improved locoregional control (Harris et al., 2015a; Janssens et al., 2012). Other attempts to improve the radiosensitivity of hypoxic tumour cells include fractionated radiotherapy, in which hypoxic cells become reoxygenated and therefore resensitised between individual dose fractions (Wardman, 2007). Dose painting has also been trialled in which the hypoxic regions of tumours are identified and the radiation dose for these areas is increased (Bassler et al., 2014). The hypoxic nitroimidazole-based radiosensitiser nimorazole has been used in clinical practice in Denmark and Norway for treatment of head and neck squamous cell carcinoma (Overgaard et al., 1998).

Hypoxia-activated prodrugs (HAPs)

HAPs are biologically inactive compounds that are selectively reduced by enzymes under hypoxic conditions, effecting a cytotoxic response on the cell (Wilson and Hay, 2011; Wardman, 2001). These agents exploit the low levels of oxygen in hypoxic regions as the enzymes that reduce the agents are upregulated in hypoxic conditions (Guise et al., 2014). By targeting the agent to hypoxic tumour cells, normal tissue is spared, reducing off target toxicity that can be seen with common chemotherapeutics (Sunakawa et al., 2016; Liapis et al., 2015).

The mechanism of action for HAPs begins with a single electron transfer to the HAP, mediated by reductases, producing a radical species (Wardman et al., 1995). In oxygenated areas, this electron can be scavenged, oxidising the HAP and producing a futile redox cycle (Brown and Wilson, 2004). Whereas in hypoxia, further reduction irreversibly transforms the HAP to its activated from. HAPs are often based on nitroimidazoles, and examples include TH302, AQ4N, tirapazamine and PR-104A. Although HAPs showed success in pre-clinical work and early-stage clinical trials, they did not show improvement in overall survival (Hunter et al., 2016; Hay et al., 2014). Reasons for this include inability to reach the hypoxic tumour cells and lack of patient stratification. Overall, there are currently no HAPs routinely used in clinical practise (Spiegelberg et al., 2019).

Oxygen modulating therapies

A more recent strategy for treatment of tumours is to reduce the hypoxia present by lowering the oxygen consumption rate (OCR) in the normoxic fraction (Ashton et al., 2016). This would correct the imbalance in oxygen supply and demand, increasing the availability of oxygen to hypoxic cells, allowing them to be killed with standard therapies (Kery and Papandreou, 2020).

The anti-diabetic drug metformin acts via inhibition of mitochondrial complex I and has been shown to reduce oxygen consumption in cancer cells as well as alleviating tumour hypoxia (Wheaton et al., 2014; Zannella et al., 2013). Over the past 15 years there has been a great interest in repurposing this drug for cancer treatment, exemplified by numerous large randomised clinical trials in varied tumour types (Lord and Harris, 2023; Kalinsky et al., 2014; Hadad et al., 2011; Curry et al., 2017; Kitson et al., 2019). However, results are currently disappointing (Vancura et al., 2018).

The anti-malarial drug atovaquone acts via inhibition of mitochondrial complex III and has been shown clinically to reduce hypoxia in NSCLC patients (Skwarski et al., 2021). Atovaquone rapidly decreases the OCR of a wide range of cancer cell lines by up to 80 %, at pharmacological concentrations (Ashton et al., 2016). Reduction of the OCR in 3D spheroid models results in a decrease of the central hypoxic region, increasing oxygen availability throughout the spheroid (Grimes et al., 2014; Kelly et al., 2014; Secomb et al., 1995). Several clinical trials have tested or are in the process of testing atovaquone as a potential cancer therapeutic (https://clinicaltrials.gov/search?intr=Atovaquone). The ATOM clinical trial showed large reductions in hypoxic tumour volumes after treatment with atovaquone in NSCLC (Skwarski et al., 2021). The ARCADIAN trial is currently establishing the maximum tolerable dose of atovaquone with radical chemotherapy for NSCLC patients (NCT04648033).

1.2.6 The biological response to hypoxia

Just as the cellular composition of the TME is heterogenous, oxygen levels also fluctuate in a spatial and temporal setting. The importance of this is that the biological response to hypoxia is dependent on the actual level of oxygen.

The DNA damage response (DDR)

The DDR occurs in severe hypoxia, where the activity of the enzyme responsible for nucleotide production (ribonucleotide reductase) is compromised, as it uses oxygen as an essential co-factor (Foskolou et al., 2017). This results in a reduction of dNTP levels and replication stress (Pires et al., 2010). The accumulation of single-stranded DNA at replication forks induces ataxia telangiectasia and rad3-related (ATR)-mediated signalling, including H2AX, CHK1 and p53 phosphorylation (Bencokova et al., 2009;

Olcina et al., 2013). Ataxia telangiectasia mutated (ATM)-mediated signalling is also activated in hypoxia, despite the lack of detectable DNA damage (Bencokova et al., 2009; Olcina et al., 2013). Together, ATR and ATM work to protect replication forks, minimising the risk of further genomic instability (Olcina et al., 2010; Bristow and Hill, 2008). More recently, the accumulation of RNA/DNA hybrids known as R-loops have been found to contribute to the hypoxia-induced DDR (Ramachandran et al., 2021; Ma et al., 2023).

The unfolded protein response (UPR)

Severe hypoxia can interfere with protein folding, leading to an accumulation of misfolded proteins and unfolded proteins, resulting in ER stress (Lee et al., 2020b; Feldman et al., 2005). To alleviate this ER stress and ensure cell survival, the UPR is triggered to reduce protein synthesis and increase protein folding capacity, through three pathways (Koumenis and Wouters, 2006; Rzymski and Harris, 2007). The UPR includes the rapid phosphorylation of eukaryotic initiation factor 2α (eIF2α) by the ER kinase PERK, leading to inhibition of mRNA translation initiation. After longer periods of stress, the mRNA cap-binding complex (eIF4F) is disrupted inhibiting the transcript recruitment step of mRNA translation (Bristow and Hill, 2008).

Hypoxia-inducible factors (HIFs)

HIF-1 is the primary transcription factor associated with hypoxia and is stabilised in both mild and severe hypoxic conditions and will be discussed in more detail next.

1.2.7 Hypoxia-inducible factors (HIFs)

The importance of oxygen to life has been known for hundreds of years, with most of eukaryotic life utilising it as the terminal electron acceptor to produce energy (Webb et al., 2009; Lee et al., 2020a). However, the mechanism of how the body senses oxygen

was elusive until the late twentieth century (Lee et al., 2020a). Semenza, Ratcliffe and Kaelin were awarded the Nobel Prize in Physiology or Medicine for their discovery of the HIF family of transcription factors as master regulators of oxygen homeostasis (Semenza, 2012a; Zhang et al., 2019b; Harris, 2002; Semenza, 2012b).

HIF-1 was discovered in renal cells, where the production of erythropoietin (EPO) was found to increase in response to low oxygen levels (Semenza and Wang, 1992; Wang et al., 1995; Wang and Semenza, 1995; Fandrey et al., 2019). EPO is a hormone that controls red blood cell production, this process increased erythrocyte production, raising the oxygen carrying capacity of the blood (Semenza and Wang, 1992; Taylor and Scholz, 2022). A DNA sequence in the 3'-flanking region of the human EPO gene that functioned as a hypoxia-inducible enhancer was identified (Semenza et al., 1991; Pugh et al., 1991). From this, the nuclear protein complex, now termed HIF-1, was discovered (Semenza and Wang, 1992). HIF-1 signalling was shown to operate in non-EPO producing hypoxic cells, implying the existence of a ubiquitous oxygen-sensing mechanism in mammalian cells (Wang and Semenza, 1993; Maxwell et al., 1993).

HIF-1 is a heterodimeric DNA-binding complex composed of two subunits containing basic helix-loop-helix domains of the PAS family (Wang et al., 1995; Jiang et al., 1996a). The heterodimer subunits are the hypoxic response factor HIF-1α and the constitutively expressed HIF-1β, also known as the aryl hydrocarbon receptor nuclear translocator (ARNT) (Yu et al., 1998; Jiang et al., 1996b). HIF-1β had been previously identified, contributing in combination with the aryl hydrocarbon receptor (AHR) to the transcriptional response to xenobiotics (Hoffman et al., 1991; Reyes et al., 1992; Reisz-Porszasz et al., 1994; Hankinson, 1995). HIF-1α is localised in the cytoplasm whereas, HIF-1β is a nuclear protein and its production is independent of oxygen level (Maxwell et

al., 2001). HIF-1 is a highly conserved transcription factor and is expressed in the nucleated cells of all metazoan species analysed to date (Semenza, 2011; Taylor and McElwain, 2010). HIF-1β heterodimerises with other basic helix-loop-helix-PAS proteins and is present in excess therefore, HIF-1α protein levels determine the transcriptional activity of the HIF-1 complex (Semenza et al., 1996). The HIF-1 protein complex affects gene transcription by binding to the hypoxia-response elements (HREs) of target genes at the core pentanucleotide sequence RCGTG (Weidemann and Johnson, 2008).

There are three isoforms of HIF-α (HIF-1α, HIF-2α and HIF-3α) all encoded by distinct gene loci (Wang et al., 1995; Tian et al., 1997; Ema et al., 1997; Flamme et al., 1997; Hara et al., 2001; Maynard et al., 2003; Heidbreder et al., 2003; Makino et al., 2001, 2002; Hoffman et al., 1991; Hirose et al., 1996; Ikeda and Nomura, 1997; Hogenesch et al., 1998, 2000). HIF-1α can be stabilised in a wide range of normal tissues whereas, HIF-2α has more limited tissue expression (Wiesener et al., 2003). The expression of HIF-3α has been less well studied and its role is not fully understood (Hara et al., 2001).

As mentioned, HIFs are present in normal tissues exposed to hypoxia, and they are required for embryogenesis (Mie Lee et al., 2001). High HIF-1 mRNA and protein levels are seen in the foetal lung, and the entire HIF system is in place as early as 8 weeks in human development (Groenman et al., 2007; Grover et al., 2007; Asikainen et al., 2005). HIFs mediate adaptive physiological responses to hypoxia to ensure the accurate regulation of oxygen delivery and consumption. Hypoxic tumour cells have hijacked the HIF-1 machinery to adapt and survive in harsh tumour conditions, promoting the continuation of tumorigenesis (Semenza, 2012b).

The mRNA levels of HIF-1α are stable in both normoxia and hypoxia however, the protein levels are different. In well oxygenated conditions, HIF-1α subunits have a short half-life whereas, at oxygen concentrations below 6 % the HIF-1α protein accumulates.

In normoxia, the von Hippel-Lindau tumour suppressor protein (VHL) binds to the protein stabilisation domain of HIF-1α and targets it for degradation (Iliopoulos et al., 1996; Kaelin and Maher, 1998). VHL is the substrate recognition component of an E3 ubiquitin ligase complex that results in polyubiquitylation of HIF-1α and its subsequent proteasomal degradation by the proteasome (Maxwell et al., 1999; Ohh et al., 2000; Tanimoto et al., 2000). Therefore, HIF-1α is continuously synthesised and degraded in normoxic cells. The binding of VHL is dependent on the hydroxylation of two proline residues (Pro-402 and Pro-564) in the oxygen-dependent degradation domain (ODDD) of HIF-1α (Jaakkola et al., 2001; Ivan et al., 2001). The presence of the hydroxyl group excludes a water molecule from the VHL:HIF-1α interface, allowing two additional hydrogen bonds to form between the proteins, stabilising the interaction and enhancing ubiquitylation. Hydroxylation of HIF-1α is catalysed by prolyl hydroxylase domain proteins (PHDs) which use molecular oxygen as a substrate, so they confer sensitivity to oxygen levels. The PHDs are non-heme Fe(II)- and 2-oxoglutarate-dependent dioxygenases that split molecular oxygen, one oxygen atom is inserted into the HIF-1α peptide at the prolyl residue and the other reacts with 2-oxoglutarate to give succinate and CO_2 as products. There are four isoforms of the PHD enzymes that have been identified, with only PHD 1-3 shown to hydroxylate HIF-1α (Epstein et al., 2001). Evidence also suggests that PHD2 is the primary isoform responsible for HIF-1α hydroxylation *in vivo*. The activity of PHDs is inhibited in hypoxia as their mode of action is dependent on

molecular oxygen. Reduced hydroxylation of HIF-1α leads to its stabilisation, allowing it to accumulate and translocate into the nucleus where it can dimerise with HIF-1β (***Figure 1.6***).

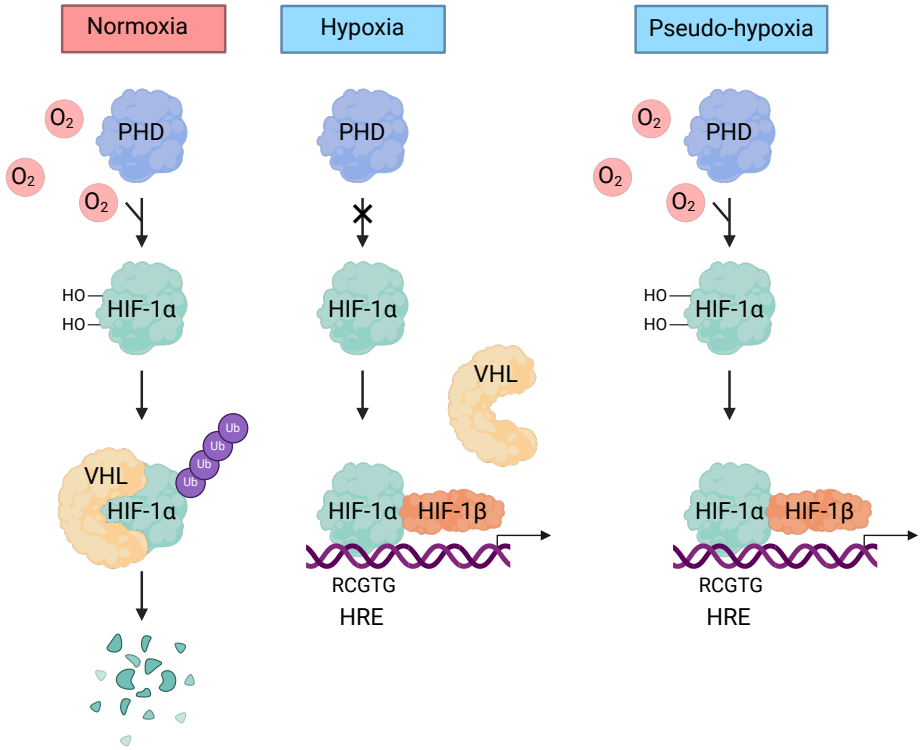


Figure 1.6: **Regulation of hypoxia-inducible factor (HIF).** HIF is regulated in normoxia by the action of VHL and PHD which lead to its ultimate degradation by the proteosome. In hypoxia these enzymes are inhibited, and HIF can be stabilised and travel to the nucleus where it can alter gene transcription. Pseudo-hypoxia can occur when VHL is lost leading to stabilised HIF-1α in normoxia. Created with BioRender.com.

The activation of gene transcription by the HIF-1 complex in the nucleus is regulated by hydroxylation. When oxygen is present, hydroxylation happens at an asparagine residue (Asn 803) within the C-terminal transactivation domain of HIF-1α. Hydroxylation is catalysed by the asparaginyl hydroxylase factor-inhibiting HIF (FIH), which uses molecular oxygen and 2-oxoglutarate as substrates and produces succinate and CO_2. This hydroxylation blocks the binding of transcriptional co-activators CBP and p300. Whereas in hypoxia, this hydroxylation does not occur, and co-activator proteins are

recruited to the HIF-1 complex. CBP and p300 interact with transactivation domains (TADs) in the C-terminal half of HIF-1α (amino acids 531-575 and 786-826) allowing binding of the HIF-1 complex to HREs within regulatory DNA regions of HIF-1 responsive genes. HIF expression activates the transcription of 100's of genes which go on to elicit a cellular response.

Mutations of VHL can frequently be seen in renal clear cell carcinoma (RCC), resulting in accumulation of HIF-1α in normoxia, and an effect known as pseudo-hypoxia. The phenotype of these tumours is characterised by the constant stabilisation of HIF-1α leading to transactivation of target genes and loss of VHL-mediated tumour suppression. HIF-1 also results in the repression of many genes via indirect mechanisms including the expression of transcriptional repressors (Mole et al., 2009; Yun et al., 2002; Kulshreshtha et al., 2007). As a result, HIF-1 has key roles in angiogenesis, cell proliferation and survival, epithelial-mesenchymal transition, stem-cell maintenance, invasion, metastasis and resistance to radiotherapy and chemotherapy (Wu et al., 2011b; Liao and Johnson, 2007; Barnhart and Simon, 2007; Suda et al., 2011; Wang et al., 2011; Zhang et al., 2007; Luo et al., 2011b; Franovic et al., 2007; Chi et al., 2009; Esteban et al., 2006; Krishnamachary et al., 2006; Mak et al., 2010; Sullivan and Graham, 2007; Krishnamachary and Semenza, 2007; Wong et al., 2011; Moeller et al., 2007; Rohwer and Cramer, 2011). As hypoxia is characterised by an imbalance in oxygen delivery and consumption, HIF-1 acts to counteract this (Denko, 2008). For example, increased oxygen delivery is achieved by enhanced expression of angiogenic growth factors, including EPO and VEGF (Giaccia, 1996; Semenza, 2001; Pepper et al., 1991, 1992; Forsythe et al., 1996). Decreased oxygen consumption is achieved by altering metabolism, a shift to glycolytic metabolism is achieved by increasing expression of

genes such as GLUT1, and oxidative phosphorylation (OxPhos) is repressed by enhancing PDK1 expression (Denko, 2008; Papandreou et al., 2006).

High HIF-1 levels within tumours are associated with aggressive phenotypes and increased risk of mortality (Kim et al., 2009; Giatromanolaki et al., 2001; Ioannou et al., 2009; Jacoby et al., 2010; Swinson et al., 2003; Yohena et al., 2009). Owing to the many roles of HIF-1 in the cell, it has been reported as a therapeutic target. A growing number of HIF-inhibitors have been identified as cancer therapeutics over the past few decades (Fukuda et al., 2007). Examples include histone-deacetylase (HDAC) inhibitors such as vorinostat, which can promote the degradation of HIF-1α protein. However, none of these inhibitors have been currently translated into the clinic for the treatment of cancer (Bui et al., 2022). Reasons for this include problems with compound development, which halted the phase I trial of EZN-2968, an agent designed to inhibit HIF-1 mRNA expression. Other factors for failure of these drugs include off-target effects, lack of patient stratification for hypoxic tumours, timing of administration particularly when used in combination with other agents and HIF-2α compensation.

1.3 Redox

1.3.1 Defining redox

The word 'redox' is comprised of reduction and oxidation. Reduction is defined as the gain of electrons, and oxidation as the loss of electrons. A key role of redox in the cell is to facilitate cellular respiration. Electrons are transferred from glucose molecules through the ETC, producing ATP. In the cell, the components of redox need to be maintained in a balanced state, otherwise damage to DNA, proteins and lipids and subsequently programmed cell death can occur (Perillo et al., 2020). A see-saw analogy is often used to depict redox balance in the cell, where ROS and antioxidants change in a dynamic fashion to alter homeostatic status and maintain redox balance (Le Gal et al., 2021) (***Figure 1.7***).

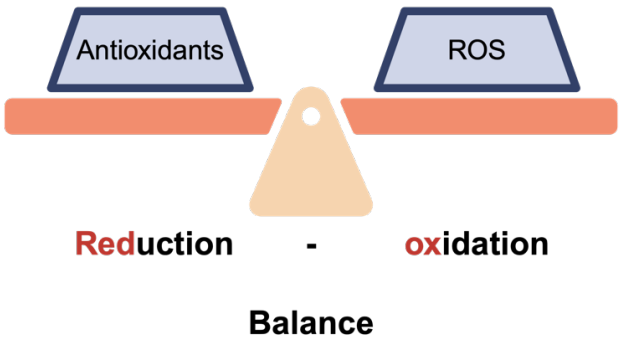


Figure 1.7: **Redox balance.** Redox homeostasis in the cell is maintained by the proportion of ROS to antioxidants, this balance is tightly regulated to ensure cell survival. Created with BioRender.com.

1.3.2 Reactive Oxygen Species (ROS)

ROS are defined as chemical species derived from molecular oxygen, that are reactive towards macromolecules in the cell (Glasauer and Chandel, 2013). ROS influence the redox environment in the cell by taking part in the transfer of electrons between different cellular components. ROS can be both beneficial and detrimental to cell survival, meaning they must be tightly regulated by the antioxidant machinery. There are other

oxidant species present in the cell as well as ROS, such as reactive nitrogen species (RNS) and oxidised lipids (***Table 1.2***).

Table 1.2: **ROS species in the cell.** Radical and non-radical oxidant species present in the cell, along with their production source, estimated half-life and function.

Oxidant species	Production	Half-life	Function
Superoxide ($O_2^{\bullet-}$)	Mitochondrial ETC (complex I and III), NOX and peroxisomes	~1-4 μs	Targets Fe-S clusters in proteins to release iron, easily dismutated to H_2O_2, can form peroxynitrite (Keyer and Imlay, 1996)
Hydroxyl radical (•OH)	Reactions of H_2O_2 with O_2 and Fenton reaction	~1 ns	Lipid peroxidation, DNA oxidation and amino acid oxidation (D'Autréaux and Toledano, 2007)
Peroxyl radical (ROO•)	Formed during lipid and other peroxidation chain reactions or derived from enzyme-generated lipid hydroperoxides	~1-10 ms	May serve as a signalling agent as it can diffuse over considerable distances (Sies et al., 2022)
Alkoxyl radical (RO•)	Formed by one-electron reduction of organic hydroperoxides by metal ions	~1 ms	Can amplify radical chain reactions, limited evidence for a direct role in signalling but can rearrange to longer-lived radicals (Sies et al., 2022)
Nitric oxide (NO•)	Nitric oxide synthase, xanthine oxidase	~1-5 s	Reacts with $O_2^{\bullet-}$ to form peroxynitrite (Radi, 2018)
Hydrogen peroxide (H_2O_2)	Mitochondria, ER, NOXs, peroxisomes, $O_2^{\bullet-}$ dismutation by SOD, xanthine oxidase	~1 ms-hrs	Main cellular signalling oxidant. Oxidises reactive Cys residues on proteins, can also target Met and Tyr (Stöcker et al., 2018)
Peroxynitrite ($ONOO^-$)	Reaction of $O_2^{\bullet-}$ with nitric oxide	~1 ms	Reacts with proteins to cause oxidation or nitration of amino acids, DNA to induce ds breaks and lipids causing lipid peroxidation (Harris and DeNicola, 2020)
Hypochlorous acid (HOCl)	Myeloperoxidase	~1-5 s	Released extracellularly, HOCl and their products are potential secondary signalling events (Sies et al., 2022)
Singlet oxygen ($^1O_2$)	Photosensitisation reactions	1-4 μs	Important mediators of damage to surface organs (Sies et al., 2022)
Ozone (O_3)	Interaction of UV radiation with O_2	~1-10 mins	Reacts with double bonds (PUFAs, cholesterol) to form peroxides (Sies et al., 2022)
Nitrosoperoxycarbonate ($ONOOCO_2^-$)	Reaction of CO_2 with $ONOO^-$	~1 ms	Decompose to $CO_3^{\bullet-}$ and $\bullet NO_2$ which in turn initiate selective oxidation and nitration of guanine

			in DNA leading to guanine-thymidine crosslinks (Shafirovich and Geacintov, 2017)
Lipid peroxide (LOOH)	Oxidation of PUFAs by ROS	~mins to hrs	Act as signalling molecules to stimulate inflammation, apoptosis, or ferroptosis (Hayes et al., 2020)

The majority of oxygen consumption in the cell takes place in the mitochondria, which is the primary source of free radical species (McElroy and Chandel, 2017). Both complex I and III are reported to produce free radical species (Chen et al., 2003). Therefore, the mitochondria act as a signalling organelle by releasing both ROS and TCA cycle metabolites to elicit a cellular change (Chandel, 2015). NADPH oxidase (NOX) enzymes are the other main point of free radical formation in the cell however, there are other sources (***Table 1.3***) (Cairns et al., 2011).

Table 1.3: **ROS producing components in the cell.** Free radical species can be produced intracellularly by specific organelles and various enzymes. (Holmström and Finkel, 2014).

ROS generator	Organelle/enzyme	ROS production
Mitochondria	Organelle	Primary source of ROS in the cell, from complex I and III
NOX enzymes	Enzyme	Produces ROS used in cell signalling and protein modulation
Lipoxygenase	Enzyme	Produces ROS as part of enzymatic reaction cycle
Xanthine oxidase	Enzyme	Produces ROS as part of enzymatic reaction cycle
Cyclooxygenase	Enzyme	Produces ROS as part of enzymatic reaction cycle
Cytochrome P450 monooxygenase	Enzyme	Produces ROS as part of enzymatic reaction cycle
Nitric oxide synthase	Enzyme	Produces ROS as part of enzymatic reaction cycle

ER	Organelle	Produces ROS predominantly when the cell is under ER stress
Peroxisomes	Organelle	Produces ROS during their role in metabolising LCFAs

1.3.3 Consequences of ROS

Among the variety of oxidant species present both inside the cell and extracellularly, hydrogen peroxide (H_2O_2) and superoxide ($O_2^{\bullet-}$) are among the most studied (D'Autréaux and Toledano, 2007; Sies et al., 2022; Harris and DeNicola, 2020) (***Figure 1.8***). H_2O_2 is often thought to be the main ROS in the cell, as it is the terminal species formed by most radicals and has increased stability over other species. The main role of H_2O_2 is to affect cell signalling via protein oxidation, which can be done at sites distal from its production, due to its ability to diffuse through membranes (Harris and DeNicola, 2020).

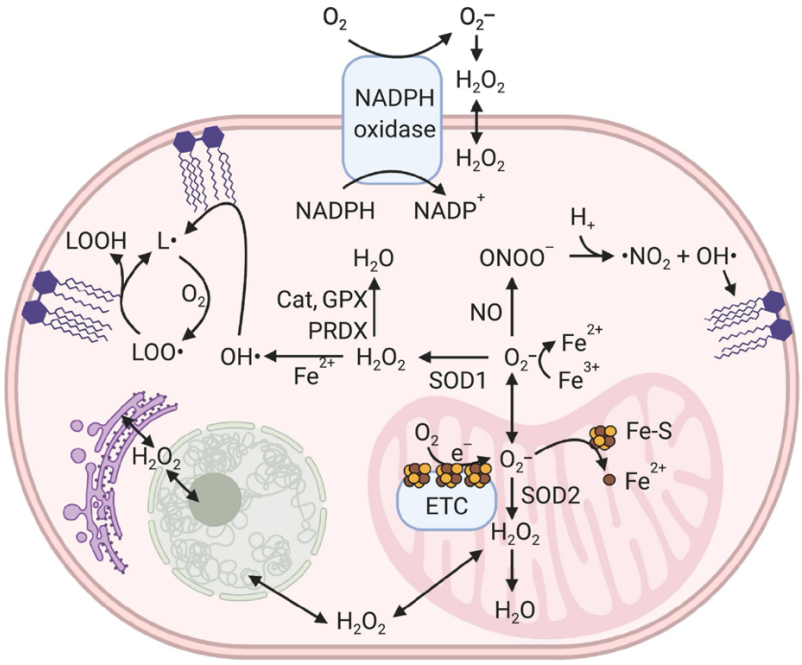


Figure 1.8: **Redox elements in the cell.** Synthesis sites for oxidant species in the cell: superoxide ($O_2^{\bullet-}$), hydrogen peroxide (H_2O_2), peroxynitrite ($ONOO^-$), peroxyl radicals (•OH), lipid radicals (L•), lipid peroxide radicals (LOO•) and lipid peroxides (LOOH) and the interconnection between them. Reprinted from (Harris and DeNicola, 2020), with permission (license number: 5873541355519).

In cells, H_2O_2 levels are usually in the low nanomolar range, in contrast to the short lived $O_2^{\bullet-}$ radical which exists at picomolar concentrations (Chance et al., 1979). $O_2^{\bullet-}$ production is a consequence of the reaction between an electron and molecular oxygen, at complex I and III of the ETC (Murphy, 2009). Complex I produces $O_2^{\bullet-}$ on the matrix side and complex III produces $O_2^{\bullet-}$ towards the matrix and IMS (Brand, 2020; Mailloux, 2021). The primary target of $O_2^{\bullet-}$ are Fe-S clusters, due to the high electrostatic attraction of $O_2^{\bullet}$, whereas Cys residues are ideally suited for H_2O_2 (D'Autréaux and Toledano, 2007). Dismutation of the short lived $O_2^{\bullet-}$ to H_2O_2 occurs via superoxide dismutases (SODs) or non-enzymatically (Harris and DeNicola, 2020). Within the cell, H_2O_2 and $O_2^{\bullet-}$ are interconnected with the other oxidant species present, such as hydroxyl radicals and peroxynitrite (*Figure 1.8*). ROS signalling can also take place outside of the cell, where H_2O_2 levels are 1-5 micromolar, and can allow signalling to the stromal cells of the TME (Forman et al., 2016; Cheung and Vousden, 2022).

1.3.4 ROS-mediated biological response

Depending on the amount of free radical species and time they are present for in the cell, different biological processes can be triggered (***Figure 1.9***). ROS are known to act as important signalling molecules. The function of ROS in altering cellular signalling pathways has been well documented however, it was seen as controversial for some time (D'Autréaux and Toledano, 2007). Scepticism arose from the fact that signalling networks are activated with high specificity in the cell in response to distinct stimuli. Whereas, for many years ROS were seen to be random and unregulated (Holmström and Finkel, 2014). It is now established that ROS carry out their function by reversible oxidation and reduction of specific Cys residues in target proteins (Holmström and Finkel, 2014). One

of the earliest observations in support of a role for ROS in signal transduction was a burst of ROS that was seen to precede Tyr phosphorylation after growth factor stimulation (Sundaresan et al., 1995; Bae et al., 1997).

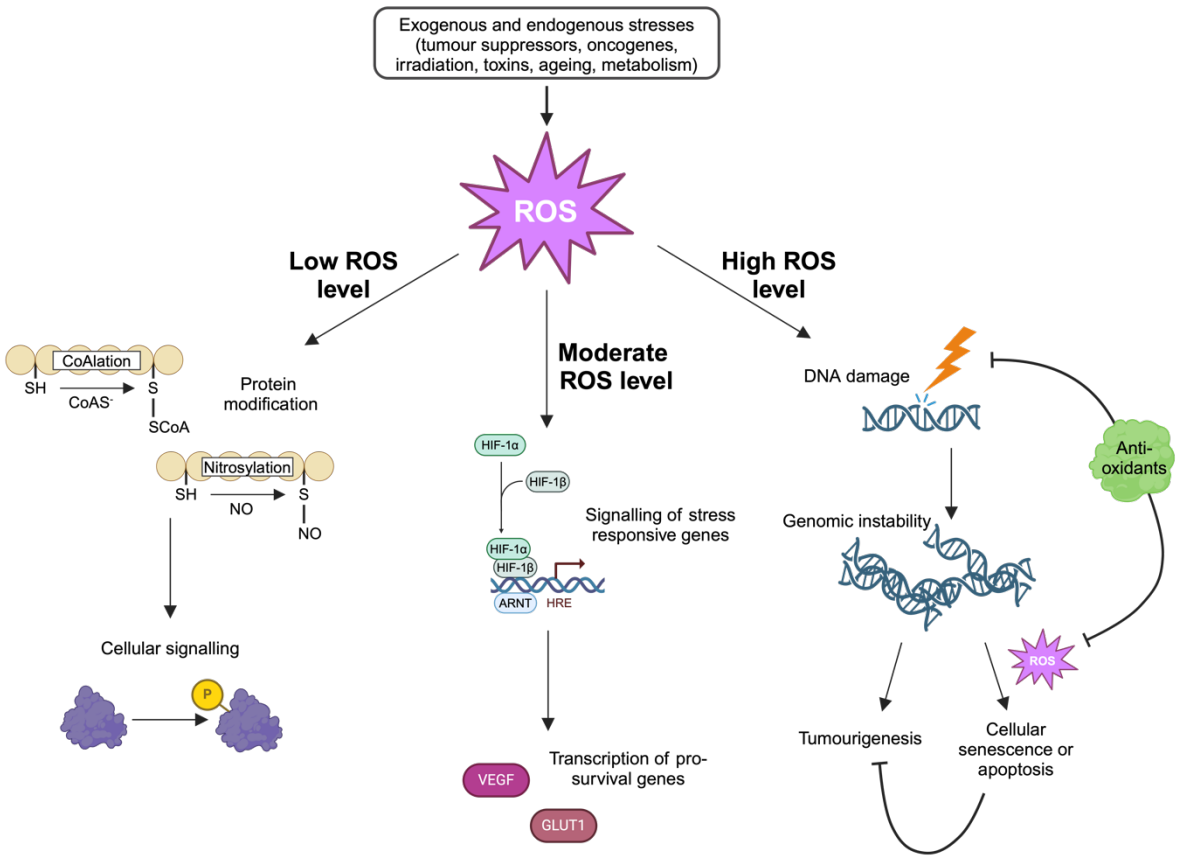


Figure 1.9: **Concentration dependent ROS signalling.** At low levels ROS can affect essential cellular signalling by inducing reversible protein modifications, at moderate levels stress responsive signals are activated to help cell survival and at high levels programmed cell death is initiated. Antioxidants limit cellular damage but also help withstand induction of cell death, accelerating tumour formation (Holmström and Finkel, 2014; Harris and DeNicola, 2020). Created with BioRender.com.

The effect ROS have on cells is dependent on concentration. At low levels ROS can increase cell proliferation and survival, through post-translational modification of kinases and phosphatases (Lee et al., 2002; Cao et al., 2009; Giannoni et al., 2005). This low-level production of ROS is thought to be driven by NADPH and NOX enzymes, and is essential for cellular signalling, highlighting ROS as critical signalling molecules within the cell (Cairns et al., 2011). At moderate levels, ROS begin to signal the expression of

stress responsive genes such as HIF-1α, which goes on to trigger downstream transcription of pro-survival genes such as VEGF and GLUT1 (Gao et al., 2007; Bell et al., 2005).

ROS elicit their effect on cell signalling via protein oxidation, both reversible and irreversible oxidation can occur. Reversible protein oxidation happens when redox-reactive cysteine residues on proteins are oxidised, forming reactive sulfenic acid (-SOH) which can form disulfide bonds with nearby cysteines (-S-S-) or undergo further oxidation to sulfinic acid ($-SO_2H$), that can later be reversed by thioredoxin/peroxiredoxin systems (Roos and Messens, 2011; van Dam et al., 2021). Further oxidation of Cys residues, in target proteins, to sulfonic acid ($-SO_3H$) is an irreversible modification and can ablate protein function (Ray et al., 2012). Other modifications including glutathionylation, CoAlation, persulfidation and *S*-nitrosothiol formation can take place to protect proteins from terminal oxidation and alter their function to cause metabolic changes (Cortese-Krott et al., 2017; Tsuchiya et al., 2018, 2017; Matsui et al., 2020). The signalling events that happen as a result of protein oxidation are coupled to metabolism, phosphorylation cascades, transcriptional regulation and more (Holmström and Finkel, 2014; Parvez et al., 2018; Forman et al., 2014). Pathways sensitive to ROS usually transduce cytoplasmic signals to the nucleus, where gene transcription is influenced (Perillo et al., 2020).

At high levels, ROS can start to damage important macromolecules in the cell including lipids, proteins and DNA (Schieber and Chandel, 2014). Excess ROS can lead to pathological states such as neurodegenerative disease, cardiovascular disease and cancer (Sies, 2015). The DNA damage produced by increased ROS is a result of oxidation of nucleobases, particularly guanine and adenine (Harris and DeNicola, 2020). Unrepaired 8-oxoguanine is considered among the most mutagenic DNA lesions, leading

to G to T conversion and eventually mutagenesis (Grollman and Moriya, 1993; Egger et al., 2004). Normal cells can have oxidised guanine in 1 in every 100,000, which increases to 35-50 % in transformed cells (Valko et al., 2006). The consequence of excessive ROS accumulation is the activation of protein kinase Cδ leading to senescence or permeabilisation of the mitochondria causing release of cytochrome *c* and apoptosis (Ramsey and Sharpless, 2006; Takahashi et al., 2006; Garrido et al., 2006; Han et al., 2003).

1.3.5 Antioxidants

Antioxidants are nucleophilic and reductant molecules able to react with oxidants (electrophiles) and give them one/two electrons (Espinosa-Diez et al., 2015). In the cell, antioxidants are substances capable of directly or indirectly minimising damage to biomolecules caused by free radical species (Stone et al., 2023). The antioxidant response is activated in the cell to counteract potentially harmful effects of oxidant pathways. Production of antioxidants come from either endogenous sources (generated *in situ*) or exogenous sources (food) (Pham-Huy et al., 2008). The antioxidant system in the cell is composed of enzymes and proteins that work together to maintain redox balance (***Table 1.4***).

Table 1.4: **Components of the antioxidant response.** Enzymatic and non-enzymatic components of the cellular antioxidant response

Antioxidant machinery component	Function
GSH pathway (GSH, GPx, GST, GR)	GPxs and GSTs use GSH to alleviate cellular stress, resulting in GSSG which can be reduced back to GSH by GR (Zhang and Forman, 2012)
Trx pathway (Trx, TrxR)	Reduced Trx orchestrates the reduction in oxidised cysteines found in numerous proteins influenced by ROS (Hasan et al., 2022)
NADPH	Co-factor that maintains GSH and Trx in a reduced state (Ju et al., 2020)
Peroxiredoxins (PRDXs/Prxs)	Abundant family of enzymes with high catalytic activities that reduce >90 % of cellular peroxides, reduce H_2O_2 to H_2O and contribute to the elimination of NO•, reduction of $ONOO^-$ and protein dinitrosylation (Elko et al., 2019)
Sulfaredoxin (Srxs)	Reduces PRDXs that are overoxidised to sulfinic acid (Harris and DeNicola, 2020)
Superoxide dismutases (SOD1, SOD2, SOD3)	SODs catalyse the dismutation of $O_2^{\bullet-}$ to H_2O_2 and O_2 (Zelko et al., 2002)
Catalase (CAT)	Principal antioxidant enzyme of the peroxisomes. Stops formation of •OH by converting H_2O_2 to O_2 and H_2O, protects tumour cells from ROS-induced apoptosis (Deisseroth and Dounce, 1970; Heinzelmanna and Bauer, 2010)
KEAP1/NRF2 pathway	KEAP1 is a ROS sensor and principal suppressor of NRF2. NRF2 is the master regulator of the antioxidant response and controls the expression of genes vital for cellular defence (Baird and Yamamoto, 2020)
GPX 1-8	Enzyme family that drives the reduction of H_2O_2 and organic hydroxides to their corresponding alcohols with GSH as the reducing agent, quenches lipid peroxides and contributes to the elimination of NO•, reduction of $ONOO^-$ and protein dinitrosylation (Benhar, 2018; Brigelius-Flohé and Maiorino, 2013)
Sestrins (SESN1, SEN2, SESN 3)	Exert indirect antioxidant activity, in part by activating NRF2 and inhibiting mTORC1 (Rhee and Bae, 2015; Sánchez-álvarez et al., 2019)
Heme oxygenase isoenzymes (HMOX1, HMOX2)	Serve as indirect antioxidants by preventing free heme released from haemoproteins forming free radicals and participate in formation of bilirubin (Gozzelino et al., 2010)
Ferritin, ferroportin, metallothionein and ceruloplasmin	Proteins that sequester transition metals or transport them from the cell, acting as indirect antioxidants by supressing the formation of •OH from H_2O_2 by Fenton chemistry (Arosio et al., 2009; Pietrangelo, 2017)
Sirtuin 3 (SIRT3)	NAD^+-dependent deacetylase that indirectly increases scavenging of $O_2^{\bullet-}$ and increases generation of NADPH in the mitochondria (Kincaid and Bossy-Wetzel, 2013; Gomes et al., 2020)
N-acetyl choline (NAC)	ROS scavenger, controversial role with studies showing no benefit (Gao et al., 2007; Aitio, 2006; Sayin et al., 2014; Gal et al., 2015; Piskounova et al., 2015)

Vitamin C	Can eliminate various oxygen free radicals (Sinbad et al., 2019)
Vitamin E	Serves as a fat-soluble antioxidant that safeguards PUFAs within membranes from oxidation (Tappel, 1962)
Selenium	Chemical element that's impact is mainly seen through its incorporation into selenoproteins e.g. GPx, TrxR (Guillin et al., 2019)
Bilirubin, melatonin	Metabolites shown to have antioxidant effects (Vasavda et al., 2019; Bantounou et al., 2022)

The most abundant endogenous antioxidant is the enzyme cofactor glutathione (GSH) (Winterbourn and Hampton, 2008; Cairns et al., 2011). This tripeptide, composed of glutamate, cysteine and glycine, is produced via an ATP-dependent two-step process (Niu et al., 2021; Wu et al., 2004). The first step is catalysed by the rate limiting γ-glutamyl-cysteine ligase (GCL) and the second by glutathione synthetase (GSS) (Lu, 2013). The enzymes glutathione S-transferases (GSTs) and glutathione peroxidases (GPxs) use GSH as a cofactor (***Figure 1.10***). GSH can react with critical Cys residues in proteins, forming mixed disulphides, that can be reverted by GSTs (Espinosa-Diez et al., 2015). The action of GSTs can detoxify xenobiotics, in particular platinum-based drugs (Traverso et al., 2013). GPxs couple the oxidation of GSH with the detoxification of H_2O_2, where two molecules of GSH become one molecule of GSSG (Musaogullari and Chai, 2020). Oxidised GSSG is recycled via the action of glutathione reductase (GR) with the aid of FAD and NADPH (Kennedy et al., 2020). Regulation of *de novo* GSH synthesis and NADPH-dependent regeneration from oxidised GSSG is key to enabling cell survival (Asantewaa and Harris, 2021).

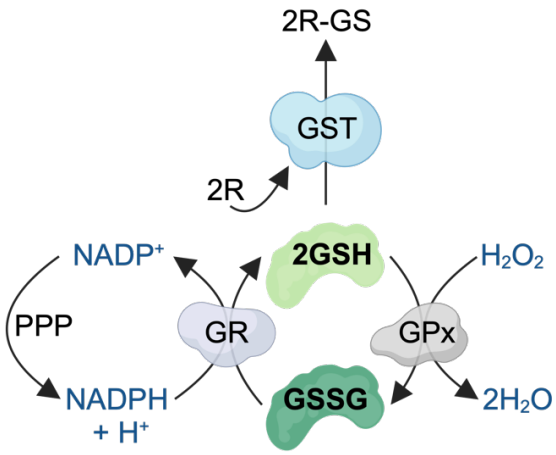


Figure 1.10: **Reactions of GSH with GPx and GST and regeneration of GSH via GR.** Glutathione peroxidase (GPx) metabolises H_2O_2, in the process oxidising 2 GSH molecules to 1 GSSG. Glutathione reductase (GR), in the presence of NADPH, reduces GSSG back to GSH. Glutathione S transferase (GST) uses GSH to conjugate and detoxify reactive electrophilic compounds (R). Created with BioRender.com.

Another key component of the antioxidant response is thioredoxin (Trx). There are three isoforms of this small redox-regulating protein identified in mammalian cells, cytosolic Trx1, mitochondrial Trx2 and SpTrx (expressed in spermatozoa) (Taniguchi et al., 1996; Spyrou et al., 1997; Miranda-Vizuete et al., 2001). There are three thioredoxin reductases (TrxR) TrxR1, TrxR2 and TGR (Sun et al., 2005). Trx can act by either directly quenching singlet oxygen and scavenging hydroxyl radicals or by indirectly reducing oxidised proteins (Powis and Montfort, 2001; Mitsui et al., 1992). Oxidised Trx can be recycled by TrxR with the assistance of NADPH, allowing it to go on and reduce more substrates (Lee et al., 2013).

Although, GSH and Trx are two of the major antioxidants in the cell, they do not act alone (***Figure 1.11***). NADPH is the critical cofactor that maintains both GSH and Trx in a reduced state (Ju et al., 2020). Another example of synergism in the antioxidant response are the Trx and sulfaredoxin (Srx) antioxidant networks. These work together to regenerate peroxiredoxins (PRDXs), a set of enzymes with high catalytic activity towards H_2O_2 (Harris

and DeNicola, 2020). PRDXs use their -SH groups as reducing equivalents and aid in the direct reduction of peroxides (e.g. H_2O_2) and different alkyl hydroperoxides (Karlenius and Tonissen, 2010). The Trx system can reduce PRDX disulphide bonds and the Srx system can reduce overoxidised PRDXs to sulfinic acid (Harris and DeNicola, 2020).

Overall, the antioxidant machinery is necessary to keep ROS within a physiological range and protect cells from excessive ROS. An imbalance in redox homeostasis, resulting in an excess of ROS can lead to cellular stress. The accumulation of ROS in the cell is the precursor to a range of pathologies.

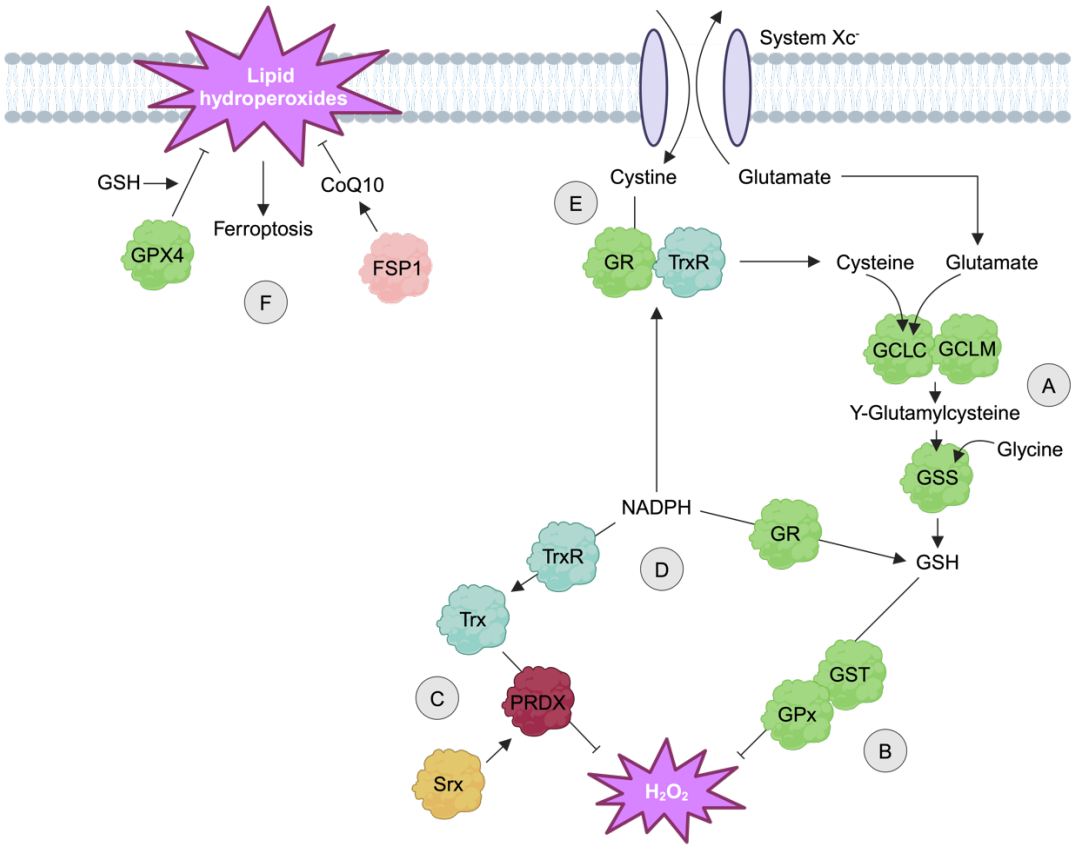


Figure 1.11: **Main components of the cellular antioxidant response.** A) GSH is synthesised in a two-step mechanism from cysteine, glutamate and glycine. B) GST and GPx use GSH as a cofactor to neutralise H_2O_2. C) Trx and Srx promote PRDX-mediated H_2O_2 detoxification. D) GR and TrxR regenerate GSH and Trx using NADPH. E) NADPH also facilitates cystine reduction to cysteine. F) Lipid peroxidation is controlled by either GPX4 or CoQ10 with ferroptosis suppressor protein 1 (FSP1). Created with BioRender.com.

1.4 Oxidative stress

1.4.1 Defining oxidative stress

An excess of free radical species in comparison to antioxidants is termed 'oxidative stress' and can be seen in a number of pathologies including neurodegenerative disease, cardiovascular disease and cancer (Sies, 2015). The cell undergoes approximately 1.5×10^5 oxidative insults per day, if this is increased or the scavenging of these species is reduced then the cell enters oxidative stress (Perillo et al., 2020). In this state, ROS lead to the transcription of genes to increase antioxidant capacity (Perillo et al., 2020). NRF2 is known as the master regulator of the antioxidant system, and once active allows for downstream detoxification governed by proteins such as GSH and Trx (Harris and DeNicola, 2020).

1.4.2 The role of NRF2 in oxidative stress

In response to an excess of ROS in the cell, NRF2 is activated (Hayes and Dinkova-Kostova, 2014; Hayes et al., 2016; Yamamoto et al., 2018). NRF2 is a basic region-leucine zipper type transcription factor, belonging to the CNC family of regulatory proteins (Espinosa-Diez et al., 2015). In unstressed conditions, NRF2 resides in the cytoplasm where it interacts with the actin-binding protein KEAP1 which is an adaptor for the E3 ligase CUL3 (Glasauer and Chandel, 2014). The complex formed between NRF2, KEAP1 and CUL3 facilitates the constitutive ubiquitylation and degradation of NRF2, giving it a half-life of 7-15 mins (Holmström and Finkel, 2014). Sulfhydryl groups within KEAP1 act as sensors for electrophiles and oxidants. Therefore, in the presence of free radical species, specific Cys residues within KEAP1 are oxidised resulting in a conformational change in the protein, preventing the binding of NRF2. The stabilisation of NRF2 increases

its half-life to 30-100 mins (Espinosa-Diez et al., 2015). In the nucleus, NRF2 can heterodimerise with small MAF proteins and go on to bind to antioxidant responsive elements (AREs) within regulatory regions of a number of genes (Glasauer and Chandel, 2014). The transcription of approximately 200 genes, whose protein products function as antioxidants, detoxification enzymes, heat-shock proteins and GSH-synthesis enzymes, are modulated by NRF2 (***Figure 1.12***) (Glasauer and Chandel, 2014).

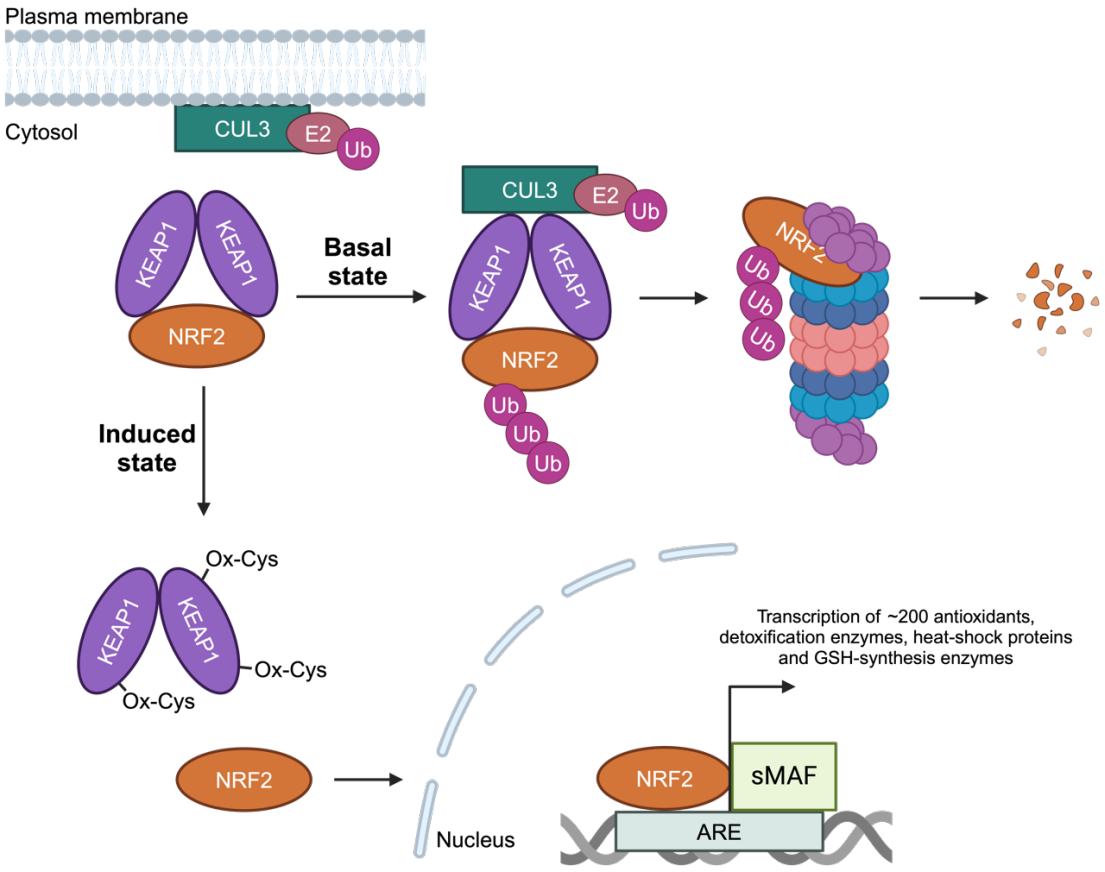


Figure 1.12: **NRF2 regulation.** In unstressed conditions NRF2 is in complex with KEAP1 and CUL3, resulting in the ubiquitination of NRF2 and its subsequent degradation. In a state of cellular stress, specific Cys residues on KEAP1 are oxidised preventing it binding with NRF2 and culminating in the translocation of NRF2 to the nucleus where it can bind small MAF proteins and lead to transcription of antioxidant genes (Espinosa-Diez et al., 2015). Created with BioRender.com.

1.4.3 Outcome of oxidative stress

NRF2 is an immediate responder to oxidative stress with contributions from other signalling pathways such as AP-1, NF-κB, FOXO, PGC-1α and HIF-1α (***Table 1.5***) (Hayes et al., 2020). These pathways act to reduce oxidative stress, returning the cell to homeostatic levels of redox. The final defence is programmed cell death (apoptosis) if the cell cannot be repaired, which can be controlled by p53 (Xiao et al., 2003). P53 can also lead to stabilisation of NRF2 in oxidative stress via p21, as p21 prevents the KEAP1-NRF2 interaction and preserves NRF2, this level of regulation is lost in cancers where p53 is mutated resulting in the loss of redox balance (Cairns et al., 2011; Chen et al., 2009).

NRF2 can regulate synthesis of GSH in two ways, the first being the expression of GCL that catalyses the rate limiting step in GSH synthesis and the second being regulation of the cysteine/glutamate antiporter (xCT) that controls the amount of cysteine in the cell, an amino acid required for GSH synthesis (Meister, 1983; Thimmulappa et al., 2002; Glasauer and Chandel, 2014). Additionally, NRF2 can promote production of NADPH by regulation of enzymes in the pentose phosphate pathway (PPP) and serine biosynthesis pathways (Harris and DeNicola, 2020; Wu et al., 2011a). Finally, Fe (II) homeostasis can also be controlled by NRF2 as one of its target genes produces heme oxygenase (HMOX1), which generates free Fe (II) from the breakdown of heme molecules. This free Fe (II) can then go on to participate in the Fenton reaction creating •OH radicals and lipid peroxides that trigger the cell death mechanism ferroptosis. This creates a paradox for NRF2, in that it is the master regulator of the antioxidant response but can also lead to oxidative stress. However, NRF2 also upregulates the expression of the genes encoding components of the ferritin complex, which converts Fe (II) to Fe (III), blocking it from entering the Fenton reaction (Orino et al., 2001).

Table 1.5: **Redox homeostasis associated genes regulated by members of the antioxidant transcription factor network.** Signalling pathways activated in response to cellular stress and the genes they transcribe that produce antioxidant proteins (Hayes et al., 2020).

Transcription factors that respond to oxidative stress / Function of gene products	NRF2	BACH1	AP-1	FOXO	PGC-1α	HIF-1α	HSF1	NF-κB	TP53
Scavenge ROS	CAT, PRDX1, PRDX6, GPX2		CAT, SOD1	CAT, PRDX1, PRDX3, PRDX5, SOD1, SOD2	CAT, PRDX3, PRDX5, GPX1, SOD2		PRDX4	CAT, GPX1, SOD1, SOD2	CAT, GPX1, SOD2
Are auxiliary antioxidants								SESN2	SESN1
Synthesise GSH	GCLC, GCLM, GSR1, SLC6A9, SLC7A11	↓GCLC, ↓GCLM, ↓SLC7A11	GCLC, GCLM		GCLM	GCLM, GLS1, SLC7A11	GCLM, GLS1	GCLC, GCLM	GLS2
Provide reduced Trx	Trx1, TrxR1	↓TrxR1		Trx2, TrxR2	Trx2		Trx2	Trx1, Trx2	
Reduce sulfinic acid	Srx1		Srx1						
Generate NADPH	G6PD, IDH1, ME1, PGD							G6PD	TIGAR
Metabolise heme/iron	FTH1, FTL1, HMOX1, SLC40A1	↓FTH1, ↓FTL1, ↓HMOX1, ↓SLC40A1	FTH1, HMOX1				FTH1, HMOX1	FTL1, HMOX1	
Detoxify xenobiotics	AKR1B10, AKR1C1, AKR1C3, ALDH3A1, CBR1, EPHX1, GSTs, NQO1, NQO2, PTGR1, UGT1A6	↓AKR1C3	GSTP1, NQO1				ALDH3B1	AKR1C1, GSTP1, NQO1	AKR1B10, ALDH4
Deacetylase activity					SIRT3				

1.4.4 Oxidative stress mediated mechanisms of cell death

The excess accumulation of ROS, that characterises oxidative stress, can result in damage to macromolecules within the cell, and oxidative cell death, of which there are various forms (An et al., 2024).

Ferroptosis

Ferroptosis is an iron-dependent form of non-apoptotic cell death, that is characterised by excessive accumulation of lipid peroxides and ROS (Pu et al., 2022; Dixon et al., 2012). Morphologically, biochemically and genetically ferroptosis is unlike other forms of cell death (Lu et al., 2018).

Ferroptosis can be triggered in both a GPX4-dependent and -independent manner. The xc^- transporter system that exchanges cystine for glutamate is key to the GPX4-dependent mechanism of ferroptosis. Cystine is reduced to cysteine which is one of the three amino acids that the cofactor GSH is composed of. If there is suppression of the xc^- transporter, then there will be reduced synthesis of GSH which is a cofactor for GPX4, an enzyme that is responsible for preventing lipid peroxidation. Therefore, reduced GPX4 function increases the occurrence of ferroptosis. FSP1 and DHODH act together in the GPX4-independent form of ferroptosis. NRF2, can have a role in ferroptosis as it induces genes involved in both the GPX4-dependent and -independent pathways (An et al., 2024). ROS produced from the ETC as a result of oxidative stress can directly lead to lipid peroxidation, and consequently ferroptosis (***Figure 1.13***). These ROS can react with ferrous ions (Fe^{2+}) to give •OH radicals which can go on to extract hydrogens from PUFAs (Subburayan et al., 2020). The highly reactive carbon centred •PUFA radicals then engage with oxygen producing PUFA peroxyradicals and culminating in the generation of PUFA

hydroperoxides (Ursini and Maiorino, 2020). The Fenton reaction can produce •OH radicals from H_2O_2 and Fe^{2+} ions (An et al., 2024).

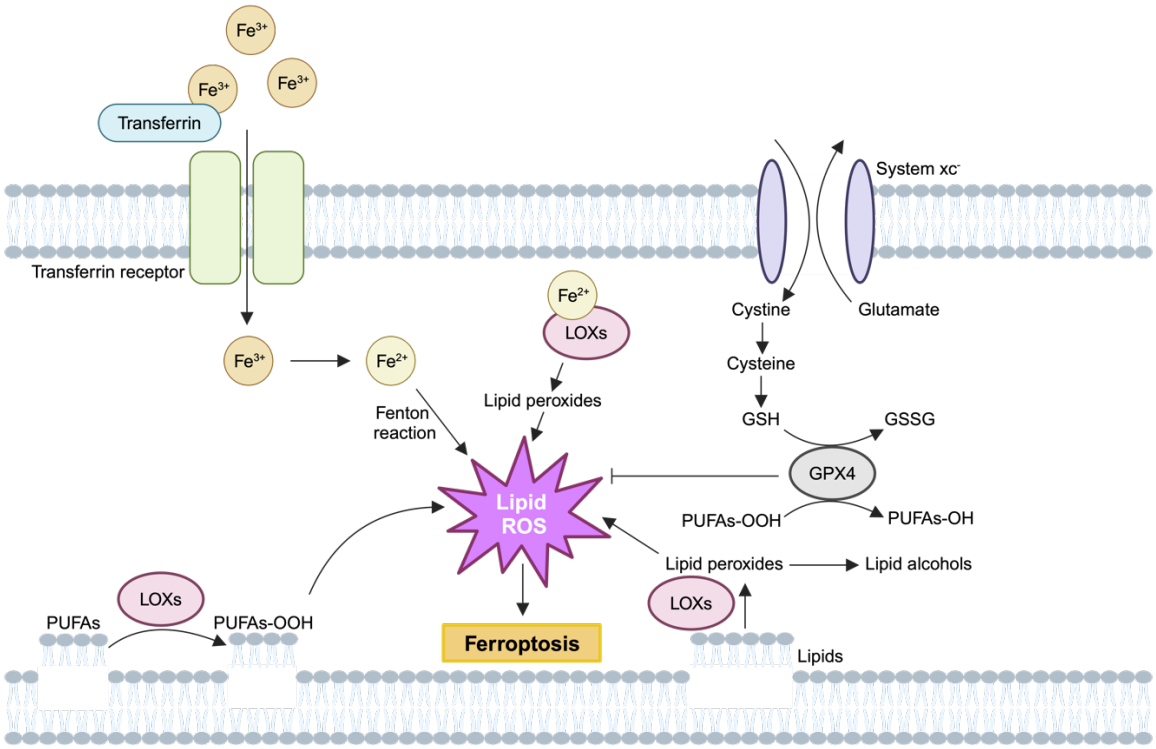


Figure 1.13: **Mechanism of ferroptosis.** Cell death via ferroptosis can occur through inhibition of the xc^- system or GPX4 activity. Lipid free radical species are also a large contributor to ferroptosis, primarily from the Fenton reaction or the peroxidation of PUFAs (Lu et al., 2018). Created with BioRender.com.

Apoptosis

Apoptosis is a well-studied form of cell death, characterised morphologically by cell shrinkage, chromatin condensation and the emergence of apoptotic bodies through cellular fragmentation (***Figure 1.14***) (Nössing and Ryan, 2022).

The mitochondrial apoptotic route responds to various stress signals including mitochondrial damage, ER stress and oxidative stress (An et al., 2024). Increased oxidative stress can lead to the formation of a mitochondrial permeability transition pore (MPTP), ultimately causing mitochondrial-driven apoptosis. The UPR can also result in apoptosis due to prolonged ER stress (Shin et al., 2014). ROS induced apoptosis is also

correlated with p53 activity, which can dampen pro-survival proteins such as MYC and BCL2 and elevate pro-apoptotic ones such as BAX (Liu et al., 2008; Shi et al., 2014; Wu et al., 2018).

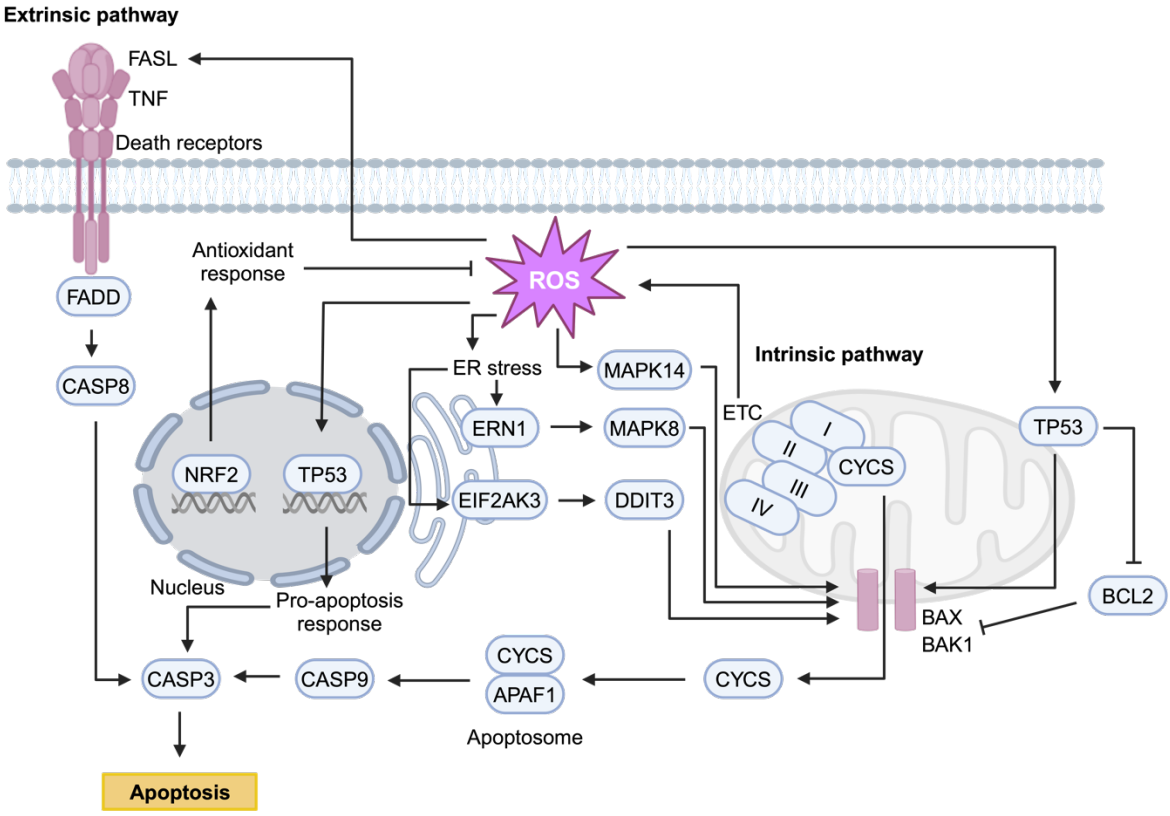


Figure 1.14: **Mechanism of apoptosis.** Cell death via apoptosis can occur via the intrinsic or extrinsic pathway (An et al., 2024; Yuan and Ofengeim, 2024). Created with BioRender.com.

Less well described mechanisms of cell death include necroptosis, pyroptosis, paraptosis, parthanatos and oxeitopsis, recently reviewed in (Park et al., 2023).

1.5 Cancer and Redox

1.5.1 ROS in cancer

Cancer cells can be characterised by a redox imbalance and specifically elevated levels of ROS (Perillo et al., 2020). Increased ROS levels in comparison to normal, untransformed cells have been reported in cancer cells and provide a therapeutic window (Szatrowski and Nathan, 1991). The increased level of ROS in cancer cells are due to elevated metabolic activity, oncogene activation (e.g. K-Ras or c-Myc mutations), increased cellular receptor signalling, mitochondrial dysfunction, peroxisome activity and increased activity of oxidases, cyclooxygenases, lipoxygenases and thymidine phosphorylase (Vafa et al., 2002; Liou and Storz, 2010; Storz, 2005; Szatrowski and Nathan, 1991; Babior, 2004).

1.5.2 Effects of elevated ROS on cancer cells

Both pro- and anti- tumorigenic effects have been documented from ROS within the cell, with a clear distinction on the level they are present at a particular time (Harris and DeNicola, 2020). Therefore, they are often termed as a double-edged sword, in which they are both essential and lethal for tumour growth and progression (Zhao et al., 2023). Cancer cells utilise ROS in cell signalling pathways to advance tumour progression. For example, ROS can cause the inactivation of tumour suppressor gene PTEN, allowing the hyper-activation of the PI3K/Akt signalling pathway, one of the most often activated signalling pathways in cancer (Singh and Manna, 2022; Silva et al., 2008; Cao et al., 2009). More recently, p53, has been shown to have pro-oxidant functions by preventing accumulation of damage (Cheung and Vousden, 2022).

If the level of ROS exceeds a certain threshold oxidative stress occurs but, to counteract this cancer cells have evolved a high antioxidant capacity, evading cell death (Gorrini et al., 2013). Exposure to increased H_2O_2 levels for a prolonged time leads to activation of redox switches GAPDH and PKM2, increasing glucose catabolism via the PPP and blocking glycolysis, resulting in elevated G6PD used for NADPH production (Hayes et al., 2020). In contrast, at the point of chronic oxidative stress, genetic programs such as HIF-1α are activated, resulting in metabolic reprogramming to evade cell death (Hayes et al., 2020).

Overall, cancer cells have both an elevated ROS component and an elevated antioxidant component, maintaining redox balance, albeit at an elevated level.

1.5.3 Therapeutically targeting redox homeostasis

The idea of targeting redox components as a form of cancer therapy has flourished in the past couple of decades, with many small molecule drugs being either synthesised or repurposed to target an element of redox biology (***Table 8.1*** (appendix)). The elevated ROS levels that cancer cells possess opens a therapeutic window between cancer and normal, suggesting reduced toxicity to normal tissues and increased specificity of the therapeutic. By effecting an aspect of the redox system, either oxidant or antioxidant, an imbalance in homeostasis would be achieved leading to oxidative cell death (***Figure 1.15***).

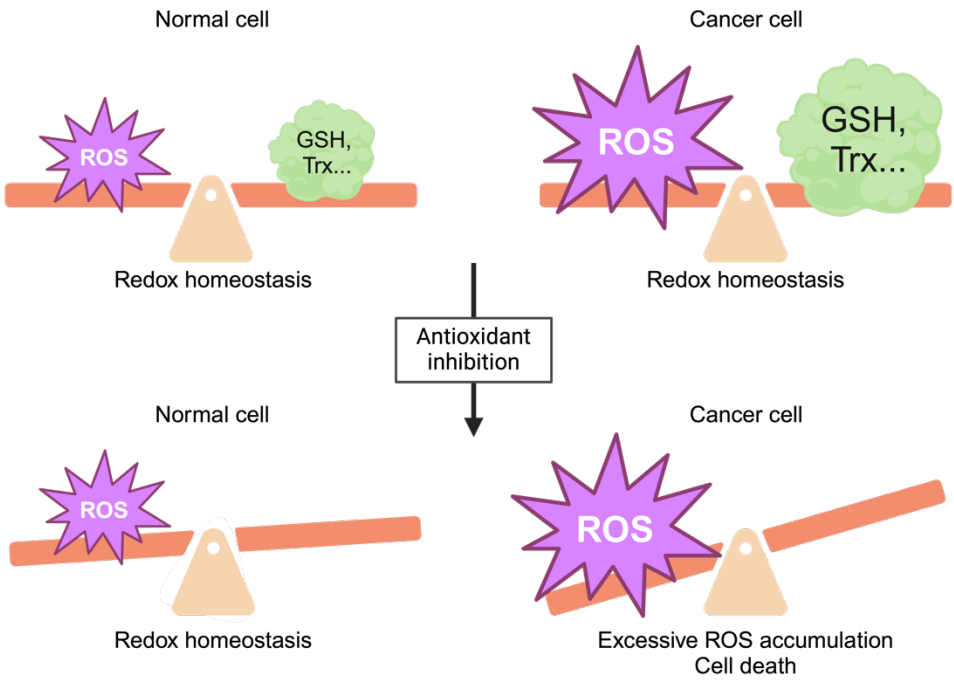


Figure 1.15: **The 'Achilles heel' of cancer cells.** In normal, untransformed cells redox homeostasis is maintained by an equal amount of ROS generation and ROS detoxification, providing a favourable signalling environment. In malignant cancer cells, both processes occur but at an increased rate, giving a higher dependence on the scavenging capacity of cancer cells. Therefore, a therapeutic that diminishes the antioxidant machinery would lead to a small overload of ROS in normal cells but they would be largely unaffected whereas, cancer cells would have a large accumulation of ROS and die to due oxidative stress (Glasauer and Chandel, 2014). Created with BioRender.com.

There are two strategies that can be explored when targeting redox. The first, known as pro-oxidant therapy aims to either directly generate ROS or target the antioxidant machinery in order to raise ROS levels, both aiming to increase oxidative stress above a threshold, resulting in cell death (Jiang et al., 2023). The second, antioxidant therapy, looks at adding antioxidants, such as vitamin C, vitamin E or NAC, into the body in order to maintain a redox homeostasis and prevent cancer. However, the majority of the antioxidant defence is composed of antioxidant enzymes/proteins, not small molecule antioxidants, so there could be a limit to how effective these antioxidant therapies can be (Forman and Zhang, 2021; He et al., 2017).

Conventional standard of care therapies such as radiotherapy and chemotherapy, are considered pro-oxidant therapies (Jiang et al., 2023). Ionising radiation generates free radicals that exhibit high reactivity toward cellular macromolecules such as DNA, lipids, and proteins, resulting in genetic instability and ultimately cell death (An et al., 2024). Many common chemotherapeutics, including doxorubicin, arsenic trioxide, cisplatin and 5-fluorouracil, have been shown to cause cell death via the accumulation of ROS (Jiang et al., 2023). For example, the therapeutic effect of the anthracycline doxorubicin is attributed to its capability to intercalate into DNA, inhibit topoisomerase II, disrupt mitochondrial function and potentiate ROS generation and oxidative damage (Kciuk et al., 2023; Carvalho et al., 2009; Tacar et al., 2013; van der Zanden et al., 2021). Additionally, As_2O_3 induces ROS generation via disruption of the ETC, impairing mitochondrial membrane potentials and depleting GSH, culminating in cell death (Woo et al., 2002; Han et al., 2008). As_2O_3 is the first-line therapy for relapsed or refractory acute promyelocytic leukaemia (Dong et al., 2021).

1.5.4 Targeting the GSH and Trx systems

Small molecule inhibitors of the antioxidant systems have also shown promise therapeutically (Kirkpatrick and Powis, 2017). As mentioned previously, GSH and Trx are key players in the antioxidant response, so it is not surprising that many drugs have been designed to target a part of these pathways.

Buthionine sulfoximine (BSO) is an example of an agent designed to decrease GSH levels. BSO works by irreversibly inhibiting GCL, the enzyme that catalyses the first-rate limiting step of GSH biosynthesis, resulting in excessive ROS accumulation and subsequently cell death which can be ferroptosis (Desideri et al., 2019; Dixon et al., 2012). The efficacy

of platinum-based compounds cisplatin and carboplatin has been seen to increase when in combination with BSO, however, its clinical applications could be limited by its short half-life (Rocha et al., 2014; Fath et al., 2011; Hamilton et al., 2007).

1-methylpropyl-2-imidazole disulfide (PX-12) was the first Trx inhibitor to enter the clinic (Jiang et al., 2023). PX-12 irreversibly inhibits Trx1 by either covalently binding to the key Cys73 residue in its structure or enhancing the dimerisation of its oxidised form (Ghareeb and Metanis, 2020). Phase I clinical trials showed that PX-12 administration was safe and well-tolerated but in phase II trials no notable clinical efficacy was seen (Ramanathan et al., 2012, 2011).

Above are just two examples of drugs, such as auranofin, Erastin and PMX464, that target part of the GSH or Trx antioxidant system (***Figure 1.16***). However, there are very few if any drugs that have been designed to target both pathways simultaneously. The GSH and Trx pathways are complementary, and redundancy exists between them (Mandal et al., 2010a; b; Harris et al., 2015b; Eriksson et al., 2015). Oxidative stress promotes the expression of enzymes in both pathways suggesting they can work in unison in response to ROS accumulation (Harris and DeNicola, 2020). This information together suggests that the GSH and Trx inhibitory compounds have failed so far, as if one pathway is inhibited the other can compensate.

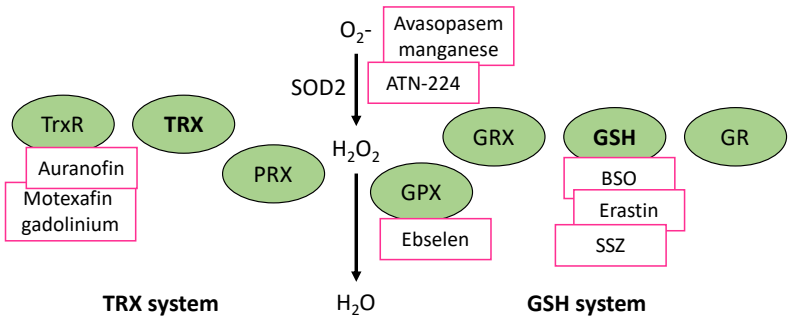


Figure 1.16: **Therapeutics targeting the GSH and Trx systems.** Each of these drugs acts on a specific part of either the GSH or Trx pathway.

1.5.5 Therapeutic molecular cluster, Ag5

The emergence of therapeutic molecular clusters (TMCs) is a relatively new concept. TMCs are small extremely stable molecules comprised of atoms covalently bonded together to give a temperature and pH stable agent. This is possible because a few atoms of a metal can display unique properties in comparison to that of the bulk material (Jena and Sun, 2018; Chakraborty and Pradeep, 2017; Jin et al., 2016; Porto et al., 2018). Synthesis of these clusters occurs through electrolysis, in which the crystals are produced on the electrode. Previously, clusters of three silver atoms (Ag3) have been shown to intercalate into DNA, eliciting a cell death response (Porto et al., 2018; Buceta et al., 2015). More recently, five atoms of silver (Ag5) covalently bonded together have been shown to target free thiols present in redox enzymes, catalysing the complete oxidation of sulphur (S^{-2}) to sulphate (S^{+6}) (Porto et al., 2022). Higher order oligomers are also present in the solution and can act in the lysosomes but do not show cell mortality. Ag5 uses ROS species as a substrate to catalyse the irreversible oxidation of thiol groups present in cysteine residues within GSH/Trx, leaving them unable to reduce free radical species and alleviate oxidative stress (***Figure 1.17***). The rate of oxidation of the free thiol is dependent on the oxidant species present in the local environment, in the order of $O_2 << H_2O_2 < \bullet OH$. A 68 % increase in oxidised sulphur species is seen when recombinant *E. coli* Trx is treated with Ag5 in the presence of H_2O_2 compared to O_2, giving a total proportion of 92 % of free S being oxidised.



Figure 1.17: **Ag5 mechanism of action.** ROS can oxidise the sulphur present in antioxidants in the cell, but this process is reversible. In the presence of Ag5 ROS can oxidise antioxidants to an irreversible state, so they cannot go on to alleviate cellular stress.

Density-functional theory (DFT) was used to theoretically determine the possible mechanism that takes place between Ag5 and sulphur containing compounds. In summary, Ag5 adsorbs oxygen molecules, activating them to superoxide like species, a disulphide is then formed. The oxygens then break the S-S bond giving a sulphinic species (R-(SO_2)-Ag5) which is further oxidised to sulphide (R-SO_3-Ag5). The sulphur is then detached from the rest of the organic molecule ((SO_3)-Ag5), and eventually the sulphate species ((SO_4)-Ag) is produced as the end product (***Figure 1.18***). Experimentally, over-oxidisation of sulphur by Ag5 to a point where reversibility is abolished has been shown however, the resulting sulphur species produced has not been determined outside of theoretical calculations.

In vitro, Ag5 can oxidise free cysteine, GSH or Trx at concentrations of 1000 times less than R-SH. Ag5 was shown to work fast, with a peak activity of 7 mins in its oxidising capabilities. It was shown that the transport of Ag5 into cells is a passive process and due to its small size, it can cross the blood brain barrier, as well as being able to travel to areas of low vascularity. PRDX3, an enzyme that resides solely in the mitochondrial matrix and plays a vital role in redox control, was shown to be oxidised by Ag5 (Rhee, 2016; Netto and Antunes, 2016). In a panel of 85 tumour cell lines PRDX3 oxidation was shown to inversely correlate with ED50 values for Ag5, confirming it as a primary mediator of Ag5 action (Song et al., 2011). The lethal effect Ag5 has on cancer cells is not seen in normal

cells, shown in unpublished data (Domínguez et al., 2023), due to the relative low levels of H_2O_2, meaning that homeostasis can be maintained in the presence of Ag5 oxidation.

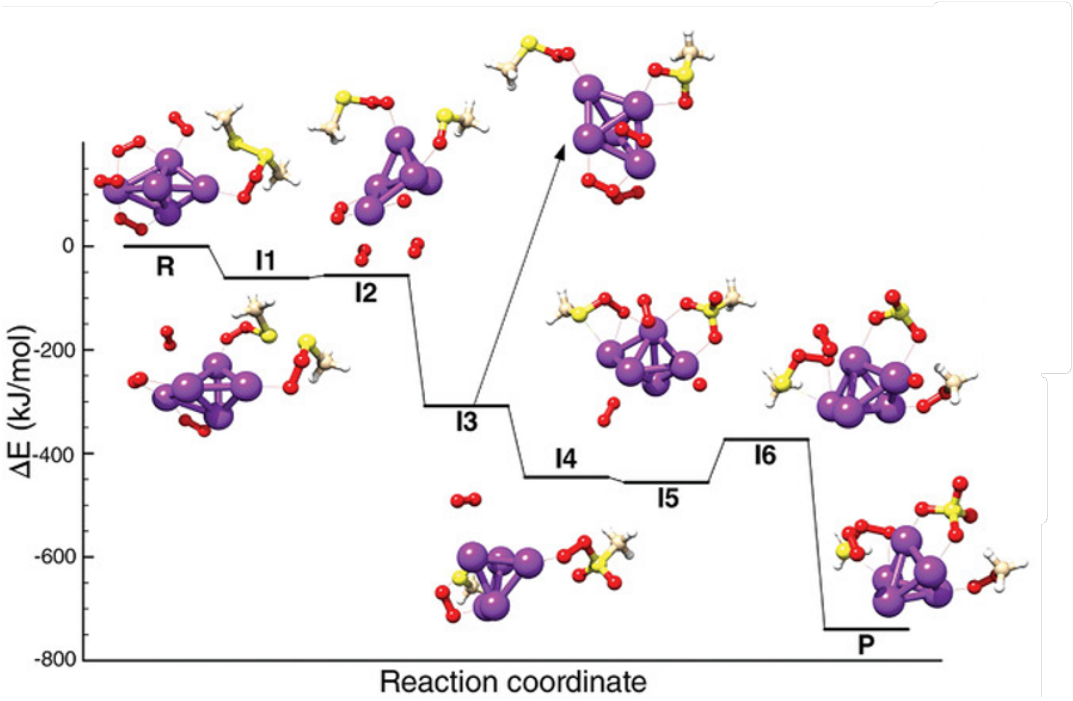


Figure 1.18: **Proposed DFT mechanism of Ag5 interaction with R-SH.** Ag5 catalyses the irreversible oxidation of the sulphur (-2) to sulphate (S^{+6}). Reprinted from (Porto et al., 2022), with permission.

1.6 Hypoxia and Redox

1.6.1 ROS in hypoxia

The impact of hypoxia on ROS levels is controversial with some studies demonstrating increased ROS production in normal and malignant cells under hypoxia, whilst others reporting the opposite. The majority of reports in the field today, document a ROS increase in hypoxia, and that ROS are required and sufficient for HIF-1α stabilisation (Ferber et al., 2012; Ogunrinu and Sontheimer, 2010; Reczek and Chandel, 2017; Bell et al., 2005; Glasauer and Chandel, 2014; Guzy et al., 2005; Sabharwal and Schumacker, 2014; Chandel et al., 2000, 1998). This is often seen to be an increase in ROS specifically

in the mitochondria, with cells depleted of mitochondrial DNA (p^0 cells) or treated with ETC inhibitors not showing a ROS increase. However, it should be noted that there are reports which suggest ROS are unaffected or decrease in response to hypoxia, and that ROS are not required for the stabilisation of HIF-1α (Sgarbi et al., 2017; Waypa et al., 2010; Wang et al., 2008; Sgarbi et al., 2018; Tuttle et al., 2007). Together, these reports suggest a complex dependence on cell line, experimental conditions and specific ROS subtype. The controversy could potentially be addressed with a rigorous screening of several cell lines, oxygen tensions and assays to confirm what actually happens to ROS in hypoxia.

1.6.2 Functions of ROS in hypoxia

The elevated levels of ROS present in hypoxia increase the expression of HIF-1α and contribute to its stability. It has also been reported that ROS can induce transcription of HIF-1α mRNA expression in a NFκB dependent manner (Bonello et al., 2007). Additionally, through ROS-dependent activation of P13K and PKC pathways, angiotensin II has been shown to increase HIF-1α mRNA and expression of HIF-1α in hypoxic tumour cells (Pagé et al., 2002; Koshikawa et al., 2009). The stabilisation of HIF-1α can also be induced by ROS produced from the ETC, in hypoxia, and it was shown that mitochondrial ROS generation specifically at complex III is required and sufficient for HIF-1α stabilisation (Gottlieb and Tomlinson, 2005; Chandel et al., 2000, 1998; Brunelle et al., 2005; Guzy et al., 2005; Mansfield et al., 2005). One mode of action for HIF-1α stabilisation is the formation of an oxidant-induced GSH-Cys^{520} adduct in the protein (Watanabe et al., 2016). Therapeutic intervention can also lead to the stabilisation of HIF-1α via ROS produced from tumour reoxygenation following radiation treatment, indicating the benefit of fractionated radiotherapy (Moeller et al., 2004). Upregulation of

HIF-1α by ROS results in the transcription of downstream target genes, allowing the tumour cell to survive and proliferate in the hypoxic conditions (Chandel et al., 1998; Guzy et al., 2005; Toth and Warfel, 2017; Tello et al., 2011; Potteti et al., 2016; Xin et al., 2020; Kim et al., 2011; Bondi et al., 2022; Loboda et al., 2009; Pan et al., 2007; Watanabe et al., 2016; Hamanaka et al., 2016; Chandel et al., 2000; Semenza, 1999; Agani et al., 2000; Haddad et al., 2000).

Additionally, ROS can modulate the HIF-1α response by regulation of PHD or FIH activity (Guzy and Schumacker, 2006; Semenza and Prabhakar, 2018; Flannigan et al., 2015; Miles et al., 2017; Bailey and Nathan, 2018; Bailey et al., 2020; Nytko et al., 2007; Hewitson et al., 2007; Koivunen et al., 2007). It has been reported that H_2O_2 can oxidise Fe^{2+}, a cofactor needed for PHD activity, to Fe^{3+}. Subsequent hydroxylation of HIF-1α cannot occur, resulting in HIF-1α stabilisation (Gerald et al., 2004). It has also been suggested that PHD inhibition can happen through Cys oxidation in its catalytic domain, initiated through oxidative stress, inducing its dimerisation and subsequent loss of activity (Lee et al., 2016).

ROS generated under hypoxia can also lead to H_2O_2-induced oxidation of Cys residues within KEAP1. This interrupts the interaction of KEAP1 with NRF2, preventing the ubiquitylation and degradation of NRF2, leading to its activation and downstream antioxidant response (Reczek and Chandel, 2017).

Overall, even though the availability of oxygen initiates the primary signal determining HIF-1 levels and activity, free radical species can alter the response, providing a mechanism to fine tune the hypoxic response in specific tissues and tumour types (Taylor and Scholz, 2022).

1.6.3 Antioxidant targets of HIF-1

The antioxidant defence in hypoxic cells is regulated by HIF-1 to maintain redox homeostasis (Qutub and Popel, 2008; Pouysségur and Mechta-Grigoriou, 2006). HIF-1 activates the transcription of target genes which go on to decrease production of mitochondrial ROS or increase production of antioxidants (Samanta and Semenza, 2017). An example of this was reported, where increased expression of enzymes needed for one-carbon metabolism (1CM) was seen in hypoxic breast cancer cells in a HIF-dependent manner (Samanta and Semenza, 2018). 1CM produces NADPH and the amino acids needed for GSH synthesis, key components of the antioxidant machinery. Additionally in hypoxic breast cancer cells, the expression of SLC7A11 and GCLM were both enhanced in a HIF-dependent manner (Lu et al., 2015). SLC7A11 encodes the xCT system and GCLM encodes the modifier subunit of GCL.

A positive association has been reported between HIF-1 and NRF2 (Bae et al., 2024). In multiple cancer cell models, NRF2 silencing has decreased HIF-1α levels, culminating in an attenuated HIF-1 response (Kim et al., 2011; Bi et al., 2020; Ji et al., 2014; Shen et al., 2014; Zhang et al., 2013; Zheng et al., 2023). Direct regulation of HIF-1α by NRF2 was reported with the identification of a conserved functional antioxidant response element (ARE) in the promoter region of the HIF-1α gene (Jin et al., 2021; Lacher et al., 2018). Also, targets of NRF2 can elicit an effect on HIF-1α, for example NQO1 can bind to HIF-1α preventing PHD binding, resulting in accumulation of HIF-1α (Oh et al., 2016). NRF2 has also been reported to bind directly to HIF-1α through the ODDD, preventing PHD and resulting in HIF-1α accumulation (Mason and Holtzman, 1975).

1.6.4 HIF upregulates glycolysis and supresses oxidative phosphorylation

Tumour cells are characterised by a high glucose level, resulting from a switch to aerobic glycolysis, identified as the Warburg effect (Koppenol et al., 2011; Vaupel et al., 1989; Helmlinger et al., 1997; Warburg, 1956). The majority of cancer cells rely on this source of energy, even in well oxygenated conditions (Warburg, 1924). Imaging can utilise this concept by using the glucose tracer 2-deoxyglucose in PET scans to detect tumours.

Hypoxic tumour cells also have an increased rate of glycolysis to provide ATP for tumour progression. It was originally thought that hypoxic cells switched to glycolysis because oxygen was limiting and OxPhos requires oxygen as the terminal acceptor in the ETC. However, HIF-1$\alpha^{-/-}$ mouse embryo fibroblasts (MEFs) exposed to 1 % O_2 do not switch from oxidative to glycolytic metabolism, producing more ATP than wildtype MEFs and indicating that 1 % O_2 is not limiting for OxPhos. The HIF-1$\alpha^{-/-}$ MEFs do however die under prolonged hypoxia due to excessive ROS levels, unlike the WT MEFs (Kim et al., 2006). These studies led to a paradigm shift in the understanding of cell metabolism regulation, as the purpose of the metabolic switch was to prevent excessive ROS production from a reduced efficiency ETC in hypoxic conditions (Chandel et al., 1998; Shimoda and Semenza, 2012). HIF-1 regulates the control of this metabolic switch, in which glycolysis is upregulated and OxPhos is repressed. The expression of HIF-1 is seen in mild hypoxia (3 % O_2), where robust OxPhos could theoretically take place as ETC function only becomes limiting at near anoxic oxygen levels (0.3 % O_2) (Jiang et al., 1996b; Papandreou et al., 2005; Wilson et al., 1988; Wheaton and Chandel, 2011). Therefore, as the HIF-1$\alpha^{-/-}$ MEFs demonstrated, HIF-1 is a critical factor for tumour cell survival in hypoxic conditions via cell metabolism regulation (***Figure 1.19***).

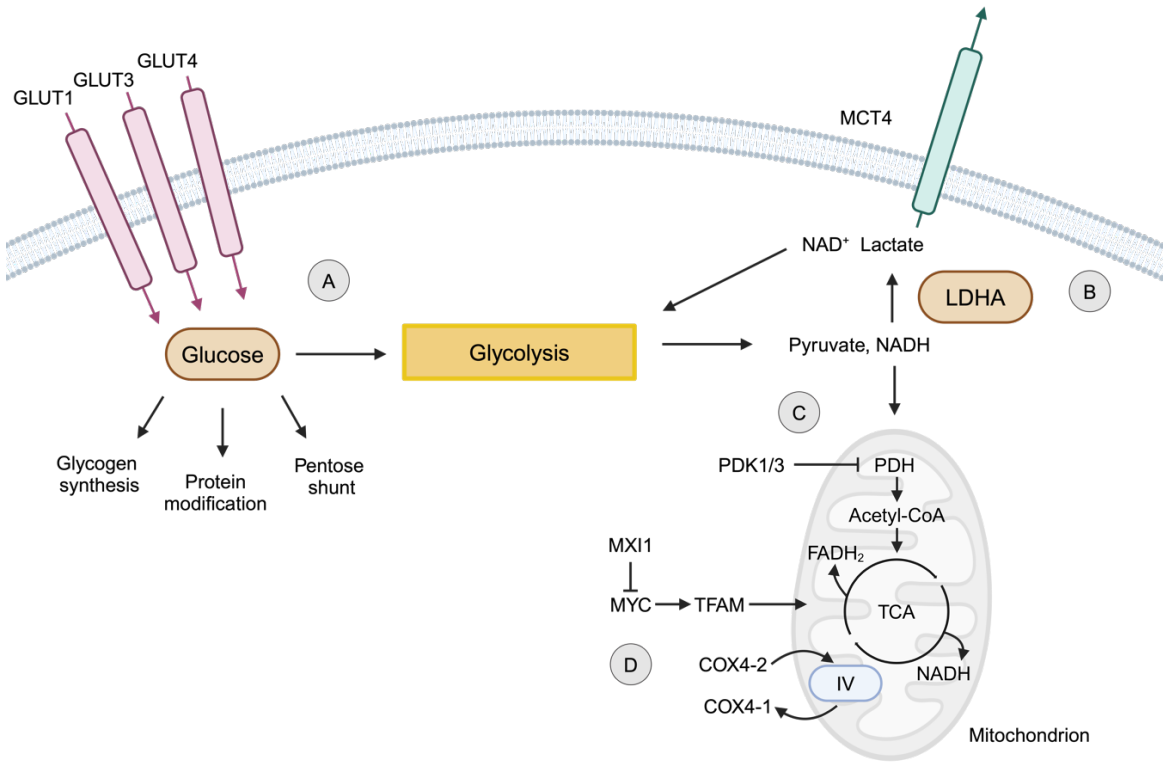


Figure 1.19: **Overview of HIF-1α mediated regulation of tumour cell metabolism.** A) Glycolytic upregulation B) Pyruvate and lactate accumulation C) OxPhos repression D) Cytochrome *c* oxidase subunit switch and reduced mitochondrial biogenesis. Created with BioRender.com.

Glycolytic upregulation

Glycolysis is the biochemical process that breaks glucose down into pyruvate and in the process produces two molecules of ATP (Brahimi-Horn et al., 2007). In comparison to the 32 ATP molecules OxPhos produces per glucose molecule, glycolysis is a much less efficient form of respiration. However, glycolysis is sufficient to sustain cellular energetics if the supply of glucose is adequate (Papandreou et al., 2005). HIF-1 ensures that there is adequate glucose to supply the hypoxic tumour cells. The largest functional group of genes consistently regulated by HIF-1 are associated with glucose metabolism (Chi et al., 2006; Allen et al., 2006; Vengellur et al., 2003). HIF-1 increases glucose uptake rates in the cell by enhancing the expression of glucose transporters GLUT1 (SLC2A1), GLUT3 (SLC2A3) and GLUT4 (SLC2A4) (Maxwell et al., 1997; Chen et al., 2001; Iyer et al.,

1998a; Maltepe et al., 1997; Ryan et al., 1998; O'Rourke et al., 1996; Sakagami et al., 2014). The role of the transporters is to move glucose down its concentration gradient from relatively high blood levels to relatively low intracellular levels, increasing the flux of glucose into the hypoxic cells. HIF-1 also enhances the level of enzymes needed for glycolytic breakdown of intracellular glucose. All twelve enzymes required for glycolysis are directly regulated, at least in part, by HIF-1, resulting in HIF-1 stimulating the whole process (Iyer et al., 1998a; Seagroves et al., 2001). Examples of the glycolytic enzymes that are upregulated include hexokinases (HK1, HK2), phosphofructokinases (PFKL, PFKP), aldolases (ALDA, ALDC), glyceraldehyde 3 phosphate dehydrogenase (GAPDH), phosphoglycerate kinase 1 (PGK1), enolases (ENO1, ENO2) and pyruvate kinase M (PKM) (Mathupala et al., 2001; Semenza et al., 1994; Minchenko et al., 2003; Semenza et al., 1996; Graven et al., 1999; Luo et al., 2011b). Glycolysis converts two ADP and two NAD^+ to two ATP, two NADH and two pyruvate molecules. In normal cells, pyruvate and NADH go into the ETC but here they need to be dealt with differently to ensure further glycolytic cycles.

Pyruvate and lactate accumulation

Pyruvate and NADH are products of glycolysis, that would normally go onto further steps in oxidative respiration. However, in hypoxic cells they instead accumulate in the cell. HIF-1 upregulates the expression of lactate dehydrogenase A (LDHA) which catalyses the conversion of pyruvate and NADH to lactate and NAD^+ (Semenza et al., 1996; Firth et al., 1995). The presence of lactate inside the cell can create an unfavourable acidic environment (the Pasteur effect), HIF-1 therefore increases expression of the monocarboxylate transporter 4 (MCT4, encoded by SLC16A3) which takes lactate from the cell into the extracellular space (Barnett, 2000; Ullah et al., 2006). Lactate in the

extracellular space creates an overall acidic TME which has been associated with poor patient prognosis (Weidemann and Johnson, 2008). The NAD^+ that is regenerated by LDHA can go on to participate in more cycles of glycolysis, as it is required by GAPDH.

OxPhos repression

Papandreou and colleagues were the first to demonstrate that HIF-1 alters cellular metabolism in hypoxia not only by upregulating glycolytic pathways but also by downregulating mitochondrial function (Papandreou et al., 2006). By repressing mitochondrial activity through OxPhos inhibition, HIF-1 actively regulates the oxygen demand of the tissue to ensure cell survival (Papandreou et al., 2006).

Pyruvate is the primary carbon source for OxPhos and would normally be converted to acetyl-CoA (along with NADH and CO_2), by pyruvate dehydrogenase (PDH), which can then enter the TCA cycle to continue oxidative respiration. The conversion of pyruvate to acetyl CoA is an irreversible step, indicating a critical juncture in cell metabolism. PDH can be regulated in three ways; acetyl CoA and NADH inhibition, stimulation by reduced cellular energy and pyruvate dehydrogenase kinase (PDK) inhibition.

The PDK family of enzymes has four members, with PDK1 and PDK3 shown to be hypoxia-inducible and targets of HIF-1 (Roche et al., 2001; Papandreou et al., 2006; Denko et al., 2003). PDK can phosphorylate the E1 subunit of PDH and inactivate it, preventing the flow of pyruvate into the mitochondria (Patel and Korotchkina, 2001; Roche et al., 2001). This mitochondrial regulation protects the cell from oxidative stress by attenuating hypoxic ROS generation (Weidemann and Johnson, 2008; Bae et al., 2024; Kim et al., 2006). The reduction in oxygen consumption by the mitochondria also creates a relative increase in intracellular oxygen tension, when total oxygen is limiting (Papandreou et al., 2006). PDK induction may also increase pyruvate to lactate conversion and subsequent regeneration

of NAD^+ for further glycolysis (Papandreou et al., 2006)1. Overall, by activating mitochondria-independent metabolism through HIF-1 the cell can survive excessive ROS accumulation.

Cytochrome c oxidase and mitochondrial biogenesis

HIF-1 also directly modifies the ETC so it can function efficiently in conditions of reduced substrate availability (Fukuda et al., 2007). This is achieved by altering the activity of cytochrome *c* oxidase (COX), which uses oxygen as the terminal electron acceptor. Under normoxic conditions, COX contains the COX4-1 subunit. In hypoxia an isoform switch in one of the regulatory subunits is needed (Fukuda et al., 2007). HIF-1 enhances the expression of the alternative COX4-2 subunit as well as increasing mitochondrial LON protease (LONP1) expression, which degrades the COX4-1 subunit (Fukuda et al., 2007). The subunit switch from COX4-1 to COX4-2 may increase the efficiency of electron transfer to oxygen and allow for continued respiration without elevated ROS when oxygen availability is mostly reduced (Fukuda et al., 2007).

Additionally, HIF-1 can also decrease mitochondrial oxygen consumption by reducing mitochondrial mass in several ways. For example, the removal of mitochondria by mitophagy is enhanced by HIF-1 via increased expression of BCL-2/adenovirus E1B 19-kDa interacting protein 3 (BNIP3) and BNIP3-like (BNIP3L) (Bellot et al., 2009; Guo et al., 2001; Sowter et al., 2001). Mitochondrial biogenesis is also reduced by HIF-1 via the elevated expression of MAX interactor 1 (MXI1) (Zhang et al., 2007; Corn et al., 2005). The transcriptional repressor MXI1 negatively regulates expression of the oncogenic transcription factor MYC, reducing mitochondrial mass (Zhang et al., 2007). This mechanism is more evident in cells that have lost VHL resulting in constitutive HIF expression (Zhang et al., 2007).

Overall, the changes in cellular metabolism induced by HIF-1 reduce the oxygen demand to the hypoxic tumour cells whilst still supplying them with sufficient energy (Denko, 2008). Subsequently, the conserved oxygen is available for oxygen-requiring cellular functions that do not produce energy such as sterol synthesis, oxidative protein folding and for use by enzymes including oxidases, hydroxylases, protein disulphide isomerases and histone demethylases (Shen et al., 2003; Hagen et al., 2003; Tu and Weissman, 2002; Forneris et al., 2005; Herst and Berridge, 2007; Rosenfeld et al., 2002). Additionally, the main benefit of these changes is the protection from oxidative stress resulting from decreased ROS production from the ETC, allowing tumour survival and progression (Kim et al., 2006).

Despite a wealth of data indicating that redox is altered in hypoxic conditions, these data are often limited to the measurement of one component of redox (either ROS or GSH for example) and do not take into consideration the kinetics of change. Furthermore, research carried out in hypoxic conditions is usually focused on one level of hypoxia and does not consider fluctuations in oxygen level, primarily due to a lack of available tools. Further characterisation of redox in hypoxia and development of tools to study this are predicated to be of significant value in exploiting oxidative stress associated with cancer for therapeutic gain.

1.7 Aims of this study

1. To develop a reversible fluorescent probe capable of sensing fluctuating levels of oxygen. The potential of this probe is the ability to identify tumours with high levels of cyclic hypoxia and therefore changes in redox.

2. Characterise the changes in redox in a range of hypoxic conditions (in the absence of reoxygenation)

3. Investigate the efficacy of novel therapeutic, Ag5, in conditions which mimic the hypoxic TME.

Chapter 2: Materials and Methods

2.1 Chemistry materials and methods

2.1.1 Chemicals

Reagents and solvents used were of commercially available reagent grade quality from Fluorochem, Sigma Aldrich, Acros, Apollo Scientific, Alfa Aesar, Fischer Scientific and Merck, and were used without further purification. Reactions carried out under an argon or nitrogen atmosphere are stated in the experimental procedure. Anhydrous solvents were obtained from an MBRAUN Solvent Purification System 5 and stored under an argon atmosphere over 3 Å molecular sieves. Concentration *in vacuo* was carried out at 40 °C for organic solvents using a Buchi™ rotary evaporator. Brine refers to a saturated aqueous solution of sodium chloride. Petroleum ether refers to the fraction of light petroleum ether boiling point in the range 40-60 °C. Celite refers to Celite® 545 filter aid, treated with sodium carbonate, flux-calcined (Sigma Aldrich).

2.1.2 Thin layer chromatography

Normal phase silica gel analytical TLC was performed on normal phase Merck silica gel 60 F_{254} aluminium-supported thin layer chromatography sheets. Visualisation was carried out by absorption of UV light (λ_{max} = 254 nm and 365 nm) or thermal development after staining in an aqueous solution of potassium permanganate or an ethanolic solution of ninhydrin.

2.1.3 Normal phase silica gel flash column chromatography

Silica gel column chromatography was performed manually on Merck Geduran® silica gel 60 (40-63 μm), eluting with solvents as supplied, under a positive pressure of

compressed, gaseous nitrogen or on a Biotage® Selekt Flash Purification System using Biotage® KP-Sil SNAP or Biotage® Sfär Silica cartridges.

2.1.4 Semi-preparative HPLC

Semi-prep HPLC was carried out on an Agilent 1260 Infinity II system with a reverse phase (RP) Agilent 5 prep C18 column (50 mm × 21.2 mm) and a prep cell (0.3 mm pathlength). Solvents used were water (0.1 % formic acid) and MeCN (0.1 % formic acid) in the percentage stated in parentheses. Compounds to be purified were dissolved in MeCN, MeOH or H_2O before injection.

2.1.5 Melting point determination

Melting points were determined using a Leica Galen III hot stage microscope and are uncorrected. The solvent from which the sample was crystalised is given in parentheses.

2.1.6 Infrared spectroscopy

Infrared spectra were obtained from thin films, using a diamond ATR module on a Bruker Tensor 27 spectrometer. Absorption maxima are reported in wavenumbers (cm^{-1}).

2.1.7 NMR

^{1}H NMR spectra were recorded on a Bruker AVIIIHD 400 (400 MHz), Bruker AVII 500 (500 MHz) with dual $^{13}C(^{1}H)$ cryoprobe, Bruker AVIIIHD 500 (500 MHz), or Bruker AVIIIHD 600 (600 MHz) spectrometer in the stated solvents as a reference for the internal deuterium lock. The chemical shift data for each signal are given as δ_H in units of ppm relative to TMS where δ_H (TMS) = 0.00 ppm. The spectra are calibrated using the solvent peak with the data provided by Fulmer *et al.* (Fulmer et al., 2010). The multiplicity of each

signal is denoted by s (singlet), d (doublet), dd (doublet of doublets), ddd (doublet of doublet of doublets), t (triplet), q (quartet), p (quintet), dt (doublet of triplets), dq (doublet of quartets), or m (multiplet). The number of protons (n) for a given resonance signal is indicated by nH. Where appropriate, coupling constants (*J*) are quoted in Hz and are recorded to the nearest 0.1 Hz. Identical proton coupling constants (*J*) are averaged in each spectrum and reported to the nearest 0.1 Hz. Coupling constants were determined using MestReNova x64 software. ^{1}H spectra were assigned using 2D NMR experiments including COSY, HMBC and HSQC.

HCIQ analysis- **HCIQ** (2 mg) was dissolved in MeOD (0.6 mL) and a ^{1}H NMR spectrum was undertaken. $Na_2S_2O_4$ in D_2O was then used as the reductant to record a spectrum of the reduced form. Varying concentrations of $Na_2S_2O_4$ were trialled and a ratio of 1 eq. of probe (6.28 mM) to 2 eq. of $Na_2S_2O_4$ (12.56 mM) was optimal to see a distinct difference in the NMR spectrum of both forms.

^{13}C NMR spectra were recorded on a Bruker AVIIIHD 400 (101 MHz), or Bruker AVII 500 (126 MHz) spectrometer, with dual ^{13}C(^{1}H) cryoprobe, in the stated solvents, with broadband decoupling and an internal deuterium lock. The chemical shift data for each signal are given as δ_C in units of ppm relative to TMS where δ_C TMS = 0.00 ppm. The spectra are calibrated using the solvent peak with the data provided by Fulmer *et al.* (Fulmer et al., 2010). The shift values of resonances are quoted to 1 decimal place. ^{13}C spectra were assigned using 2D NMR experiments including HMBC and HSQC.

2.1.8 Electrospray ionisation mass spectrometry

LRMS spectra were acquired on an Agilent 6120 using ESI from solutions of MeOH, MeCN or H_2O. *m/z* values are reported in Daltons to the nearest whole number and are followed by their percentage abundance in parentheses.

HRMS spectra were acquired on a Bruker microToF spectrometer using ESI from solutions of MeOH, MeCN or H_2O. *m/z* values are reported in Daltons to 4 decimal places.

2.1.9 Analytical high performance liquid chromatography

HPLC was undertaken using either a PerkinElmer Flexar system with a Binary LC Pump and UV/Vis LC detector or an Agilent 1260 Infinity II system with a Poroshell 120 EC-C18 column (4 μm). For the PerkinElmer system a Dionex Acclaim® 120 C18 column [5 μm, 12 Å, 150 nm × 4.6 mm] reverse phase column was used with a constant flow rate of 1.5 mL min^{-1} and gradient method of 10 min from 95:5 H_2O/MeCN (0.1 % trifluoroacetic acid) to 5:95 H_2O/MeCN (0.1 % trifluoroacetic acid) with a 5 min hold. For the Agilent system a flow rate of 1 mL min^{-1} was used, and the column temperature was 40 °C and solvents used were H_2O (0.1 % formic acid) and MeCN (0.1 % formic acid). The wavelengths of detection for calculating the purity of the samples were 210, 254 or 280 nm. Samples to be tested were dissolved in either MeCN, MeOH or H_2O to give a concentration of 1 mg mL^{-1}.

2.1.10 Liquid chromatography-mass spectrometry (LCMS)

LCMS was undertaken using an Agilent 1260 Infinity II system employed with a ZORBAX SB-C18 column (1.8 μm) at a 0.4 mL min^{-1} flow rate with a column temperature of 40 °C. Solvents used were H_2O (0.1 % formic acid) and MeCN (0.1 % formic acid) with the

gradient method used specific to the sample ran and stated with it. The samples were dissolved in MeCN, MeOH or H_2O prior to injection. Wavelengths analysed were 210, 254, 280 and 365 nm as a standard and then wavelengths specific to the absorption spectra of the probe when stated.

HCIQ analysis- This involved running a sample of **HCIQ** through the LCMS column and then reducing it with $Na_2S_2O_4$. The same ratio of probe:$Na_2S_2O_4$ was used as in the NMR experiments described prior however, it was greatly scaled down as the LCMS detector is very sensitive.

2.1.11 Electrochemistry

Voltammetry measurements were made using an Autolab PGSTAT 12 with a 3 mm glassy carbon working electrode, platinum wire counter electrode and $Ag/AgNO_3$ (0.01 M in MeCN) reference electrode. Voltammograms were referenced to the Fc/Fc^+ couple (0.0 V) as an internal reference. The electrolyte used was 0.1 M tetrabutylammonium hexafluorophosphate. The reaction cell was oven dried before use and degassed before each measurement was taken.

HCIQ analysis- A 10 mM stock solution of the probe was made in acetonitrile and also a 0.1 M stock solution of the electrolyte to be used (tetrabutylammonium hexafluorophosphate) in acetonitrile. Prior to adding the solutions to the reaction cell, it was washed and oven dried, 1.5 mL of the tetrabutylammonium hexafluorophosphate solution was then added before sealing the system and adding the three electrodes (reference, working and counter). The solution was then degassed for a couple of minutes before running a blank using the potentiostat software. All voltammograms were ran

between determined potential values for three cycles. After the blank was obtained, the sample was added to give a final concentration of between 0.1 – 1 mM of the probe in the reaction cell. Another voltammogram was then undertaken. Initially the whole potential window was scanned, and then particular windows of interest were investigated.

2.1.12 UV/Vis spectroscopy

Absorption spectra were recorded using a JASCO V-770 spectrophotometer at 25 °C using these parameters: UV/VIS bandwidth of 1 nm, NIR bandwidth of 20 nm and UV/VIS and NIR response of 0.24 s. The scan speed used was 1000 nm min^{-1} with a light source at 350 nm and a detector at 850 nm. The concentration and solvent used and nm window recorded are specified for the particular sample ran.

HCIQ analysis- The UV/Vis measurements were carried out in distilled water as this proved to give clearer results over other options trialled, such as PBS buffer and methanol. A blank spectrum of distilled water was obtained before adding 6 µL of an MeCN stock solution (10 mM) of the oxidised probe, to give a final concentration of 20 µM in the sample cuvette. A spectrum of this solution was then recorded between the wavelengths of 250 nm to 700 nm to give the absorption of the oxidised probe. The reduction was chemically induced via the addition of $Na_2S_2O_4$ in distilled water. 10 µL of a $Na_2S_2O_4$ stock solution (150 mM) in distilled water was added to the sample cuvette to give a final $Na_2S_2O_4$ concentration of 0.5 mM within the cuvette. Another spectrum was then recorded to show the absorption of the reduced probe.

2.1.13 Fluorolog

Luminescence data was measured using a Horiba Fluorolog-3 system, with parameters, such as grating width and excitation wavelength, altered depending on the specific sample. A 500 nm filter was used when appropriate to prevent overexposure to the detector. The data generated was processed using Origin® software.

HCIQ analysis- The same concentrations of **HCIQ** and $Na_2S_2O_4$ were used in these experiments as for prior in the UV/Vis spectroscopy. The oxidised and reduced probe samples were excited at all the maxima within their respective absorption spectrum; 300, 400 and 500 nm for the oxidised sample and 313, 400 and 530 nm for the reduced sample. The emission spectrum for each separate excitation wavelength was recorded from (excitation wavelength + 15 nm) to (excitation wavelength $\times$ 2 – 15 nm). If double scattering would have been present in the middle of the range that wanted to be recorded (200 nm to 800 nm) then two separate spectrums were recorded with overlapping regions and a 500 nm filter was used for the second spectrum to stop overexposure to the detector. The two spectrums were joined together to give the whole range of emission. A background spectrum of distilled water was then recorded at all the excitation wavelengths so this could be subtracted from the sample spectra to remove Raman scattering. Once Raman scattering had been removed from the spectra, only peaks affording to the probe sample would be seen.

2.1.14 Hypoxia chamber

A RUSKINN INVIVO$_2$ 400 was used to carry out enzymatic assays in hypoxia. The chamber was set to 0.1 % oxygen and 37 ^{o}C for the time course of the assay. The chamber was filled with compressed, gaseous nitrogen to remove the presence of oxygen. Equipment and

solvents were equilibrated in the chamber for at least 12 h before the assay was undertaken.

2.1.15 Enzyme assay

Phosphate buffer (pH 7.0), MeCN and MQ water were equilibrated in the hypoxia chamber 16 h prior to the assay. Fresh solutions of probe stock (1 mM in DMSO) and β-NADPH (1 mM in phosphate buffer (pH 7.0)) were prepared shortly before carrying out the assay. The enzyme buffer was changed (storage buffer to phosphate buffer (pH 7.0)) following a PD spintrap G-25 protocol. The protocol was followed as detailed: the medium was suspended in the spintrap column by vortexing before loosening the cap and twisting off the bottom closure. The column was then placed in an appropriate size collection tube and the storage solution was removed by centrifugation (3000 rpm, 1 min). Phosphate buffer (pH 7.0, 400 µL) was then added to the column, and it was centrifuged (3000 rpm, 1 min) to equilibrate the column. The flow-through was discarded and this process was repeated four times. The used collection tube was then discarded and replaced with a clean one for sample collection. The enzyme sample (50 µL) was slowly added to the middle of the packed bed along with a stacker volume of phosphate buffer (pH 7.0, 130 µL). The sample was then eluted into the collection tube via centrifugation (3000 rpm, 2 min). The enzyme in phosphate buffer (pH 7.0) was then kept on ice along with the β-NADPH solution to ensure no denaturation of these samples. The assay components (phosphate buffer (pH 7.0, 680 µL), DMSO probe stock (100 µL), β-NADPH (200 µL) and cytochrome p450 enzyme (20 µL, 4.4 µg)) were placed into the sample vial and mixed before the 0 h timepoint. For samples analysed by LCMS the enzyme and phosphate buffer needed to be removed prior. The samples were first

centrifuged (13000 × g, 10 min, 4 °C) and the supernatant was collected. The samples were then extracted with EtOAc (2 × 200 μL) before allowing for solvent evaporation overnight. MeCN (60 μL) was then added to the vials and the sample was transferred to narrow mass spec vials before removing from the hypoxia chamber and running via LCMS. Additional assay information can be seen in ***Table 2.1***.

Table 2.1: **Enzyme assay variants.**

Assay	Timepoints	Alterations
1	0, 1, 3, 6,24 h	/
2	0, 2, 5, 30, 60 min	/
3	0, 1, 3, 6, 24 h	Three enzyme volumes used: 1, 10, 20 μL
4	0, 1, 3, 6, 24 h	Assay components: phosphate buffer (5 mM, pH 7.4), oxidised probe (4 μM), enzyme solution (2 μg) and β-NADPH solution (33.3 μM). Absorption spectrum recorded from 250 nm to 750 nm.

2.2 Biology materials and methods

2.2.1 Materials

Lab plasticware was supplied by either CoStar®, Corning® and Sarstedt®. All glassware was autoclaved prior to use.

Table 2.2: **Cell lines used in this study.**

Name	Tissue type	Culture media	Origin
A549	Non-small cell lung carcinoma	DMEM	ATCC
H460	Non-small cell lung carcinoma	DMEM	Prof. Higgins, University of Oxford
RKO	Colorectal carcinoma	DMEM	ATCC
RKO$^{HIF\text{-}1\alpha\text{-}/\text{-}}$	Colorectal carcinoma	DMEM	(Dang et al., 2006)
RKO$^{shPDK1/3}$	Colorectal carcinoma	DMEM	Prof. Nicholas Denko, The Ohio State University(Papandreou et al., 2006)
OE21	Oesophageal squamous cell carcinoma	DMEM	Dr Ricky Sharma, University of Oxford
OE33	Oesophageal adenocarcinoma	RPMI	Dr Ricky Sharma, University of Oxford
SKGT4	Oesophageal adenocarcinoma	RPMI	Dr Ricky Sharma, University of Oxford
FLO1	Oesophageal adenocarcinoma	DMEM	Dr Ricky Sharma, University of Oxford
HCT116	Colorectal carcinoma	DMEM	Prof. Bert Vogelstein, Johns Hopkins, USA
RCC4	Renal clear cell carcinoma	DMEM	Prof. Peter Ratcliffe, University of Oxford
RCC4$^{VHL\text{-}/\text{-}}$	Renal clear cell carcinoma	DMEM	Prof. Peter Ratcliffe, University of Oxford
MRC5	Lung fibroblast	DMEM	Prof. Higgins, University of Oxford
HFL-1	Lung fibroblast	F12 HAM	Prof. Higgins, University of Oxford

Table 2.3: **Chemicals and reagents used in this study.**

Name	Supplier
Acetonitrile	Sigma-Aldrich
Anaerobic indicator	Thermo Scientific
β-mercaptoethanol	Fisher Scientific
Intercept® blocking buffer	LiCor
BSA	Fisher Scientific
DEPC water	Fisher Scientific
DMEM	Sigma-Aldrich
DMSO	Fisher Scientific
Ethanol	Fisher Scientific
FBS	Autogen Bioscience
HCl	Sigma-Aldrich
Hoechst 33342, trihydrochloride, trihydrate	Invitrogen
Methanol	Fisher Scientific
MMTS	Sigma-Aldrich

Nitrocellulose membrane	Bio-Rad
PFA	Fisher Scientific
PBS	Fisher Scientific
Penicillin-streptomycin (P/S)	Sigma-Aldrich
4-20 % polyacrylamide gel	Bio-Rad
ProLong™ Diamond antifade mountant (with Dapi)	Invitrogen/Life technologies
ProLong™ Diamond antifade mountant (Dapi-free)	Invitrogen/Life technologies
Protease inhibitor	Roche
Protein ladder	Precision plus protein standards, Bio-Rad
RPMI	Sigma-Aldrich
SDS	Fisher Scientific
Tris-Base	Sigma-Aldrich
Triton-X-100	Fisher Scientific
Trypsin 0.05% EDTA	Sigma-Aldrich
Tween 20	Fisher Scientific
Urea	Fisher Scientific

Table 2.4: **Commercially available and in-house synthesised compounds used in this study.**

Name	Solubility and storage temp.	Supplier
Ag5	Water, rt	Arjuna therapeutics
HCIQ (reversible probe)	DMSO, -20 ºC	Synthesised (Chapter 3)
Locked probe	DMSO, -20 ºC	Synthesised (Chapter 3)
Resorufin probe	DMSO, -20 ºC	Synthesised (Conway group)
Phenol control	DMSO, -20 ºC	Synthesised (Conway group)
FL-1	DMSO, -20 ºC	Synthesised (Dr Adam Sedgwick)
Hydrogen peroxide (H_2O_2)	Water, 4 ºC	Sigma-Aldrich
Menadione	DMSO, -20 ºC	Sigma-Aldrich
MitoPQ	DMSO, -20 ºC	Abcam
MitoTempo	DMSO, -20 ºC	Sigma-Aldrich
NAC (*N*-acetylcysteine)	DMSO, -20 ºC	Sigma-Aldrich
NEM (*N*-ethylmalemide)	DMSO, -20 ºC	Sigma-Aldrich
Erastin	DMSO, -20 ºC	Sigma-Aldrich
Ferrostatin	DMSO, -20 ºC	Sigma-Aldrich
TCEP (Tris(2-carboxyethyl)phosphine	DMSO, -20 ºC	Sigma-Aldrich

Table 2.5: **Commercially available detection kits used in this study.**

Name	Purpose of kit	Supplier
MTT	Cell viability	Invitrogen
Crystal violet	Cell viability	Sigma-Aldrich
BODIPY™ 581/591 lipid peroxidation sensor	Lipid peroxidation	Invitrogen, D3861
CellROX™ Green	Total ROS detection	Thermo Fisher Scientific, C10444
MitoSOX™ Red	Mitochondrial ROS detection	Thermo Fisher Scientific, M36008
GSH-Glo assay	GSH detection	Promega, V6911
TrxR assay	TrxR activity	AbCam, ab83463

Table 2.6: **Primary antibodies used in this study.**

Name	Species	Dilution	Application	Supplier and catalogue no.
HIF-1α	Mouse	1:500	WB	BDBiosciences, 610959

β-Actin	Mouse	1:2000	WB	Santa Cruz, 69879
VHL	Rabbit	1:500	WB	Cell Signaling, 68547
GAPDH	Mouse	1:1000	WB	Protein tech, 60004-1-1g
p53 (DO-1)	Mouse	1:1000	WB	Santa Cruz, sc-126
P53 (S15)	Rabbit	1:1000	WB	Cell Signaling, 92845
PRXD3	Rabbit	1:1000	WB	Abcam, ab129206
PDK1	Mouse	1:1000	WB	AbCam, ab110025
PDK3	Rabbit	1:1000	WB	AbCam, 154549

Table 2.7: **Secondary antibodies used in this study.**

Name	Species	Dilution	Application	Supplier and catalogue no.
IRDye 800CW donkey anti-mouse IgG	Mouse	1:10,000	WB	LI-COR, 926-32212
IRDye 680RD donkey anti-mouse IgG	Mouse	1:10,000	WB	LI-COR, 926-68072
IRDye 800CW donkey anti-rabbit IgG	Rabbit	1:10,000	WB	LI-COR, 926-32213
IRDye 680RD donkey anti-rabbit IgG	Rabbit	1:10,000	WB	LI-COR, 926-68073

2.2.2 Tissue culture

Cells were cultured in either DMEM, RPMI or nutrient mixture F12 HAM media (***Table 2.2***), supplemented with 10 % FBS and 1 % P/S. Cells were maintained in a humified incubator at 37 °C with 5 % CO_2 and passaged two-three times a week depending on growth rate. Routine tissue culture involved removing the culture media, washing the cells with PBS and adding trypsin-EDTA followed by incubation (5 min at 37 °C). It was ensured that the cells were free from the bottom of the flask and then the trypsin-EDTA was quenched with media before centrifuging (390 x g, 5 min). The cell pellet was resuspended in fresh media before either seeding for an experiment, in which the cell density was determined using a haemocytometer or putting the cells into a new flask.

2.2.3 Mycoplasma testing

Cells were routinely tested for mycoplasma using test strips (InvivoGen), a HEK Blue detection kit (InvivoGen) or a Lonza MycoAlert® mycoplasma detection assay (Lonza) following the manufacturer's instructions.

2.2.4 Cryopreservation of cells

Cell lines were frozen down by producing a cell pellet from a 70 % confluent flask, and then resuspending in FBS with 10 % DMSO and transferring to a cryovial, ensuring they contained 2-3 million cells each. Cryovials were placed in a Mr Frosty™ at -80 °C for 24 h, before transferring to liquid nitrogen for long term storage.

2.2.5 Thawing of cells

Cryovials were removed from liquid nitrogen and thawed rapidly at 37 °C. The contents of the vial were then added to media (5 mL) and centrifuged (390 x g, 5 min). The supernatant was removed, and the remaining pellet was resuspended in fresh media and transferred to a flask and normal TC conditions.

2.2.6 Hypoxia treatment

Cells were exposed to hypoxia using a Bactron II anaerobic chamber (Shel labs) for experiments at <0.1 % O_2 and an M35 workstation (Don Whitley) for experiments in the range of 0.5-4 % O_2. Glass dishes were used for hypoxia experiments, except when plastic plates were required e.g., for MTT, GSH or colony assays. The oxygen concentration of the hypoxia chambers was periodically confirmed using anaerobic indicator strips (Fisher scientific) or an OxyLite probe (Oxford Optronix).

2.2.7 Ag5 treatment

A stock solution of Ag5 was prepared in water and stored at room temperature, protected from light. The stock solution was sonicated for 30-60 min prior to every use and diluted in serum-free media before adding to cells. Cells were exposed to Ag5/ Ag+ for 1 h in serum-free media, except for the PRDX3 assay in which treatment was 15 min and the ROS assay in which treatment was 5 min, which was then replaced with complete media. In hypoxic conditions, serum-free media and complete media were equilibrated to the desired O_2 concentration before use.

2.2.8 MTT assay

Cells were seeded at the appropriate density, depending on the cell line (***Table 2.8***) in clear, flat bottomed 96 well plates to give a total volume of 100 µL per well. Each treatment condition was performed in triplicate. After treatment, 3-(4,5-Dimethyl-2-yl)-2,5-diphenyltetrazolium bromide (10 µL, 0.5 mg/mL) was added to each well and then the plate was incubated (37 °C, 2-3 h) away from light. The plate was checked under a light microscope to ensure that purple crystals had formed inside the cells within the untreated wells. Media was carefully removed from the wells and DMSO (100 µL/well) was added before incubating the plate (37 °C, 15 min) away from light. The contents of each well were mixed, and the absorbance (570 nm) was read immediately (POLARstar plate reader, BMG LabTech). Cell viability was calculated as a percentage relative to the untreated control.

Table 2.8: **Seeding numbers for MTT assay.**

Cell line	Seeding number
OE21	2500
FLO1	4000
OE33	5000
SKGT4	5000
RKO	9000

RKO HIF$^{-/-}$	12000
A549	4000
H460	4000
MRC5	20000
HFL-1	20000
RCC4	5000
RCC4 VHL$^{-/-}$	10000

2.2.9 Radiation treatment

Irradiation was undertaken using γ-rays from a Cs-137 irradiator (GSM: GSR D1) at a dose rate of 1.7 Gy/min, at rt. For irradiating experiments in hypoxia, cells were transferred to airtight Perspex plastic boxes within the hypoxia chamber to allow for transportation to and from the irradiator (Anbalagan et al., 2012). The OER was assessed for every experiment to ensure that no reoxygenation had occurred.

2.2.10 Colony survival assay

Cells were seeded at the appropriate density, depending on the cell line, dose of radiation and dose of drug, in 6-well plates to give a total volume of 2 mL per well. Seeding of cells was calculated to give a plating efficiency above 50 % for the untreated condition. Each treatment was carried out in triplicate. After treatment (drug/IR/hypoxia), colonies were allowed to grow in a humified incubator (37 °C, 5 % CO_2) for 7-14 days. Once the colonies had grown to a sufficient size (>50 cells), the media was removed and the plates were stained with crystal violet (0.5 % w/v in 50 % MeOH and 20 % EtOH) for 1 h, before washing thoroughly with water. Colonies were counted using a manual cell counter (Stuart Scientific). The survival fraction was calculated by number of colonies counted/ (number of cells seeded × plating efficiency) where the plating efficiency was the number of colonies counted/ number of cells seeded for untreated control. Colony curves were fitted using =exp(-α×radiation dose - β×radiation dose^2), where alpha and beta come from the equation of the graph of the natural log of the survival fraction ($y = -\beta\chi^2 - \alpha\chi$).

2.2.11 Protein lysate preparation

Cell pellets were harvested in UTB lysis buffer (9 M urea, 75 mM Tris-HCl pH 7.5, 0.15 M 2-Mercaptoethanol), with volume used dependent on the pellet size. The lysed samples were sonicated using a probe (20 secs on, 10 secs on ice, 20 secs on) and then centrifuged (4 °C, 13, 000 x g) for 10 min. The supernatant was collected, and the protein concentration was determined using a nanodrop1000 (DEPC water served as a blank).

2.2.12 Immunoblotting

The chosen quantity of protein for the samples were added to Laemmli buffer (3.3 % SDS, 6 mM urea, 17 mM Tris-HCl, pH 7.5, 0.07 M β-mercaptoethanol, 0.01 % bromophenol blue), heated (100 °C, 5 min) and centrifuged briefly. Proteins were separated on a 4-20 % polyacrylamide gel alongside a protein ladder for 1 h 30 min at 100 V in Tris-glycine running buffer (25 mM Tris base, 192 mM glycine, 0.1 % (w/v) SDS). Gels were transferred onto nitrocellulose membrane using the Trans-Blot® Turbo™ transfer system (Bio-Rad). The membranes were then blocked in 1:1 blocking buffer: TBS (50 mM Tris-HCl, pH 7.6, 150 mM NaCl) for 1 h at rt, with gentle shaking. Membranes were probed with primary antibody (***Table 2.6***) diluted in 1:1 blocking buffer: TBS overnight at 4 °C, with gentle shaking. Membranes were then washed (3 x 5 min) with TBS-T (0.1 % v/v Tween) and probed with secondary antibody (***Table 2.7***) diluted in 1:1 blocking buffer: TBS for 1 h at rt, with gentle shaking. Membranes were then washed (3 x 5 min) with TBS-T and stored in TBS before visualising using an Odyssey Infrared Imaging System (LI-COR Biosciences).

2.2.13 Immunofluorescence

Cells were seeded at the appropriate density depending on cell line and experiment, to reach a confluency of 70-80 % on the glass coverslip when imaging. After treatment, cells were fixed with 4 % PFA (10 min), away from light. If the experiment was carried out in hypoxia, fixing took place inside the chamber. The PFA was then removed, and the cells were washed with PBS (3×), followed by Hoechst staining (0.1 μg/mL) for 30 min at rt, away from light. The cells were then washed with PBS (3×) and the cover slips were mounted with DAPI-free mounting media. The slides were analysed using a LSM710 confocal microscope (Carl Zeiss Microscopy Ltd).

2.2.14 Lipid peroxidation assay

Cells were seeded (150,000/well for A549) in a 6-well plate and allowed to adhere overnight. Ferrostatin (5 μM) was used as a positive control and was added at the same time as seeding. After drug treatment, the media was removed and the cells were incubated with BODIPY (2 μM) in PBS for 30 min at 37 °C, away from light. The PBS was then removed and 500 μL of trypsin-EDTA was added for 5 min at 37 °C, away from light. 500 μL of media was then used to quench the samples before pelleting them. The pellet was resuspended in FACs buffer (100-200 μL, PBS, 2 % FBS, 0.5 mM EDTA) and the samples were analysed on a CytoFLEX flow cytometer (Beckman Coulter) using CytExpert software. Analysis was carried out for a cell count of 10,000 events for each treatment condition. FloJo software (BD Biosciences) was used to analyse the data.

2.2.15 GSH-Glo assay

Cells were seeded (4000/well) in white walled, flat bottomed 96 well plates, to give a total volume of 100 μL per well and allowed to adhere overnight. Each treatment condition was performed in triplicate. NEM (200 μM) was used as a control and incubated with the cells for 6 h. After drug/ hypoxia treatment was complete the GSH-Glo assay was undertaken according to the manufacturer's instructions (using half of the reagents that are stated in the protocol for each well). A standard curve was generated for the untreated control and GSH concentration for the sample conditions was calculated against this.

2.2.16 FL-1 GSH assay

Cells were seeded (4000/well) in clear, flat bottomed 96 well plates, to give a total volume of 100 μL per well and allowed to adhere overnight. Each treatment condition was performed in triplicate. NEM (200 μM) was used as a control and incubated with the cells for 6 h. 1 h before drug/ hypoxia treatment was complete, FL-1 (10 μM) was added to each well and the contents of the well was mixed by pipetting. After 1 h, the fluorescence was measured (ex 485 nm, em 520 nm) (POLARstar plate reader, BMG LabTech).

2.2.17 TrxR assay

Cells were seeded in glass dishes and allowed to adhere overnight. After drug/ hypoxia treatment dishes were washed once with PBS, then scraped into PBS and pelleted. The pellet was resuspended in Trx assay buffer (200 μL). The samples were then analysed (using half the quantity of reagents suggested in the protocol for each well), following the manufacturer's instructions and absorbance was measured (POLARstar plate reader, BMG LabTech).

2.2.18 Mitochondrial ROS assay

Cells were seeded in chamber slides in order to achieve 70-80 % confluency at the end of the experiment. 10 min prior to the end of hypoxia treatment MitoSOX (5 μM) was added to the cells and they were returned to their incubator for 10 min. MitoPQ (10 μM) or menadione (100 μM) was used as a positive control and incubated for 6 h with the cells prior to staining. The cells were then fixed with 4 % PFA (10 min, dark), washed with PBS (3 × 1 min) and mounted with DAPI-containing mounting media. Microscopy imaging was carried out using a Zeiss 780 or 710 confocal Microscope (Carl Zeiss Ag, Jena, Germany) at 60x magnification and at least 100 cells were counted per condition for quantification.

2.2.19 Total ROS assay

Cells were seeded in chamber slides in order to achieve 70-80 % confluency at the end of the experiment. 30 min prior to the end of drug/hypoxia treatment CellROX (10 μM) was added to the wells and they were returned to their incubator for 30 min. Menadione (100 μM) was used as a positive control and incubated for 6 h with the cells prior to staining. The cells were then fixed with 4 % PFA (10 min, dark), washed with PBS (3 × 1 min) and mounted with DAPI-containing mounting media. Microscopy imaging was carried out using a Zeiss 780 or 710 confocal Microscope (Carl Zeiss Ag, Jena, Germany) at 60x magnification and at least 100 cells were counted per condition for quantification.

2.2.20 PRDX3 assay

Dishes were seeded with 500,000 cells and allowed to adhere overnight, prior to drug/hypoxia treatment. The media was then replaced with 80 mM methyl methanethiosulfonate (MMTS) enriched media to prevent oxidation of reduced thiols (10

min). The dishes were then washed (2 × ice cold PBS), followed by addition of 75 µL RIPA buffer (50 mM Tris, pH 7.5, 150 mM NaCl, 1 % (v/v) Triton-X100, 0.1 % (w/v) SDS, 0.5 % (w/v) sodium deoxycholate) supplemented with 1× protease inhibitor cocktail and 80 mM MMTS, and incubation for 20 min on ice. The cells were then scraped into the RIPA buffer and the samples were sonicated (30 % amplitude, 1 sec on, 1 sec off ×10) and then centrifuged (14,000 rpm, 20 min, 4 °C). Samples were mixed with loading buffer (250 mM Tris-Cl (pH 6.8), 8 % SDS, 0.1 % bromophenol blue, 40 % (v/v) glycerol, H_2O) (non-oxidising), heated (96 °C, 5 mins) and electrophoresed on a 15 % acrylamide gel (250 V, 50 A). The gel was transferred (1 h) onto a PVDF membrane and blocked with milk powder (1 h), washed 3 × TNT (0.1 % TWEEN) and incubated with 1° antibody (4 °C, overnight). The membrane was then washed ×3 with TNT (0.1 % TWEEN) and incubated with 2° antibody (rt, 1 h) followed by ×3 washing with TNT (0.1 % TWEEN). ECL reagent was then added, and the gels were visualised using a ChemiDoc Imaging System (Bio-Rad).

2.2.21 Statistical analysis

GraphPad Prism software (GraphPad software Inc.) was used to carry out all statistical analysis, including two-way ANOVA for MTT assays, non-linear regression for colony survival assays and unpaired t-tests for ROS/antioxidant assays. Data is presented as mean + SEM. Statistical testing is described in each figure legend. *p<0.05, **p<0.01, ***p<0.001, ****p<0.0001, ns= not significant.

Chapter 3: Design, synthesis, and validation of a reversible, fluorescent probe for measuring real time hypoxia

3.1 Introduction

We investigated the concept of creating a non-invasive imaging modality that could take repeat measurements and change its output to reflect the dynamic changes of its oxygen environment. As a starting point, we used fluorescent imaging to develop the probe with the goal of extending these studies to MRI or PET in the future. Overall, our aim was to synthesise a reversible, fluorescent, hypoxia sensing probe that would aid pre-clinical testing of hypoxia-targeted therapies.

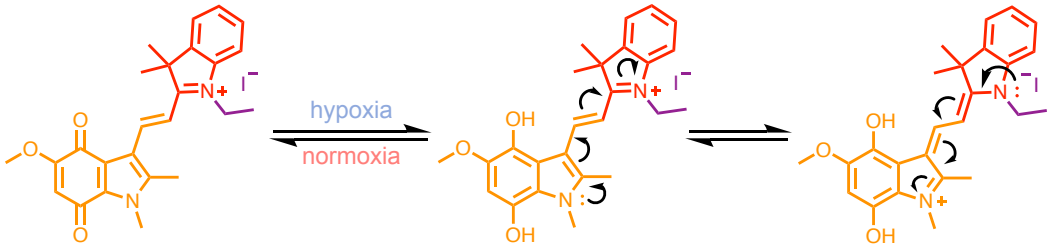
3.1.1 Current hypoxia sensing probes

The dynamic nature of hypoxia, involving repeated re-oxygenation cycles, has led to the development of various chemical probes that can monitor oxygen levels, with a fluorescent output. In 2012, Takahashi and colleagues claimed to have synthesised the first reversible fluorescence probe that could detect repeated hypoxia-normoxia cycles using bioreductase activity (Takahashi et al., 2012). A FRET based system was used to produce the probe and it was seen to withstand three hypoxic-normoxic cycles induced by adding a coverslip on top of A549 cells. At a similar time, a novel fluorogenic compound, image-iT™, was reported to measure hypoxia in real-time, via oxygen-dependent quenching of phosphorescence (Zhang et al., 2010). At oxygen concentrations of below 5 % O_2 the image-iT™ probe emits a red fluorescence capable of penetrating tissue, when the O_2 partial pressure increases this fluorescence is lost. In 2021, a reversible arylazo-based NIR probe to monitor cyclic hypoxia was reported (Zhang et al., 2021). This construct became highly emissive at an oxygen level of 10 % O_2 which is not generally considered hypoxic. The 2021 model was later modified and able to image acute and chronic hepatic injury, showing a 7-fold fluorescent increase at 0.1 %

O_2 and participation in hypoxic/reoxygenation cycles (Yao et al., 2024). Overall, there have been various attempts to produce a probe capable of measuring fluctuating oxygen levels in pathological states. Taking this in mind, we sought to produce a reversible fluorescent probe to measure hypoxia, that we could later modify to target specific organelles, or add MRI/PET detection groups or sense specific oxygen concentrations.

3.1.2 Probe design

The probe was designed to include three moieties: a hypoxia sensing group, a fluorophore and a targeting group. To allow for reversible communication an extended conjugation system was included (***Scheme 3.1***). The hypoxia-sensitive quinone group is electron withdrawing, therefore in normoxia the rate of release of electrons from the nitrogen is slow, whereas in hypoxia the quinone is now electron rich and this process is accelerated. The change in electronics upon reduced oxygen levels will result in altered photophysical properties, allowing for differentiation between the two forms of the probe.



Scheme 3.1: **Chemical structure and proposed mechanism of action for initial target probe.** The probe consists of an indolequinone group (hypoxia sensing group), hemicyanine dye (fluorophore) and control group (targeting element). The probe would undergo reduction to the dihydroxy-form under hypoxia and this would be able to resonate between two forms. The probes change in structure would give a visual readout.

Hypoxia sensing group

The hypoxia sensing group chosen was an indolequinone modality. Quinone structures have been previously documented to undergo accelerated bioreduction in hypoxic

conditions, but the reduction is quenched by the presence of oxygen in normoxia (Komatsu et al., 2010; Wallabregue et al., 2023). This oxygen-sensitive mechanism can be combined with a fluorophore, resulting in emission under hypoxic conditions. Bioreduction of functional groups, including nitrobenzyls, nitroimidazoles, azides and quinones, is carried out primarily by nitroreductases and cytochromes, whose expression is upregulated in hypoxia. Quinones are reduced from a hydroquinone to benzoquinone functionality by cytochrome p450, with the exact mechanism unknown.

Fluorophore

The mode of visualisation used for the probe was fluorescence, with the chosen fluorophore comprising a hemi-cyanine dye. This was employed as it has shown to emit in the NIR region, which is desirable for visualisation (Rivera et al., 2007). ICG contains structures similar to the fluorophore chosen and has been shown as a valuable probe when evaluating tumours in surgery, indicating the probe would be tolerated in the body (Lim et al., 2023).

Targeting group

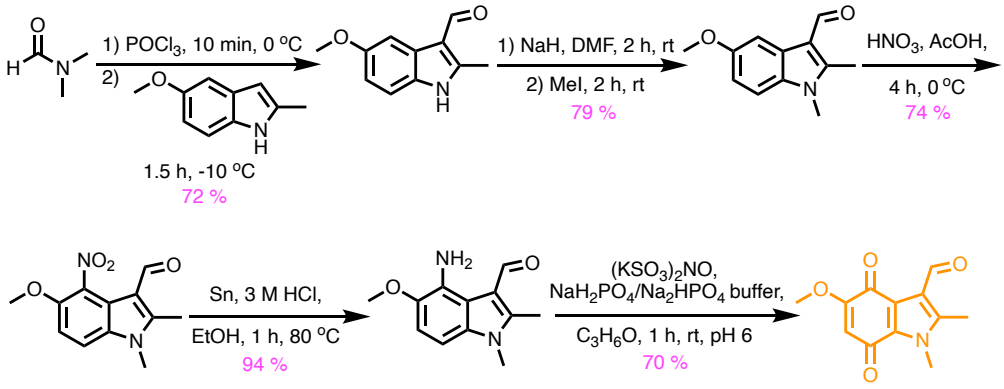
The targeting group would allow the probe to be directed to specific subcellular compartments within the cell. In the initial target probe, there is an ethyl chain, displayed in purple, that would act as an attachment point for targeting groups in later iterations. By producing a small library of probes with different organelle targeting groups, the nature of specific organelles could be studied, a concept that has not been investigated before (Gao et al., 2019).

3.2 Results

3.2.1 Probe synthesis

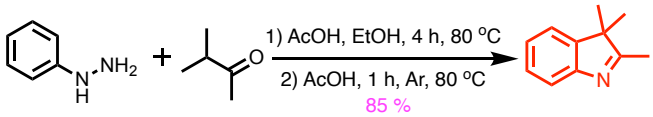
Probe synthesis took the form of constructing each individual component and then combining them to give the target compound.

The indolequinone group was synthesised (***Scheme 3.2***) from the commercially available starting material 5-methoxy-2-methyl-1*H*-indole (Huang et al., 2010; Phillips et al., 1999). Formylation via a Vilsmeier-Haack reaction to allow for later attachment of the fluorophore was achieved, followed by alkylation of the nitrogen via NaH deprotonation and MeI addition. HNO_3 in AcOH was used install a nitro group before subsequent tin reduction to the amine and oxidative condensation to the desired indolequinone using potassium nitrosodisulfonate (Fremy's salt) (Zimmer et al.). In its yellow, solid form Fremy's salt exists as a dimeric species whereas, when added to an aqueous solution such as sodium phosphate buffer, a deep violet solution is formed containing monomeric nitrosodisulfonate ions. Two equivalents of Fremy's salt are needed to react with the substituted aniline to give the *p*-benzoquinone in a good yield (70 %). It has been shown that di-ortho substituted anilines display better yields then di-meta substituted ones, potentially due to less steric hindrance occurring when oxygen enters para to the amine group, or side reactions of the quinone oxygen with the amine being more hindered in the ortho option, or the stability of the developing radical which will control subsequent quinone formation. In the case of the amine here, it has an ortho methoxy substituent and then the indole ring fills both the ortho and meta position on the other side of the ring.



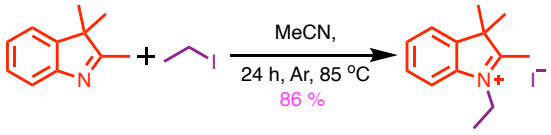
Scheme 3.2: **Synthesis of 5-Methoxy-1,2-dimethyl-4,7-dioxo-4,7-dihydro-1*H*-indole-3-carbaldehyde.** Indolequinone synthesis starting from 5-methoxy-2-methyl-1*H*-indole (Huang et al., 2010).

The hemicyanine dye was synthesised via a one-step Fischer indole synthesis, involving a crucial [3,3]-sigmatropic rearrangement, from commercially available Phenylhydrazine and 3-methylbutan-2-one (***Scheme 3.3***) (Yang et al., 2020).



Scheme 3.3: **Synthesis of 2,3,3-Trimethoxy-3*H*-indole.** Hemicyanine dye synthesis via Fischer indole mechanism (Yang et al., 2020).

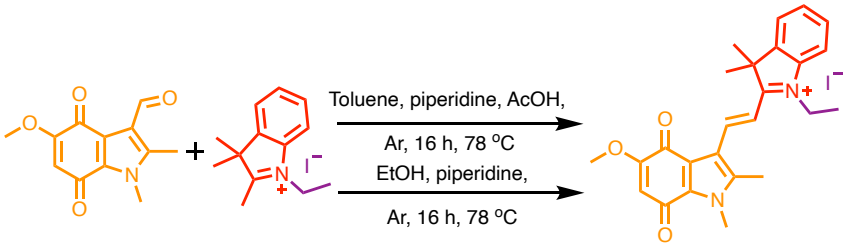
Alkylation with EtI gave the desired fluorophore with the control group attached (***Scheme 3.4***) (Wang et al., 2020a).



Scheme 3.4: **Synthesis of 1-Ethyl-2,3,3-trimethyl-3*H*-indol-1-ium.** Alkylation of 2,3,3-trimethoxy-3*H*-indole (Wang et al., 2020a).

Once both the hypoxia sensing group and fluorophore with control group attached were in hand, a Knoevenagel condensation was employed to join the two halves of the probe together. Knoevenagel condensation is a variation of the common aldol condensation.

Two common conditions for this reaction were used (***Scheme 3.5***). Upon completion of the reaction, indicated by TLC analysis, the correct calculated mass could be seen in the LRMS. However, the ^{1}H NMR spectrum appeared to be at a very low concentration, even with high amounts of reaction product in the NMR sample. Additionally, the compound was extremely insoluble, with many deuterated solvents trialled. Overall, this indicated that the reaction had not given the desired product.



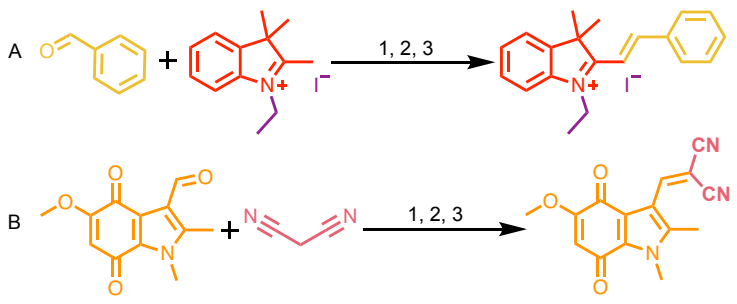
Scheme 3.5: **Initial probe synthesis route.** Knoevenagel condensation to combine the hypoxia sensing group and the fluorophore containing the control group together, with two sets of standard conditions.

The synthesis of more soluble probe derivatives was attempted by functionalising the hemicyanine dye with solubilising PEG groups. A halide PEG linker was synthesised and attached to the hemi cyanine dye via an SN2 reaction (Descotes and Pralyet, 1986). A C16-chain version of the hemicyanine dye was also achieved. C12- and C16-chains have been shown to target the plasma membrane of cells therefore, this probe could be part of the targeting library. The ethanol Knoevenagel conditions (*Scheme 3.5*) were used, as these produced a greater mass of potential compound before. However, the target product was not produced but this compound was able to dissolve in $CDCl_3$ therefore, solubility had improved as predicted.

The challenge with the synthetic route was the Knoevenagel condensation to join both parts of the probe together, allowing electrons to flow up and down the system when in hypoxia/normoxia. Previous synthetic strategies in the Conway group to join two parts of

a hypoxia sensitive probe together utilised reactions that would then fall apart in hypoxic conditions to release the active moiety. However, this was the first case where it was essential for the system to stay intact when entering hypoxia, so the Knoevenagel condensation reaction was investigated further.

Each component of the probe was paired with a simpler reacting partner to assess the reactivity of each half of the probe in the reaction (***Scheme 3.6***). Benzaldehyde and malononitrile were chosen as the basic reacting partners as it was predicted that they would have similar reactivity to the original reacting partners, and they have both been shown to participate in Knoevenagel condensations (Saghian et al., 2023; Dalessandro et al., 2017). Both reactions were trialled with all common Knoevenagel conditions (***Table 3.1***), and the desired product was produced in two out of the three cases for each reaction. The toluene conditions were the most promising for both trial reactions, with the correct product being formed in each case. These conditions were taken forward for future experiments. Overall, we confirmed that both components of the probe could participate in the reaction therefore, the Knoevenagel condensation should be able to occur.

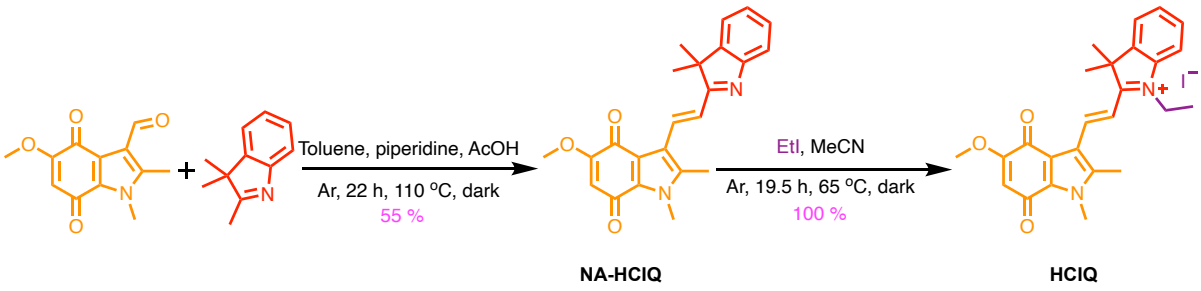


Scheme 3.6: **Problem solving for Knoevenagel condensation.** Knoevenagel condensation of indole with benzaldehyde (A) and indolequinone with malononitrile (B), attempted with various conditions (*Table 3.1*).

***Table 3.1:* Common Knoevenagel reaction conditions.** Conditions trialled for Knoevenagel condensation A and B (*Scheme 3.5*).

Knoevenagel condensation	Toluene, piperidine, AcOH	EtOH, piperidine	Acetic anhydride
A	Produced desired product	Produced desired product	No product observed
B	Produced desired product	No product observed	Produced desired product

A Knoevenagel condensation was then attempted using the indolequinone and the indole without the control group attached. The toluene, piperidine and AcOH conditions were used (*Table 3.2*). This reaction gave full conversion to the desired product within 22 h, judged by TLC, and the correct mass in LRMS. Once purified via silica gel flash column chromatography, it was confirmed that the desired product had been synthesised via ^{1}H NMR analysis. Alkylation of the product was then undertaken (*Scheme 3.4*) to afford the final probe. Overall, a synthetic route to produce the initial target probe (hemicyanine indolequinone-**HCIQ**) was devised (***Scheme 3.7***).



***Scheme 3.7:* Synthesis route to produce target probe.** Optimised synthetic route to produce **HCIQ** starting from 5-Methoxy-1,2-dimethyl-4,7-dioxo-4,7-dihydro-1*H*-indole-3-carbaldehyde and 2,3,3-Trimethoxy-3*H*-indole.

3.2.2 Electrochemistry

To assess the reversibility of **HCIQ**, electrochemistry was employed. This process looks at reactions involving electron transfers and relates this to chemical changes, such as reduction or oxidation of a compound. In an experimental setting a voltage is applied to an electrode, in this case made from glassy carbon, via a potentiostat. When the energy of the electrons on the electrode is higher than the energy of the LUMO of the compound,

an electron is transferred to the compound, and it is reduced. The converse is true for the other half of the experiment. This gives peaks on a cyclic voltammogram, which displays the trace from an experiment, with the applied potential on the x-axis and the resulting current passed on the y-axis. So, a peak would indicate that at a particular potential applied, a rise in the resulting current can be seen, which is due to the gain/loss of an electron (Elgrishi et al., 2017).

Cyclic voltammetry, a variant of electrochemistry, was used to determine the redox chemistry of **HCIQ** under electrochemical conditions. This procedure shows the oxidation and reduction processes that take place in the sample, and it is commonly done against the universal reference ferrocene. As the potential range sweeps around what has been inputted into the potentiostat, electrons are added or taken away from the sample leading to a peak or trough in the working electrode current. **HCIQ** showed a potentially reversible process, within the potential window (***Figure 3.1***). This can be seen when a reduction peak on the voltammogram has a corresponding oxidation peak or vice versa. A reduction peak was seen at ~0.4 V, with a corresponding oxidation peak of a similar voltage. However, the peaks are not completely symmetrical indicating instability. This suggests that the probe was reduced via a redox process, but decomposition occurred leading to the oxidation of a slightly different species. The cyclic voltammetry therefore shows that a redox process is occurring as the probe was designed for but, there is chemical instability present. A clear example of a reversible process is the ferrocene standard, in which the peaks are completely symmetrical. The reduction potential for the probe in comparison to the ferrocene standard was +0.26 V vs Fc/Fc^{+}.

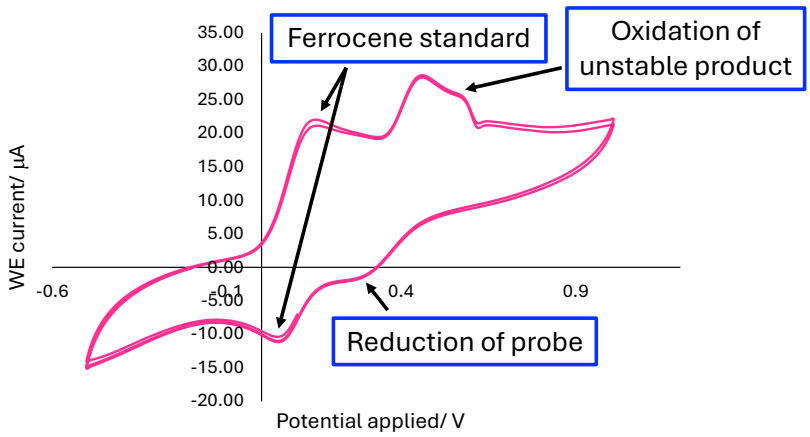
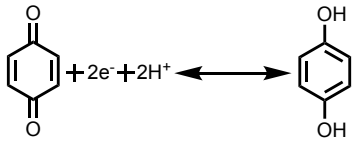


Figure 3.1: **Reversibility seen for HCIQ electrochemically via cyclic voltammetry.** Cyclic voltammogram of **HCIQ** against a ferrocene reference, showing a potentially reversible reduction process.

Aside from the potentially reversible peaks shown, there were also some irreversible processes present where there was just one oxidation/reduction peak on its own with no corresponding peak seen for the reverse process. This irreversibility seen within some of the sweeps could be due to the harsh conditions of the electrochemistry. This technique cannot be directly comparable to a cellular environment as other areas of the probe could be affected here, aside from where cytochrome p450 reductase would interact with the indolequinone group in a cell.

The non-alkylated version of the probe (**NA-HCIQ**) was also tested under these electrochemical conditions as a control. The non-alkylated system is much simpler in terms of its redox abilities. It is not conjugated throughout the chemical structure; therefore, the only reversible part of the probe should be the reduction of benzoquinone to hydroquinone and then oxidation back to benzoquinone (***Scheme 3.8***). The cyclic voltammogram for **NA-HCIQ** showed a completely reversible process in all three sweeps (***Figure 3.2***). The reduction potential changed from +0.26 V vs Fc/Fc^+ for **HCIQ** to -1.27 V vs Fc/Fc^+ for **NA-HCIQ**, indicating the differences in the two species.



Scheme 3.8: **Reversible electrochemical reduction of benzoquinone to hydroquinone.**

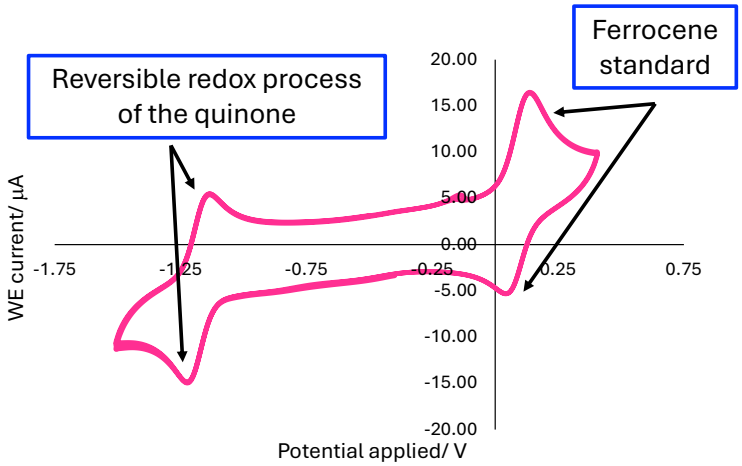


Figure 3.2: **Reversibility seen for NA-HCIQ electrochemically via cyclic voltammetry.** Cyclic voltammogram of **NA-HCIQ** displaying the completely reversible oxidation/reduction process occurring at the quinone part of the structure.

3.2.3 Chemistry characterisation

Characterisation of the redox chemistry of **HCIQ** was done using standard techniques. NMR analysis was undertaken both before and after the addition of sodium dithionite ($Na_2S_2O_4$), a compound that chemically mimics hypoxic reduction (***Figure 3.3***). The most notable difference between the two spectra was seen for the aromatic proton of the indolequinone component. The chemical shift of this resonance moved 0.63 ppm downfield when in the reduced form. This can be accounted for by the fact this proton is now attached to an aromatic system therefore, it is shifted more towards the aromatic region in the ^1H NMR. There was also a dramatic colour change seen, with the oxidised form a bright orange colour and the reduced form a deep purple colour, allowing for visualisation of the two forms with the naked eye.

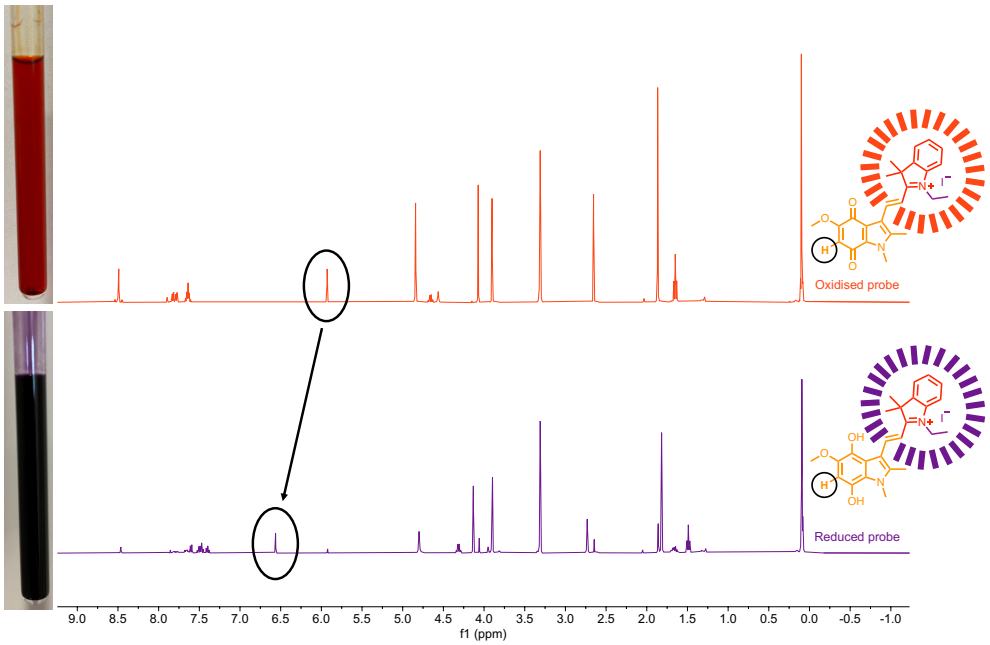


***Figure 3.3:* Chemical characterisation of oxidised and reduced HCIQ.** Stacked ^{1}H NMR spectra of the oxidised and reduced form of **HCIQ** with the respective NMR tubes, displaying the shift changes between the two forms.

The reduced NMR sample was seen to return to the colour of the oxidised form overnight, potentially due to re-oxidation from oxygen in the tube (***Figure 3.4***). An NMR spectrum taken once the orange colour had completely returned did not match the oxidised spectrum, potentially due to probe stability or adverse effects of $Na_2S_2O_4$ (***Figure 3.5***).



***Figure 3.4:* Colour change displaying the reversibility of HCIQ.** NMR tube containing the reduced probe sample that can be seen to be re-oxidised by oxygen present in the top of the NMR tube.

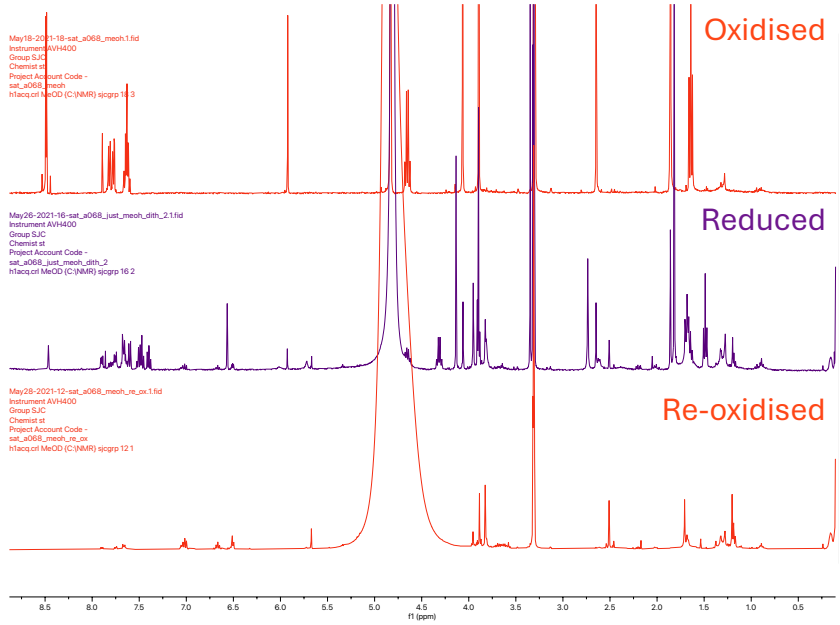


Figure 3.5: **Comparison of oxidised, reduced and re-oxidised HCIQ.** Stacked ^{1}H NMR spectra of oxidised, reduced and re-oxidised **HCIQ**. A sample of HCIQ was chemically reduced with $Na_2S_2O_4$ and then left to re-oxidise in an oxygenated environment, with an NMR spectrum recorded at each point.

ESI-MS was also recorded for both the oxidised and chemically reduced form of **HCIQ** where the expected mass for both versions of the probe was seen in their respective samples. However, the oxidised mass was also seen in the reduced probe sample, potentially due to MeOH in the sample vial re-oxidising some of the sample, less than 100 % conversion to the reduced species or introduction of oxygen when entering the mass spectrometer. This is comparable to the NMR spectrum, where a small peak denoting the hydrogen present in the indolequinone of the oxidised probe is seen in the reduced spectrum. LCMS analysis showed a 73 % conversion to the oxidised form upon $Na_2S_2O_4$ reduction, but oxygen infiltration could occur here as well (***Figure 3.6***). The reduced MS sample turned colourless over time, potentially due to the harsh $Na_2S_2O_4$ conditions.

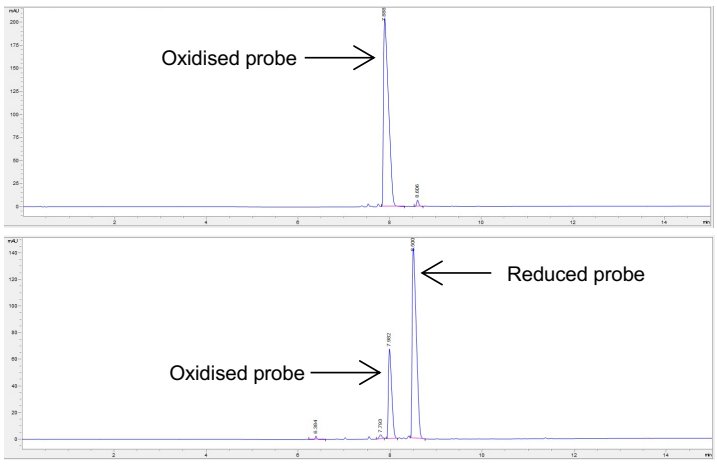


Figure 3.6: **LCMS analysis of HCIQ chemical reduction.** LCMS traces (mAU against time) of both the oxidised (top) and reduced (bottom) versions of the probe. A gradient method of 98:2 H_2O/MeCN for 2 min to 5:95 H_2O/MeCN by 10 min with a 5 min hold, with a constant flow rate of 0.4 mL min^{-1} and an injection volume of 10 μL was used.

Overall, many of the common chemistry techniques utilised to study both the oxidised and reduced form of the probe were challenging as oxygen could not be excluded from the samples or equipment. However, this did allow for the reversibility of the probe to be visualised, through a colour change, upon oxygen infiltration.

NMR and ESI-MS experiments were undertaken with **NA-HCIQ** as a control compound, where the indolequinone region would be reduced from a benzoquinone to a hydroquinone. But, in comparison to **HCIQ** no communication with the fluorophore would be possible, denoting that this region of the probe should remain unchanged in the analysis. The NMR tube for this experiment went from a red colour for **NA-HCIQ** to a deep purple colour for the reduced species, with a shift change for the same hydrogen in **HCIQ**, depicting the reduction of the quinone group. However, there were other peaks in the spectrum, potentially indicating that another species was present. In contrast to the ESI-MS and NMR of **HCIQ**, no peak denoting the oxidised form of **NA-HCIQ** was present in the reduced sample spectrums, suggesting the conjugation in **HCIQ** is significantly

different from **NA-HCIQ**. This indicates that **HCIQ** can quickly revert to its oxidised form upon the introduction of a small amount of oxygen, altering the characterisation outcome.

3.2.4 UV/Vis and Fluorescence studies

UV/Vis spectroscopy was employed to obtain an absorption spectrum for the oxidised and chemically reduced form of **HCIQ**. This analytical technique gives a unique spectrum for a particular sample according to the wavelength of UV or visible light absorbed by the sample or transmitted through it. The absorption maxima shifted to a higher wavelength for the reduced sample and the peak increased in absorption intensity compared to the oxidised probe (***Figure 3.7***). This demonstrated that the reduced probe would emit fluorescence in the NIR region as it was absorbing in the red region of the spectrum. The same distinct colour change as seen in the NMR experiments (Figure 3.3) was also visualised here (*Figure 3.7*).

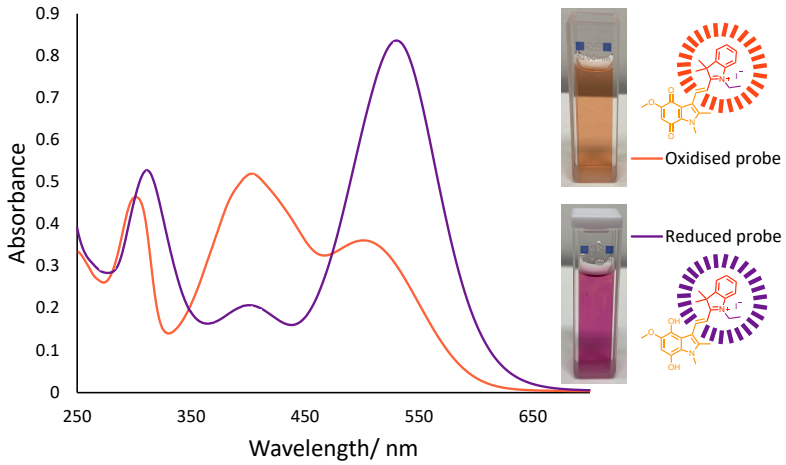


Figure 3.7: **Absorption spectrum of oxidised and chemically reduced HCIQ.** Sample measured in distilled water and then with the addition of $Na_2S_2O_4$, between 250 nm and 750 nm. Comparison in colour for oxidised **HCIQ** and reduced **HCIQ** samples shown.

Approximately one minute after the addition of $Na_2S_2O_4$ to the sample, the colour of the reduced purple sample began to change back to orange at the top of the cuvette, where oxygen was present (***Figure 3.8***). This was indicative that the sample was being oxidised, similar to the NMR experiment (*Figure 3.3*), but the sample went colourless overnight.



Figure 3.8: **Cuvette containing a reduced sample of HCIQ.** The chemically reduced sample can be seen to be interacting with the oxygen present in the top of the cuvette and returning to the colour of the original oxidised species.

Next, fluorimetry was undertaken. This process involves shining a defined wavelength of light onto a sample and then detecting the wavelength of light emitted. Emission spectra were collected for the oxidised and chemically reduced form of **HCIQ**. As expected, no emission was seen for the oxidised species. However, only approximately 2000th of amount of fluorescence desired for cellular visualisation was seen for the reduced sample (***Figure 3.9***).

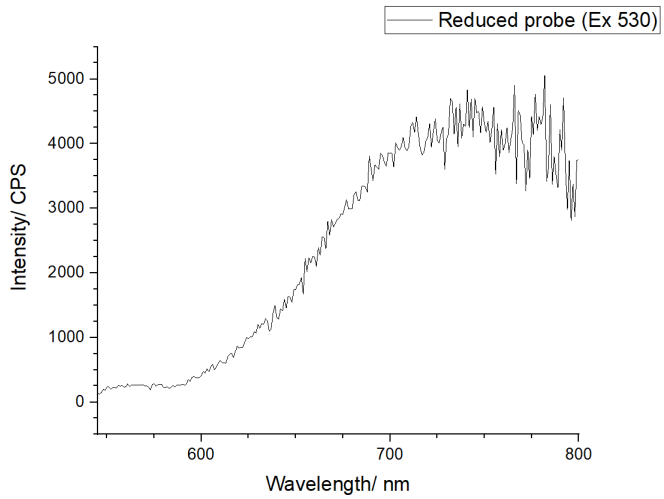


Figure 3.9: **Emission spectrum of chemically reduced HCIQ.** Sample excited at 530 nm in distilled water, using $Na_2S_2O_4$ as a chemical reducing agent.

3.2.5 Cytochrome P450 assay

To investigate if the harsh $Na_2S_2O_4$ conditions were inhibiting emission from the reduced sample, an enzyme-based assay was used, to give a more physiological approach. The enzyme assay simulates a cellular environment better than chemical reductants but allows for focus on the core reduction reaction, without interference from other species that would be present in cells.

Several optimisation assays were carried out with **HCIQ** in normoxia and hypoxia (***Table 3.2***). In the first assay the sample vials turned purple upon addition of the enzyme in hypoxia as expected (***Figure 3.10***) but then turned orange again after some time. The following assays tried to investigate this unusual observation by altering the sample collection method, amount of assay components and analysis technique.

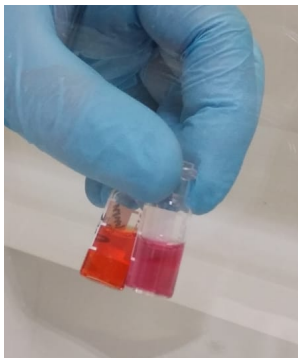


Figure 3.10: **Enzyme assay samples of HCIQ with and without enzyme addition.** Picture of sample vial containing the **HCIQ** probe a few mins after addition of enzyme (RHS) in comparison to a stock solution of **HCIQ** (LHS).

Table 3.2: **Enzyme assays trialled.** Assay description, visual observations and analytical observations.

Assay	Norm/Hyp	Visual observations	Analysis method	Analytical observations
1: Original assay	Hypoxia (0.1 % O_2)	T_0: Colour change from orange to purple upon reduction T_1: Sample had changed from purple to light orange	LCMS	T_1: Oxidised mass and a mass that would account for addition of hydroxyl group present but no reduced mass
2: Shorter time course	Hypoxia (0.1 % O_2)	T_0-T_1 = 1 h: Sample stayed purple for time course however, turned orange when added to MeCN (at 0.1 % O_2 for 3-4 days) for analysis	LCMS	Same as 1st assay
3: Varying the amount of enzyme	Normoxia and Hypoxia (0.1 % O_2)	Samples turned purple in hypoxia for all 3 enzyme concentrations but turned orange when added to MeCN (degassed for 1 h and overnight at 0.1 % O_2). Further sample aliquots were split between MeCN or EtOAc. EtOAc aliquots stayed purple to begin with but were orange when taken out of -20 °C for analysis. After 3 h at 0.1 % O_2 all sample vials had turned orange. All normoxic samples stayed orange throughout the experiment.	LCMS	All 3 normoxic sample vials showed the oxidised mass of the probe throughout the time course, showing it was stable in the conditions used
4: Different analysis technique	Normoxia and Hypoxia (0.1 % O_2)	No quenching of the reaction with MeCN/EtOAc was needed so change in colour was not seen upon sample aliquot collection	UV/Vis	Easier analysis technique as no need to quench reaction but quantity of enzyme was not optimum here

Overall, it was determined that the probe system was more complex than initially hypothesised and that further chemical modification would be needed to improve the fluorescent emission and eventually allow for cellular visualisation.

3.2.6 Theories for why the probe was not emitting fluorescence

As described above, **HCIQ** was not seen to be fluorescent, in either the oxidised or the reduced form. The primary hypothesis for this was quenching of the reduced probe by other species present in the sample. The other species would either block the excited electron in the probe falling back down to the ground state or the excited electron would be transferred to the empty molecular orbital of the other species instead of falling to the ground state, with either scenario preventing the emission of a photon. $Na_2S_2O_4$ did not fully reduce the probe, shown in the chemical and photophysical analysis, therefore remaining oxidised probe could be quenching the fluorescence. The benzoquinone group of the oxidised probe is electron deficient meaning that the excited electron within the reduced probe could be donated here. To test this theory and collect accurate characterisation data for the reduction endpoint, synthesis of a positive control was proposed (***Figure 3.11***). A valuable positive control is a probe that is permanently locked in the reduced state so that 100 % of it could be tested in a sample, eliminating interference from any other species. This would also mean no $Na_2S_2O_4$ would be needed to determine this probes photophysical properties so other parts of the probe would remain intact.

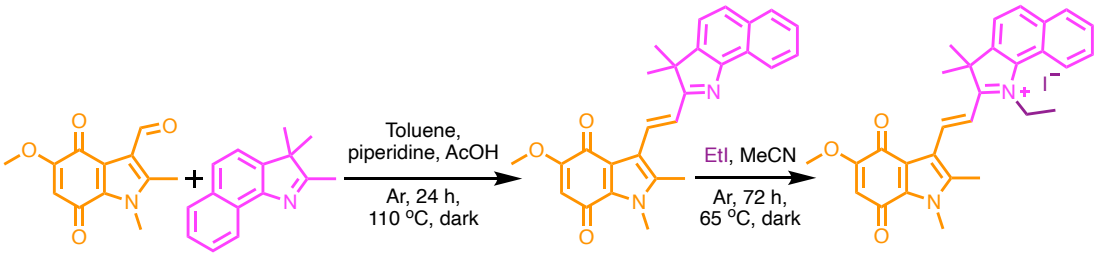
An alternative hypothesis is that PET quenching could take place within the system. This can be explained by looking at the hypoxia sensing group and the fluorophore as separate molecular orbitals (Dias et al., 2018). The benzoquinone group is electron poor whereas

the hydroxyquinone group is electron rich. This means that in the oxidised form, the fluorophore is an electron donor, and the benzoquinone group is an electron acceptor. Therefore, when the probe is excited the electron that moves from the ground state to S_1 in the fluorophore can then go into the LUMO of the benzoquinone group instead of going back down to the ground state in the fluorophore and emitting a photon. In the reduced form, the opposite could be observed: so, the fluorophore would be the acceptor and the hydroxyquinone would be the donor. In this scenario, when the reduced probe is excited, the electron will again move up to S_1 and an electron from the hydroxyquinone group will donate an electron to the ground state molecular orbital of the fluorophore meaning that the electron in S_1 of the fluorophore cannot relax back down to the ground state and release a photon. Analysing this theory, neither form of the probe would be seen as fluorescent. Therefore, to push one form of the probe to be fluorescent, the HOMO-LUMO gaps between the donors and acceptors need to be altered. In order to do this, the fluorophore could be altered to alter the energies of its molecular orbitals. These energies could then be calculated using cyclic voltammetry. Therefore, a fluorophore variation was hypothesised and synthesised (***Scheme 3.9***).

3.2.7 Fluorophore variation

Altering the fluorophore could enhance the fluorescent properties of the probe by changing the HOMO-LUMO energy gaps and stopping potential PET quenching. The fluorophore was chosen to be altered as changing the indolequinone could abolish its hypoxia sensing ability. Naphthalene rings are seen in many fluorescent probes due to their high quantum yield and large π-electron conjugated system, therefore a naphthalene-based fluorophore was synthesised (Lin et al., 2018). The synthesis started

from commercially available 2,3,3-trimethyl-3*H*-benzo[*g*]indole. A Knoevenagel condensation was used to join the fluorophore to the indolequinone, before alkylating to produce the final probe (*Scheme 3.9*).



Scheme 3.9: **Synthesis route for (*E*)-1-ethyl-2-(2-(5-methoxy-1,2-dimethyl-4,7-dioxo-4,7-dihydro-1*H*-indol-3-yl)vinyl)-3,3-dimethyl-3*H*-benzo[*g*]indol-1-ium.**

The naphthalene derivative of the probe was tested for its emissive properties; however, it did not show a significant increase in fluorescence compared to **HCIQ** when reduced with $Na_2S_2O_4$. Therefore, this portion of the project was not continued.

3.2.8 Locked form synthesis

To investigate whether the fluorescence of reduced **HCIQ** was being quenched by remaining oxidised probe, a positive control/completely locked form of the reduced probe was designed (*Figure 3.11*). This probe would be locked chemically in the reduced form by adding blocking groups to the hydroxyls of the hydroxyquinone, keeping the probe in the hydroquinone form regardless of the O_2 concentration. The photophysical properties of this probe could be investigated, without interference from other chemical species and it would serve as a positive control in cell studies. However, the locked form would not contain the acidic OH functionality that reduced **HCIQ** would have, therefore there is redox chemistry not available to the locked probe that would be available to reduced **HCIQ**.

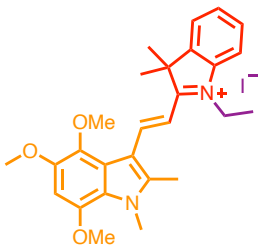
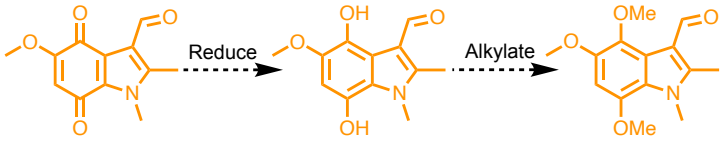


Figure 3.11: **Structure of target locked probe.** Proposed structure of the locked form of **HCIQ**, with methyl groups blocking potential reduction.

Numerous routes were trialled to produce a locked probe, with the main three detailed below.

Reduction of 5-methoxy-1,2-dimethyl-4,7-dioxo-4,7-dihydro-1H-indole-3-carbaldehyde



Scheme 3.10: **Initial proposed synthesis to obtain the locked indolequinone.** Reduction of quinone, followed by installation of methyl groups, trialled with various conditions (***Table 3.3***) (Jung and Hagenah, 1987; Bauch et al., 2017).

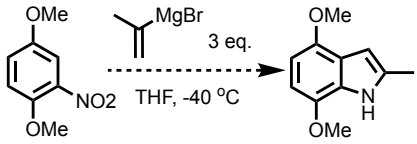
Table 3.3: **Conditions trialled for reduction and methylation to give the locked indolequinone.** (Jung and Hagenah, 1987; Bauch et al., 2017).

Components	Outcome
$Na_2S_2O_4$ (2.0 eq.), pyridine (5.0 eq.), MeI (5.0 eq.), H_2O, MeCN	Starting material recovered
$Na_2S_2O_4$ (2.0 eq.), K_2CO_3 (10.0 eq.), MeI (10.0 eq.), H_2O, MeCN	Starting material recovered
1)$Na_2S_2O_4$ (7.43 eq.), ether, H_2O 2)K_2CO_3 (11.12 eq.), Me_2SO_4 (6.69 eq.), acetone	No product
1)$Na_2S_2O_4$ (10.0 eq.), ether, H_2O 2)K_2CO_3 (11.05 eq.), Me_2SO_4 (0.0065 eq.), acetone	Very low yield
1)$Na_2S_2O_4$ (10.0 eq.), ether, H_2O 2)K_2CO_3 (15.0 eq.), Me_2SO_4 (15.0 eq.), acetone	Very low yield
$Na_2S_2O_4$ (15.0 eq.), EtOAc, H_2O, Na_2SO_4, K_2CO_3 (15.0 eq.), Me_2SO_4 (15.0 eq.)	Starting material recovered
Zinc dust (1.5 eq.), NaOH (12.0 eq.), EtOH, H_2O, methyl p-toluene sulfonate (12.0 eq.)	Very low yield
$Na_2S_2O_4$ (30.0 eq.), EtOAc, H_2O, K_2CO_3 (15.0 eq.), MeI (15.0 eq.)	No product

Bartoli indole synthesis

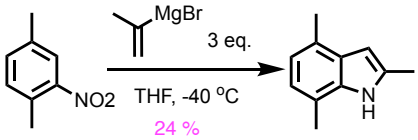
The reaction mechanism requires three equivalents of Grignard to transform the nitro derivative to an indole (***Scheme 3.11***). Instead of the desired product, LRMS and 1H NMR

indicated formation of a nitroso compound, suggesting only one equivalent of Grignard had reacted. Further addition of Grignard did not drive the reaction forwards.



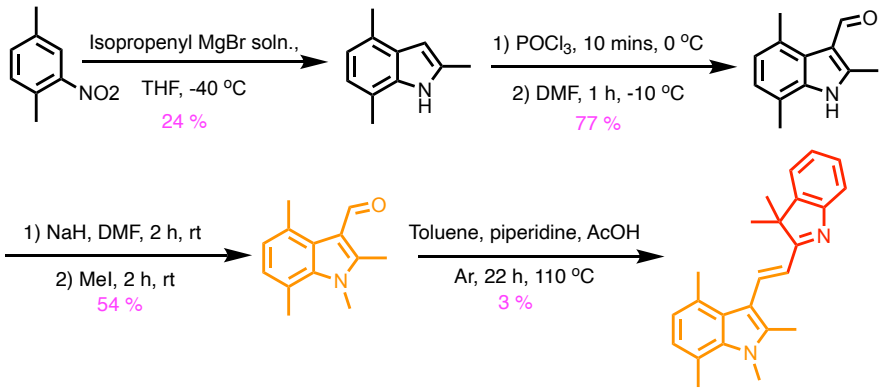
Scheme 3.11: **Bartoli indole synthesis route proposed to produce locked quinone.**

The literature starting material was purchased to troubleshoot the issues with the Bartoli indole mechanism, and the documented indole was produced (***Scheme 3.12***) (Zhang et al., 2019a). Solubility of the starting materials in THF was determined to be the problem of the first reaction (*Scheme 3.11*), which did not improve when other solvents were trialled.



Scheme 3.12: **Literature mechanism for Bartoli indole synthesis** (Zhang et al., 2019a).

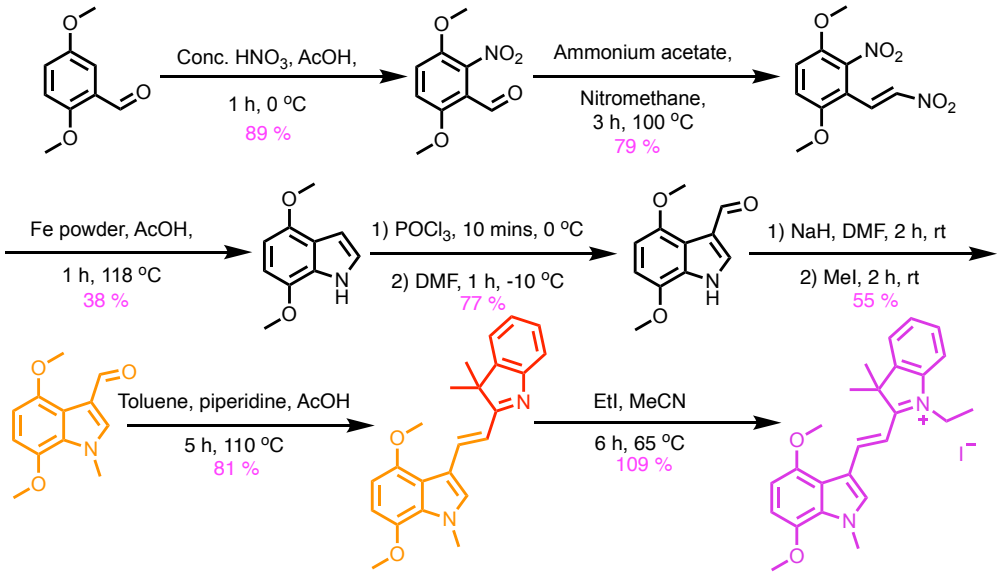
The synthesis route was continued from 2,4,7-trimethyl-1*H*-indole (***Scheme 3.13***). Alkylation to achieve the final probe was extremely slow, accounting to the less activated system however, the reaction spot produced on TLC was fluorescent under UV light. Overall, the yield of the final product with the ethyl chain attached was too small to be able to carry out chemical characterisation therefore, this probe was not taken forward to photophysical testing.



Scheme 3.13: **Synthesis of (*E*)-3-(2-(3,3-dimethyl-3*H*-indol-2-yl)vinyl)-1,2,4,7-tetramethyl-1*H*-indole.** (Zhang et al., 2019a).

Branched route

It was predicted that the trimethoxybenzene ring was too activated for ring formation to occur on a hydrogen in the ring. Therefore, a branched route was proposed in which two arms would come off the trimethoxybenzene and then be reduced to join together. The unsymmetric nature of trimethoxybenzene did not direct the functional groups to be added in the correct positions. Therefore, a starting material with just two, symmetrical methoxy groups was chosen. The synthesis route followed addition of a nitro group, conversion of an aldehyde to a nitrovinyl and then iron reduction to close the ring, before following the initial probe synthesis route as close as possible to produce the positive control (***Scheme 3.14***). In comparison to the target compound (*Figure 3.10*), a methyl and methoxy group were missing but this probe was taken forward as the closest version to the desired positive control.



Scheme 3.14: **Synthesis of (*E*)-2-(2-(4,7-dimethoxy-1-methyl-1*H*-indol-3-yl)vinyl)-1-ethyl-3,3-dimethyl-3*H*-indol-1-ium.** Optimised synthetic route for the locked form of the probe.

3.2.9 UV/Vis and Fluorescence studies

The photophysical properties of the locked probe were characterised to assess its fluorescence. The UV/Vis spectrum of the locked probe (***Figure 3.12***) showed peaks at a similar wavelength and intensity ratio as the chemically reduced **HCIQ** probe (*Figure 3.6*), confirming their similarity.

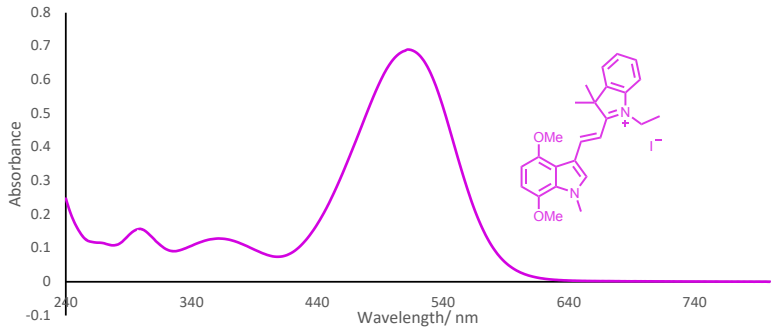


Figure 3.12: **Absorption spectrum of locked probe.** Sample measured in distilled water between 250 nm and 750 nm.

The locked probe showed emission of fluorescence at 80000000 arbitrary units (***Figure 3.13***), which was 1385× more than the chemically reduced **HCIQ** probe (*Figure 3.9*). Overall, this proved that the locked form of the probe was fluorescent. In this experiment no other chemical species were added to the sample, supporting the theory that another species present in the chemically reduced **HCIQ** sample was affecting fluorescence emission, whether it was $Na_2S_2O_4$ or oxidised **HCIQ**. Overall, it was thought that this level of fluorescent emission would be sufficient to be visualised in cells, so the positive control and **HCIQ** were taken forward.

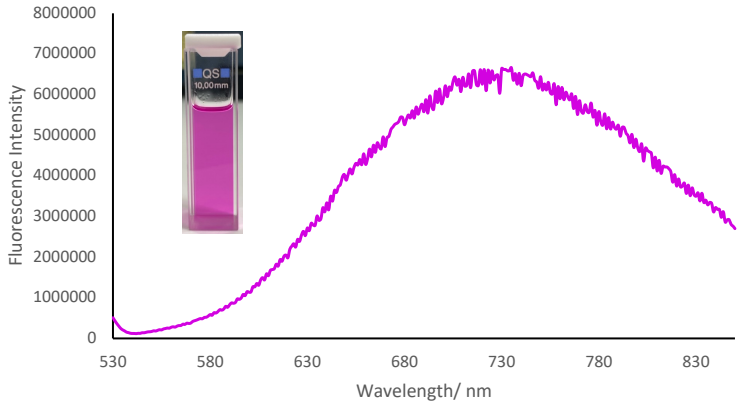


Figure 3.13: **Emission spectrum of locked probe.** Sample excited at 530 nm in distilled water.

3.2.10 Cellular testing of HCIQ and locked probe

An oesophageal cancer cell line (OE21) was selected for testing **HCIQ** as it forms good spheroids which is a useful 3D model of tumour hypoxia, and oesophageal cancer can be examined via endoscope which can detect fluorescent probes (El Harane et al., 2023; Paiji and Sedarat, 2022).

The positive control was used to determine if the probe could enter cells. The emission/excitation wavelength couple of the probe was unique but using laser settings for an mOrange fluorophore (Ex 546 nm, Em 563 nm) and extending the emission range

allowed for detection. The locked probe was visualised in cells at concentrations upwards of 10 μM in the cytoplasm of the majority of treated cells (***Figure 3.14***).

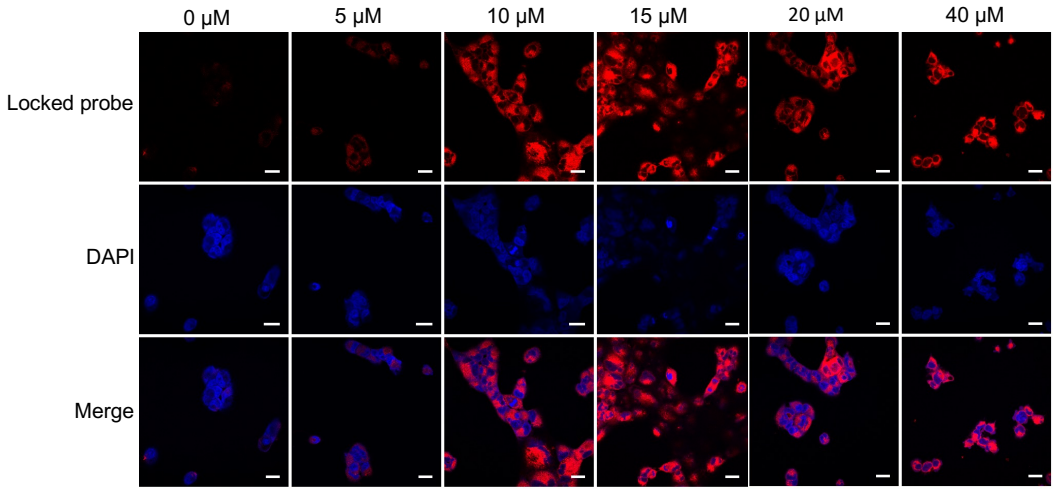


Figure 3.14: **OE21 cells treated with locked probe.** OE21 cells incubated with locked probe (5, 10, 15, 20, 40 μM) in normoxia (2 h). Scale bar = 20 μm.

The locked probe could be visualised using a wide range of wavelength settings, indicating it could be detected by standard red lasers, enhancing its applications. (***Figure 3.15***).

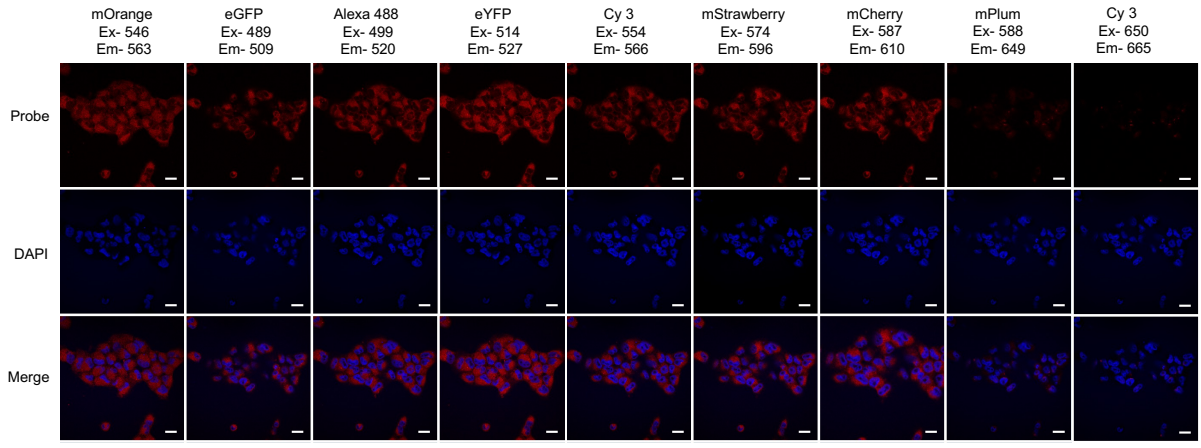


Figure 3.15: **Ex/Em wavelength range of locked probe.** OE21 cells incubated with locked probe in normoxia for 2 h and imaged with various lasers. Scale bar = 20 μm.

The fluorescence of **HCIQ** in cells, under hypoxic conditions, was assessed using a ClarioStar plate reader with an atmospheric control unit (ACU). To verify hypoxic conditions could be achieved in the ClarioStar, a previously validated probe from the Conway group containing the same hypoxia sensing group as **HCIQ**, but with a resorufin fluorophore that is released in hypoxia was tested (***Figure 3.16B***) (Wallabregue et al., 2023). An increase in fluorescence was seen when A549 cells were treated with the resorufin probe in the ACU set to hypoxic conditions (***Figure 3.16***). The phenol control was used to show the fluorescence intensity that the resorufin probe would give if 100 % of it was reduced in hypoxia (***Figure 3.16A, C***).

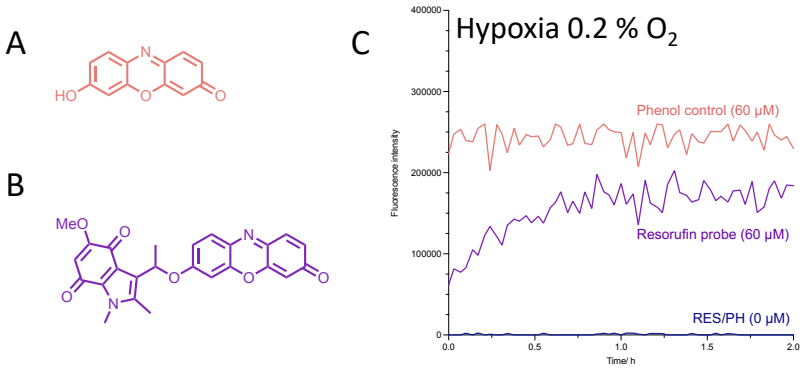


Figure 3.16: **The atmospherically controlled plate reader can be maintained at 0.2 % O_2.** A. Structure of phenol control B. Structure of resorufin probe C. A549 cells exposed to 0.2 % O_2, 5 % CO_2 and incubated with resorufin probe (60 µM) and phenol control (60 µM). Fluorescence intensity measured using a ClarioStar plate reader with an atmospheric control unit over a period of 2 h.

To determine if the locked probe could be visualised in the ClarioStar, A549 cells were incubated with a range of concentrations of the locked probe in both normoxia and hypoxia. The locked probe could be seen in the plate reader and in a concentration dependent manner (***Figure 3.17***). It was shown that concentrations as low as 1 µM of the locked probe could be visualised.

The reversible probe was tested in both normoxia and hypoxia but there was no obvious change in fluorescence intensity between the two conditions (***Figure 3.17C, D***). The reversible probe was tested at a maximum concentration of 6 mM, which is 6000× more concentrated than needed to visualise the locked probe under the same conditions.

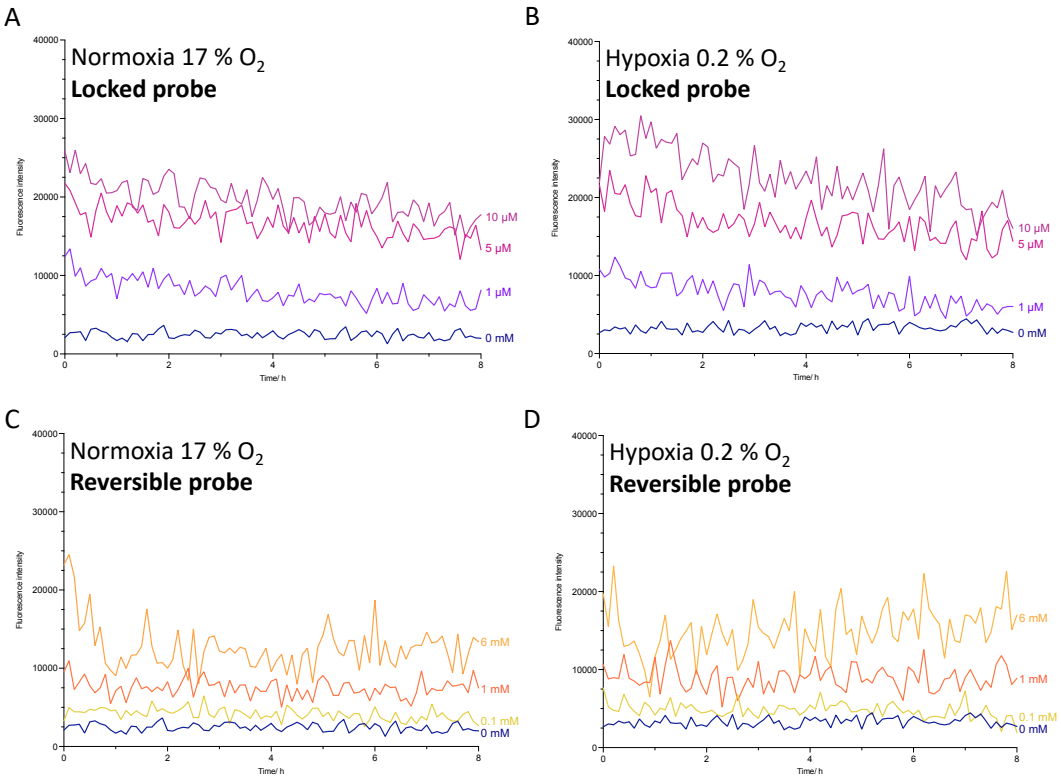


Figure 3.17: **Fluorescence intensity of HCIQ and locked probe in A549 cells over time in both normoxia and hypoxia.** A. A549 cells exposed to 17 % O_2, 5 % CO_2 and incubated with locked probe at varying concentrations B. A549 cells exposed to 0.2 % O_2, 5 % CO_2 and incubated with locked probe at varying concentrations C. A549 cells exposed to 17 % O_2, 5 % CO_2 and incubated with reversible probe at varying concentrations D. A549 cells exposed to 0.2 % O_2, 5 % CO_2 and incubated with reversible probe at varying concentrations.

3.3 Discussion

Overall, the initial target probe (**HCIQ**) was synthesised, and chemical reduction suggested the form of the probe we would expect to see in hypoxia. The probe was also

shown to be reversible. Overall, this was indicative that a redox process was happening as expected. However, signs of instability were seen within the chemical assays, a factor that should be addressed in future derivatives of the probe.

A vivid colour change was seen between the two forms of the probe. We considered if this could be exploited as this strategy has been shown to be effective previously (Laurieri et al., 2013) however, we decided that the colour change from orange to purple was not significant enough to be useful. The system was found to not display fluorescence emission when tested with chemical reductants. It was hypothesised that this could be due to a variety of factors such as the inability to exclude all oxygen from the equipment or the harsh chemical conditions needed. In the future, alternative chemical reductants could be trialled, in addition to $Na_2S_2O_4$. The hypothesis that PET quenching was taking place in the probe system, blocking a fluorescent output, would also be an avenue of interest to explore further. This would involve altering parts of the probe and investigating the change in redox chemistry via electrochemistry. We described a naphthalene variation of the probe in which the fluorophore was altered however, this did not alter the photophysical properties. Further alterations could be made such as using a commercially available fluorophore or adding groups to the quinone such as CF_3 in order to alter its chemical properties.

A locked form of the probe was synthesised in order to assess if the desired final product showed fluorescence emission, as well as to aid cell testing. This positive control did show emission of fluorescence. The locked form of the probe was tested in cells and shown to be both cell permeable and detectable using standard microscopy. An atmospherically controlled plate reader was then used to test the reversible probe, which did not show a turn on response of increased fluorescence in hypoxia. To conclude, it was

determined that the reversible probe was either not responding to hypoxia and converting to the desired reduced form or that it was not fluorescent enough to be seen as so little of the probe was actually being converted to the fluorescent form or that it was unstable when reduced. Overall, future work would include investigating the stability of the current probe and producing derivatives with altered photophysical properties in order to prevent potential PET quenching and produce the desired fluorescent output.

Chapter 4: Hypoxia-mediated changes in redox

4.1 Introduction

Here, we sought to determine what happens to critical components of the redox system in a range of hypoxic conditions. Experimentally, the challenge of redox analysis in hypoxia stems from the need to ensure hypoxic conditions are maintained throughout the assay, as reoxygenation results in significant changes (Hammond et al., 2003). In order to measure both ROS and antioxidant levels, all samples were processed or fixed in hypoxic conditions to avoid any impact of reoxygenation. For comparison, normoxic assays were carried out in standard tissue culture conditions (21 % O_2). Our aim was to determine how both arms of redox, ROS and antioxidants, are altered in hypoxia and ultimately, how this could potentially impact the efficacy of redox-dependent anti-cancer agents.

4.2 Results

4.2.1 Hypoxia and redox-dependent therapy

Our hypothesis is that redox changes in hypoxia likely underpin sensitivity to therapeutic agents and in particular those known to have a ROS-dependent mechanism of action. The most obvious example of this is the impact of hypoxia on radiosensitivity (Bristow and Hill, 2008). To demonstrate this, A549 cells were exposed to a range of hypoxic conditions (2 and <0.1 % O_2) and normoxia (21 % O_2), followed by irradiation (0, 2, 4 Gy). To avoid reoxygenation during irradiation, the 6-well plates were transferred to air-tight Perspex boxes prior to being removed from the hypoxia chamber (Anbalagan et al., 2012). After this, all plates were transported to the Cs irradiator, specified plates were irradiated and then after 30 mins the plates were removed from the Perspex boxes and colonies were allowed to form in standard tissue culture conditions. As expected, the cells exposed to

radiation in hypoxic conditions were significantly less sensitive and the cells exposed to the lowest concentration of O_2 (<0.1 %) were the most resistant to radiation (***Figure 4.1***). The impact of hypoxia on radiation response is well-known. However, oxygen level and redox in general is often not considered when testing more novel therapies. Therefore, we characterised redox in a range of hypoxic conditions.

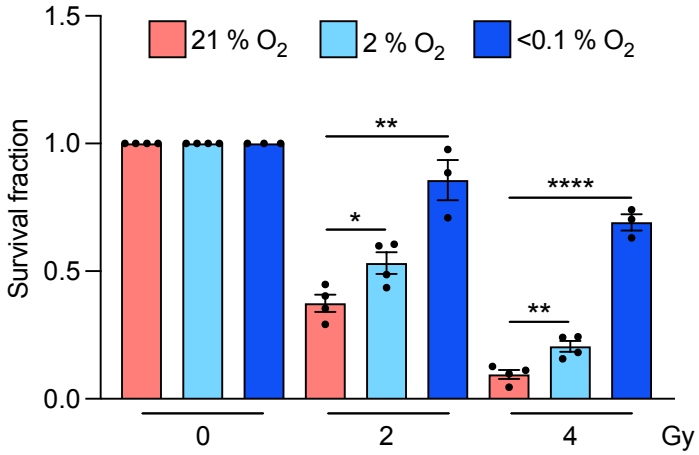


Figure 4.1: **Radiosensitivity significantly decreases with decreasing O_2 concentration.** A549 cells were exposed to 21, 2 and <0.1 % O_2 (5 h) and then exposed to radiation (0, 2, 4 Gy) without reoxygenation, followed by a colony survival assay. Data shown is n=3/4. Black dots on the graph represent biological repeats (each of which was carried out in triplicate). Data presented as mean + SEM, with 0 Gy readings for each % O_2 normalised to give a survival fraction of 1.0. Statistical testing was done using an unpaired t-test, where *p<0.05, **p<0.01, ****p<0.0-01.

4.2.2 ROS levels in hypoxia

First, the oxidative component of redox, primarily ROS was focused on. ROS levels in hypoxia have been investigated by others in the past and we sought to confirm the current consensus in our hands, that ROS increase in hypoxic conditions. Commercially available probes were utilised to assess both the total ROS levels and mitochondrial ROS levels present in A549 cells experiencing a range of oxygen tensions (21, 2 and <0.1 % O_2). It was important to consider mitochondrial ROS levels, as this is a critical organelle involved in the redox homeostasis of cells. CellROX green was used to analyse total ROS

levels, as it is sensitive to hydrogen peroxide, superoxide, hydroxyl radicals and peroxynitrite (H_2O_2, $O_2^{\bullet-}$, $^{\bullet}OH$ and $ONOO^-$). Upon oxidation by these ROS species, CellROX produces photostable fluorescence and subsequent binding to DNA. MitoSOX red was used to quantify mitochondrial ROS species, this probe produces a fluorescent signal upon interaction with specifically superoxide ($O_2^{\bullet-}$). The structure of the reactive entity for both CellROX and MitoSOX is the same however, MitoSOX has a triphenyl phosphonium salt attached meaning it is transported into the mitochondria due to the membrane potential of this organelle. Both total and mitochondrial ROS levels increased in all hypoxic conditions tested in comparison to normoxia, as can be seen by an increase in the fluorescent signal produced by both probes (***Figure 4.2 and 4.3***, with assistance from Dr Lina Hacker).

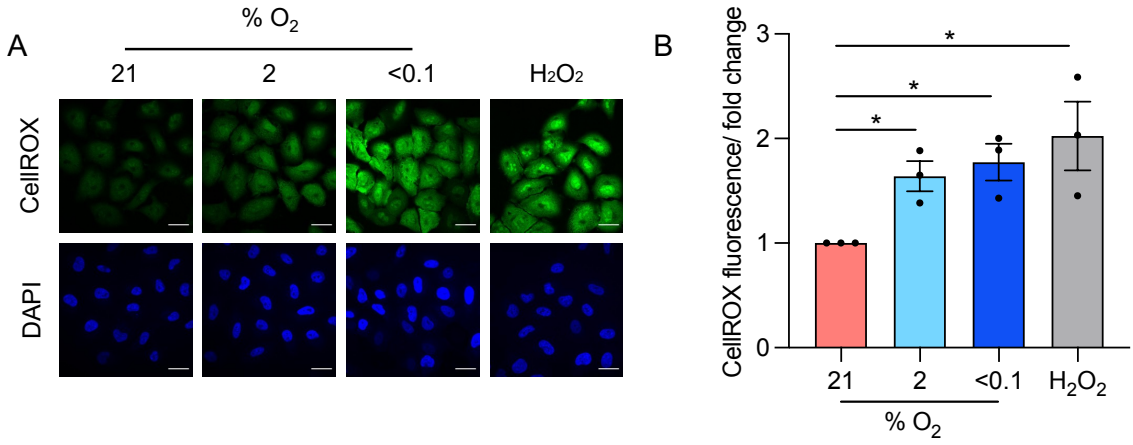


Figure 4.2: **Total ROS levels increase significantly in hypoxia.** A. A549 cells were exposed to 21, 2 and <0.1 % O_2 (6 h) followed by staining for total ROS (CellROX). H_2O_2 (25 µM, 3 h) was used as a positive control to induce ROS. Representative images are shown. Scale bar=12 µm. B. Quantification of part A. Data shown is n=3. Black dots on the graphs shown represent biological repeats. Data presented as mean + SEM, with normoxic values normalised to give a fold change of 1. Statistical testing was done using an unpaired t test, where *p<0.05.

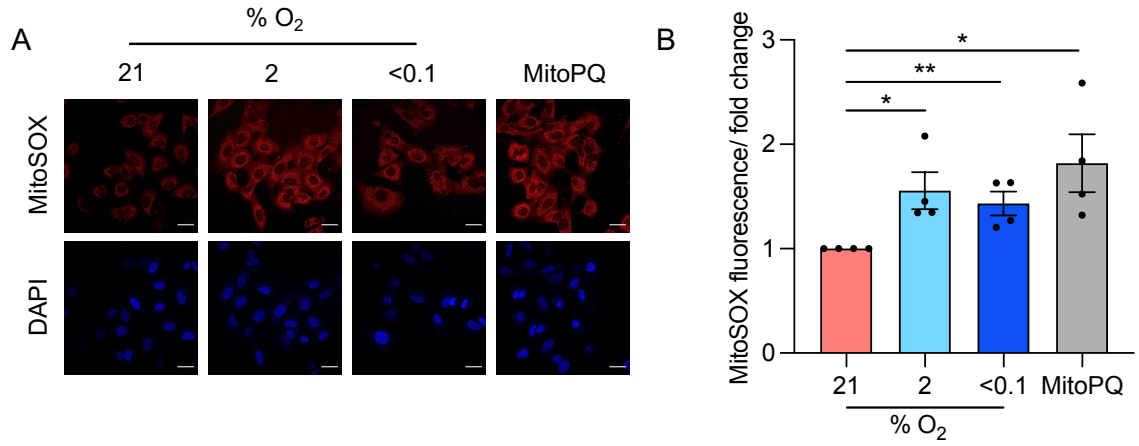


Figure 4.3: **Mitochondrial ROS levels increase significantly in hypoxia.** A. A549 cells were exposed to 21, 2 and <0.1 % O_2 (6 h) followed by staining for mitochondrial ROS (MitoSOX). MitoPQ (10 µM, 6 h) was used as a positive control. Representative images are shown. Scale bar=12 µm. B. Quantification of part A. Data shown is n=3/4. Black dots on the graphs shown represent biological repeats. Data presented as mean + SEM, with normoxic values normalised to give a fold change of 1. Statistical testing was done using an unpaired t test, where *p<0.05, **p<0.01.

4.2.3 Antioxidant levels in hypoxia

Next, the main cellular antioxidants, GSH and Trx, were investigated in hypoxia. To assess GSH levels under hypoxia a commercially available kit that reads cellular GSH levels as a measure of luminescence was utilised (***Figure 4.4***). The assay was carried out in a range of hypoxic conditions, with normoxia (21 % O_2) as a comparison. All samples were lysed in the condition being investigated. The GSH concentration of the samples were determined against a GSH standard curve.

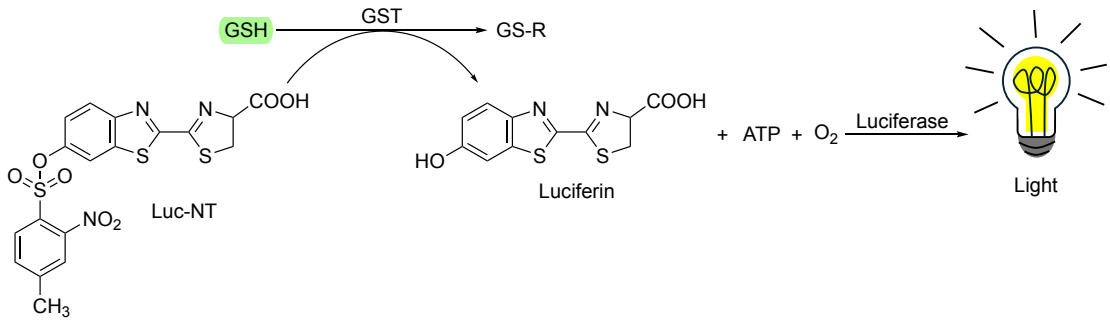


***Figure 4.4:* GSH assay outline.** A commercially available GSH assay based on the conversion of a luciferin derivative into luciferin in the presence of GSH, catalysed by GST. The signal generated is proportional to the amount of GSH present.

GSH levels increased significantly at both 2 and <0.1 % O_2 in comparison to 21 % O_2 (***Figure 4.5***). This was in agreement with previous reports (Duranteau et al., 1998; Kennedy et al., 2020; Rouschop et al., 2013; Khramtsov and Gillies). N-Ethylmaleimide (NEM) was included as a negative control to confirm the cellular GSH level measurements, as NEM contains an alkene functional group which reacts with thiols present on the cysteines within GSH.

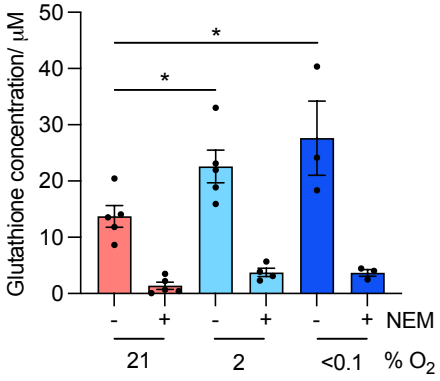


***Figure 4.5:* GSH levels increase significantly in hypoxic conditions.** A549 cells were exposed to 21, 2 and <0.1 % O_2 (6 h) and GSH levels were determined (GSH-GLO assay). In each case NEM (200 µm, 6 h) was included to verify that the luminescence recorded was due to GSH and values were compared to a GSH standard curve. Data shown is n=3/4. Black dots on the graph shown represent biological repeats (each of which was carried out in triplicate). Data presented as mean + SEM. Statistical testing was done using an unpaired t test, where *p<0.05.

The cell contains both reduced GSH which is ready to reduce free radical species, and oxidised GSSG which has fulfilled its role of reducing free radical species and is waiting to be regenerated to reduced GSH. These two pools of reduced and oxidised GSH comprise the total levels in the cell. To measure the total GSH content of the cell (reduced GSH and oxidised GSSG) cells were treated with Tris(2-carboxyethyl)phosphine (TCEP), which reduces the oxidised form. Total GSH levels increased significantly in hypoxic conditions (2 and <0.1 % O_2), showing the same trend as reduced GSH in hypoxia (***Figure 4.6***). Going forward, we concluded measuring reduced GSH levels was sufficient to show the changes in GSH levels.

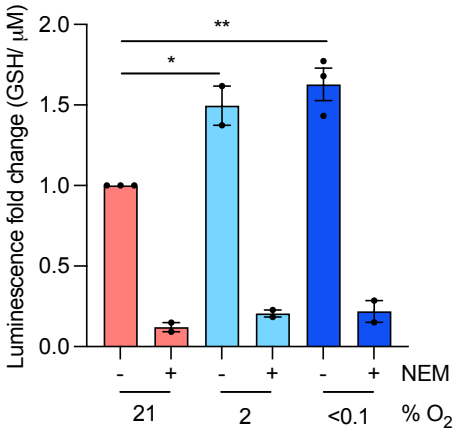


Figure 4.6: **Total GSH levels increase significantly in hypoxic conditions.** RKO cells were treated with TCEP (500 µM-1 mM) and exposed to 21, 2 and <0.1 % O_2 (6 h). The GSH levels were then determined (GSH-GLO assay). In each case NEM (200 µm, 6 h) was included to verify that the luminescence recorded was due to GSH and values were compared to a GSH standard curve. Data shown is n=2/3. Black dots on the graph shown represent biological repeats (each of which was carried out in triplicate). Data presented as mean + SEM, with normoxic values normalised to give a fold change of 1.0. Statistical testing was done using an unpaired t test, where *p<0.05, **p<0.01.

To investigate GSH levels further, in collaboration (Dr Adam Segdwick, KCL) we synthesised a thiol responsive fluorescent probe (FL-1), that utilised the thiol reactive 2,4-DNB protecting group to mask the fluorophore 3-O-methylfluorescein and quench

the fluorescence emission (Malla et al., 2020). Thus, upon reaction with GSH, the 2,4-DNB unit is removed, and the highly fluorescent fluorescein moiety is released allowing the measurement of changes in GSH concentrations (***Figure 4.7A***). GSH-mediated changes were confirmed in solution via UV/Vis and fluorescence spectroscopy, along with thiol selectivity against cysteine and lysine (***Figure 4.7B-D***).

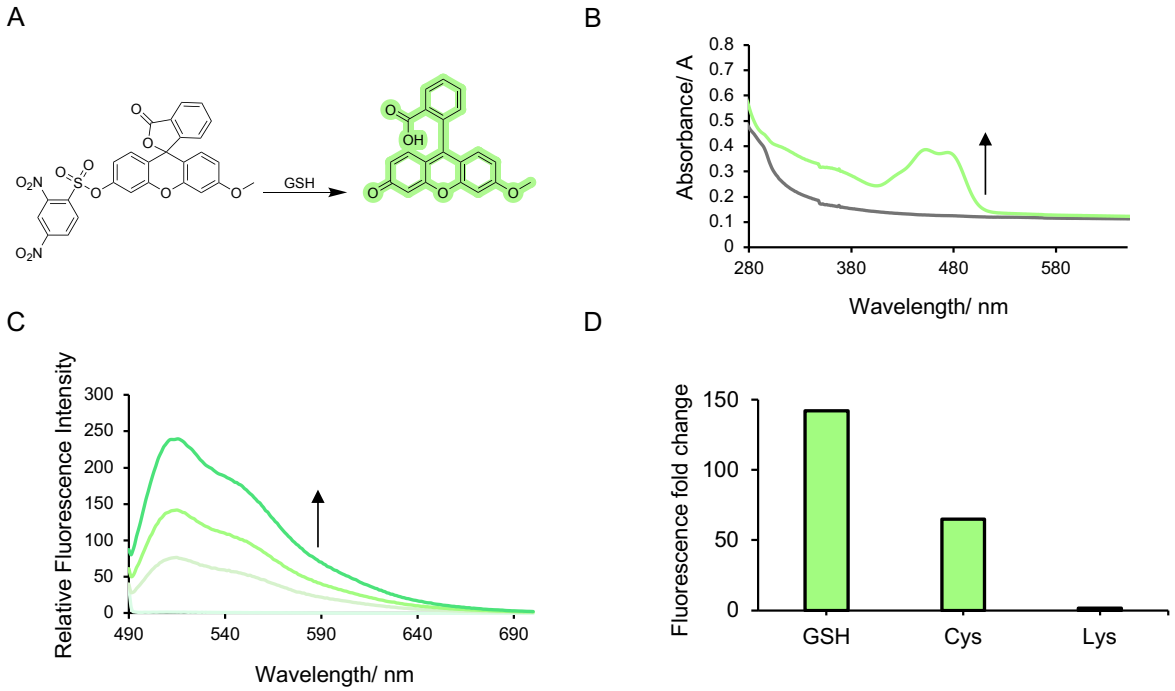


Figure 4.7: **In solution validation of novel GSH probe (FL-1).** A. The proposed reaction of FL-1 with GSH to afford highly fluorescent 3-O-Methylfluorescein B. UV-Vis spectra of FL-1 (25 μM) with and without the addition of GSH (1 mM) in PBS buffer (pH = 7.40, 1 % DMSO) C. Fluorescence spectra of FL-1 (5 μM) with increasing additions of GSH (250 μM, 500 μM, 2 mM- 30 min incubation) in PBS buffer (pH = 7.40, 1 % DMSO). λ_{ex} = 480 nm, Slit widths: 10 nm and 2.5 nm D. Fluorescence fold change of FL-1 (5 μM) with GSH (2 mM- 30 min incubation), Cys (2 mM- 30 min incubation), and Lys (2 mM- 30 min incubation) in PBS buffer (pH = 7.40, 1 % DMSO). λ_{ex} = 480 nm, Slit widths: 10 nm and 2.5 nm. Data provided by Dr Adam Sedgwick.

Cell permeability and visualisation of FL-1 was determined by incubating the probe with A549 cells and recording the fluorescence on a plate reader (***Figure 4.8***). Controls NAC and NEM were used to increase or decrease GSH levels, respectively. This validated the

use of the FL-1 probe in cells. However, both NAC and NEM controls have caveats. NAC increases GSH levels by acting as a precursor for cysteine, the rate limiting amino acid in GSH synthesis. However, NAC is a thiol-containing compound and can react directly with other thiol containing molecules such as GSH or the FL-1 probe, participating in disulphide exchange reactions and mixed disulphide formation. NEM, as mentioned prior, sequesters the signal from GSH by forming a thioether bond with the reduced version, preventing it from forming GSSG. However, NEM can sequester other thiols, not specifically GSH.

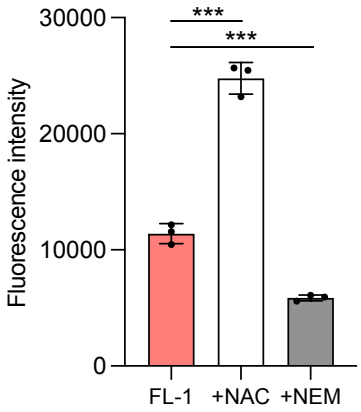


Figure 4.8: **Cellular validation of novel GSH probe (FL-1).** A549 cells were treated with FL-1 (10 mM, 1 h), followed by fluorescence measurement in a POLARstar plate reader. NEM (200 μM, 20 min) and NAC (2 mM, 5 h) were used as controls to ensure the signal measured was due to the presence of GSH. Data shown is n= 3. Black dots on the graph shown represent biological repeats (each of which was carried out in triplicate). Data presented as mean + SEM. Statistical testing was done using an unpaired t-test, where ***p<0.001.

Next, FL-1 was tested in a range of oxygen tensions (21, 2 and <0.1 % O_2), with NEM as a control to ensure GSH was being measured (***Figure 4.9***). GSH was shown to increase significantly in hypoxia, in agreement with the commercially available kit.

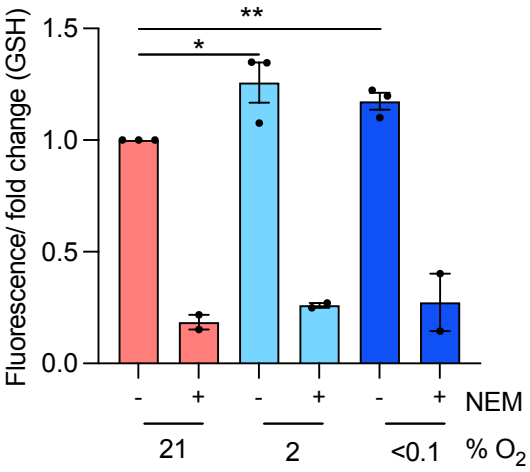


***Figure 4.9:* GSH levels increase significantly in hypoxia.** A549 cells were exposed to 21, 2 and <0.1 % O_2 (6 h), followed by 1 h treatment with FL-1 and determination of GSH levels. In each case NEM (200 µm, 6 h) was included to verify that the fluorescence recorded was due to GSH. Data shown is n= 3. Black dots on the graph shown represent biological repeats (each of which was carried out in triplicate). Data presented as mean + SEM, with normoxic values normalised to give a fold change of 1.0. Statistical testing was done using an unpaired t-test, where *p<0.05, **p<0.01.

To measure the fluorescence produced by FL-1, the plate was removed from its specified oxygen tension, allowing for a potential increase in fluorescence when the plate is moved from hypoxia to normoxia. However, GSH species are thought to change at a slower rate than free radical species and the proximity of the chamber to the plate reader was less than a 30 sec walk, so it was predicted the plate would be read before alterations in redox status could occur. To ensure that reoxygenation was not changing the GSH status, the experiment was repeated in duplicate with one set of plates fixed with PFA inside the chamber. The same trend in fluorescence was seen for both fixed and non-fixed plates, so it was concluded fixing was not necessary (***Figure 4.10***). The signal was significantly reduced for the fixed plates, suggesting the probe was being washed out of the cell, a common effect of washing steps for probes not conjugated to macromolecules in the cell.

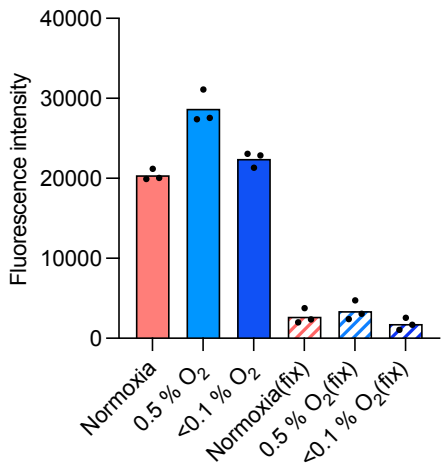


Figure 4.10: **Comparison of fixed and non-fixed cells treated with FL-1.** A549 cells were exposed to 21, 0.5 and <0.1 % O_2 (6 h), followed by 1 h treatment with FL-1 and then either immediate reading of the plate or PFA fixing and washing before reading to determine the GSH levels. Data shown is n= 3. Black dots on the graph shown represent biological repeats (each of which was carried out in triplicate).

Trx levels were also assessed under hypoxia. A commercially available thioredoxin reductase (TrxR) activity kit was used to investigate Trx levels, as TrxR specifically catalyses the reduction of Trx. 5,5'-Dithiobis(2-nitrobenzoic) acid (DTNB) can be reduced by TrxR to 5-Thio-2-nitrobenzoic acid (TNB^{2-}) with the aid of NADPH, this process produces a strong yellow colour of which the optical density can be read on a plate reader. DTNB can be reduced by other enzymes such as GR and GPx therefore, two sets of measurements are needed, with and without a TrxR specific inhibitor and then the difference will give the specific TrxR activity (***Figure 4.11***). The TrxR assay was carried out in a range of oxygen tensions (21, 2 and <0.1 % O_2), with the hypoxic samples lysed inside the hypoxia chamber. There was no significant change in either of the hypoxic conditions tested in comparison to normoxia (***Figure 4.12***).

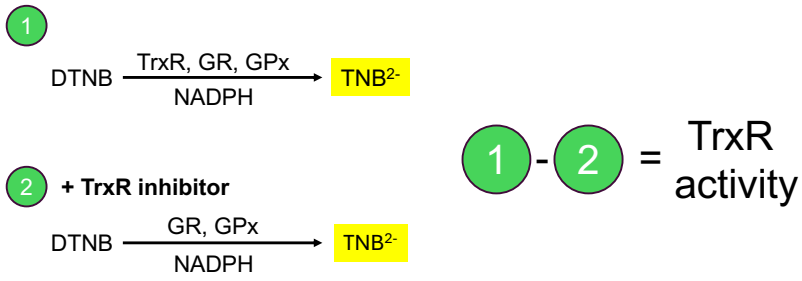


Figure 4.11: **TrxR assay outline.** Commercially available TrxR assay based on the reduction of DTNB to TNB^{2-}. The assay must be carried out with and without a TrxR inhibitor, with the difference giving the value of the TrxR activity. The result is measured via the optical density.

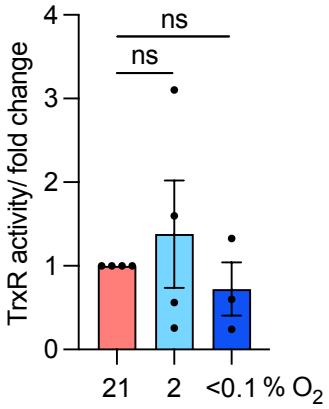


Figure 4.12: **TrxR activity does not significantly change in hypoxia.** A549 cells were exposed to 21, 2 and <0.1 % O_2 (6 h). The samples were then lysed and analysed for TrxR activity. Data shown is n= 3. Black dots on the graph shown represent biological repeats (each of which was carried out in triplicate). Data presented as mean + SEM, with normoxic values normalised to give a fold change of 1. Statistical testing was done using an unpaired t-test, where ns= non-significant.

4.2.4 Redox changes over time in hypoxia

Together, we showed that both ROS and GSH increase in hypoxia whereas Trx activity remains unchanged. Importantly, all assays were carried out without including reoxygenation and therefore reflect redox status in the hypoxic conditions described at the time of testing. However, the measurements do not reflect redox changes over time when exposed to hypoxia. The apparent simultaneous increase of both ROS and GSH at

the 6 h time point in hypoxic conditions prompted us to explore further the kinetics of these changes.

Mitochondrial ROS and GSH levels were determined over a 12 h period for A549 cells exposed to 2 % O_2. We focused on mitochondrial ROS instead of total ROS, as the mitochondria are the key site of redox activity within the cell. 2 % O_2 was chosen as the hypoxic environment to be studied, as it became the predominant oxygen condition in the last chapter. In future studies, more oxygen tensions and ROS probes would be used. As previously, both ROS and GSH were significantly increased after exposure to 2 % O_2 for 6 h, however these data also demonstrated that ROS levels had peaked by 30 mins of exposure to hypoxia (***Figure 4.13A, 4.14***). In contrast, GSH levels did not peak until 6 h exposure to hypoxia (***Figure 4.13B***) confirming differential kinetics of GSH and ROS with the antioxidant response lagging behind the initial burst in oxidative stress (***Figure 4.15***). The observed changes in redox likely underpin differential sensitivities to cancer therapeutics in hypoxia.

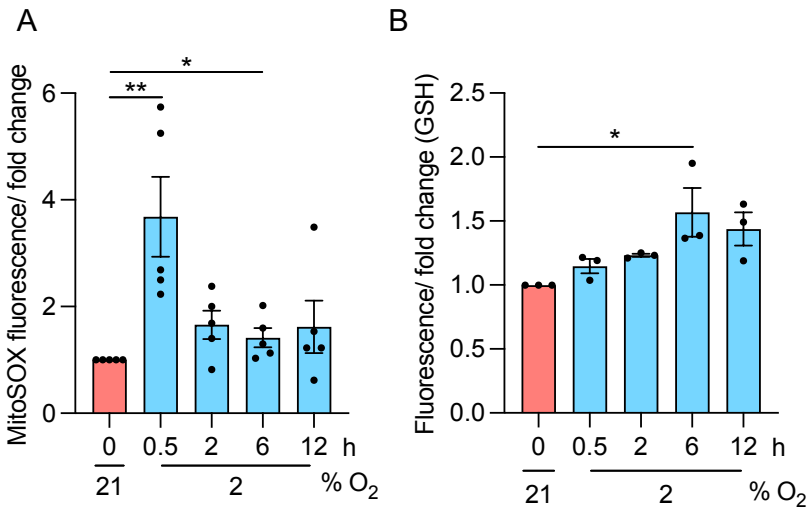


Figure 4.13: **Mitochondrial ROS and GSH changes over time in hypoxia (2 % O_2).** A. A549 cells were exposed to 2 % O_2 (0, 0.5, 2, 6, 12 h) followed by staining for mitochondrial ROS (MitoSOX). B. A549 cells were exposed to 2 % O_2 (0, 0.5, 2, 6, 12 h) followed by determination of GSH levels using FL-1. Data shown in A and B are n=3/5. Black dots on the graphs shown represent biological repeats (each of which was carried out in triplicate). Data presented as mean + SEM, with normoxic values normalised to give a fold change of 1.0. Statistical testing was done using an unpaired t test. *p<0.05, **p<0.01.

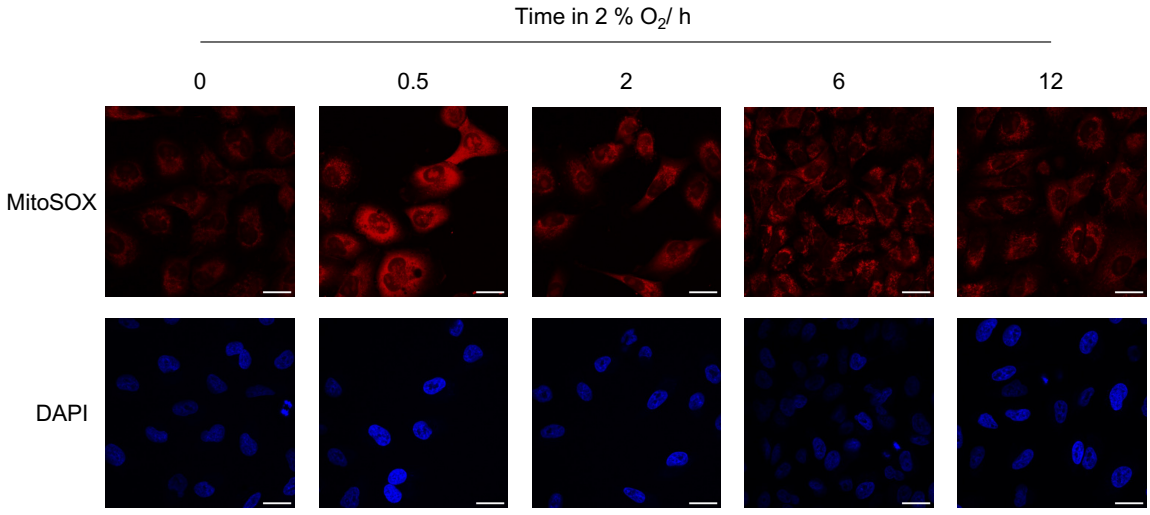


Figure 4.14: **Mitochondrial ROS increase in hypoxia.** Representative images of A549 cells exposed to 2 % O_2 (0, 0.5, 2, 6, 12 h) and stained for mitochondrial ROS (MitoSOX). Data shown are representative images of data in *Figure 4.13A*.

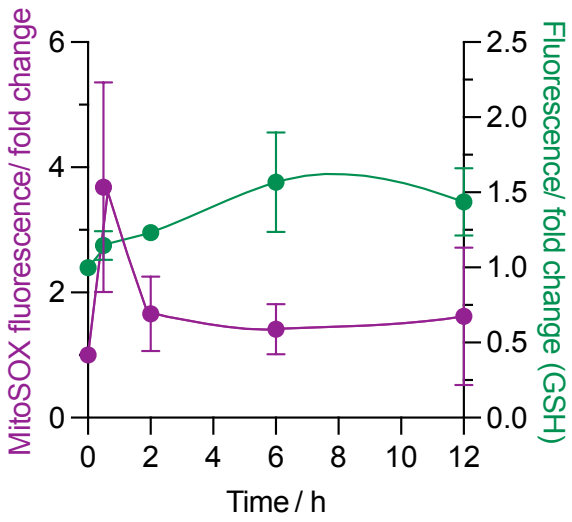


Figure 4.15: **Redox changes over time in hypoxia (2 % O_2).** Differential kinetics of hypoxia induced mitochondrial ROS levels (MitoSOX) and GSH levels (FL-1) in A549 cells exposed to 2 % O_2 (0, 0.5, 2, 6, 12 h). Data shown is the same data as shown in *Figure 4.13*. Data presented as mean + SEM.

4.2.5 Impact of HIF-1 signalling on redox

As there was a change in the redox system upon exposure to hypoxia, we next sought to investigate how HIF-1, the major transcription factor stabilised in hypoxia, affected both ROS and GSH levels under hypoxia. The genetically matched RKO and RKO$^{HIF\text{-}1\alpha\text{-}/\text{-}}$ colorectal cancer cell lines were employed to investigate the role of HIF-1 in redox. Both cell lines are identical except, the RKO$^{HIF\text{-}1\alpha\text{-}/\text{-}}$ line is produced by targeting exon 3 and 4 of HIF-1α for disruption, leading to deletion of 226 base pairs of HIF-1α, so even in hypoxic conditions HIF-1 cannot be stabilised (Dang et al., 2006). HIF-1α is comprised of 15 exons, interrupted by 14 introns, exons 3 and 4 are involved in encoding the PAS domain which are identified as stabilising HIF heterodimer formation via protein-protein interactions allowing for its transcriptional activity to take place (Iyer et al., 1998b; Rogers et al., 2013). In normoxia, neither cell line will have HIF-1α stabilised and in hypoxia, only the wildtype RKO cells with have HIF-1α stabilised. The ROS and antioxidant assays employed prior (CellROX, MitoSOX and GSH detection assays) were used to determine if

the redox response seen was HIF-1 dependent. Trx activity was not investigated here, as Trx activity did not significantly alter in hypoxia (*Figure 4.12*), suggesting that it would not be affected by the presence or absence of HIF-1. A timepoint of 6 h in hypoxia was chosen, in which both ROS and GSH had been seen to be significantly increased in comparison to normoxia.

To explore the impact of HIF-1α on ROS levels, RKO and RKO$^{HIF\text{-}1\alpha\text{-}/\text{-}}$ cells were exposed to 21 or 2 % O_2 and total cellular ROS levels were assessed (***Figure 4.16***). As expected, total cellular ROS levels increased in hypoxia, confirming the earlier finding (*Figure 4.2*). However, no significant difference was observed between the cell lines indicating that total ROS levels were not altered in a HIF-1 dependent manner.

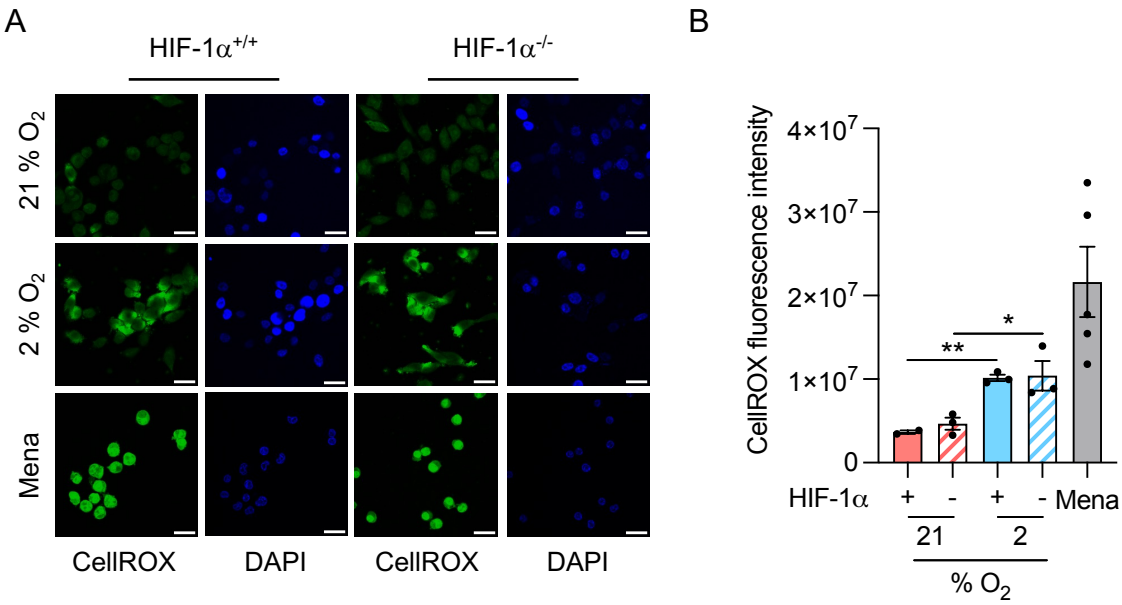


Figure 4.16: **Total ROS levels increase significantly in hypoxia in a HIF-independent manner.** A. RKO and RKO$^{HIF\text{-}1a\text{-}/\text{-}}$ cells were exposed to 21 and 2 % O_2 (6 h) followed by staining for total ROS (CellROX). Menadione (100 µM, 6 h) was used as a positive control to induce ROS. Scale bar = 20 µm. B. Quantification of part A. Data shown in A and B are n=3. Black dots on the graphs shown represent biological repeats. Data presented as mean + SEM. Statistical testing was done using an unpaired t-test, where *p<0.05, **p<0.01.

To explore the role of HIF-1 on mitochondrial ROS, RKO and RKO$^{HIF\text{-}1\alpha\text{-}/\text{-}}$ cells were exposed to 21 or 2 % O_2 and mitochondrial ROS levels were assessed (***Figure 4.17***). As expected, mitochondrial ROS levels increased significantly in hypoxia, confirming the earlier finding (*Figure 4.3*). In contrast to total cellular ROS levels, mitochondrial ROS levels increased in a HIF-1 dependent manner. The loss of HIF-1α lead to a further increase in mitochondrial ROS levels, indicating that HIF-1 plays a role in reducing mitochondrial ROS in hypoxia to maintain redox homeostasis.

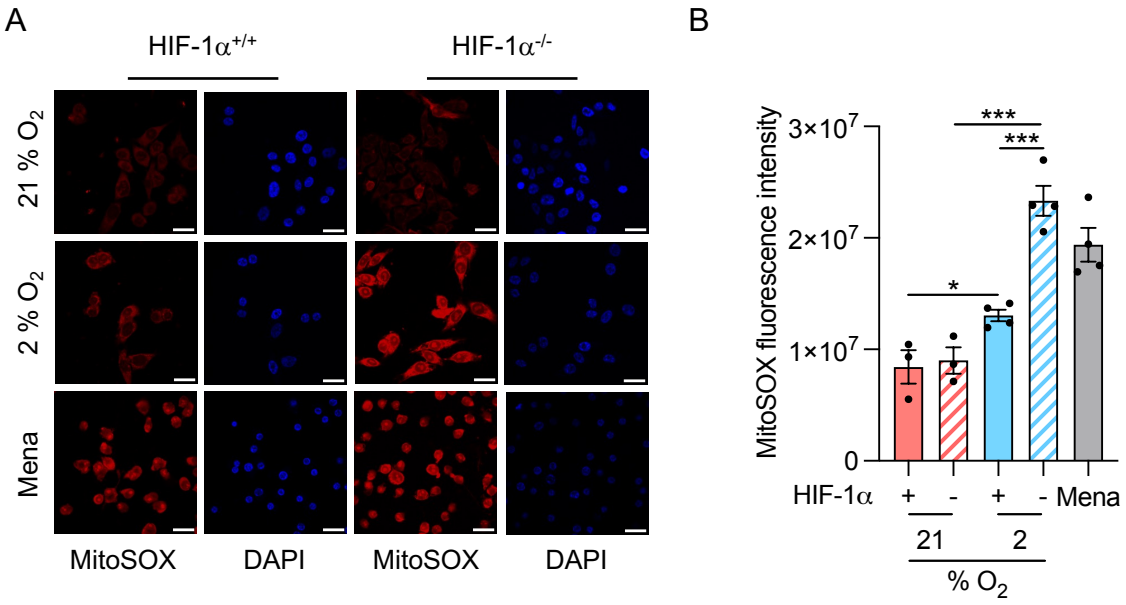


Figure 4.17: **Mitochondrial ROS levels increase significantly in hypoxia in a HIF-dependent manner.** A. RKO and RKO$^{HIF\text{-}1\alpha\text{-}/\text{-}}$ cells were exposed to 21 and 2 % O_2 (6 h) followed by staining for mitochondrial ROS (MitoSOX). Menadione (100 μM, 6 h) was used as a positive control to induce ROS. Scale bar = 20 μm. B. Quantification of part A. Data shown in A and B are n=3/4. Black dots on the graphs shown represent biological repeats. Data presented as mean + SEM. Statistical testing was done using an unpaired t-test, where *p<0.05, **p<0.01, ***p<0.001.

The difference in specificity between CellROX and MitoSOX can be seen by the localisation of the staining in the cell (***Figure 4.18***). MitoSOX accumulates in the mitochondria due to the lipophilic cation within its structure. Therefore, the fluorescence is seen to be localised to specific bright spots within the cytoplasm of the cell, indicative

of mitochondrial localisation. However, a limitation of MitoSOX is that it can traverse any membrane with a potential, so could enter other organelles such as the peroxisomes. In comparison, the fluorescent signal produced by CellROX can be seen to be pan-cytoplasmic, indicating that it is not confined to a specific place in the cell, but instead encompasses the overall ROS status of the cell.

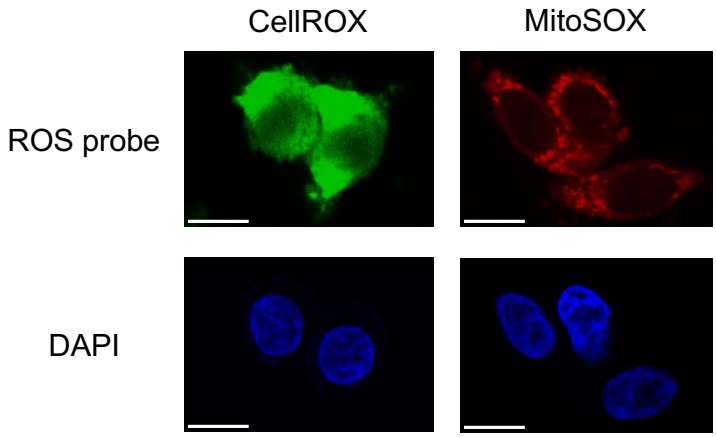


Figure 4.18: **Comparison of CellROX and MitoSOX localisation.** RKO$^{HIF\text{-}1\alpha\text{-}/\text{-}}$ cells were exposed to 21 and 2 % O_2 (6 h) followed by staining for total ROS (CellROX) and mitochondrial ROS (MitoSOX). Scale bar = 10 μm.

In order to test if HIF-1 played a significant role in the hypoxic increase of GSH, GSH levels were measured in the RKO and RKO$^{HIF\text{-}1\alpha\text{-}/\text{-}}$ cells in normoxic and hypoxic (2 and <0.1 % O_2) conditions. As previously in both assays, GSH levels increased significantly in hypoxia but, were not significantly altered by loss of HIF-1α (***Figure 4.19***). NEM was included in both experiments as a control to demonstrate that it was GSH being measured.

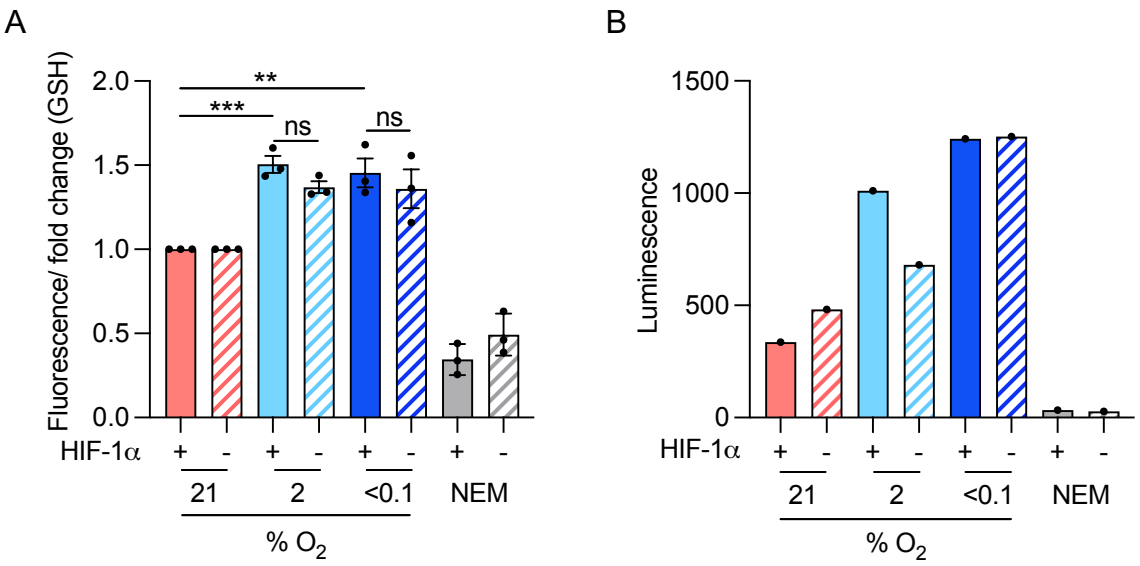


Figure 4.19: **GSH levels increase significantly in hypoxia in a HIF-independent manner.** A. RKO and RKO$^{Hif\text{-}1a\text{-}/\text{-}}$ cells were exposed to 21, 2 and <0.1 % O_2 (6 h) and GSH levels determined (FL-1). B. RKO and RKO$^{HIF\text{-}/\text{-}}$ cells were exposed to 21, 2 and <0.1 % O_2 (6 h) and GSH levels were determined (GSH GLO assay). In each case NEM (200 µM, 6 h) was included to verify that the fluorescence/luminescence recorded was due to GSH. Data shown in A is n=3 and data shown in B is n=1. Black dots on the graphs shown represent biological repeats (each of which was carried out in triplicate). Data presented as mean + SEM, with normoxic values normalised to give a fold change of 1.0 in part A. Statistical testing was done using an unpaired t-test, where **p<0.01, ***p<0.001 ns= non-significant.

4.3 Discussion

Here, we have measured both ROS and antioxidant levels to provide the first comprehensive report of kinetic changes in redox in response to hypoxia. A detailed characterisation of changes in ROS (total and mitochondrial) and the major antioxidant systems (GSH and Trx) is provided. Our study demonstrates that, in the absence of reoxygenation, hypoxia leads to an increase in ROS and GSH levels, whilst Trx levels are unchanged.

Importantly, we demonstrate that the kinetics of the increase in ROS and GSH differ. ROS levels peak quickly (within 30 minutes) and subsequently decrease over time but remain

significantly higher than normoxic ROS levels at 6 h of exposure (2 % O_2). GSH levels lag behind ROS levels, with a gradual increase over the time course and are also significantly increased at 6 h. In the future, it would be interesting to investigate earlier timepoints (before 30 minutes) to pinpoint when ROS levels peak upon exposure to hypoxia. A 12 h radius was studied in the kinetic assay due to experimental limitations e.g. ensuring MitoSOX was imaged whilst the fluorescence was still viable. However, it would be interesting to investigate what happens at timepoints in which long standing hypoxia has arisen, particularly in a 3D system as this is more representative of an *in vivo* system and therefore potentially more clinically relevant. Additionally, comparison of the redox environment in mild hypoxia (2 % O_2) and radiobiological hypoxia (<0.1 % O_2) over time would be interesting for future work.

Mitochondrial ROS levels began to decrease before GSH began to rise, indicating that processes other than the GSH system have a role in alleviating cellular stress. These kinetics could be explained by molecular mechanisms of hypoxia, driven primarily by HIF-1, such as SOD enzyme activity. The increase in mitochondrial ROS was found to be HIF-1α dependent. In contrast, total cellular ROS and GSH levels were not impacted by HIF-1α activity in our hands. Notably, a previous study found GSH synthesis to be induced by chemotherapy in a HIF-dependent manner in triple negative breast cancer (TNBC) (Lu et al., 2015). This indicates that there is likely a dependence on experimental conditions as to how GSH is affected by HIF-1.

This chapter utilised the lung adenocarcinoma cell line A549, with focus on varying the oxygen levels the cells experience whilst measuring various redox species over time. In the future a more comprehensive study would include multiple cancer cell lines, alongside normal tissue models. As described prior, redox in hypoxia is documented in

the literature, however, controversy arises as different systems have resulted in differing conclusions. This suggests that the outcome of an assay could be cell line/model dependent. Therefore, to confirm our conclusions a wider study would be needed, and the use of 3D models that could more accurately represent the *in vivo* redox environment. Overall, the changes seen to redox components in hypoxic conditions could determine the efficacy of redox-dependent therapies tested in physiological conditions. We hypothesis that therapeutics with a mode of action dependent on ROS or antioxidants would show a different response in hypoxic conditions, which we go on to investigate in *Chapter 5*.

Chapter 5: The activity of therapeutic molecular cluster Ag5 is dependent on oxygen level and HIF-1 mediated signalling

5.1 Introduction

Having provided a comprehensive assessment of the redox changes that occur in hypoxia (*Chapter 4*), we sought to investigate the efficacy of the redox-dependent agent Ag5 in hypoxic conditions. To recap, Ag5 is a novel therapeutic molecular cluster, composed of five atoms of silver covalently bonded together. Ag5 has been reported to inhibit the GSH and Trx antioxidant pathways, leading to the accumulation of ROS in the cell, and resulting in apoptosis (Porto et al., 2022). Although we reported on redox changes of increased ROS and GSH levels, the specific impact that this has on Ag5 action remained unclear. Increased ROS in hypoxia would predict increased efficacy of Ag5, however increased GSH levels in hypoxia would predict decreased efficacy of Ag5. Therefore, the redox species with the more biologically relevant increase in hypoxia would determine the response to Ag5 in hypoxic conditions. Overall, our aim was to determine how alterations of the redox environment in hypoxia affects the efficacy of Ag5.

5.2 Results

5.2.1 Ag5 leads to loss of viability in cancer but not normal cells

Ag5 has been reported previously to elicit a cell death response in cancer cells (Porto et al., 2022). Initially, we sought to confirm the toxicity of Ag5 in our hands. The response to Ag5 was determined using lung adenocarcinoma cell lines, A549 and H460. MTT assays were utilised to analyse cell viability in response to increasing concentrations of Ag5. There was a significant decrease in cell viability with increasing concentration of Ag5, in both the lung cancer cell lines tested (***Figure 5.1***). Non-transformed lung cell lines, MRC5 and HFL-1, were treated with Ag5 and also analysed via MTT. There was little to no effect

on viability of the normal cells upon increasing dose of Ag5 (***Figure 5.1***). This demonstrated that Ag5 is extremely selective for cancer cells and kills in a dose dependent manner but leaves normal cells unharmed, in the cancer and normal cell lines tested. In the clinic, minimising off target effects to improve patient outcome is an important consideration and the finding that Ag5 selectively targets cancer cells is an extremely beneficial characteristic of this agent.

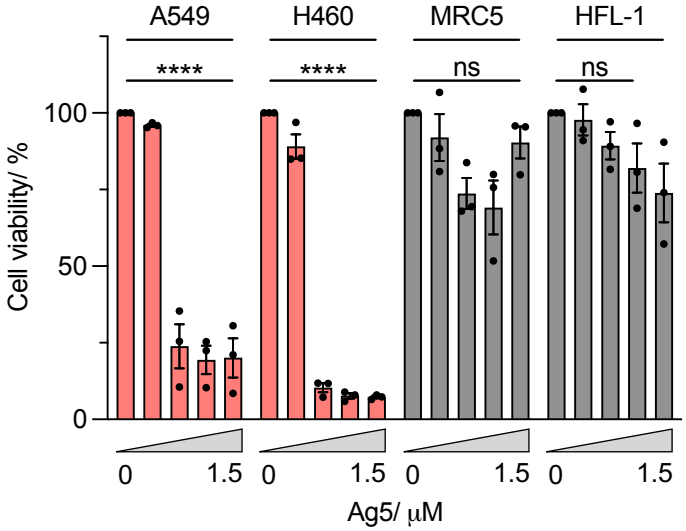


Figure 5.1: **Ag5 is toxic to cancer cells but not non-transformed cells.** Lung adenocarcinoma cell lines (A549 and H460) and non-transformed lung cell lines (MRC5 and HFL-1) were treated with Ag5 (0, 0.5, 1, 1.25, 1.5 μM) for 1 h and analysed via MTT assay 20 h later. Data shown is n=3. Black dots on the graph shown represent biological repeats (each of which was carried out in triplicate). Data presented as mean + SEM, with untreated readings for each cell line normalised to give 100 % cell viability. Statistical testing was done using a two-way ANOVA test, where ****p<0.0001, ns= non-significant.

IC50 values are often used to inform on a drug's efficacy, indicating how much of an agent is needed to produce a 50 % inhibition. A549 cells were treated with additional doses of Ag5 to calculate an associated IC50 of approximately 0.67 μM, via nonlinear regression (***Figure 5.2***). In comparison, an IC50 value could not be determined for the non-transformed MRC5 cells, at the same doses of Ag5.

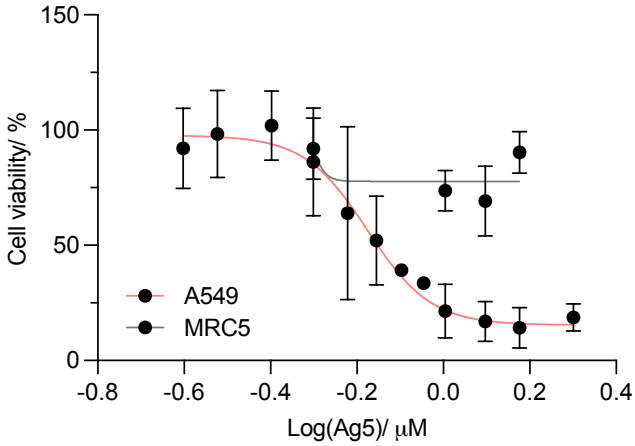


Figure 5.2: **IC50 curves for Ag5 in A549 and MRC5 cell lines.** A549 and MRC5 cells were treated with Ag5 (0, 0.25, 0.3, 0.4, 0.5, 0.6, 0.7, 0.8, 0.9, 1, 1.25, 1.5, 2 μM) for 1 h and analysed via MTT 20 h later. Data shown is n=3. Black dots on the graph shown represent biological repeats (each of which was carried out in triplicate). Data presented as mean + SEM, with untreated readings for each cell line normalised to give 100 % cell viability.

To confirm that the toxicity produced by Ag5 was not due to the presence of silver ions, we used a control compound (Ag+). In both A549 and H460 cell lines, Ag+ did not impact cell survival when used at the same concentrations used previously for Ag5 (***Figure 5.3***).

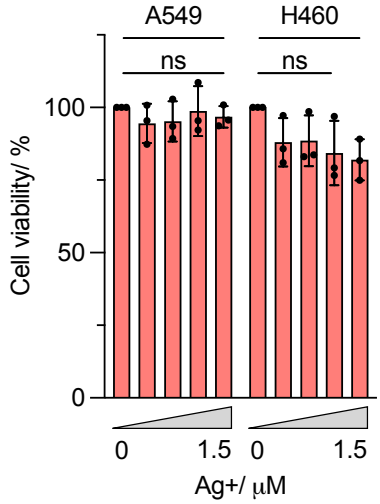


Figure 5.3: **Ag5 effect is independent of silver ion toxicity.** A549 and H460 cells were treated with the control compound, Ag+ (0, 0.5, 1, 1.25, 1.5 μM) for 1 h, followed by an MTT assay 20 h later. Data shown is n=3. Black dots on the graph shown represent biological repeats (each of which was carried out in triplicate). Data presented as mean + SEM, with untreated readings for each cell line normalised to give 100 % cell viability. Statistical testing was done using a two-way ANOVA test, where ns= non-significant.

The reported mechanism of Ag5 is via an accumulation of ROS, resulting in cell death due to excessive stress. Cancer cells are known to have elevated ROS levels in comparison to normal cells. A549 and MRC5 cells were assessed for their respective baseline ROS levels. As expected, the levels of ROS (mitochondrial) were found to be significantly higher in the A549 cells compared to the non-transformed MRC5 cells, supporting the Ag5 mechanism of action (***Figure 5.4***).

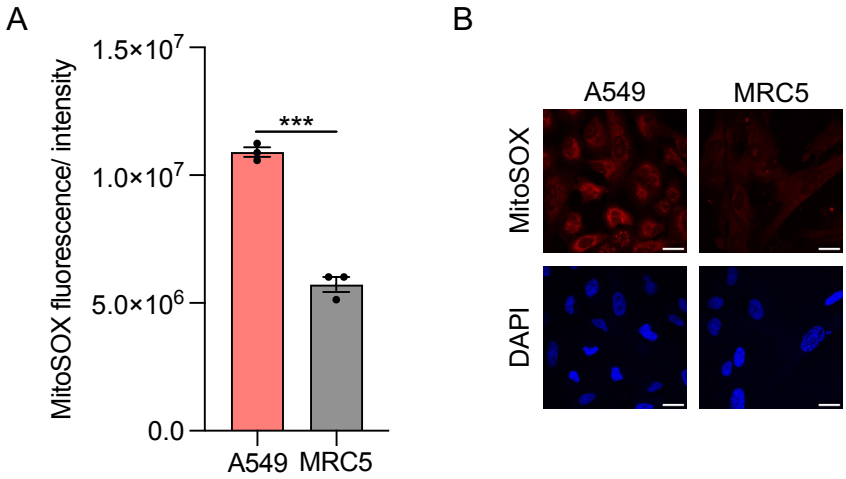


Figure 5.4: **ROS levels are higher in cancer cells than non-transformed cells.** A. A549 and MRC5 cells were stained for mitochondrial ROS (MitoSOX) B. Representative images from part A. Data shown are n=3. Black dots on the graph shown represent biological repeats. Data presented as mean + SEM. Statistical testing was done using an unpaired t-test, where ***p<0.001.

To demonstrate that Ag5 activity was not restricted to lung cancer cell lines, a panel of oesophageal cancer lines were tested. A dose-dependent loss of viability to Ag5 was observed for all the oesophageal cancer lines, as before with the lung cancer lines (***Figure 5.5***). Notably, the sensitivity to Ag5 appeared similar in all cell lines tested despite having a range of mutational profiles (***Table 8.2*** (appendix)). This indicated that Ag5 action is not dependent on the presence of specific mutations.

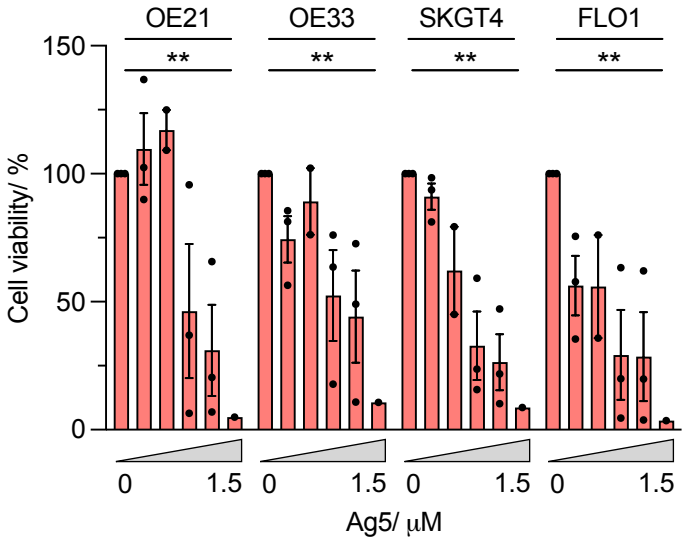


Figure 5.5: **Toxicity of Ag5 is not cancer cell line dependent.** A panel of oesophageal cancer cell lines (OE21, OE33, SKGT4, FLO1) were treated with Ag5 (0, 0.5, 1, 1.25, 1.5 μM) for 1 h and an MTT assay was carried out 20 h later. Data shown is n=3. Black dots on the graph shown represent biological repeats (each of which was carried out in triplicate). Data presented as mean + SEM, with untreated readings for each cell line normalised to give 100 % cell viability. Statistical testing was done using a two-way ANOVA test, where **p<0.01.

5.2.2 Ag5 mechanism of cell death

The mechanism of death for Ag5 had previously been reported to be apoptosis (Porto et al., 2022). A549 cells were treated with Ag5 and an apoptosis assay, combining annexin V and 7-amino-actinomycin D (7-AAD) staining, was carried out. Early apoptotic cells express phosphatidylserine residues on the extracellular side of the plasma membrane, which can be identified using annexin V staining. Late-stage apoptosis and necrosis can be determined with 7-AAD staining, which can enter cells through compromised cell membranes and subsequently bind to DNA, fixing it in the cell. As expected, Ag5 was shown to induce apoptosis in cancer cells (***Figure 5.6***).

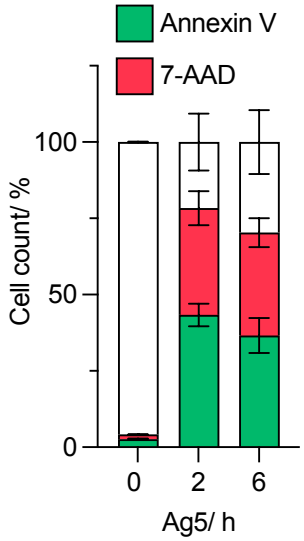


***Figure 5.6:* Ag5 induces cell death via apoptosis.** A549 cells were treated with Ag5 (1 μM) for 1 h followed by annexin-V and 7-AAD assay for apoptosis after 2 and 6 h. Data shown is n=3. Data presented as mean + SEM. Data provided by Dr Vanesa Porto.

We hypothesised that other cell death mechanisms could be involved in the mechanism of action of Ag5, specifically ferroptosis. Ferroptosis is a ROS-dependent form of cell death resulting from lipid peroxidation (Lu et al., 2018). Therefore, lipid peroxidation can be analysed as an indicator of ferroptosis. No significant increase in lipid peroxidation was found in response to Ag5 treatment in A549 cells, suggesting increased ferroptosis is not a relevant cell death mechanism here (***Figure 5.7***).

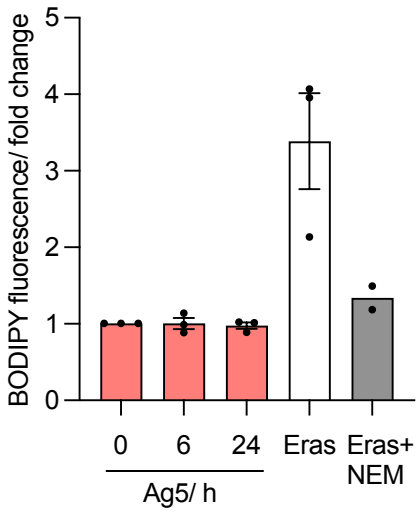


Figure 5.7: **Ag5 did not result in increased lipid peroxidation.** A549 cells were treated with Ag5 (1 μM) for 1 h, followed by a lipid peroxidation assay 6 and 24 h after drug treatment. Erastin (10 μM) was used as a positive control and NEM (200 μM) to verify that the fluorescence recorded was due to lipid peroxidation. Data shown is n=3 except for the Erastin +NEM condition which is n=2. Black dots on the graph shown represent biological repeats (each of which was carried out in triplicate). Data presented as mean + SEM.

5.2.3 Hypoxic cells are less sensitive to Ag5

Having demonstrated that redox homeostasis is changed by hypoxia, we hypothesised that the sensitivity to Ag5 would be impacted by hypoxia. A549 cells were exposed to a range of oxygen tensions (21, 2, 0.5, <0.1 % O_2) followed by treatment with Ag5 (***Figure 5.8A***). As expected, HIF-1α was stabilised in response to all the hypoxic conditions tested (2, 0.5, <0.1 % O_2), and this was not impacted by the addition of Ag5 (***Figure 5.8B***). A549 cells were significantly less sensitive to Ag5 in all of the hypoxic conditions tested, in comparison to normoxia (***Figure 5.8C***).

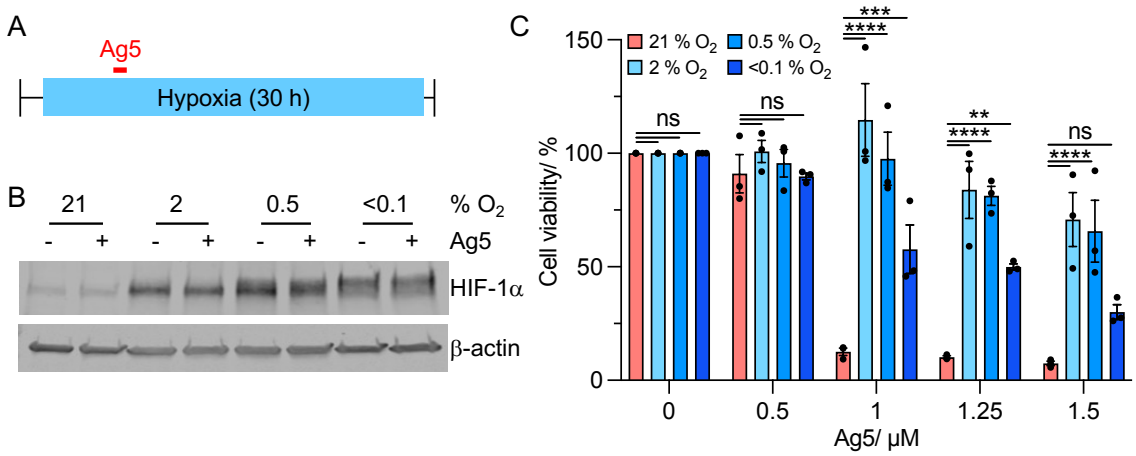


Figure 5.8: **Hypoxic cells are less sensitive to Ag5.** A. Schematic representation of cell viability assays with Ag5 with pre-exposure to hypoxic conditions. Cells were placed in hypoxia for 6 h and then treated with Ag5 for 1 h. B. A549 cells were exposed to 21, 2, 0.5 and <0.1 % O_2 (6 h) before treatment with or without Ag5 (1 μM) for 1 h. After 20 h samples were harvested for western blotting of HIF-1α and β-actin as a loading control. C. A549 cells were exposed to 21, 2, 0.5 and <0.1 % O_2 (6 h) and then treated with Ag5 (0, 0.5, 1, 1.25, 1.5 μM) for 1 h, followed by an MTT assay 20 h later. Data shown in C is n=3. Black dots on the graph shown represent biological repeats (each of which was carried out in triplicate). Data presented as mean + SEM, with untreated readings for each % O_2 normalised to give 100 % cell viability. Statistical testing was done using a two-way ANOVA test with each bar compared to the 21 % O_2 counterpart, where **p<0.01, ***p<0.001, ****p<0.0001, ns= non-significant.

Notably, no significant difference was seen between 2 and 0.5 % O_2 in response to Ag5 but, the cells treated at <0.1 % O_2 were more sensitive to Ag5 in comparison to the milder hypoxic conditions (2 and 0.5 % O_2). The biological response to hypoxia is oxygen dependent and it is likely that accumulation of replication stress and subsequent DNA damage response signalling specifically at <0.1 % O_2 may explain the increased sensitivity to Ag5, compared to milder levels of hypoxia (***Figure 5.9***) (Ma et al., 2023).

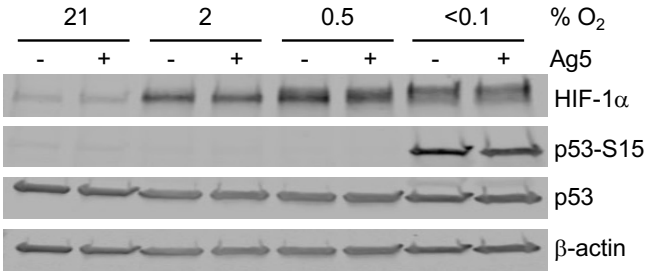


***Figure 5.9:* <0.1 % O_2 shows a different biological response to milder hypoxia (2, 0.5 % O_2).** A549 cells were exposed to the indicated oxygen concentrations for 6 h. Where indicated Ag5 (1 μM) was added for 1 h prior to harvesting. Western blotting was then carried out for HIF-1α, p53-S15, p53 and β-actin as a loading control. Data shown is n=2.

To determine whether the loss of sensitivity to Ag5 in hypoxia was a cell line dependent effect, H460 cells were exposed to a range of oxygen tensions (21, 2, 0.5, <0.1 % O_2) and treated with Ag5, as before with A549 cells. Importantly, the H460 cell line also displayed an oxygen-dependent sensitivity, with the same trend of cells in mild hypoxia (2 and 0.5 % O_2) showing the least sensitivity to Ag5 (***Figure 5.10***).

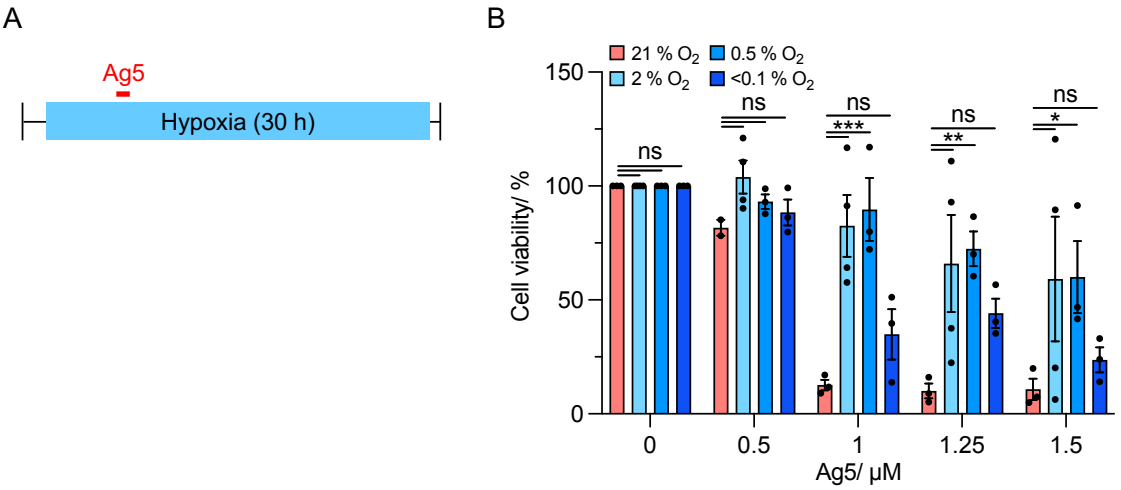


***Figure 5.10:* Reduced sensitivity to Ag5 in hypoxia is independent of cancer cell line.** A. Schematic representation of cell viability assays with Ag5 with pre-exposure to hypoxic conditions. Cells were placed in hypoxia for 6 h and then treated with Ag5 for 1 h. B. H460 cells were exposed to 21, 2, 0.5 and <0.1 % O_2 (6 h) and then treated with Ag5 (0, 0.5, 1, 1.25, 1.5 μM) for 1 h, followed by an MTT assay 20 h later. Data shown in B is n=3. Black dots on the graph shown represent biological repeats (each of which was carried out in triplicate). Data presented as mean + SEM, with untreated readings for each % O_2 normalised to give 100 % cell viability. Statistical testing was done using a two-way

ANOVA test with each bar compared to the 21 % O_2 counterpart. *p<0.05, **p<0.01, ***p<0.001, ns= non-significant.

Cell viability was evaluated in these conditions using an MTT assay. An MTT assay relies on the ability of the mitochondria to reduce mono-tetrazolium salts to water insoluble formazan crystals via dehydrogenases and oxidoreductases (***Figure 5.11***) (Ghasemi et al., 2021). The mitochondria are not only the powerhouse of the cell, but also a key source of redox and metabolic activity. Ag5 and hypoxia both effect redox and metabolism therefore, the reliability of the MTT assay could be impaired in this instance.

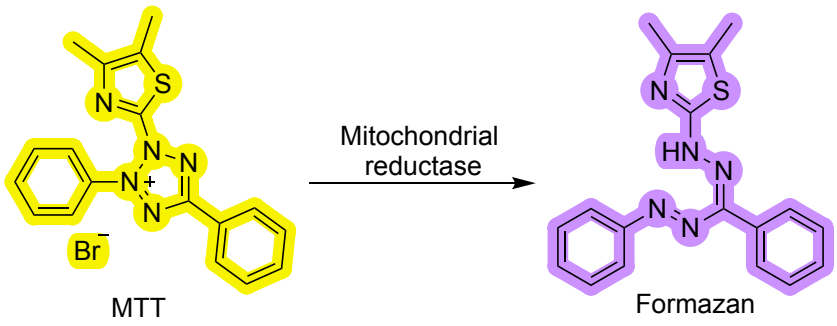


Figure 5.11: **Mechanism of MTT reduction in the cell.** MTT is a mono-tetrazolium salt consisting of a positively charged quaternary tetrazole ring core with four nitrogen atoms, surrounded by three atomic rings including two phenyl moieties and one thiazolyl ring. In the cell, reduction of MTT disrupts the core tetrazole ring and formation of water insoluble formazan occurs, which is a distinctive purple colour (Ghasemi et al., 2021).

To confirm the reduced sensitivity seen to Ag5 in hypoxia, shown in the MTT assays, clonogenic studies were undertaken. Colony survival assays are the gold standard for the determination of cell survival/viability. A549 cells were exposed to 21 or 2 % O_2 and treated with Ag5, prior to a colony survival assay. Verifying the previous findings, hypoxic cells were significantly less sensitive to Ag5, compared to normoxic cells (***Figure 5.12***).

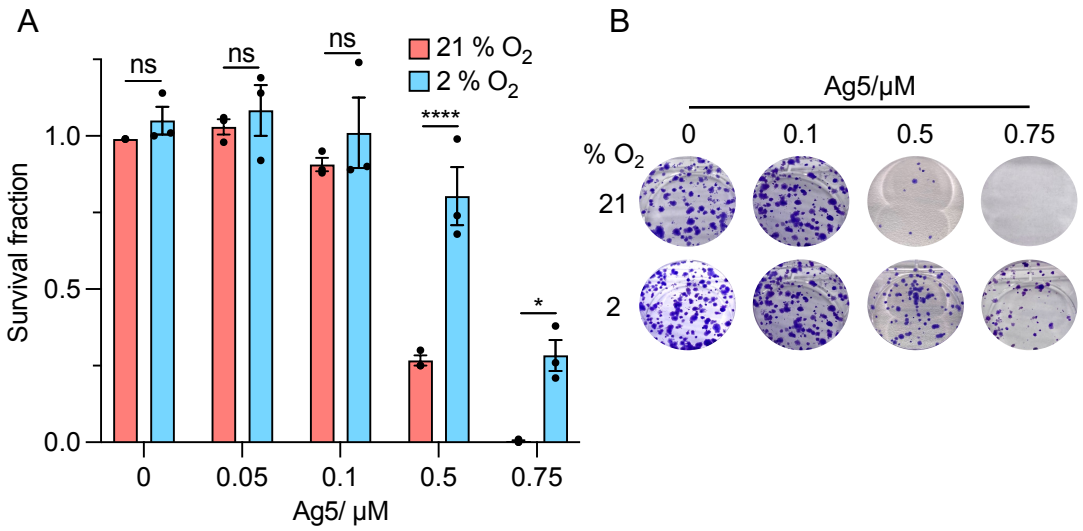


Figure 5.12: **Hypoxic cells are less sensitive to Ag5 in clonogenic studies.** A. A549 cells were exposed to 21, 2, 0.5 and <0.1 % O_2 (6 h) and then treated with Ag5 (0, 0.5, 1, 1.25, 1.5 µM) for 1 h, followed by a colony survival assay. B. Representative images of the colonies formed in part A. Data shown in A and B are n=3. Black dots on the graph shown represent biological repeats (each of which was carried out in triplicate). Data presented as mean + SEM, with untreated readings for 21 % O_2 normalised to give a survival fraction of 1.0. Statistical testing was done using a two-way ANOVA test with each bar compared to the 21 % O_2 counterpart. * p<0.05, ****p<0.0001, ns= non-significant.

5.2.4 Ag5 shows reduced activity in hypoxia

Together, the reduced sensitivity to Ag5 seen in hypoxia suggests that Ag5 is less active in hypoxic conditions. Ag5 acts via blocking antioxidant pathways, leading to an accumulation of ROS. A reduction in Ag5 activity would be expected to coincide with reduced ROS accumulation. Therefore, we measured ROS (mitochondrial) after exposure to Ag5 in both normoxic and mild hypoxic (2 % O_2) conditions, as sensitivity to Ag5 was lowest at mild hypoxia. As expected, there was a significant increase in ROS in normoxia after Ag5 treatment but not in hypoxia, suggesting a reduced effect of Ag5 in hypoxic conditions (***Figure 5.13***).

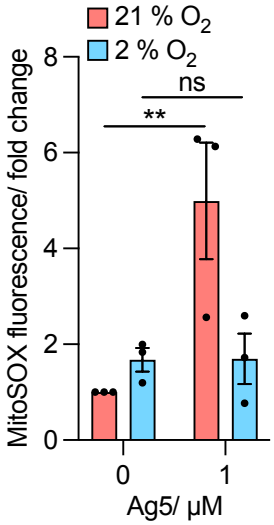


Figure 5.13: **Ag5 leads to a ROS increase in normoxia but not hypoxia.** A549 cells were exposed to 21 or 2 % O_2 (4 h) followed by Ag5 treatment (5 min) and staining for mitochondrial ROS (MitoSOX). Data shown is n=3. Black dots on the graph shown represent biological repeats (each of which was carried out in triplicate). Data presented as mean + SEM, with the fold change of untreated normoxic readings set to 1. Statistical testing was done using a two-way ANOVA test, where **p<0.01, ns= non-significant.

Next, we asked if the decreased response seen to Ag5 in hypoxia was a result of decreased therapeutic activity. The oxidation/reduction ratio of the mitochondrial-localised antioxidant enzyme, thioredoxin-dependent peroxide reductase (PRDX3), has been shown previously to be a primary mediator of Ag5 action (Porto et al., 2022). PRDX3 relies on both the GSH and Trx system, targets of Ag5, for its function (Elko et al., 2019). Therefore, we pre-exposed A549 and H460 cells to hypoxia (2 % O_2), followed by Ag5 treatment (*Figure 5.8A*) and determined the oxidation status of PRDX3 (***Figure 5.14, 5.15***). As expected, in normoxia the level of oxidised PRDX3 increased and the level of reduced PRDX3 decreased in an Ag5-dependent manner. The increase in % oxidised protein/ total protein was significant after a short period of treatment with Ag5 (15 mins). This confirmed that the reduction/oxidation ratio of PRDX3 could be used as a marker of Ag5 activity. The ratio of oxidised/reduced PRDX3 was decreased in hypoxia compared to

normoxia upon Ag5 treatment. These data indicate that Ag5 is less active in hypoxic conditions, correlating with the reduced toxicity observed.

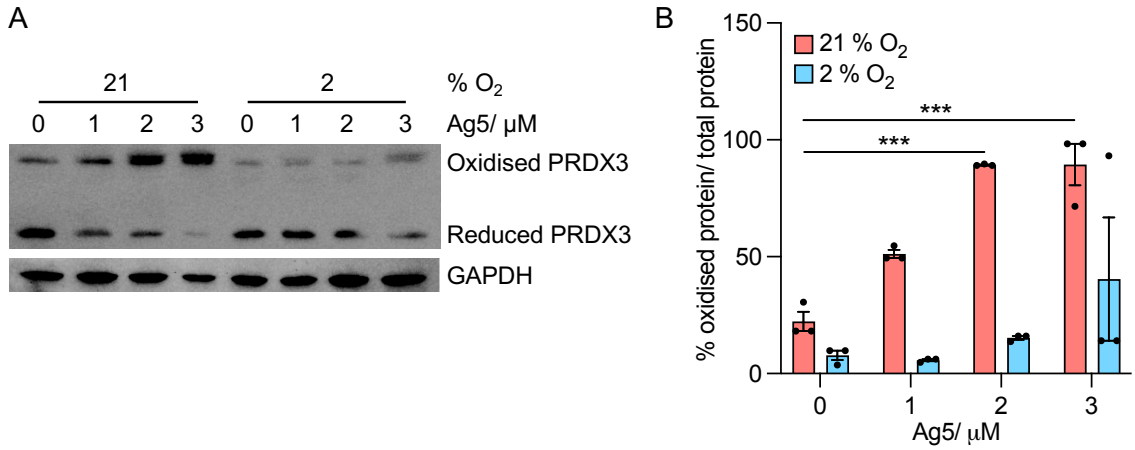


Figure 5.14: **Ag5-induced PRDX3 oxidation increases in a dose-dependent manner in normoxia, but not hypoxia.** A. A549 cells were exposed to 21 and 2 % O_2 (4 h) and then treated with Ag5 (0, 1, 2, 3 μM) for 15 min, followed by western blotting for PRDX3, with GAPDH as a loading control. B. Quantification of part A. Data shown in A and B are n=3. Black dots on the graph shown represent biological repeats. Data presented as mean + SEM. Statistical testing was done using a two-way ANOVA test with each bar compared to the 21 % O_2 counterpart, where ***p<0.001.

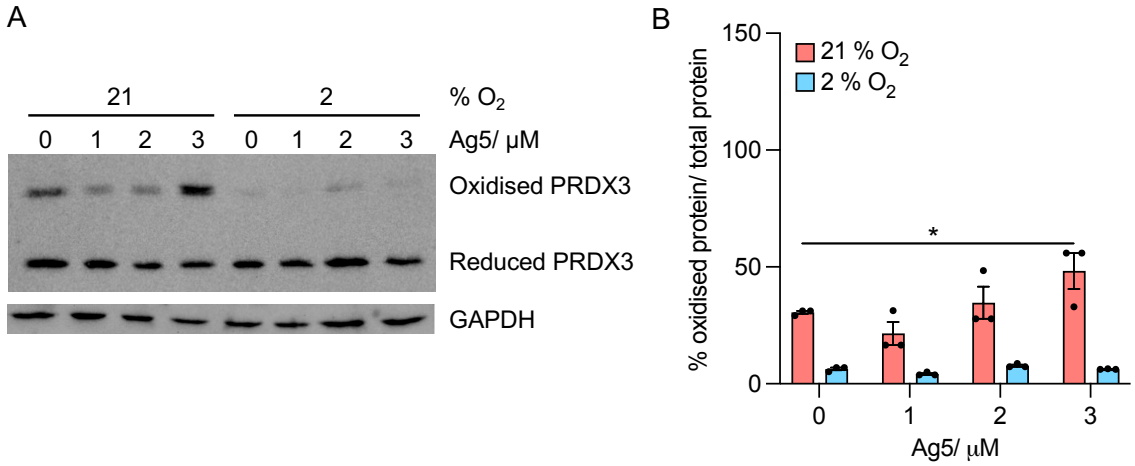


Figure 5.15: **PRDX3 oxidation changes due to Ag5 are not cell line specific.** A. H460 cells were exposed to 21 and 2 % O_2 (4 h) and then treated with Ag5 (0, 1, 2, 3 μM) for 15 min, followed by western blotting for oxidised and reduced PRDX3, with GAPDH as a loading control. B. Quantification of part A. Data shown in A and B are n=3. Black dots on the graph shown represent biological repeats. Data presented as mean + SEM. Statistical testing was done using a two-way ANOVA test with each bar compared to the 21 % O_2 counterpart, where *p<0.05.

5.2.5 Cells are sensitive to Ag5 upon immediate hypoxic exposure

As we had shown that ROS levels spike upon exposure to hypoxia, followed behind by an elevation of GSH (*Figure 4.13*), we hypothesised that cells treated with Ag5 in normoxia and then immediately introduced to hypoxia would show similar sensitivity to cells maintained in normoxia. To investigate this, A549 and H460 cells were treated with Ag5 and then immediately moved to a range of oxygen tensions (21, 4, 2, 0.5, <0.1 % O_2) (***Figure 5.16A***). As expected, HIF-1α was stabilised in response to hypoxic conditions (2, 0.5, <0.1 % O_2) and was unaffected by the presence of Ag5 (***Figure 5.15B***). Using this schedule, there was no significant difference in viability between normoxia and hypoxia in both cell lines (***Figure 5.16C, 5.17***). Together with the previous data, this indicates that the increase in GSH levels observed in hypoxia have more of an impact on sensitivity to Ag5 than the changes in ROS levels. These data also suggest that factors which alter the metabolism of cells in hypoxia would result in differing sensitivities to Ag5.

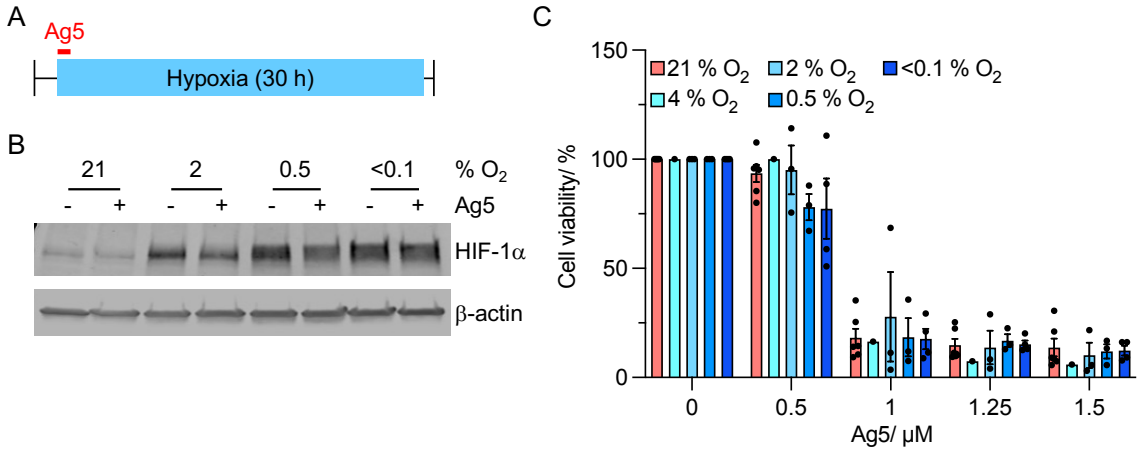


Figure 5.16: **Cells are sensitive to Ag5 upon immediate exposure to Ag5.** A. Schematic representation of cell viability assays with Ag5 with no pre-exposure to hypoxic conditions. Cells were exposed to Ag5 for 1 h. B. A549 cells were treated with Ag5 (1 μM) and then immediately exposed to 21, 2, 0.5 and <0.1 % O_2. Media was changed after 1 h and western blotting was carried out 20 h later for HIF-1a with β-actin as a loading control. C. A549 cells were treated with Ag5 (0, 0.5, 1, 1.25, 1.5 mM) and then immediately exposed to 21, 2, 0.5 and <0.1 % O_2. Media was changed after 1 h and an MTT assay was

carried out 20 h later. Data shown in C is n= ≥3 except for 4 % O_2 which is n=1. Black dots on the graph shown represent biological repeats (each of which was carried out in triplicate). Data presented as mean + SEM, with untreated readings for each % O_2 normalised to give 100 % cell viability.

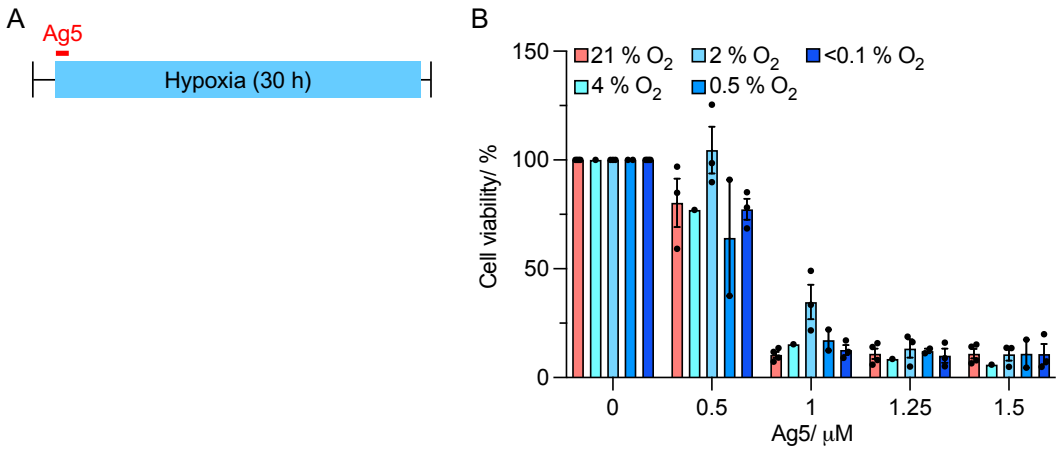


Figure 5.17: **Sensitivity to Ag5 upon immediate hypoxia exposure is independent of cell line.** A. Schematic representation of cell viability assays with Ag5 with no pre-exposure to hypoxic conditions. Cells were exposed to Ag5 for 1 h. B. H460 cells were treated with Ag5 (0, 0.5, 1, 1.25, 1.5 mM) and then immediately exposed to 21, 2, 0.5 and <0.1 % O_2. Media was changed after 1 h and an MTT assay was carried out 20 h later. Data shown in C is n= ≥3 except for 4 % O_2 which is n=1. Black dots on the graph shown represent biological repeats (each of which was carried out in triplicate). Data presented as mean + SEM, with untreated readings for each % O_2 normalised to give 100 % cell viability.

5.2.6 Sensitivity to Ag5 in hypoxia is rescued by loss of HIF-1α

Given the necessity of pre-exposure to hypoxia to decrease response to Ag5, we hypothesised that HIF-1 could play a role in determining sensitivity to Ag5, as it was seen that a biological response to hypoxia was causing the effect. HIF-1α was stabilised in all hypoxic conditions tested and is the major transcriptional regulator in hypoxia. Two models were used to investigate the role of HIF-1 in the reduced sensitivity seen in hypoxia to Ag5.

First, the genetically matched colorectal carcinoma cell lines ($RKO^{HIF\text{-}1\alpha+/+}$ and $RKO^{HIF\text{-}1\alpha-/-}$) were used. As expected, HIF-1α was not stabilised in either cell line in normoxic

conditions (21 % O_2) (***Figure 5.18***). There was no significant difference in sensitivity to Ag5 between the two cell lines in normoxia (***Figure 5.19A***). In hypoxic conditions (2 % O_2), HIF-1α was stabilised in the RKO$^{HIF\text{-}1\alpha+/+}$ cells but not the RKO$^{HIF\text{-}1\alpha-/-}$ cells, as expected (*Figure 5.18*). The cells lacking HIF-1α were significantly more sensitive to Ag5 in hypoxia (2 % O_2) than the cells with stabilised HIF-1α (***Figure 5.19B***). These data indicated that HIF-1α was playing a role in determining the sensitivity of cancer cells to Ag5. In agreement with the previous findings in A549 and H460 cells, the wildtype RKO cells were significantly less sensitive to Ag5 in hypoxia than normoxia (***Figure 5.20***).

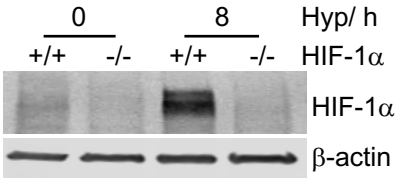


***Figure 5.18:* HIF-1α is stabilised in RKO$^{HIF\text{-}1\alpha+/+}$ cells at 2 % O_2, but not in RKO$^{HIF\text{-}1\alpha-/-}$ cells.** RKO and RKO$^{HIF\text{-}1\alpha-/-}$ cells were exposed to 21 % and <0.1 % O_2 (8 h) followed by western blotting for HIF-1α, with β-actin as a loading control.

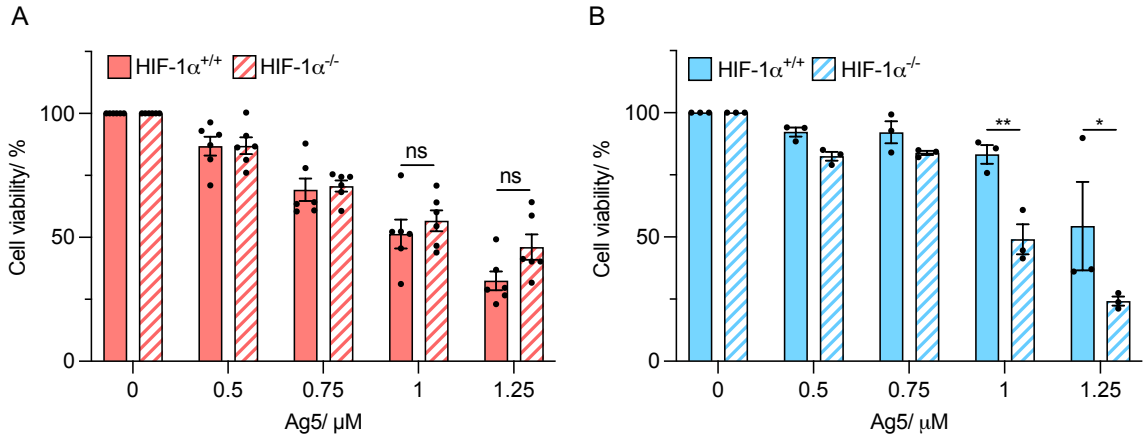


***Figure 5.19:* Sensitivity to Ag5 is HIF-1α dependent.** A. RKO and RKO$^{HIF\text{-}1\alpha-/-}$ cells were treated with Ag5 (0, 0.5, 0.75, 1, 1.25 mM) for 1 h in 21 % O_2 followed by an MTT assay 20 h later. B. RKO and RKO$^{HIF\text{-}1\alpha-/-}$ cells were exposed to 2 % O_2 (6 h), followed by treatment with Ag5 (0, 0.5, 0.75, 1, 1.25 mM) for 1 h and then an MTT assay 20 h later. Data shown in A and B are n= ≥3. Black dots on the graphs shown represent biological repeats (each of which was carried out in triplicate). Data presented as mean + SEM, with untreated readings for each cell line normalised to give 100 % cell viability. Statistical testing was done using a two-way ANOVA test, where *p<0.05, **p<0.01, ns= non-significant.

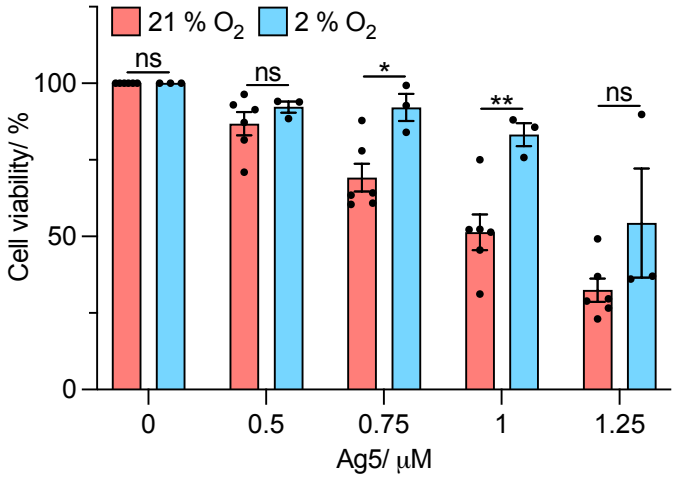


***Figure 5.20:* RKO cells are less sensitive to Ag5 in hypoxia (2 % O_2).** RKO cells were exposed to 21 and 2 % O_2 (6 h) and then treated with Ag5 (0, 0.5, 0.75, 1, 1.25 μM) for 1 h, followed by an MTT assay 20 h later. Data shown is n= ≥3. Black dots on the graph shown represent biological repeats (each of which was carried out in triplicate). Data presented as mean + SEM, with untreated readings for each % O_2 normalised to give 100 % cell viability. Statistical testing was done using an unpaired t-test, where *p<0.05, **p<0.01, ns= non-significant.

Secondly, to verify that HIF-1α determined sensitivity of cancer cells to Ag5 we used another model of hypoxia. Renal clear cell carcinoma patients often display a mutation in the tumour suppressor VHL, leading to a state of pseudohypoxia in which HIF-1α is present in normoxia (Anbalagan et al., 2012). Therefore, we used $RCC4^{VHL+/+}$ and $RCC4^{VHL-/-}$ cell lines as a model of pseudohypoxia. As expected, VHL was present in the $RCC4^{VHL+/+}$ cells in normoxia (21 % O_2, resulting in no stabilisation of HIF-1α) (***Figure 5.21A***). Whereas VHL was not present in the $RCC4^{VHL-/-}$ cells, leading to HIF-1α stabilisation (*Figure 5.21A*). In normoxia, cells lacking VHL, therefore with stabilised HIF-1α, were significantly less sensitive to Ag5 compared to the VHL proficient cells which did not stabilise HIF-1α. These data further supported the role of HIF-1α in mediating Ag5 sensitivity (***Figure 5.21B***).

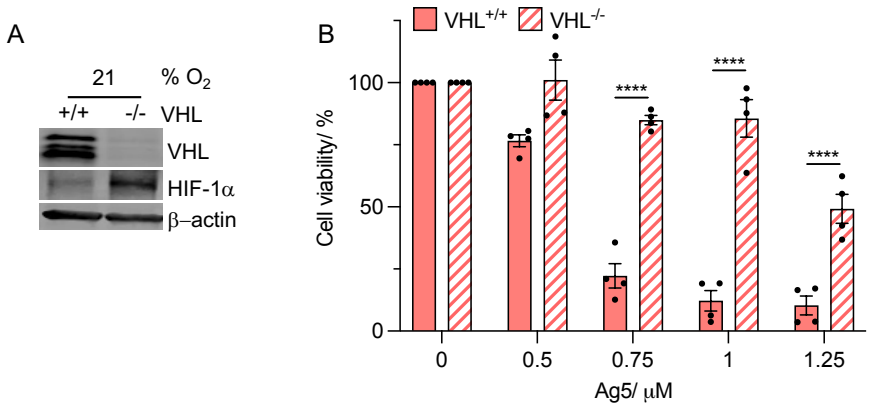


Figure 5.21: **Cells with stabilised HIF-1α are less sensitive to Ag5.** A. Untreated RCC4 and RCC4$^{VHL-/-}$ cells were western blotted for VHL, HIF-1α and a loading control (β-actin). B. RCC4 and RCC4$^{VHL-/-}$ cells were treated with Ag5 (0, 0.5, 0.75, 1, 1.25 mM) for 1 h in 21 % O_2 followed by an MTT assay 20 h later. Data shown in B is n=3. Black dots on the graph shown represent biological repeats (each of which was carried out in triplicate). Data presented as mean + SEM, with untreated readings for each cell line normalised to give 100 % cell viability. Statistical testing was done using a two-way ANOVA test, where ****p<0.0001.

5.2.7 Sensitivity to Ag5 is restored in hypoxia by loss of PDK1/3

We have shown that the activity of Ag5 is dependent on mitochondrial ROS levels, as cells treated with Ag5 and then immediately exposed to hypoxic conditions, in which a spike of mitochondrial ROS is experienced in the first 30 mins of exposure, are sensitive to Ag5. Whereas cells pre-exposed to hypoxia and then treated with Ag5 showed reduced sensitivity compared to normoxia. This indicated that an aspect of the biological response to hypoxia that could alter redox was affecting Ag5 sensitivity and this was shown to be HIF-1. Therefore, these data support the hypothesis that loss of HIF-1α restores sensitivity to Ag5 by increasing mitochondrial ROS, which is expected to enhance Ag5 activity, and likely by also reducing HIF-1 mediated signalling to genes with antioxidant functions (Qutub and Popel, 2008; Pouysségur and Mechta-Grigoriou, 2006).

The specific ratio of O_2/H_2O_2 has been described as critical for the action of Ag5. H_2O_2 binds to Ag5 with a lower adsorption energy than it binds to O_2, however, the catalytic activity of Ag5 is increased when bound to H_2O_2 in comparison to O_2 (Porto et al., 2022). Therefore, an increase in mitochondrial ROS, which would elevate H_2O_2 levels, would result in an increase in Ag5 activity. To test this hypothesis A549 cells were treated with a combination of Ag5 and FCCP, which leads to an increase in ROS through uncoupling of mitochondrial oxidative phosphorylation (Demine et al., 2019). As predicted, the combination of Ag5 and FCCP had a greater impact on cell viability compared to either agent alone (***Figure 5.22***). This supported the theory that changes in mitochondrial ROS impact sensitivity to Ag5.

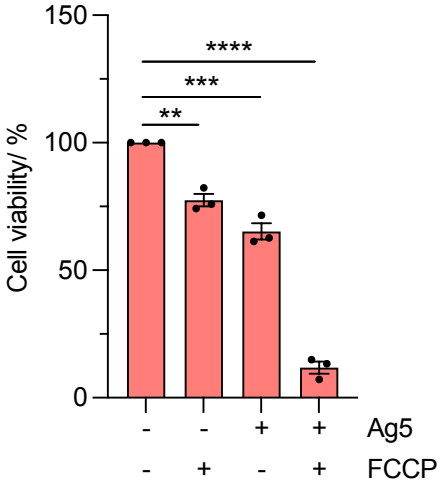


Figure 5.22: **Increasing mitochondrial ROS, increases sensitivity to Ag5.** A549 cells were either untreated, treated with FCCP (6 h), Ag5 (1 h) or both FCCP (6 h) and Ag5 (1 h) followed by an MTT assay 20 h later. Data shown is n=3. Black dots on the graph shown represent biological repeats (each of which was carried out in triplicate). Data presented as mean + SEM, with untreated readings normalised to give 100 % cell viability. Statistical testing was done using a two-way ANOVA test, where **p<0.01, ***p<0.001, ****p<0.0001.

As a recap, in response to hypoxia the glycolytic pathways are upregulated, due to increased expression of glucose transporters e.g. GLUT1, which are HIF-1 targets (Kierans

and Taylor, 2021; Semenza, 2008; Airley et al., 2003). In contrast, OxPhos is repressed in hypoxia via HIF-1 mediated increases in PDK expression which prevents PDH fuelling the TCA cycle with pyruvate (Papandreou et al., 2006). By blocking PDH, the amount of oxygen available in the mitochondria is increased, therefore altering the ratio of O_2/H_2O_2 (***Figure 5.23***).

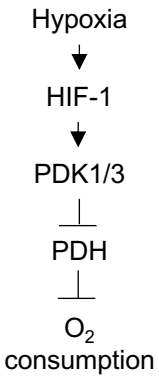


Figure 5.23: **OxPhos is repressed in hypoxia by the action of PDK1/3.** Hypoxia results in the stabilisation of HIF-1 which in turn leads to a host of downstream responses. One response is the activation of PDK1/3 which blocks PDH feeding pyruvate to the TCA cycle, leading to an increase in the local oxygen level of the mitochondria.

Both PDK1/3 are well characterised targets of HIF-1α (Papandreou et al., 2006; Lu et al., 2008; Wang et al., 2021). We predicted that in the absence of PDK1/3, the local ratio of O_2/H_2O_2 in the cell in hypoxia would be more similar to that in normoxia and sensitivity to Ag5 would be restored. In order to test this hypothesis, RKO cells with reduced expression of PDK1 and PDK3 were utilised (***Figure 5.24A***) (Papandreou et al., 2006). As expected, mitochondrial ROS levels increased more in response to hypoxia when PDK1/3 levels were depleted (***Figure 5.24B***).

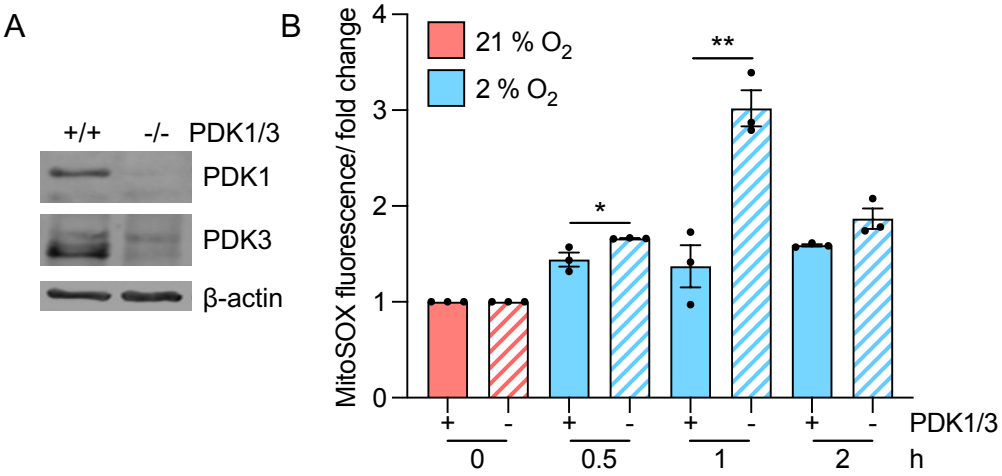


Figure 5.24: **Depletion of PDK1 and PDK3 results in increased mitochondrial ROS in hypoxia.** A. Untreated RKO and RKO$^{shPDK1//3}$ cells were western blotted for PDK1 and PDK3 with β-actin as a lading control. B. RKO and RKO$^{shPDK1/3}$ cells were exposed to 2 % O_2 (0, 0.5, 1, 2 h) followed by staining for mitochondrial ROS (MitoSOX). Data shown in B is n=3. Black dots on the graph shown represent biological repeats. Data presented as mean + SEM, with untreated readings for each cell line normalised to give a fold change of 1. Statistical testing was done using a two-way ANOVA test, where *p<0.05, **p<0.01.

To test the hypothesis that depletion of PDK1/3 would restore sensitivity to Ag5, RKO and RKO$^{shPDK1/3}$ cells were exposed to normoxia or hypoxia (2 % O_2) and treated with Ag5, following the pre-exposure scheduling (*Figure 5.8A*). As shown previously, RKO cells were less sensitive to Ag5 in hypoxia (2 % O_2) compared to normoxia. In normoxic conditions (21 % O_2), there was no significant difference in sensitivity to Ag5 between the two cell lines (***Figure 5.25A***). However, the RKO$^{shPDK1/3}$ cells were significantly more sensitive to Ag5 in hypoxia (2 % O_2), compared to the wildtype RKO cells (***Figure 5.25B***). These data demonstrate that sensitivity to Ag5 in hypoxia can be restored through loss of PDK1/3 and more broadly through combination with agents which lead to increased mitochondrial ROS levels.

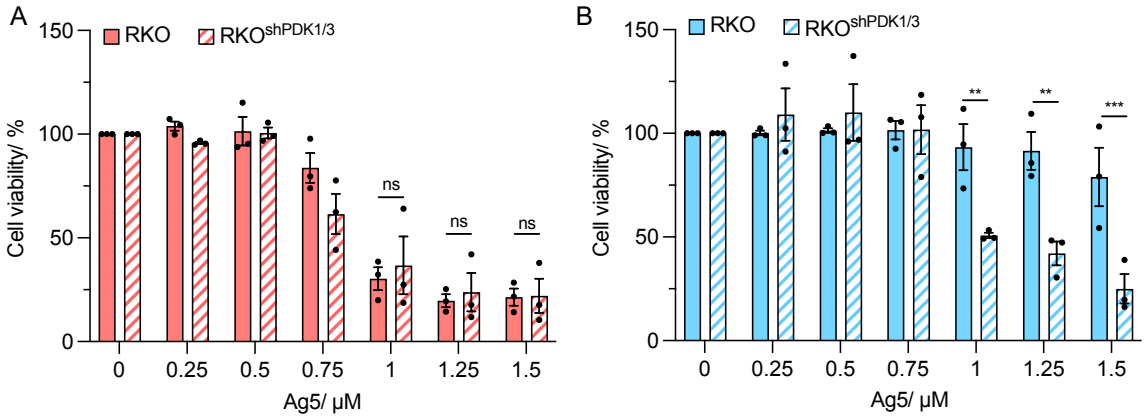


Figure 5.25: **Sensitivity to Ag5 in hypoxia can be rescued by loss of PDK1/3.** A. RKO and RKO$^{shPDK1/3}$ cells were treated with Ag5 (0, 0.25, 0.5, 0.75, 1, 1.25 mM) for 1 h in normoxia (21 % O_2) followed by an MTT assay 20 h later. B. RKO and RKO$^{shPDK1/3}$ cells were exposed to hypoxia (2 % O_2) (6 h), followed by treatment with Ag5 (0, 0.5, 0.75, 1, 1.25 mM) for 1 h followed by an MTT assay 20 h later. Data shown in A and B are n=3. Black dots on the graphs shown represent biological repeats (each of which was carried out in triplicate). Data presented as mean + SEM, with untreated readings for each cell line and % O_2 normalised to give 100 % cell viability Statistical testing was done using a two-way ANOVA test, where **p<0.01, ***p<0.001, ns= non-significant.

5.2.8 Ag5 increases the radiosensitivity of hypoxic cells

Despite the reduced sensitivity to Ag5 in hypoxia, or conditions where HIF-1 is expressed, Ag5 is a promising anti-cancer agent due to the lack of toxicity observed in non-transformed cells (*Figure 5.1*). In the clinic, Ag5 is unlikely to be used as a single agent therapy. Radiation in the form of radiotherapy leads to the generation of •OH radicals from the hydrolysis of H_2O which cause DNA damage and cell death (Wu et al., 2021). Radiotherapy is commonly used to treat solid tumours, particularly in lung cancer. Therefore, we asked if the combination of Ag5 and radiation would be effective. Importantly, we investigated the impact of Ag5 on radiosensitivity in hypoxic conditions as hypoxia is a major mechanism of radiation resistance (Bristow and Hill, 2008). The most significant radioresistance is seen in cells experiencing <0.1 % O_2, known as radiobiological hypoxia, therefore this oxygen tension was used for Ag5-radiation

experiments. A549 cells were exposed to radiobiological hypoxia (<0.1 % O_2) and treated with both Ag5 and radiation (0, 2, 4 Gy) and a colony survival assay was carried out (***Figure 5.26A***). Importantly, cells were maintained under hypoxic conditions throughout the drug and irradiation treatment, by transfer into air-tight boxes (Anbalagan et al., 2012). As expected, HIF-1α was stabilised in all the hypoxic conditions tested and its expression was not impacted by addition of Ag5 (***Figure 5.26B***). The combination of Ag5 and radiation had a significantly greater effect on cell survival compared to either agent alone (***Figure 5.26C***). Together, these data suggest that the combination of Ag5 and radiotherapy would be efficacious and does not increase hypoxia-induced radioresistance.

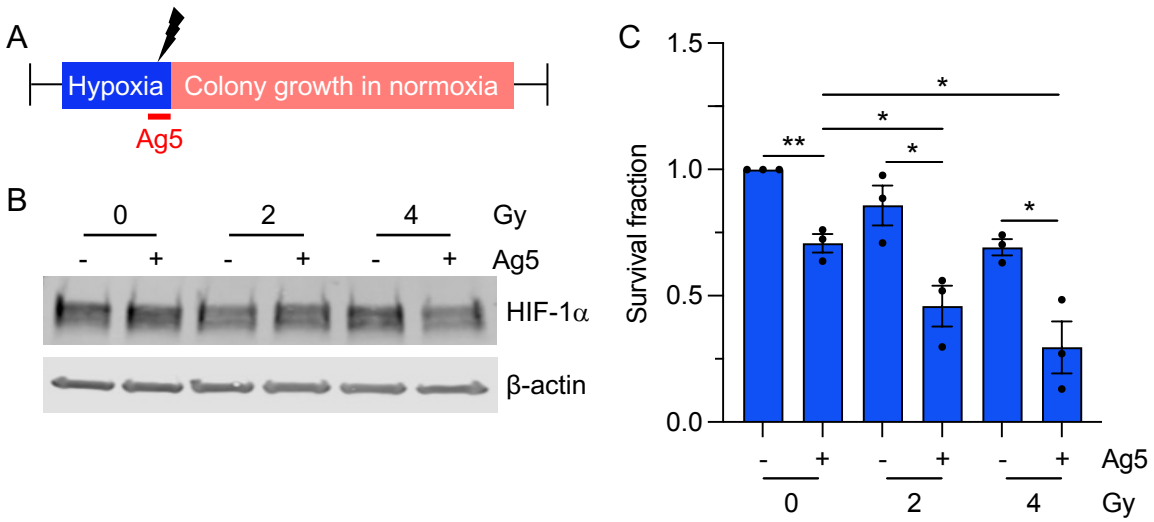


Figure 5.26: **Ag5 increases the radiosensitivity of hypoxic (<0.1 % O_2) cells.** A. Schematic representation of the experimental set up for combining Ag5 with radiation in hypoxia (not to scale). Importantly, radiation (indicated with black lightning strike) was delivered in hypoxic conditions i.e. without reoxygenation. Colonies were then allowed to form in normoxic (21 % O_2) conditions. B. A549 cells were exposed to <0.1 % O_2 (4 h), followed by treatment with Ag5 (1 μM) for 1 h. During Ag5 treatment, cells were irradiated (0, 2, 4 Gy) in hypoxic conditions. Cells were harvested after the 1 h treatment and western blotted for HIF-1α, with β-actin as a loading control. C. A549 cells were treated as in part A followed by return to normoxic conditions (21 % O_2), and colony survival assay. Data shown in C is n=3. Black dots on the graph shown represent biological repeats (each of which was carried out in triplicate). Data presented as mean + SEM, with

untreated readings normalised to give a survival fraction of 1.0. Statistical testing was done using an unpaired t-test, where *p<0.05.

5.3 Discussion

The therapeutic molecular cluster Ag5 leads to significant loss of viability in all the cancer cell lines tested but not non-transformed cells. This profile makes Ag5 an attractive potential anti-cancer agent. We investigated how the activity of Ag5 was impacted by conditions which reflect the physiological levels of oxygen commonly found in solid tumours. In all of the hypoxic conditions tested, cells were less sensitive to Ag5 compared to normoxic (21 % O_2) conditions. It is important to note that the hypoxic cancer cells were still more sensitive to Ag5 compared to the non-transformed cells. Normal cells experiencing the levels of hypoxia found in tumours and tested here are rare within the normal body providing an exploitable therapeutic window. Importantly, the combination of radiation and Ag5 significantly increased cell death in hypoxia compared to radiation alone. The decreased sensitivity to Ag5 observed in hypoxia was found to be HIF-1α dependent and more specifically dependent on the HIF-1 target genes PDK1/3. Our data supports the hypothesis that loss of PDK1/3 in hypoxic conditions relieves the inhibitory effect of PDH on oxygen consumption and therefore increases available oxygen and ROS in the mitochondria which is the site of Ag5 action. Ag5 is known to be exquisitely sensitive to the ratio of O_2/H_2O_2 (Porto et al., 2022).

In summary, Ag5 is an exciting addition to the class of redox dependent agents with anti-cancer activity. The high potency of Ag5 in cancer cells is likely underpinned by targeting both GSH and Trx pathways, therefore preventing cancer cells circumventing reduced antioxidant capacity. Our study highlights the importance of testing anti-cancer agents in

conditions which mimic the hypoxic tumour microenvironment as Ag5 is less toxic in these conditions. However, Ag5 remains a promising anti-cancer approach as it shows selective activity in cancer compared to normal cells and combines well with radiation. In the future, combinations of Ag5 with other agents would be tested. For example, we showed that the addition of FCCP led to a significant decrease in cell viability, indicating that other oxygen modulating therapies could be efficacious in combination with Ag5. Atovaquone leads to an increase in available oxygen for hypoxic tissues, therefore reoxygenating them which could mean Ag5 would work as it does in normoxia and lead to significant decreases in cell viability. H_2O_2 could also reoxygenate tissue, increasing the activity of Ag5 (Nimalasena et al., 2024). The next step would be to understand combinations of Ag5 with other agents, as the timing would be crucial to the effect seen. 3D systems such as spheroids would also be investigated in order to provide data that would be closer to what would be seen in the clinic. Further next steps for the use of Ag5 will be discussed in *Chapter 6*.

Chapter 6: Discussion

Redox is highly dynamic and particularly so in cancer (Perillo et al., 2020). Our goals were to understand redox changes in cancer cells experiencing hypoxia and the impact this has on therapy, along with the generation of a novel probe to measure changes in oxygen levels.

Oxygen is a key component of redox. Over the years, it has become apparent that hypoxia is not a static condition but one that can include repeated cycles of reoxygenation, leading to a heterogenous oxygen environment and distinct biological responses (Bader et al., 2020, 2021). Tools that have been developed or are in development to image hypoxia do not reflect the dynamic nature of redox instead only informing on the oxygen condition at time of administration. An ideal imaging technique would allow for repeat measurements to be possible and practical, or the agent would be able to inform on the dynamic nature of hypoxia. Therefore, we designed a novel probe that would report on oxygenation by fluorescing in hypoxia and then be able to return to a non-fluorescent form upon return to normal oxygen levels. We used fluorescence as an output to allow for troubleshooting of complex chemistry in an overall straight forward system, with the goal of ultimately advancing to an MRI/PET probe. Reversibility of the generated probe was confirmed however insufficient levels of fluorescent emission resulted in disappointing findings in cellular testing. Indication of instability upon reduction of the probe was also seen under the experimental conditions tested. A variation of the probe was produced with naphthalene rings to increase the π conjugation of the system and enhance the fluorescent output but did not show a significant improvement. The concept of a dynamic imaging method to visualise oxygen fluctuations in hypoxic tumours is still an important goal for the field, for example to monitor the action of oxygen modulating therapies, such

as atovaquone (Ashton et al., 2016; Skwarski et al., 2021). The production of second-generation probes could include changing the fluorophore to a commercially available one such as BODIPY, which has well-understood spectral properties that have been exploited successfully in cellular systems. Additionally, the stability of commercially available fluorophores is known, therefore the current decomposition seen would be eliminated. With this in mind, Dr Antoine Wallabregue (Conway lab) has implemented a new design for a reversible probe where the hypoxia sensing group (indolequinone) is attached to a BODIPY fluorophore. Using this probe a weakly fluorescent signal under normoxia has been observed and the reversibility of the probe has been determined *in vitro* through bioreductive and oxidative assays. However, preliminary results from cell-based experiments indicate moderate fluorescence reversibility. Future work is focused on optimising the redox properties of the probe to address this limitation. For example, altering the quinone moiety to include groups such as CF_3, which have been seen as attachments in literature probes to enhance the electron withdrawing nature of the quinone, prior to enzymatic reduction in hypoxia (Zhang et al., 2021). This would hopefully increase the conversion of oxidised to reduced probe, removing the chance of quenching by any remaining oxidised probe and increasing the output signal. Overall, alterations to either end of the probe would be made in isolation and then the change to the probes photophysical properties would be tested until they were deemed bright enough to be visualised in cells, in which testing would advance to 2D and eventually 3D models.

Controversy appeared in the hypoxia field as to what happens to redox in hypoxia, primarily due to differences in experimental conditions, however there is a majority consensus that ROS increase in hypoxia (Ferber et al., 2012; Ogunrinu and Sontheimer,

2010; Reczek and Chandel, 2017; Bell et al., 2005; Glasauer and Chandel, 2014; Guzy et al., 2005; Sabharwal and Schumacker, 2014; Chandel et al., 2000, 1998). Redox in hypoxia is somewhat paradoxical, with an increase in ROS levels and a resultant elevation in local oxygen experienced in the mitochondria. In this study, we provided a comprehensive report of the kinetic changes to redox in response to hypoxia. Both ROS and GSH increased in response to reduced oxygen levels, however they showed very different kinetics, with ROS peaking early and GSH lagging behind.

It was impossible to ignore the contribution of HIF-mediated signalling in this study as it has been implicated in redox homeostasis (Chandel et al., 1998; Guzy et al., 2005; Toth and Warfel, 2017; Tello et al., 2011; Potteti et al., 2016; Xin et al., 2020; Kim et al., 2011; Bondi et al., 2022; Loboda et al., 2009; Pan et al., 2007; Watanabe et al., 2016; Hamanaka et al., 2016; Chandel et al., 2000; Semenza, 1999; Agani et al., 2000; Haddad et al., 2000). HIF-1α upregulates glycolytic pathways through increased expression of glucose transporters, whilst repressing oxidative phosphorylation via PDK1/3 activation (Denko, 2008; Papandreou et al., 2006). Inhibition of the electron transport chain, results in a reduction of mitochondrial ROS, ensuring cell survival (Kim et al., 2006). An apparent increase in oxygen is seen in the cell as it is no longer needed as the terminal acceptor for oxidative phosphorylation, allowing other essential functions to be carried out (Shen et al., 2003; Hagen et al., 2003; Tu and Weissman, 2002; Forneris et al., 2005; Herst and Berridge, 2007; Rosenfeld et al., 2002). The antioxidant machinery is activated in response to the elevated ROS levels, in part mediated by HIF-1α (Qutub and Popel, 2008; Pouysségur and Mechta-Grigoriou, 2006). The steady increase of the main cellular antioxidant GSH, aids in alleviating cellular stress and bringing the ROS levels down from their peak height.

A limitation of the study presented is a failure to consider other ROS/RNS that are participating in the redox changes that take place in hypoxia. A number of probes are available that detect particular free radical species, such as peroxynitrite or nitric oxide, that could be included in future work (Geng et al., 2023; Murphy et al., 2022). Additionally, specific antioxidants could be investigated, including peroxiredoxins and sulfaredoxins. Overall, this would give a more detailed picture of redox and show changes to specific elements. Additionally, how redox is impacted when cells experience a change in oxygen level, for example from severe levels of hypoxia (<0.1 % O_2) to milder hypoxia (2 % O_2) was not considered here, and is likely to have a significant impact on biological signalling (Bader et al., 2020). Clinically, patients will experience fluctuating oxygen levels in their tumour, therefore this data could inform on when best to administer redox-sensitive agents to produce the most effective outcome. Despite the limitations in the current study, it was clear that the redox balance in hypoxic cells is significantly different to that of a cell in standard tissue culture conditions (21 % O_2), and this likely underpins differential sensitivities to redox-dependent agents.

We went on to investigate the efficacy of the redox-targeting agent Ag5 in hypoxic conditions. Ag5 is an exciting new anti-cancer agent, designed to inhibit antioxidant pathways, resulting in ROS accumulation and cell death (Porto et al., 2022). We predicted that the sensitivity to Ag5 would be altered in hypoxic conditions, and it was shown that hypoxic cells were less sensitive to Ag5 in a range of cancer cell lines and oxygen tensions. Importantly, hypoxic cancer cells were still more sensitive to Ag5 than non-transformed cells. The reduced sensitivity to Ag5 was found to be dependent on HIF-1α mediated PDK1/3 action, as blocking PDH results in reduced mitochondrial ROS and a

local increase in oxygen. Therefore, sensitivity to Ag5 was restored by inhibiting HIF-1α or PDK1/3 expression or increasing mitochondrial ROS levels (Twigger et al., 2024).

The future of cancer treatment will increasingly look at personalised approaches and unique combinations of agents (Gambardella et al., 2020). Ag5 is unlikely to be used as a single agent therapy. Radiation treatment produces free radicals, which we hypothesised would increase the activity of Ag5. Hypoxic tumours are well characterised to be radioresistant and notably Ag5 combined well with radiation to give a greater loss in viability than either approach alone. Fractionated radiotherapy leads to reoxygenation therefore, in addition to increased ROS, hypoxic tumours cells could be reoxygenated and re-sensitised to Ag5. Intratumoural H_2O_2 has also been shown to reoxygenate tissues, indicating that it would make an efficacious combination with Ag5 (Nimalasena et al., 2024). By utilising H_2O_2 there is also the possibility that it could supercharge Ag5 as the catalytic activity of Ag5 is increased significantly in the presence of H_2O_2. The combination of radiation and H_2O_2 alongside Ag5 could also be investigated (Nimalasena et al., 2020). Consequently, future work should include pre-clinical testing of Ag5 in combination with radiotherapy/H_2O_2 to assess the most effective timeline for delivery of the agents, before moving into the clinic. The next steps for Ag5 would be *in vivo* testing and eventually moving into a phase I clinical trial to determine a safely tolerated dose, along with potential side effects and metabolism of the drug in the body.

Overall, this study demonstrates the importance of understanding the hypoxic tumour microenvironment to aid the pre-clinical and clinical development of cancer therapeutics.

Chapter 7: References

Afify, S.M., and M. Seno. 2023. On the Origin of Cancer. *Methods Cancer Stem Cell Biol.* 1–21.

Agani, F.H., P. Pichiule, J.C. Chavez, and J.C. LaManna. 2000. The role of mitochondria in the regulation of hypoxia-inducible factor 1 expression during hypoxia. *J. Biol. Chem.* 275:35863–35867.

Airley, R.E., J. Loncaster, J.A. Raleigh, A.L. Harris, S.E. Davidson, R.D. Hunter, C.M.L. West, and I.J. Stratford. 2003. GLUT-1 and CAIX as intrinsic markers of hypoxia in carcinoma of the cervix: Relationship to pimonidazole binding. *Int. J. Cancer.* 104:85–91.

Aitio, M.L. 2006. N-acetylcysteine -- passe-partout or much ado about nothing? *Br. J. Clin. Pharmacol.* 61:5–15.

Allen, J.W., S.R. Khetani, R.S. Johnson, and S.N. Bhatia. 2006. In vitro liver tissue model established from transgenic mice: role of HIF-1alpha on hypoxic gene expression. *Tissue Eng.* 12:3135–3147.

An, X., W. Yu, J. Liu, D. Tang, L. Yang, and X. Chen. 2024. Oxidative cell death in cancer: mechanisms and therapeutic opportunities. *Cell Death Dis.* 15:556.

Anbalagan, S., I.M. Pires, C. Blick, M.A. Hill, D.J.P. Ferguson, D.A. Chan, and E.M. Hammond. 2012. Radiosensitization of renal cell carcinoma in vitro through the induction of autophagy. *Radiother. Oncol.* 103:388–393.

Anderson, N.M., and M.C. Simon. 2020. The tumor microenvironment. *Curr. Biol.* 30:R921–R925.

Arosio, P., R. Ingrassia, and P. Cavadini. 2009. Ferritins: a family of molecules for iron storage, antioxidation and more. *Biochim. Biophys. Acta.* 1790:589–599.

Asantewaa, G., and I.S. Harris. 2021. Glutathione and its precursors in cancer. *Curr. Opin. Biotechnol.* 68:292–299.

Ashton, T.M., E. Fokas, L.A. Kunz-Schughart, L.K. Folkes, S. Anbalagan, M. Huether, C.J. Kelly, G. Pirovano, F.M. Buffa, E.M. Hammond, M. Stratford, R.J. Muschel, G.S. Higgins, and W.G. McKenna. 2016. The anti-malarial atovaquone increases radiosensitivity by alleviating tumour hypoxia. *Nat. Commun. 2016 71.* 7:1–13.

Asikainen, T.M., A. Ahmad, B.K. Schneider, and C.W. White. 2005. Effect of preterm birth on hypoxia-inducible factors and vascular endothelial growth factor in primate lungs. *Pediatr. Pulmonol.* 40:538–546.

Babior, B.M. 2004. NADPH oxidase. *Curr. Opin. Immunol.* 16:42–47.

Bader, S.B., M.W. Dewhirst, and E.M. Hammond. 2020. Cyclic Hypoxia: An Update on Its Characteristics, Methods to Measure It and Biological Implications in Cancer. *Cancers (Basel).* 13:23.

Bader, S.B., T.S. Ma, C.J. Simpson, J. Liang, S.E.B. Maezono, M.M. Olcina, F.M. Buffa, and E.M. Hammond. 2021. Replication catastrophe induced by cyclic hypoxia leads to increased APOBEC3B activity. *Nucleic Acids Res.* 49:7492–7506.

Bae, T., S.P. Hallis, and M.K. Kwak. 2024. Hypoxia, oxidative stress, and the interplay of HIFs and NRF2 signaling in cancer. *Exp. Mol. Med. 2024 563.* 56:501–514.

Bae, Y.S., S.W. Kang, M.S. Seo, I.C. Baines, E. Tckle, P.B. Chock, and S.G. Rhee. 1997. Epidermal growth factor (EGF)-induced generation of hydrogen peroxide: Role in EGF receptor-mediated tyrosine phosphorylation. *J. Biol. Chem.* 272:217–221.

Baghban, R., L. Roshangar, R. Jahanban-Esfahlan, K. Seidi, A. Ebrahimi-Kalan, M. Jaymand, S. Kolahian, T. Javaheri, and P. Zare. 2020. Tumor microenvironment complexity and therapeutic implications at a glance. *Cell Commun. Signal. 2020*

181. 18:1–19.
Bailey, P.S.J., and J.A. Nathan. 2018. Metabolic Regulation of Hypoxia-Inducible Transcription Factors: The Role of Small Molecule Metabolites and Iron. *Biomed. 2018, Vol. 6, Page 60*. 6:60.
Bailey, P.S.J., B.M. Ortmann, A.W. Martinelli, J.W. Houghton, A.S.H. Costa, S.P. Burr, R. Antrobus, C. Frezza, and J.A. Nathan. 2020. ABHD11 maintains 2-oxoglutarate metabolism by preserving functional lipoylation of the 2-oxoglutarate dehydrogenase complex. *Nat. Commun. 2020 111*. 11:1–15.
Baird, L., and M. Yamamoto. 2020. The Molecular Mechanisms Regulating the KEAP1-NRF2 Pathway. *Mol. Cell. Biol.* 40.
Bantounou, M., J. Plascevic, and H.F. Galley. 2022. Melatonin and Related Compounds: Antioxidant and Anti-Inflammatory Actions. *Antioxidants*. 11.
Barnett, J. 2000. A history of research on yeasts 2: Louis Pasteur and his contemporaries, 1850-1880. *Yeast*. 16:755–771.
Barnhart, B.C., and M.C. Simon. 2007. Metastasis and stem cell pathways. *Cancer Metastasis Rev.* 26:261–271.
Baskar, R., K.A. Lee, R. Yeo, and K.W. Yeoh. 2012. Cancer and Radiation Therapy: Current Advances and Future Directions. *Int. J. Med. Sci.* 9:193.
Bassler, N., J. Toftegaard, A. Lühr, B.S. Sorensen, E. Scifoni, M. Krämer, O. Jäkel, L.S. Mortensen, J. Overgaard, and J.B. Petersen. 2014. LET-painting increases tumour control probability in hypoxic tumours. *Acta Oncol.* 53:25–32.
Batchelder, R.M., W.R. Wilson, M.P. Hay, and W.A. Denny. 1996. Oxygen dependence of the cytotoxicity of the enediyne anti-tumour antibiotic esperamicin A1. *Br. J. Cancer. Suppl.* 27:S52.
Bauch, M., M. Klaper, and T. Linker. 2017. Intermediates in the cleavage of endoperoxides. *J. Phys. Org. Chem*. 30.
Begg, A.C., F.A. Stewart, and C. Vens. 2011. Strategies to improve radiotherapy with targeted drugs. *Nat. Rev. Cancer*. 11:239–253.
Bell, E.L., B.M. Emerling, and N.S. Chandel. 2005. Mitochondrial regulation of oxygen sensing. *Mitochondrion*. 5:322–332.
Bellot, G., R. Garcia-Medina, P. Gounon, J. Chiche, D. Roux, J. Pouysségur, and N.M. Mazure. 2009. Hypoxia-induced autophagy is mediated through hypoxia-inducible factor induction of BNIP3 and BNIP3L via their BH3 domains. *Mol. Cell. Biol.* 29:2570–2581.
Bencokova, Z., M.R. Kaufmann, I.M. Pires, P.S. Lecane, A.J. Giaccia, and E.M. Hammond. 2009. ATM Activation and Signaling under Hypoxic Conditions. *Mol. Cell. Biol.* 29:526.
Benhar, M. 2018. Roles of mammalian glutathione peroxidase and thioredoxin reductase enzymes in the cellular response to nitrosative stress. *Free Radic. Biol. Med.* 127:160–164.
Berger, A. 2002. How does it work?: Magnetic resonance imaging. *BMJ Br. Med. J.* 324:35.
Berger, A. 2003. How Does It Work?: Positron emission tomography. *BMJ Br. Med. J.* 326:1449.
Bhandari, V., C. Hoey, L.Y. Liu, E. Lalonde, J. Ray, J. Livingstone, R. Lesurf, Y.J. Shiah, T. Vujcic, X. Huang, S.M.G. Espiritu, L.E. Heisler, F. Yousif, V. Huang, T.N. Yamaguchi, C.Q. Yao, V.Y. Sabelnykova, M. Fraser, M.L.K. Chua, T. van der Kwast, S.K. Liu, P.C.

Boutros, and R.G. Bristow. 2019. Molecular landmarks of tumor hypoxia across cancer types. *Nat. Genet. 2019 512*. 51:308–318.

Bi, Z., Q. Zhang, Y. Fu, P. Wadgaonkar, W. Zhang, B. Almutairy, L. Xu, M. Rice, Y. Qiu, C. Thakur, and F.C. Dr. 2020. Nrf2 and HIF1α converge to arsenic-induced metabolic reprogramming and the formation of the cancer stem-like cells. *Theranostics*. 10:4134.

Boekstegers, P., R. Riessen, and W. Seyde. 1990. Oxygen partial pressure distribution within skeletal muscle: indicator of whole body oxygen delivery in patients? *Adv. Exp. Med. Biol.* 277:507–514.

Bondi, C.D., B.M. Rush, H.L. Hartman, J. Wang, M.M. Al-Bataineh, R.P. Hughey, and R.J. Tan. 2022. Suppression of NRF2 Activity by HIF-1α Promotes Fibrosis after Ischemic Acute Kidney Injury. *Antioxidants (Basel, Switzerland)*. 11.

Bonello, S., C. Zähringer, R.S. BelAiba, T. Djordjevic, J. Hess, C. Michiels, T. Kietzmann, and A. Görlach. 2007. Reactive oxygen species activate the HIF-1alpha promoter via a functional NFkappaB site. *Arterioscler. Thromb. Vasc. Biol.* 27:755–761.

Brahimi-Horn, M.C., J. Chiche, and J. Pouysségur. 2007. Hypoxia signalling controls metabolic demand. *Curr. Opin. Cell Biol.* 19:223–229.

Brand, M.D. 2020. Riding the tiger - physiological and pathological effects of superoxide and hydrogen peroxide generated in the mitochondrial matrix. *Crit. Rev. Biochem. Mol. Biol.* 55:592–661.

Breasted, J.H. 1930. Bulging Tumors on the Breast. *Edwin Smith Surg. Papyrus*. 1:403–406.

Brigelius-Flohé, R., and M. Maiorino. 2013. Glutathione peroxidases. *Biochim. Biophys. Acta*. 1830:3289–3303.

Bristow, R.G., and R.P. Hill. 2008. Hypoxia, DNA repair and genetic instability. *Nat. Rev. Cancer*. 8:180–192.

Brizel, D.M., S.P. Scully, J.M. Harrelson, L.J. Layfield, J.M. Bean, L.R. Prosnitz, and M.W. Dewhirst. 1996. Tumor Oxygenation Predicts for the Likelihood of Distant Metastases in Human Soft Tissue Sarcoma1. *CANCER Res.* 56:941–943.

Brizel, D.M., G.S. Sibley, L.R. Prosnitz, R.L. Scher, and M.W. Dewhirst. 1997. Tumor hypoxia adversely affects the prognosis of carcinoma of the head and neck. *Int. J. Radiat. Oncol. Biol. Phys.* 38:285–289.

Brooks, A.J., J. Eastwood, I.J. Beckingham, and K.J. Girling. 2004. Liver tissue partial pressure of oxygen and carbon dioxide during partial hepatectomy. *Br. J. Anaesth.* 92:735–737.

Brown, J.M. 1979. Evidence for acutely hypoxic cells in mouse tumours, and a possible mechanism of reoxygenation. *Br. J. Radiol.* 52:650–656.

Brown, J.M., and B.G. Slim. 1996. Hypoxia-Specific Cytotoxins in Cancer Therapy. *Semin. Radiat. Oncol.* 6:22–36.

Brown, J.M., and W.R. Wilson. 2004. Exploiting tumour hypoxia in cancer treatment. *Nat. Rev. Cancer*. 4:437–447.

Brown, J.M.Y., and A. Giaccia. 1998. The unique physiology of solid tumors: opportunities (and problems) for cancer therapy. *Cancer Res.*

Brunelle, J.K., E.L. Bell, N.M. Quesada, K. Vercauteren, V. Tiranti, M. Zeviani, R.C. Scarpulla, and N.S. Chandel. 2005. Oxygen sensing requires mitochondrial ROS but not oxidative phosphorylation. *Cell Metab.* 1:409–414.

Buceta, D., N. Busto, G. Barone, J.M. Leal, F. Domínguez, L.J. Giovanetti, F.G. Requejo,

B. García, and M.A. Lõpez-Quintela. 2015. Ag2 and Ag3 clusters: synthesis, characterization, and interaction with DNA. *Angew. Chem. Int. Ed. Engl.* 54:7612–7616.

Bui, B.P., P.L. Nguyen, K. Lee, and J. Cho. 2022. Hypoxia-Inducible Factor-1: A Novel Therapeutic Target for the Management of Cancer, Drug Resistance, and Cancer-Related Pain. *Cancers (Basel).* 14.

Bussink, J., C.M.L. van Herpen, J.H.A.M. Kaanders, and W.J.G. Oyen. 2010. PET-CT for response assessment and treatment adaptation in head and neck cancer. *Lancet. Oncol.* 11:661–669.

Cai, Q., T. Yu, W. Zhu, Y. Xu, and X. Qian. 2015. A turn-on fluorescent probe for tumor hypoxia imaging in living cells. *Chem. Commun.* 51:14739–14741.

Cairns, R.A., I.S. Harris, and T.W. Mak. 2011. Regulation of cancer cell metabolism. *Nat. Rev. Cancer 2011 112*. 11:85–95.

Cancer Research UK. Cancer Statistics for the UK.

Cao, J., J. Schulte, A. Knight, N.R. Leslie, A. Zagozdzon, R. Bronson, Y. Manevich, C. Beeson, and C.A. Neumann. 2009. Prdx1 inhibits tumorigenesis via regulating PTEN/AKT activity. *EMBO J.* 28:1505.

Carreau, A., B. El Hafny-Rahbi, A. Matejuk, C. Grillon, and C. Kieda. 2011. Why is the partial oxygen pressure of human tissues a crucial parameter? Small molecules and hypoxia. *J. Cell. Mol. Med.* 15:1239–1253.

Carvalho, C., R. Santos, S. Cardoso, S. Correia, P. Oliveira, M. Santos, and P. Moreira. 2009. Doxorubicin: the good, the bad and the ugly effect. *Curr. Med. Chem.* 16:3267–3285.

Chakraborty, I., and T. Pradeep. 2017. Atomically Precise Clusters of Noble Metals: Emerging Link between Atoms and Nanoparticles. *Chem. Rev.* 117:8208–8271.

Chan, J., S.C. Dodani, and C.J. Chang. 2012. Reaction-based small-molecule fluorescent probes for chemoselective bioimaging. *Nat. Chem.* 4:973–984.

Chance, B., H. Sies, and A. Boveris. 1979. Hydroperoxide metabolism in mammalian organs. *Physiol. Rev.* 59:527–605.

Chandel, N.S. 2015. Evolution of Mitochondria as Signaling Organelles. *Cell Metab.* 22:204–206.

Chandel, N.S., E. Maltepe, E. Goldwasser, C.E. Mathieu, M.C. Simon, and P.T. Schumacker. 1998. Mitochondrial reactive oxygen species trigger hypoxia-induced transcription. *Proc. Natl. Acad. Sci. U. S. A.* 95:11715–11720.

Chandel, N.S., D.S. McClintock, C.E. Feliciano, T.M. Wood, J.A. Melendez, A.M. Rodriguez, and P.T. Schumacker. 2000. Reactive oxygen species generated at mitochondrial complex III stabilize hypoxia-inducible factor-1alpha during hypoxia: a mechanism of O2 sensing. *J. Biol. Chem.* 275:25130–25138.

Chaplin, D.J. 1991. Chemical modifiers of tumor blood flow. *Tumour blood supply Metab. Microenviron.* 20:65–85.

Chaplin, D.J., P.L. Olive, and R.E. Durand. 1987a. Hypoxia — a key regulatory factor in tumour growth. *Cancer Res.* 47:597–601.

Chaplin, D.J., P.L. Olive, and R.E. Durand. 1987b. Intermittent Blood Flow in a Murine Tumor: Radiobiological Effects1 | Cancer Research | American Association for Cancer Research. *Cancer Res.* 47:597–601.

Chapman, J.D. 1979. Hypoxic sensitizers--implications for radiation therapy. *N. Engl. J. Med.* 301:1429–1432.

Chapman, J.D., E.L. Engelhardt, C.C. Stobbe, R.F. Schneider, and G.E. Hanks. 1998. Measuring hypoxia and predicting tumor radioresistance with nuclear medicine assays. *Radiother. Oncol.* 46:229–237.

Chen, C., N. Pore, A. Behrooz, F. Ismail-Beigi, and A. Maity. 2001. Regulation of glut1 mRNA by hypoxia-inducible factor-1. Interaction between H-ras and hypoxia. *J. Biol. Chem.* 276:9519–9525.

Chen, Q., E.J. Vazquez, S. Moghaddas, C.L. Hoppel, and E.J. Lesnefsky. 2003. Production of Reactive Oxygen Species by Mitochondria: CENTRAL ROLE OF COMPLEX III. *J. Biol. Chem.* 278:36027–36031.

Chen, W., Z. Sun, X.J. Wang, T. Jiang, Z. Huang, D. Fang, and D.D. Zhang. 2009. Direct interaction between Nrf2 and p21Cip1/WAF1 upregulates the Nrf2-mediated antioxidant response. *Mol. Cell*. 34:663.

Cheung, E.C., and K.H. Vousden. 2022. The role of ROS in tumour development and progression. *Nat. Rev. Cancer 2022 225*. 22:280–297.

Chi, J.T., Z. Wang, D.S.A. Nuyten, E.H. Rodriguez, M.E. Schaner, A. Salim, Y. Wang, G.B. Kristensen, Å. Helland, A.L. Børresen-Dale, A. Giaccia, M.T. Longaker, T. Hastie, G.P. Yang, M.J. Van De Vijver, and P.O. Brown. 2006. Gene expression programs in response to hypoxia: cell type specificity and prognostic significance in human cancers. *PLoS Med.* 3:395–409.

Chi, K.L., F.Y. Zhen, D.W. Ho, M.N. Ng, G.C.T. Yeoh, R.T.P. Poon, and T.F. Sheung. 2009. An Akt/hypoxia-inducible factor-1alpha/platelet-derived growth factor-BB autocrine loop mediates hypoxia-induced chemoresistance in liver cancer cells and tumorigenic hepatic progenitor cells. *Clin. Cancer Res.* 15:3462–3471.

Cline, J.M., G.L. Rosner, J.A. Raleigh, and D.E. Thrall. 1997. Quantification of CCI-103F labeling heterogeneity in canine solid tumors. *Int. J. Radiat. Oncol. Biol. Phys.* 37:655–662.

Comerford, K.M. 2002. Hypoxia-inducible factor-1-dependent regulation of the multidrug resistance (MDR1) gene. *Cancer Res*. 62:3387–3394.

Connell, A., P.J. Holliman, M.L. Davies, C.D. Gwenin, S. Weiss, M.B. Pitak, P.N. Horton, S.J. Coles, and G. Cooke. 2014. A study of dye anchoring points in half-squarylium dyes for dye-sensitized solar cells. *J. Mater. Chem. A*. 2:4055–4066.

Corn, P.G., M.S. Ricci, K.A. Scata, A.M. Arsham, M.C. Simon, D.T. Dicker, and W.S. El-Deiry. 2005. Mxi1 is induced by hypoxia in a HIF-1-dependent manner and protects cells from c-Myc-induced apoptosis. *Cancer Biol. Ther.* 4:1285–1294.

Cortese-Krott, M.M., A. Koning, G.G.C. Kuhnle, P. Nagy, C.L. Bianco, A. Pasch, D.A. Wink, J.M. Fukuto, A.A. Jackson, H. Van Goor, K.R. Olson, and M. Feelisch. 2017. The Reactive Species Interactome: Evolutionary Emergence, Biological Significance, and Opportunities for Redox Metabolomics and Personalized Medicine. *Antioxid. Redox Signal.* 27:684.

Curry, J., J. Johnson, P. Tassone, M.D. Vidal, D.W. Menezes, J. Sprandio, M. Mollaee, P. Cotzia, R. Birbe, Z. Lin, K. Gill, E. Duddy, T. Zhan, B. Leiby, M. Reyzer, D. Cognetti, A. Luginbuhl, M. Tuluc, and U. Martinez-Outschoorn. 2017. Metformin effects on head and neck squamous carcinoma microenvironment: Window of opportunity trial. *Laryngoscope*. 127:1808–1815.

D'Autréaux, B., and M.B. Toledano. 2007. ROS as signalling molecules: mechanisms that generate specificity in ROS homeostasis. *Nat. Rev. Mol. Cell Biol. 2007 810*. 8:813–824.

Dalessandro, E. V., H.P. Collin, L.G.L. Guimarães, M.S. Valle, and J.R. Pliego. 2017. Mechanism of the Piperidine-Catalyzed Knoevenagel Condensation Reaction in Methanol: The Role of Iminium and Enolate Ions. *J. Phys. Chem. B*. 121:5300–5307.

van Dam, L., M. Pagès-Gallego, P.E. Polderman, R.M. van Es, B.M.T. Burgering, H.R. Vos, and T.B. Dansen. 2021. The human 2-cys peroxiredoxins form widespread, cysteine-dependent-and isoform-specific protein-protein interactions. *Antioxidants*. 10:627.

Dang, D.T., F. Chen, L.B. Gardner, J.M. Cummins, C. Rago, F. Bunz, S. V. Kantsevoy, and L.H. Dang. 2006. Hypoxia-Inducible Factor-1α Promotes Nonhypoxia-Mediated Proliferation in Colon Cancer Cells and Xenografts. *Cancer Res*. 66:1684–1693.

Deisseroth, A., and A.L. Dounce. 1970. Catalase: Physical and chemical properties, mechanism of catalysis, and physiological role. *Physiol. Rev.* 50:319–375.

Delaney, G., S. Jacob, C. Featherstone, and M. Barton. 2005. The role of radiotherapy in cancer treatment: estimating optimal utilization from a review of evidence-based clinical guidelines. *Cancer*. 104:1129–1137.

Demine, S., P. Renard, and T. Arnould. 2019. Mitochondrial Uncoupling: A Key Controller of Biological Processes in Physiology and Diseases. *Cells*. 8.

Denko, N.C. 2008. Hypoxia, HIF1 and glucose metabolism in the solid tumour. *Nat. Rev. Cancer*. 8:705–713.

Denko, N.C., L.A. Fontana, K.M. Hudson, P.D. Sutphin, S. Raychaudhuri, R. Altman, and A.J. Giaccia. 2003. Investigating hypoxic tumor physiology through gene expression patterns. *Oncogene*. 22:5907–5914.

Descotes, G., and J. Pralyet. 1986. Carbohydrate Research. 148:137–142.

Desideri, E., F. Ciccarone, and M.R. Ciriolo. 2019. Targeting Glutathione Metabolism: Partner in Crime in Anticancer Therapy.

DeVita, V.T. 1978. The evolution of therapeutic research in cancer. *N. Engl. J. Med*. 298:907–910.

DeVita, V.T., and E. Chu. 2008. A history of cancer chemotherapy. *Cancer Res*. 68:8643–8653.

Dewhirst, M.W., and S.R. Birer. 2016. Oxygen-enhanced MRI is a major advance in tumor hypoxia imaging. *Cancer Res*. 76:769–772.

Dewhirst, M.W., and T.W. Secomb. 2017. Transport of drugs from blood vessels to tumour tissue. *Nat. Rev. Cancer*. 17:738–750.

Dias, G.G., A. King, F. De Moliner, M. Vendrell, and E.N. Da Silva Júnior. 2018. Quinone-based fluorophores for imaging biological processes. *Chem. Soc. Rev*. 47:12–27.

Dings, J., J. Meixensberger, A. Jäger, and K. Roosen. 1998. Clinical experience with 118 brain tissue oxygen partial pressure catheter probes. *Neurosurgery*. 43:1082–1094.

Dixon, S.J., K.M. Lemberg, M.R. Lamprecht, R. Skouta, E.M. Zaitsev, C.E. Gleason, D.N. Patel, A.J. Bauer, A.M. Cantley, W.S. Yang, B. Morrison, and B.R. Stockwell. 2012. Ferroptosis: an iron-dependent form of nonapoptotic cell death. *Cell*. 149:1060–1072.

Dong, C., N.J. Zhang, and L.J. Zhang. 2021. Oxidative stress in leukemia and antioxidant treatment. *Chin. Med. J. (Engl)*. 134:1897.

Durand, R.E. 1994. The influence of microenvironmental factors during cancer therapy. *In Vivo*. 8:691–702.

Duranteau, J., N.S. Chandel, A. Kulisz, Z. Shao, and P.T. Schumacker. 1998. Intracellular signaling by reactive oxygen species during hypoxia in

cardiomyocytes. *J. Biol. Chem.* 273:11619–11624.
Egger, G., G. Liang, A. Aparicio, and P.A. Jones. 2004. Epigenetics in human disease and prospects for epigenetic therapy. *Nat. 2004 4296990*. 429:457–463.
Elgrishi, N.N., K.J. Rountree, B.D. Mccarthy, E.S. Rountree, T.T. Eisenhart, and J.L. Dempsey. 2017. A Practical Beginner's Guide to Cyclic Voltammetry.
Elko, E.A., B. Cunniff, D.J. Seward, S.B. Chia, R. Aboushousha, C. Van De Wetering, J. Van Der Velden, A. Manuel, A. Shukla, N.H. Heintz, V. Anathy, A. Van Der Vliet, and Y.M.W. Janssen-Heininger. 2019. Peroxiredoxins and Beyond; Redox Systems Regulating Lung Physiology and Disease. *Antioxid. Redox Signal.* 31:1070.
Elmes, R.B.P. 2016. Bioreductive fluorescent imaging agents: applications to tumour hypoxia. *Chem. Commun.* 52:8935–8956.
Ema, M., S. Taya, N. Yokotani, K. Sogawa, Y. Matsuda, and Y. Fujii-Kuriyama. 1997. A novel bHLH-PAS factor with close sequence similarity to hypoxia-inducible factor 1alpha regulates the VEGF expression and is potentially involved in lung and vascular development. *Proc. Natl. Acad. Sci. U. S. A.* 94:4273–4278.
Epstein, A.C.R., J.M. Gleadle, L.A. McNeill, K.S. Hewitson, J. O'Rourke, D.R. Mole, M. Mukherji, E. Metzen, M.I. Wilson, A. Dhanda, Y.M. Tian, N. Masson, D.L. Hamilton, P. Jaakkola, R. Barstead, J. Hodgkin, P.H. Maxwell, C.W. Pugh, C.J. Schofield, and P.J. Ratcliffe. 2001. C. elegans EGL-9 and mammalian homologs define a family of dioxygenases that regulate HIF by prolyl hydroxylation. *Cell*. 107:43–54.
Eriksson, S., J.R. Prigge, E.A. Talago, E.S.J. Arnér, and E.E. Schmidt. 2015. Dietary methionine can sustain cytosolic redox homeostasis in the mouse liver. *Nat. Commun. 2015 61*. 6:1–9.
Espinosa-Diez, C., V. Miguel, D. Mennerich, T. Kietzmann, P. Sánchez-Pérez, S. Cadenas, and S. Lamas. 2015. Antioxidant responses and cellular adjustments to oxidative stress. *Redox Biol.* 6:183.
Esteban, M.A., M.G.B. Tran, S.K. Harten, P. Hill, M.C. Castellanos, A. Chandra, R. Raval, T.S. O'Brien, and P.H. Maxwell. 2006. Regulation of E-cadherin expression by VHL and hypoxia-inducible factor. *Cancer Res.* 66:3567–3575.
Fandrey, J., J. Schödel, K.U. Eckardt, D.M. Katschinski, and R.H. Wenger. 2019. Now a Nobel gas: oxygen. *Pflugers Arch.* 471:1343–1358.
Fath, M.A., I.M. Ahmad, C.J. Smith, J. Spence, and D.R. Spitz. 2011. Enhancement of carboplatin-mediated lung cancer cell killing by simultaneous disruption of glutathione and thioredoxin metabolism. *Clin. Cancer Res.* 17:6206.
Feldman, D.E., V. Chauhan, and A.C. Koong. 2005. The unfolded protein response: a novel component of the hypoxic stress response in tumors. *Mol. Cancer Res.* 3:597–605.
Ferber, E.C., B. Peck, O. Delpuech, G.P. Bell, P. East, and A. Schulze. 2012. FOXO3a regulates reactive oxygen metabolism by inhibiting mitochondrial gene expression. *Cell Death Differ.* 19:968–979.
Fernández, E., V. Morillo, M. Salvador, A. Santafé, I. Beato, M. Rodríguez, and C. Ferrer. 2021. Hyperbaric oxygen and radiation therapy: a review. *Clin. Transl. Oncol.* 23:1047–1053.
Firth, J.D., B.L. Ebert, and P.J. Ratcliffe. 1995. Hypoxic regulation of lactate dehydrogenase A. Interaction between hypoxia-inducible factor 1 and cAMP response elements. *J. Biol. Chem.* 270:21021–21027.
Flamme, I., T. Fröhlich, M. Von Reutern, A. Kappel, A. Damert, and W. Risau. 1997. HRF,

a putative basic helix-loop-helix-PAS-domain transcription factor is closely related to hypoxia-inducible factor-1 alpha and developmentally expressed in blood vessels. *Mech. Dev.* 63:51–60.

Flannigan, K.L., T.A. Agbor, J.P. Motta, J.G.P. Ferraz, R. Wang, A.G. Buret, and J.L. Wallace. 2015. Proresolution effects of hydrogen sulfide during colitis are mediated through hypoxia-inducible factor-1α. *FASEB J.* 29:1591–1602.

Fleming, I.N., R. Manavaki, P.J. Blower, C. West, K.J. Williams, A.L. Harris, J. Domarkas, S. Lord, C. Baldry, and F.J. Gilbert. 2014. Imaging tumour hypoxia with positron emission tomography. *Br. J. Cancer 2015 1122*. 112:238–250.

Folkman, J. 1990. What is the evidence that tumors are angiogenesis dependent? *J. Natl. Cancer Inst.* 82:4–7.

Forman, H.J., A. Bernardo, and K.J.A. Davies. 2016. What is the concentration of hydrogen peroxide in blood and plasma? *Arch. Biochem. Biophys.* 603:48–53.

Forman, H.J., F. Ursini, and M. Maiorino. 2014. An overview of mechanisms of redox signaling. *J. Mol. Cell. Cardiol.* 73:2–9.

Forman, H.J., and H. Zhang. 2021. Targeting oxidative stress in disease: promise and limitations of antioxidant therapy. *Nat. Rev. Drug Discov.* 20:689–709.

Forneris, F., C. Binda, M.A. Vanoni, A. Mattevi, and E. Battaglioli. 2005. Histone demethylation catalysed by LSD1 is a flavin-dependent oxidative process. *FEBS Lett.* 579:2203–2207.

Forsythe, J.A., B.-H. Jiang, N. V. Iyer, F. Agani, S.W. Leung, R.D. Koos, and G.L. Semenza. 1996. Activation of vascular endothelial growth factor gene transcription by hypoxia-inducible factor 1. *Mol. Cell. Biol.* 16:4604–4613.

Foskolou, I.P., C. Jorgensen, K.B. Leszczynska, M.M. Olcina, H. Tarhonskaya, B. Haisma, V. D'Angiolella, W.K. Myers, C. Domene, E. Flashman, and E.M. Hammond. 2017. Ribonucleotide Reductase Requires Subunit Switching in Hypoxia to Maintain DNA Replication. *Mol. Cell*. 66:206-220.e9.

Frankenberg-Schwager, M., D. Frankenberg, and R. Harbich. 1991. Different oxygen enhancement ratios for induced and unrejoined DNA double- strand breaks in eukaryotic cells. *Radiat. Res.* 128:243–250.

Franovic, A., L. Gunaratnam, K. Smith, I. Robert, D. Patten, and S. Lee. 2007. Translational up-regulation of the EGFR by tumor hypoxia provides a nonmutational explanation for its overexpression in human cancer. *Proc. Natl. Acad. Sci. U. S. A.* 104:13092–13097.

Fukuda, R., H. Zhang, J. whan Kim, L. Shimoda, C. V. Dang, and G.L.L. Semenza. 2007. HIF-1 regulates cytochrome oxidase subunits to optimize efficiency of respiration in hypoxic cells. *Cell*. 129:111–122.

Fulmer, G.R., A.J.M. Miller, N.H. Sherden, H.E. Gottlieb, A. Nudelman, B.M. Stoltz, J.E. Bercaw, and K.I. Goldberg. 2010. NMR chemical shifts of trace impurities: Common laboratory solvents, organics, and gases in deuterated solvents relevant to the organometallic chemist. *Organometallics*. 29:2176–2179.

Fyles, A.W., M. Milosevic, M. Pintilie, and R.P. Hill. 1998. Cervix cancer oxygenation measured following external radiation therapy. *Int. J. Radiat. Oncol. Biol. Phys.* 42:751–753.

Gal, K. Le, M.X. Ibrahim, C. Wiel, V.I. Sayin, M.K. Akula, C. Karlsson, M.G. Dalin, L.M. Akyürek, P. Lindahl, J. Nilsson, and M.O. Bergo. 2015. Antioxidants can increase melanoma metastasis in mice. *Sci. Transl. Med.* 7.

Le Gal, K., E.E. Schmidt, V.I. Sayin, L. Gal, and K.; Schmidt. 2021. Cellular Redox Homeostasis Citation.

Gambardella, V., N. Tarazona, J.M. Cejalvo, P. Lombardi, M. Huerta, S. Roselló, T. Fleitas, D. Roda, and A. Cervantes. 2020. Personalized Medicine: Recent Progress in Cancer Therapy. *Cancers 2020, Vol. 12, Page 1009*. 12:1009.

Gao, P., W. Pan, N. Li, and B. Tang. 2019. Fluorescent probes for organelle-targeted bioactive species imaging.

Gao, P., H. Zhang, R. Dinavahi, F. Li, Y. Xiang, V. Raman, Z.M. Bhujwalla, D.W. Felsher, L. Cheng, J. Pevsner, L.A. Lee, G.L. Semenza, and C. V. Dang. 2007. HIF-dependent Anti-tumorigenic Effect of Anti-oxidants In Vivo. *Cancer Cell*. 12:230.

Garrido, C., L. Galluzzi, M. Brunet, P.E. Puig, C. Didelot, and G. Kroemer. 2006. Mechanisms of cytochrome c release from mitochondria. *Cell Death Differ. 2006 139*. 13:1423–1433.

Gatenby, R.A., H.B. Kessler, J.S. Rosenblum, L.R. Coia, P.J. Moldofsky, W.H. Hartz, and G.J. Broder. 1988. Oxygen distribution in squamous cell carcinoma metastases and its relationship to outcome of radiation therapy. *Int. J. Radiat. Oncol. Biol. Phys.* 14:831–838.

Geng, Y., Z. Wang, J. Zhou, M. Zhu, J. Liu, and T.D. James. 2023. Recent progress in the development of fluorescent probes for imaging pathological oxidative stress. *Chem. Soc. Rev.* 52:3873–3926.

Gerald, D., E. Berra, Y.M. Frapart, D.A. Chan, A.J. Giaccia, D. Mansuy, J. Pouysségur, M. Yaniv, and F. Mechta-Grigoriou. 2004. JunD reduces tumor angiogenesis by protecting cells from oxidative stress. *Cell*. 118:781–794.

Ghareeb, H., and N. Metanis. 2020. The Thioredoxin System: A Promising Target for Cancer Drug Development. *Chem. – A Eur. J.* 26:10175–10184.

Ghasemi, M., T. Turnbull, S. Sebastian, and I. Kempson. 2021. The mtt assay: Utility, limitations, pitfalls, and interpretation in bulk and single-cell analysis. *Int. J. Mol. Sci.* 22.

Giaccia, A.J. 1996. Hypoxic Stress Proteins: Survival of the Fittest. *Semin. Radiat. Oncol.* 6:46–58.

Giannoni, E., F. Buricchi, G. Raugei, G. Ramponi, and P. Chiarugi. 2005. Intracellular Reactive Oxygen Species Activate Src Tyrosine Kinase during Cell Adhesion and Anchorage-Dependent Cell Growth. *Mol. Cell. Biol.* 25:6391.

Giatromanolaki, A., M.I. Koukourakis, E. Sivridis, H. Turley, K. Talks, F. Pezzella, K.C. Gatter, and A.L. Harris. 2001. Relation of hypoxia inducible factor 1α and 2α in operable non-small cell lung cancer to angiogenic/molecular profile of tumours and survival. *Br. J. Cancer*. 85:881.

Glasauer, A., and N.S. Chandel. 2013. ROS. *Curr. Biol.* 23:R100–R102.

Glasauer, A., and N.S. Chandel. 2014. Targeting antioxidants for cancer therapy. *Biochem. Pharmacol.* 92:90–101.

Gomes, P., S.D. Viana, S. Nunes, A.P. Rolo, C.M. Palmeira, and F. Reis. 2020. The yin and yang faces of the mitochondrial deacetylase sirtuin 3 in age-related disorders. *Ageing Res. Rev.* 57.

Gorrini, C., I.S. Harris, and T.W. Mak. 2013. Modulation of oxidative stress as an anticancer strategy. *Nat. Rev. Drug Discov. 2013 1212*. 12:931–947.

Gottlieb, E., and I.P.M. Tomlinson. 2005. Mitochondrial tumour suppressors: a genetic and biochemical update. *Nat. Rev. Cancer*. 5:857–866.

Gozzelino, R., V. Jeney, and M.P. Soares. 2010. Mechanisms of cell protection by heme oxygenase-1. *Annu. Rev. Pharmacol. Toxicol.* 50:323–354.

Grammel, M., and H.C. Hang. 2013. Chemical reporters for biological discovery. *Nat. Chem. Biol.* 9:475–484.

Graven, K.K., Q. Yu, D. Pan, J.S. Roncarati, and H.W. Farber. 1999. Identification of an oxygen responsive enhancer element in the glyceraldehyde-3-phosphate dehydrogenase gene. *Biochim. Biophys. Acta*. 1447:208–218.

Gray, L.H., A.D. Conger, M. Ebert, S. Hornsey, and O.C. Scott. 1953. The Concentration of Oxygen Dissolved in Tissues at the Time of Irradiation as a Factor in Radiotherapy. *Br. J. Radiol.* 26:638–648.

Grimes, D.R., C. Kelly, K. Bloch, and M. Partridge. 2014. A method for estimating the oxygen consumption rate in multicellular tumour spheroids. *J. R. Soc. Interface*. 11.

Groenman, F., M. Rutter, I. Caniggia, D. Tibboel, and M. Post. 2007. Hypoxia-inducible factors in the first trimester human lung. *J. Histochem. Cytochem.* 55:355–363.

Grollman, A.P., and M. Moriya. 1993. Mutagenesis by 8-oxoguanine: an enemy within. *Trends Genet.* 9:246–249.

Gross, M.W., U. Karbach, K. Groebe, A.J. Franko, and W. Mueller-Klieser. 1995. Calibration of misonidazole labeling by simultaneous measurement of oxygen tension and labeling density in multicellular spheroids. *Int. J. Cancer*. 61:567–573.

Grover, T.R., T.M. Asikainen, J.P. Kinsella, S.H. Abman, and C.W. White. 2007. Hypoxia-inducible factors HIF-1alpha and HIF-2alpha are decreased in an experimental model of severe respiratory distress syndrome in preterm lambs. *Am. J. Physiol. Lung Cell. Mol. Physiol.* 292.

Guillin, O.M., C. Vindry, T. Ohlmann, and L. Chavatte. 2019. Selenium, Selenoproteins and Viral Infection. *Nutrients*. 11.

Guisán-Ceinos, S., A. R. Rivero, F. Romeo-Gella, S. Simón-Fuente, S. Gómez-Pastor, N. Calvo, A.H. Orrego, J.M. Guisán, I. Corral, F. Sanz-Rodriguez, and M. Ribagorda. 2022. Turn-on Fluorescent Biosensors for Imaging Hypoxia-like Conditions in Living Cells. *J. Am. Chem. Soc.* 144:8185–8193.

Guise, C.P., A.M. Mowday, A. Ashoorzadeh, R. Yuan, W.H. Lin, D.H. Wu, J.B. Smaill, A. V. Patterson, and K. Ding. 2014. Bioreductive prodrugs as cancer therapeutics: targeting tumor hypoxia. *Chin. J. Cancer*. 33:80.

Guo, K., G. Searfoss, D. Krolikowski, M. Pagnoni, C. Franks, K. Clark, K.T. Yu, M. Jaye, and Y. Ivashchenko. 2001. Hypoxia induces the expression of the pro-apoptotic gene BNIP3. *Cell Death Differ. 2001 84*. 8:367–376.

Guzy, R.D., B. Hoyos, E. Robin, H. Chen, L. Liu, K.D. Mansfield, M.C. Simon, U. Hammerling, and P.T. Schumacker. 2005. Mitochondrial complex III is required for hypoxia-induced ROS production and cellular oxygen sensing. *Cell Metab.* 1:401–408.

Guzy, R.D., and P.T. Schumacker. 2006. Oxygen sensing by mitochondria at complex III: the paradox of increased reactive oxygen species during hypoxia. *Exp. Physiol.* 91:807–819.

Hadad, S., T. Iwamoto, L. Jordan, C. Purdie, S. Bray, L. Baker, G. Jellema, S. Deharo, D.G. Hardie, L. Pusztai, S. Moulder-Thompson, J.A. Dewar, and A.M. Thompson. 2011. Evidence for biological effects of metformin in operable breast cancer: A pre-operative, window-of-opportunity, randomized trial. *Breast Cancer Res. Treat.*

128:783–794.
Haddad, J.J.E., R.E. Olver, and S.C. Land. 2000. Antioxidant/pro-oxidant equilibrium regulates HIF-1alpha and NF-kappa B redox sensitivity. Evidence for inhibition by glutathione oxidation in alveolar epithelial cells. *J. Biol. Chem.* 275:21130–21139.
Hagen, T., C.T. Taylor, F. Lam, and S. Moncada. 2003. Redistribution of intracellular oxygen in hypoxia by nitric oxide: effect on HIF1alpha. *Science*. 302:1975–1978.
Hall, E.J., and A.J. Giaccia. 2018. Radiobiology for the Radiologist.
Hamanaka, R.B., S.E. Weinberg, C.R. Reczek, and N.S. Chandel. 2016. The Mitochondrial Respiratory Chain Is Required for Organismal Adaptation to Hypoxia. *Cell Rep.* 15:451–459.
Hamilton, D., H.W. Jian, and G. Batist. 2007. Structure-based identification of novel human gamma-glutamylcysteine synthetase inhibitors. *Mol. Pharmacol.* 71:1140–1147.
Hammond, E.M., M.C. Asselin, D. Forster, J.P.B. O'Connor, J.M. Senra, and K.J. Williams. 2014. The Meaning, Measurement and Modification of Hypoxia in the Laboratory and the Clinic. *Clin. Oncol.* 26:277–288.
Hammond, E.M., M.J. Dorie, and A.J. Giaccia. 2003. ATR/ATM targets are phosphorylated by ATR in response to hypoxia and ATM in response to reoxygenation. *J. Biol. Chem.* 278:12207–12213.
Han, D., F. Antunes, R. Canali, D. Rettori, and E. Cadenas. 2003. Voltage-dependent anion channels control the release of the superoxide anion from mitochondria to cytosol. *J. Biol. Chem.* 278:5557–5563.
Han, Y.H., S.Z. Kim, S.H. Kim, and W.H. Park. 2008. Arsenic trioxide inhibits the growth of Calu-6 cells via inducing a G2 arrest of the cell cycle and apoptosis accompanied with the depletion of GSH. *Cancer Lett.* 270:40–55.
Hanahan, D. 2022. Hallmarks of Cancer: New Dimensions. *Cancer Discov.* 12:31–46.
Hanahan, D., and R.A. Weinberg. 2000. The Hallmarks of Cancer Review evolve progressively from normalcy via a series of pre. *Cell*. 100:57–70.
Hanahan, D., and R.A. Weinberg. 2011. Hallmarks of cancer: The next generation. *Cell*. 144:646–674.
Hankinson, O. 1995. The aryl hydrocarbon receptor complex. *Annu. Rev. Pharmacol. Toxicol.* 35:307–340.
Hara, S., J. Hamada, C. Kobayashi, Y. Kondo, and N. Imura. 2001. Expression and Characterization of Hypoxia-Inducible Factor (HIF)-3α in Human Kidney: Suppression of HIF-Mediated Gene Expression by HIF-3α. *Biochem. Biophys. Res. Commun.* 287:808–813.
El Harane, S., B. Zidi, N. El Harane, K.H. Krause, T. Matthes, and O. Preynat-Seauve. 2023. Cancer Spheroids and Organoids as Novel Tools for Research and Therapy: State of the Art and Challenges to Guide Precision Medicine. *Cells*. 12.
Harris, A.L. 2002. Hypoxia - A key regulatory factor in tumour growth. *Nat. Rev. Cancer*. 2:38–47.
Harris, B.H.L., A. Barberis, C.M.L. West, and F.M. Buffa. 2015a. Gene Expression Signatures as Biomarkers of Tumour Hypoxia. *Clin. Oncol.* 27:547–560.
Harris, I.S., and G.M. DeNicola. 2020. The Complex Interplay between Antioxidants and ROS in Cancer. *Trends Cell Biol.* 30:440–451.
Harris, I.S., A.E. Treloar, S. Inoue, M. Sasaki, C. Gorrini, K.C. Lee, K.Y. Yung, D. Brenner, C.B. Knobbe-Thomsen, M.A. Cox, A. Elia, T. Berger, D.W. Cescon, A. Adeoye, A.

Brüstle, S.D. Molyneux, J.M. Mason, W.Y. Li, K. Yamamoto, A. Wakeham, H.K. Berman, R. Khokha, S.J. Done, T.J. Kavanagh, C.W. Lam, and T.W. Mak. 2015b. Glutathione and Thioredoxin Antioxidant Pathways Synergize to Drive Cancer Initiation and Progression. *Cancer Cell*. 27:211–222.

Harrison, J.S., P. Rameshwar, V. Chang, and P. Bandari. 2002. Oxygen saturation in the bone marrow of healthy volunteers. *Blood*. 99:394.

Hasan, A.A., E. Kalinina, V. Tatarskiy, and A. Shtil. 2022. The Thioredoxin System of Mammalian Cells and Its Modulators. *Biomed. 2022, Vol. 10, Page 1757*. 10:1757.

Hay, M.P., K.O. Hicks, and J. Wang. 2014. Hypoxia-directed drug strategies to target the tumor microenvironment. *Adv. Exp. Med. Biol.* 772:111–145.

Hayes, J.D., and A.T. Dinkova-Kostova. 2014. The Nrf2 regulatory network provides an interface between redox and intermediary metabolism. *Trends Biochem. Sci.* 39:199–218.

Hayes, J.D., A.T. Dinkova-Kostova, and K.D. Tew. 2020. Oxidative Stress in Cancer. *Cancer Cell*. 38:167–197.

Hayes, J.D., K. Ebisine, R.S. Sharma, S. Chowdhry, A.T. Dinkova-Kostova, and C. Sutherland. 2016. Regulation of the CNC-bZIP transcription factor Nrf2 by Keap1 and the axis between GSK-3 and β-TrCP. *Curr. Opin. Toxicol.* 1:92–103.

He, L., T. He, S. Farrar, L. Ji, T. Liu, and X. Ma. 2017. Antioxidants Maintain Cellular Redox Homeostasis by Elimination of Reactive Oxygen Species. *Cell. Physiol. Biochem.* 44:532–553.

Heidbreder, M., F. Fröhlich, O. Jöhren, A. Dendorfer, F. Qadri, and P. Dominiak. 2003. Hypoxia rapidly activates HIF-3alpha mRNA expression. *FASEB J.* 17:1–19.

Heinzelmanna, S., and G. Bauer. 2010. Multiple protective functions of catalase against intercellular apoptosis-inducing ROS signaling of human tumor cells. *Biol. Chem.* 391:675–693.

Helmlinger, G., F. Yuan, M. Dellian, and R.K. Jain. 1997. Interstitial pH and pO2 gradients in solid tumors in vivo: high-resolution measurements reveal a lack of correlation. *Nat. Med.* 3:177–182.

Herst, P.M., and M. V. Berridge. 2007. Cell surface oxygen consumption: a major contributor to cellular oxygen consumption in glycolytic cancer cell lines. *Biochim. Biophys. Acta*. 1767:170–177.

Hewitson, K.S., B.M.R. Liénard, M.A. McDonough, I.J. Clifton, D. Butler, A.S. Soares, N.J. Oldham, L.A. McNeill, and C.J. Schofield. 2007. Structural and mechanistic studies on the inhibition of the hypoxia-inducible transcription factor hydroxylases by tricarboxylic acid cycle intermediates. *J. Biol. Chem.* 282:3293–3301.

Hirose, K., M. Morita, M. Ema, J. Mimura, H. Hamada, H. Fujii, Y. Saijo, O. Gotoh, K. Sogawa, and Y. Fujii-Kuriyama. 1996. cDNA cloning and tissue-specific expression of a novel basic helix-loop-helix/PAS factor (Arnt2) with close sequence similarity to the aryl hydrocarbon receptor nuclear translocator (Arnt). *Mol. Cell. Biol.* 16:1706–1713.

Höckel, M., K. Schienger, B. Aral, M. Mitze, U. Schäffer, and P. Vaupel. 1996a. Association between Tumor Hypoxia and Malignant Progression in Advanced Cancer of the Uterine Cervix1 | Cancer Research | American Association for Cancer Research. *Cancer Res.* 56:4509–4515.

Höckel, M., K. Schlenger, B. Aral, M. Mitze, U. Schäffer, and P. Vaupel. 1996b. Association between tumor hypoxia and malignant progression in advanced

cancer of the uterine cervix. *Cancer Res*.
Hoffman, E.C., H. Reyes, F.F. Chu, F. Sander, L.H. Conley, B.A. Brooks, and O. Hankinson. 1991. Cloning of a factor required for activity of the Ah (dioxin) receptor. *Science*. 252:954–958.
Hogenesch, J.B., Y.Z. Gu, S. Jain, and C.A. Bradfield. 1998. The basic-helix-loop-helix-PAS orphan MOP3 forms transcriptionally active complexes with circadian and hypoxia factors. *Proc. Natl. Acad. Sci. U. S. A.* 95:5474–5479.
Hogenesch, J.B., Y.Z. Gu, S.M. Moran, K. Shimomura, L.A. Radcliffe, J.S. Takahashi, and C.A. Bradfield. 2000. The basic helix-loop-helix-PAS protein MOP9 is a brain-specific heterodimeric partner of circadian and hypoxia factors. *J. Neurosci.* 20.
Holmström, K.M., and T. Finkel. 2014. Cellular mechanisms and physiological consequences of redox-dependent signalling. *Nat. Rev. Mol. Cell Biol. 2014 156*. 15:411–421.
Horsman, M.R., L.S. Mortensen, J.B. Petersen, M. Busk, and J. Overgaard. 2012. Imaging hypoxia to improve radiotherapy outcome. *Nat. Rev. Clin. Oncol.* 9:674–687.
Horsman, M.R., and P. Vaupel. 2016. Pathophysiological basis for the formation of the tumor microenvironment. *Front. Oncol.* 6:182504.
Huang, B., A. Desai, S. Tang, T.P. Thomas, and J.R. Baker. 2010. The Synthesis of a c(RGDyK) Targeted SN38 Prodrug with an Indolequinone Structure for Bioreductive Drug Release. *Org. Lett.* 12:1384–1387.
Huang, Y., J. Fan, Y. Li, S. Fu, Y. Chen, and J. Wu. 2021. Imaging of Tumor Hypoxia With Radionuclide-Labeled Tracers for PET. *Front. Oncol.* 11.
Hunter, F.W., B.G. Wouters, and W.R. Wilson. 2016. Hypoxia-activated prodrugs: paths forward in the era of personalised medicine. *Br. J. Cancer 2016 11410*. 114:1071–1077.
Ikeda, M., and M. Nomura. 1997. cDNA cloning and tissue-specific expression of a novel basic helix-loop-helix/PAS protein (BMAL1) and identification of alternatively spliced variants with alternative translation initiation site usage. *Biochem. Biophys. Res. Commun.* 233:258–264.
Iliopoulos, O., A.P. Levy, C. Jiang, W.G. Kaelin, and M.A. Goldberg. 1996. Negative regulation of hypoxia-inducible genes by the von Hippel-Lindau protein. *Proc. Natl. Acad. Sci. U. S. A.* 93:10595–10599.
Ioannou, M., R. Papamichali, E. Kouvaras, I. Mylonis, D. Vageli, T. Kerenidou, S. Barbanis, A. Daponte, G. Simos, K. Gourgoulianis, and G.K. Koukoulis. 2009. Hypoxia inducible factor-1 alpha and vascular endothelial growth factor in biopsies of small cell lung carcinoma. *Lung*. 187:321–329.
Iqbal, H., and Q. Pan. 2016. Image guided surgery in the management of head and neck cancer. *Oral Oncol.* 57:32–39.
Ivan, M., K. Kondo, H. Yang, W. Kim, J. Valiando, M. Ohh, A. Salic, J.M. Asara, W.S. Lane, and J. Kaelin. 2001. HIFalpha targeted for VHL-mediated destruction by proline hydroxylation: implications for O2 sensing. *Science*. 292:464–468.
Iyer, N. V., L.E. Kotch, F. Agani, S.W. Leung, E. Laughner, R.H. Wenger, M. Gassmann, J.D. Gearhart, A.M. Lawler, A.Y. Yu, and G.L. Semenza. 1998a. Cellular and developmental control of O2 homeostasis by hypoxia-inducible factor 1 alpha. *Genes Dev.* 12:149–162.
Iyer, N. V., S.W. Leung, and G.L. Semenza. 1998b. The human hypoxia-inducible factor 1α gene: HIF1A structure and evolutionary conservation. *Genomics*. 52:159–165.

Jaakkola, P., D.R. Mole, Y.M. Tian, M.I. Wilson, J. Gielbert, S.J. Gaskell, A. Von Kriegsheim, H.F. Hebestreit, M. Mukherji, C.J. Schofield, P.H. Maxwell, C.W. Pugh, and P.J. Ratcliffe. 2001. Targeting of HIF-alpha to the von Hippel-Lindau ubiquitylation complex by O2-regulated prolyl hydroxylation. *Science*. 292:468–472.

Jacoby, J.J., B. Erez, M. V. Korshunova, R.R. Williams, K. Furutani, O. Takahashi, L. Kirkpatrick, S.M. Lippman, G. Powis, M.S. O'Reilly, and R.S. Herbst. 2010. Treatment with HIF-1alpha antagonist PX-478 inhibits progression and spread of orthotopic human small cell lung cancer and lung adenocarcinoma in mice. *J. Thorac. Oncol.* 5:940–949.

Janssens, G.O., S.E. Rademakers, C.H. Terhaard, P.A. Doornaert, H.P. Bijl, P. Den Van Ende, A. Chin, H.A. Marres, R. De Bree, A.J. Van Der Kogel, I.J. Hoogsteen, J. Bussink, P.N. Span, and J.H. Kaanders. 2012. Accelerated radiotherapy with carbogen and nicotinamide for laryngeal cancer: results of a phase III randomized trial. *J. Clin. Oncol.* 30:1777–1783.

Jena, P., and Q. Sun. 2018. Super Atomic Clusters: Design Rules and Potential for Building Blocks of Materials. *Chem. Rev.* 118:5755–5870.

Ji, X., H. Wang, J. Zhu, L. Zhu, H. Pan, W. Li, Y. Zhou, Z. Cong, F. Yan, and S. Chen. 2014. Knockdown of Nrf2 suppresses glioblastoma angiogenesis by inhibiting hypoxia-induced activation of HIF-1α. *Int. J. cancer*. 135:574–584.

Jiang, B.H., E. Rue, G.L. Wang, R. Roe, and G.L. Semenza. 1996a. Dimerization, DNA binding, and transactivation properties of hypoxia-inducible factor 1. *J. Biol. Chem.* 271:17771–17778.

Jiang, B.H., G.L. Semenza, C. Bauer, and H.H. Marti. 1996b. Hypoxia-inducible factor 1 levels vary exponentially over a physiologically relevant range of O2 tension. *Am. J. Physiol.* 271.

Jiang, H., J. Zuo, B. Li, R. Chen, K. Luo, X. Xiang, S. Lu, C. Huang, L. Liu, J. Tang, and F. Gao. 2023. Drug-induced oxidative stress in cancer treatments: Angel or devil? *Redox Biol.* 63:102754.

Jin, R., C. Zeng, M. Zhou, and Y. Chen. 2016. Atomically Precise Colloidal Metal Nanoclusters and Nanoparticles: Fundamentals and Opportunities. *Chem. Rev.* 116:10346–10413.

Jin, X., L. Gong, Y. Peng, L. Li, and G. Liu. 2021. Enhancer-bound Nrf2 licenses HIF-1α transcription under hypoxia to promote cisplatin resistance in hepatocellular carcinoma cells. *Aging (Albany NY)*. 13:364.

Ju, H.Q., J.F. Lin, T. Tian, D. Xie, and R.H. Xu. 2020. NADPH homeostasis in cancer: functions, mechanisms and therapeutic implications. *Signal Transduct. Target. Ther. 2020 51*. 5:1–12.

Jung, M.E., and J.A. Hagenah. 1987. Synthetic Approach to Aklavinone Using 2-Oxo-2H-pyran-5-carboxylate (Coumalate) Intermediates. *J. Org. Chem.* 52:1889–1902.

Kaelin, W.G., and E.R. Maher. 1998. The VHL tumour-suppressor gene paradigm. *Trends Genet.* 14:423–426.

Kaelin, W.G., and P.J. Ratcliffe. 2008. Oxygen Sensing by Metazoans: The Central Role of the HIF Hydroxylase Pathway. *Mol. Cell*. 30:393–402.

Kalinsky, K., K.D. Crew, S. Refice, T. Xiao, A. Wang, S.M. Feldman, B. Taback, A. Ahmad, S. Cremers, H. Hibshoosh, M. Maurer, and D.L. Hershman. 2014. Presurgical Trial of Metformin in Overweight and Obese Patients with Newly Diagnosed Breast

Cancer. *Cancer Invest.* 32:150–157.
Karlenius, T.C., and K.F. Tonissen. 2010. Thioredoxin and Cancer: A Role for Thioredoxin in all States of Tumor Oxygenation. *Cancers (Basel).* 2:209.
Kciuk, M., A. Gielecí Nska, S. Mujwar, D. Kołat, Z. Kałuzí Nska-Kołat, I. Celik, and R. Kontek. 2023. Doxorubicin-An Agent with Multiple Mechanisms of Anticancer Activity.
Keating, J., J. Tchou, O. Okusanya, C. Fisher, R. Batiste, J. Jiang, G. Kennedy, S. Nie, and S. Singhal. 2016. Identification of breast cancer margins using intraoperative near-infrared imaging. *J. Surg. Oncol.* 113:508–514.
Kelly, C.J., K. Hussien, E. Fokas, P. Kannan, R.J. Shipley, T.M. Ashton, M. Stratford, N. Pearson, and R.J. Muschel. 2014. Regulation of O2 consumption by the PI3K and mTOR pathways contributes to tumor hypoxia. *Radiother. Oncol.* 111:72–80.
Kennedy, L., J.K. Sandhu, M.E. Harper, and M. Cuperlovic-culf. 2020. Role of Glutathione in Cancer: From Mechanisms to Therapies. *Biomolecules*. 10:1–27.
Kery, M., and I. Papandreou. 2020. Emerging strategies to target cancer metabolism and improve radiation therapy outcomes. *Br. J. Radiol.* 93.
Keyer, K., and J.A. Imlay. 1996. Superoxide accelerates DNA damage by elevating free-iron levels. *Proc. Natl. Acad. Sci. U. S. A.* 93:13635–13640.
Khramtsov, V. V, and R.J. Gillies. Janus-Faced Tumor Microenvironment and Redox.
Kierans, S.J., and C.T. Taylor. 2021. Regulation of glycolysis by the hypoxia-inducible factor (HIF): implications for cellular physiology. *J. Physiol.* 599:23–37.
Kim, J.W., I. Tchernyshyov, G.L. Semenza, and C. V. Dang. 2006. HIF-1-mediated expression of pyruvate dehydrogenase kinase: a metabolic switch required for cellular adaptation to hypoxia. *Cell Metab.* 3:177–185.
Kim, T.H., E.G. Hur, S.J. Kang, J.A. Kim, D. Thapa, Y. Mie Lee, S.K. Ku, Y. Jung, and M.K. Kwak. 2011. NRF2 blockade suppresses colon tumor angiogenesis by inhibiting hypoxia-induced activation of HIF-1α. *Cancer Res.* 71:2260–2275.
Kim, W.Y., S.H. Oh, J.K. Woo, W.K. Hong, and H.Y. Lee. 2009. Targeting Heat Shock Protein 90 Overrides the Resistance of Lung Cancer Cells by Blocking Radiation-induced Stabilization of Hypoxia-inducible Factor 1α. *Cancer Res.* 69:1624.
Kimura, H., R.D. Braun, E.T. Ong, R. Hsu, T.W. Secomb, D. Papahadjopoulos, K. Hong, and M.W. Dewhirst. 1996. Fluctuations in red cell flux in tumor microvessels can lead to transient hypoxia and reoxygenation in tumor parenchyma. *Cancer Res.* 56:5522–5528.
Kincaid, B., and E. Bossy-Wetzel. 2013. Forever young: SIRT3 a shield against mitochondrial meltdown, aging, and neurodegeneration. *Front. Aging Neurosci.* 5.
Kirkpatrick, D.L., and G. Powis. 2017. Clinically Evaluated Cancer Drugs Inhibiting Redox Signaling. *Antioxid. Redox Signal.* 26:262.
Kitahara, Y., S. Nakahara, R. Numata, and A. Kubo. 1985. Synthesis of 4,7-Indolequinones. The Oxidative Demethylation of 4,7-Dimethoxyindoles with Ceric Ammonium Nitrate. *Chem. Pharm. Bull.* 33:2122–2128.
Kitson, S.J., Z. Maskell, V.N. Sivalingam, J.L. Allen, S. Ali, S. Burns, K. Gilmour, R. Latheef, R.J. Slade, P.W. Pemberton, J. Shaw, W. David Ryder, H.C. Kitchener, and E.J. Crosbie. 2019. PRE-surgical metformin in uterine malignancy (PREMIUM): A multi-center, randomized double-blind, placebo-controlled phase III trial. *Clin. Cancer Res.* 25:2424–2432.
Kiyose, K., K. Hanaoka, D. Oushiki, T. Nakamura, M. Kajimura, M. Suematsu, H.

Nishimatsu, T. Yamane, T. Terai, Y. Hirata, and T. Nagano. 2010. Hypoxia-sensitive fluorescent probes for in vivo real-time fluorescence imaging of acute ischemia. *J. Am. Chem. Soc*. 132:15846–15848.

Koivunen, P., M. Hirsilä, A.M. Remes, I.E. Hassinen, K.I. Kivirikko, and J. Myllyharju. 2007. Inhibition of hypoxia-inducible factor (HIF) hydroxylases by citric acid cycle intermediates: possible links between cell metabolism and stabilization of HIF. *J. Biol. Chem*. 282:4524–4532.

Komatsu, H., H. Harada, K. Tanabe, M. Hiraoka, and S.I. Nishimoto. 2010. Indolequinone-rhodol conjugate as a fluorescent probe for hypoxic cells: enzymatic activation and fluorescence properties. *Medchemcomm*. 1:50–53.

Koppenol, W.H., P.L. Bounds, and C. V. Dang. 2011. Otto Warburg's contributions to current concepts of cancer metabolism. *Nat. Rev. Cancer*. 11:325–337.

Koshikawa, N., J.I. Hayashi, A. Nakagawara, and K. Takenaga. 2009. Reactive oxygen species-generating mitochondrial DNA mutation up-regulates hypoxia-inducible factor-1alpha gene transcription via phosphatidylinositol 3-kinase-Akt/protein kinase C/histone deacetylase pathway. *J. Biol. Chem*. 284:33185–33194.

Koumenis, C., and B.G. Wouters. 2006. Subject Review "'Translating'" Tumor Hypoxia: Unfolded Protein Response (UPR)-Dependent and UPR-Independent Pathways. *Mol Cancer Res*. 4:423–459.

Krishnamachary, B., and G.L. Semenza. 2007. Analysis of hypoxia-inducible factor 1alpha expression and its effects on invasion and metastasis. *Methods Enzymol*. 435:347–354.

Krishnamachary, B., D. Zagzag, H. Nagasawa, K. Rainey, H. Okuyama, J.H. Baek, and G.L. Semenza. 2006. Hypoxia-inducible factor-1-dependent repression of E-cadherin in von Hippel-Lindau tumor suppressor-null renal cell carcinoma mediated by TCF3, ZFHX1A, and ZFHX1B. *Cancer Res*. 66:2725–2731.

Kulshreshtha, R., M. Ferracin, S.E. Wojcik, R. Garzon, H. Alder, F.J. Agosto-Perez, R. Davuluri, C.-G. Liu, C.M. Croce, M. Negrini, G.A. Calin, and M. Ivan. 2007. A microRNA signature of hypoxia. *Mol. Cell. Biol*. 27:1859–1867.

Lacher, S.E., D.C. Levings, S. Freeman, and M. Slattery. 2018. Identification of a functional antioxidant response element at the HIF1A locus. *Redox Biol*. 19:401.

Laurieri, N., J.E. Egleton, A. Varney, C.C. Thinnes, C.E. Quevedo, P.T. Seden, S. Thompson, F. Rodrigues-Lima, J. Dairou, J.M. Dupret, A.J. Russell, and E. Sim. 2013. A Novel Color Change Mechanism for Breast Cancer Biomarker Detection: Naphthoquinones as Specific Ligands of Human Arylamine N-Acetyltransferase 1. *PLoS One*. 8.

Le, Q.T., E. Chen, A. Salim, H. Cao, C.S. Kong, R. Whyte, J. Donington, W. Cannon, H. Wakelee, R. Tibshirani, J.D. Mitchell, D. Richardson, K.J. O'Byrne, A.C. Koong, and A.J. Giaccia. 2006. An evaluation of tumor oxygenation and gene expression in patients with early stage non-small cell lung cancers. *Clin. Cancer Res*. 12:1507–1514.

Le, Q.T., and D. Courter. 2008. Clinical Biomarkers for Hypoxia Targeting. *Cancer Metastasis Rev*. 27:351.

Lee, C.C., C.Y. Wu, and H.Y. Yang. 2020a. Discoveries of how cells sense oxygen win the 2019 Nobel Prize in Physiology or medicine. *Biomed. J*. 43:434.

Lee, G., H.S. Won, Y.M. Lee, J.W. Choi, T.I. Oh, J.H. Jang, D.K. Choi, B.O. Lim, Y.J. Kim, J.W. Park, P. Puigserver, and J.H. Lim. 2016. Oxidative Dimerization of PHD2 is

Responsible for its Inactivation and Contributes to Metabolic Reprogramming via HIF-1α Activation. *Sci. Reports 2016 61*. 6:1–12.

Lee, M.K., J. Williams, R.J. Twieg, J. Rao, and W.E. Moerner. 2012. Enzymatic activation of nitro-aryl fluorogens in live bacterial cells for enzymatic turnover-activated localization microscopy. *Chem. Sci.* 4:220–225.

Lee, P., N.S. Chandel, and M.C. Simon. 2020b. Cellular adaptation to hypoxia through hypoxia inducible factors and beyond. *Nat. Rev. Mol. Cell Biol.* 21:268–283.

Lee, S., S.M. Kim, and R.T. Lee. 2013. Thioredoxin and Thioredoxin Target Proteins: From Molecular Mechanisms to Functional Significance. *Antioxid. Redox Signal.* 18:1165.

Lee, S.R., K.S. Yang, J. Kwon, C. Lee, W. Jeong, and S.G. Rhee. 2002. Reversible inactivation of the tumor suppressor PTEN by H2O2. *J. Biol. Chem.* 277:20336–20342.

Lee, S.T., and A.M. Scott. 2007. Hypoxia positron emission tomography imaging with 18f-fluoromisonidazole. *Semin. Nucl. Med.* 37:451–461.

Li, Y., Y. Sun, J. Li, Q. Su, W. Yuan, Y. Dai, C. Han, Q. Wang, W. Feng, and F. Li. 2015. Ultrasensitive near-infrared fluorescence-enhanced probe for in vivo nitroreductase imaging. *J. Am. Chem. Soc.* 137:6407–6416.

Liao, D., and R.S. Johnson. 2007. Hypoxia: a key regulator of angiogenesis in cancer. *Cancer Metastasis Rev.* 26:281–290.

Liapis, V., A. Labrinidis, I. Zinonos, S. Hay, V. Ponomarev, V. Panagopoulos, M. DeNichilo, W. Ingman, G.J. Atkins, D.M. Findlay, A.C.W. Zannettino, and A. Evdokiou. 2015. HYPOXIA-ACTIVATED PRO-DRUG TH-302 EXHIBITS POTENT TUMOUR SUPPRESSIVE ACTIVITY AND COOPERATES WITH CHEMOTHERAPY AGAINST OSTEOSARCOMA. *Cancer Lett.* 357:160.

Lim, Z.Y., S. Mohan, S. Balasubramaniam, S. Ahmed, C.C.H. Siew, and V.G. Shelat. 2023. Indocyanine green dye and its application in gastrointestinal surgery: The future is bright green. *World J. Gastrointest. Surg.* 15:1841.

Lin, B., L. Fan, J. Ge, W. Zhang, C. Zhang, C. Dong, and S. Shuang. 2018. A naphthalene-based fluorescent probe with a large Stokes shift for mitochondrial pH imaging. *Analyst*. 143:5054–5060.

Lindholm, M.E., and H. Rundqvist. 2016. Skeletal muscle hypoxia-inducible factor-1 and exercise. *Exp. Physiol.* 101:28–32.

Liou, G.Y., and P. Storz. 2010. Reactive oxygen species in cancer. *Free Radic. Res.* 44:479–496.

Liu, B., Y. Chen, and D.K. St. Clair. 2008. ROS and p53: a versatile partnership. *Free Radic. Biol. Med.* 44:1529–1535.

Liu, S., Y. Zheng, D. Volpi, M. El-Kasti, D. Klotz, I. Tullis, A. Henricks, L. Campo, K. Myers, A. Laios, P. Thomas, T. Ng, S. Dhar, C. Becker, B. Vojnovic, and A.A. Ahmed. 2015. Toward operative in vivo fluorescence imaging of the c-Met proto-oncogene for personalization of therapy in ovarian cancer. *Cancer*. 121:202–213.

Loboda, A., A. Stachurska, U. Florczyk, D. Rudnicka, A. Jazwa, J. Wegrzyn, M. Kozakowska, K. Stalinska, L. Poellinger, A.L. Levonen, S. Yla-Herttuala, A. Jozkowicz, and J. Dulak. 2009. HIF-1 induction attenuates Nrf2-dependent IL-8 expression in human endothelial cells. *Antioxid. Redox Signal.* 11:1501–1517.

Lord, S.R., and A.L. Harris. 2023. Is it still worth pursuing the repurposing of metformin as a cancer therapeutic? *Br. J. Cancer 2023 1286*. 128:958–966.

Lu, B., X.B. Chen, M.D. Ying, Q.J. He, J. Cao, and B. Yang. 2018. The Role of Ferroptosis in Cancer Development and Treatment Response. *Front. Pharmacol.* 8:1–8.

Lu, C.W., S.C. Lin, K.F. Chen, Y.Y. Lai, and S.J. Tsai. 2008. Induction of Pyruvate Dehydrogenase Kinase-3 by Hypoxia-inducible Factor-1 Promotes Metabolic Switch and Drug Resistance. *J. Biol. Chem.* 283:28106–28114.

Lu, H., D. Samanta, L. Xiang, H. Zhang, H. Hu, I. Chen, J.W. Bullen, and G.L. Semenza. 2015. Chemotherapy triggers HIF-1-dependent glutathione synthesis and copper chelation that induces the breast cancer stem cell phenotype. *Proc. Natl. Acad. Sci. U. S. A.* 112:E4600–E4609.

Lu, S.C. 2013. Glutathione synthesis. *Biochim. Biophys. Acta*. 1830:3143–3153.

Luo, S., E. Zhang, Y. Su, T. Cheng, and C. Shi. 2011a. A review of NIR dyes in cancer targeting and imaging. *Biomaterials*. 32:7127–7138.

Luo, W., H. Hu, R. Chang, J. Zhong, M. Knabel, R. O'Meally, R.N. Cole, A. Pandey, and G.L. Semenza. 2011b. Pyruvate kinase M2 is a PHD3-stimulated coactivator for hypoxia-inducible factor 1. *Cell*. 145:732–744.

Lyng, H., K. Sundfør, and E.K. Rofstad. 1997. Oxygen tension in human tumours measured with polarographic needle electrodes and its relationship to vascular density, necrosis and hypoxia. *Radiother. Oncol.* 44:163–169.

Ma, T.S., K.R. Worth, C. Maher, N. Ng, C. Beghè, N. Gromak, A.M. Rose, and E.M. Hammond. 2023. Hypoxia-induced transcriptional stress is mediated by ROS-induced R-loops. *Nucleic Acids Res*. 51:11584–11599.

Mailloux, R.J. 2021. An update on methods and approaches for interrogating mitochondrial reactive oxygen species production. *Redox Biol.* 45.

Mak, P., I. Leav, B. Pursell, D. Bae, X. Yang, C.A. Taglienti, L.M. Gouvin, V.M. Sharma, and A.M. Mercurio. 2010. ERβ Impedes Prostate Cancer EMT by Destabilizing HIF-1α and Inhibiting VEGF-Mediated Snail Nuclear Localization: Implications for Gleason Grading. *Cancer Cell*. 17:319.

Makino, Y., R. Cao, K. Svensson, G. Bertilsson, M. Asman, H. Tanaka, Y. Cao, A. Berkenstam, and L. Poellinger. 2001. Inhibitory PAS domain protein is a negative regulator of hypoxia-inducible gene expression. *Nature*. 414:550–554.

Makino, Y., A. Kanopka, W.J. Wilson, H. Tanaka, and L. Poellinger. 2002. Inhibitory PAS domain protein (IPAS) is a hypoxia-inducible splicing variant of the hypoxia-inducible factor-3alpha locus. *J. Biol. Chem.* 277:32405–32408.

Malla, J.A., R.M. Umesh, S. Yousf, S. Mane, S. Sharma, M. Lahiri, and P. Talukdar. 2020. A Glutathione Activatable Ion Channel Induces Apoptosis in Cancer Cells by Depleting Intracellular Glutathione Levels. *Angew. Chemie Int. Ed.* 59:7944–7952.

Maltepe, E., J. V. Schmidt, D. Baunoch, C.A. Bradfield, and M.C. Simon. 1997. Abnormal angiogenesis and responses to glucose and oxygen deprivation in mice lacking the protein ARNT. *Nature*. 386:403–407.

Maman, S., and I.P. Witz. 2018. A history of exploring cancer in context. *Nat. Rev. Cancer 2018 186*. 18:359–376.

Mandal, P.K., M. Schneider, P. Kölle, P. Kuhlencordt, H. Förster, H. Beck, G.W. Bornkamm, and M. Conrad. 2010a. Loss of thioredoxin reductase 1 renders tumors highly susceptible to pharmacologic glutathione deprivation. *Cancer Res.* 70:9505–9514.

Mandal, P.K., A. Seiler, T. Perisic, P. Kölle, A.B. Canak, H. Förster, N. Weiss, E. Kremmer, M.W. Lieberman, S. Bannai, P. Kuhlencordt, H. Sato, G.W. Bornkamm,

and M. Conrad. 2010b. System xc− and Thioredoxin Reductase 1 Cooperatively Rescue Glutathione Deficiency. *J. Biol. Chem*. 285:22244.

Mansfield, K.D., R.D. Guzy, Y. Pan, R.M. Young, T.P. Cash, P.T. Schumacker, and M.C. Simon. 2005. Mitochondrial dysfunction resulting from loss of cytochrome c impairs cellular oxygen sensing and hypoxic HIF-α activation. *Cell Metab*. 1:393.

Martin Brown, J., J. Evans, and M.S. Kovacs. 1992. The prediction of human tumor radiosensitivity in situ: an approach using chromosome aberrations detected by fluorescence in situ hybridization. *Int. J. Radiat. Oncol. Biol. Phys*. 24:279–286.

Mason, R.P., and J.L. Holtzman. 1975. The role of catalytic superoxide formation in the O2 inhibition of nitroreductase. *Biochem. Biophys. Res. Commun*. 67:1267–1274.

Mathupala, S.P., A. Rempel, and P.L. Pedersen. 2001. Glucose catabolism in cancer cells: identification and characterization of a marked activation response of the type II hexokinase gene to hypoxic conditions. *J. Biol. Chem*. 276:43407–43412.

Matsui, R., B. Ferran, A. Oh, D. Croteau, D. Shao, J. Han, D.R. Pimentel, and M.M. Bachschmid. 2020. Redox Regulation via Glutaredoxin-1 and Protein S-Glutathionylation. *Antioxid. Redox Signal*. 32:677.

Maxwell, P.H., G.U. Dachs, J.M. Gleadle, L.G. Nicholls, A.L. Harris, I.J. Stratford, O. Hankinson, C.W. Pugh, and P.J. Ratcliffe. 1997. Hypoxia-inducible factor-1 modulates gene expression in solid tumors and influences both angiogenesis and tumor growth. *Proc. Natl. Acad. Sci. U. S. A*. 94:8104–8109.

Maxwell, P.H., C.W. Pugh, and P.J. Ratcliffe. 1993. Inducible operation of the erythropoietin 3' enhancer in multiple cell lines: evidence for a widespread oxygen-sensing mechanism. *Proc. Natl. Acad. Sci. U. S. A*. 90:2423.

Maxwell, P.H., C.W. Pugh, and P.J. Ratcliffe. 2001. Activation of the HIF pathway in cancer. *Curr. Opin. Genet. Dev*. 11:293–299.

Maxwell, P.H., M.S. Wlesener, G.W. Chang, S.C. Clifford, E.C. Vaux, M.E. Cockman, C.C. Wykoff, C.W. Pugh, E.R. Maher, and P.J. Ratcliffe. 1999. The tumour suppressor protein VHL targets hypoxia-inducible factors for oxygen-dependent proteolysis. *Nature*. 399:271–275.

Maynard, M.A., H. Qi, J. Chung, E.H.L. Lee, Y. Kondo, S. Hara, R.C. Conaway, J.W. Conaway, and M. Ohh. 2003. Multiple splice variants of the human HIF-3 alpha locus are targets of the von Hippel-Lindau E3 ubiquitin ligase complex. *J. Biol. Chem*. 278:11032–11040.

McElroy, G.S., and N.S. Chandel. 2017. Mitochondria control acute and chronic responses to hypoxia. *Exp. Cell Res*. 356:217–222.

Meaney, C., G.G. Powathil, A. Yaromina, L.J. Dubois, P. Lambin, and M. Kohandel. 2019. Role of hypoxia-activated prodrugs in combination with radiation therapy: An in silico approach. *Math. Biosci. Eng*. 16:6257–6273.

Meister, A. 1983. Selective modification of glutathione metabolism. *Science*. 220:472–477.

Mie Lee, Y., C. Jeong, S. Koo, M. Jin Son, H. Seok Song, S. Bae, J.A. Raleigh, H. Chung, M. Yoo, and K. Kim. 2001. Determination of Hypoxic Region by Hypoxia Marker in Developing Mouse Embryos In Vivo: A Possible Signal for Vessel Development.

Miles, A.L., S.P. Burr, G.L. Grice, and J.A. Nathan. 2017. The vacuolar-ATPase complex and assembly factors, TMEM199 and CCDC115, control HIF1α prolyl hydroxylation by regulating cellular iron levels. *Elife*. 6.

Minchenko, O., I. Opentanova, and J. Caro. 2003. Hypoxic regulation of the 6-

phosphofructo-2-kinase/fructose-2,6- bisphosphatase gene family (PFKFB-1-4) expression in vivo. *FEBS Lett*. 554:264–270.

Miranda-Vizuete, A., J. Ljung, A.E. Damdimopoulos, J.Å. Gustafsson, R. Oko, M. Pelto-Huikko, and G. Spyrou. 2001. Characterization of Sptrx, a novel member of the thioredoxin family specifically expressed in human spermatozoa. *J. Biol. Chem*. 276:31567–31574.

Mitsui, A., T. Hirakawa, and J. Yodoi. 1992. Reactive oxygen-reducing and protein-refolding activities of adult t cell leukemia-derived factor /human thioredoxin. *Biochem. Biophys. Res. Commun*. 186:1220–1226.

Moeller, B.J., Y. Cao, C.Y. Li, and M.W. Dewhirst. 2004. Radiation activates HIF-1 to regulate vascular radiosensitivity in tumors: Role of reoxygenation, free radicals, and stress granules. *Cancer Cell*. 5:429–441.

Moeller, B.J., R.A. Richardson, and M.W. Dewhirst. 2007. Hypoxia and radiotherapy: Opportunities for improved outcomes in cancer treatment. *Cancer Metastasis Rev*. 26:241–248.

Mole, D.R., C. Blancher, R.R. Copley, P.J. Pollard, J.M. Gleadle, J. Ragousis, and P.J. Ratcliffe. 2009. Genome-wide association of hypoxia-inducible factor (HIF)-1alpha and HIF-2alpha DNA binding with expression profiling of hypoxia-inducible transcripts. *J. Biol. Chem*. 284:16767–16775.

Müller, M., W. Padberg, E. Schindler, J. Sticher, C. Osmer, S. Friemann, and G. Hempelmann. 1998. Renocortical tissue oxygen pressure measurements in patients undergoing living donor kidney transplantation. *Anesth. Analg*. 87:474–476.

Murphy, M.P. 2009. How mitochondria produce reactive oxygen species. *Biochem. J*. 417:1–13.

Murphy, M.P., H. Bayir, V. Belousov, C.J. Chang, K.J.A. Davies, M.J. Davies, T.P. Dick, T. Finkel, H.J. Forman, Y. Janssen-Heininger, D. Gems, V.E. Kagan, B. Kalyanaraman, N.G. Larsson, G.L. Milne, T. Nyström, H.E. Poulsen, R. Radi, H. Van Remmen, P.T. Schumacker, P.J. Thornalley, S. Toyokuni, C.C. Winterbourn, H. Yin, and B. Halliwell. 2022. Guidelines for measuring reactive oxygen species and oxidative damage in cells and in vivo. *Nat. Metab. 2022 46*. 4:651–662.

Musaogullari, A., and Y.C. Chai. 2020. Redox Regulation by Protein S-Glutathionylation: From Molecular Mechanisms to Implications in Health and Disease. *Int. J. Mol. Sci*. 21:1–25.

NCI. What Is Cancer?

Neeman, M., H. Dafni, O. Bukhari, R.D. Braun, and M.W. Dewhirst. 2001. In vivo BOLD contrast MRI mapping of subcutaneous vascular function and maturation: validation by intravital microscopy. *Magn. Reson. Med*. 45:887–898.

Netto, L.E.S., and F. Antunes. 2016. The Roles of Peroxiredoxin and Thioredoxin in Hydrogen Peroxide Sensing and in Signal Transduction. *Mol. Cells*. 39:65–71.

Nimalasena, S., S. Anbalagan, C. Box, S. Yu, J.K.R. Boult, N. Bush, L. Howell, V. Sinnett, W. Murphy, J. Yarnold, S.P. Robinson, and N. Somaiah. 2024. Tumour reoxygenation after intratumoural hydrogen peroxide (KORTUC) injection: a novel approach to enhance radiosensitivity. *BJC Reports 2024 21*. 2:1–9.

Nimalasena, S., L. Gothard, S. Anbalagan, S. Allen, V. Sinnett, K. Mohammed, G. Kothari, A. Musallam, C. Lucy, S. Yu, G. Nayamundanda, A. Kirby, G. Ross, E. Sawyer, F. Castell, S. Cleator, I. Locke, D. Tait, C. Westbury, V. Wolstenholme, C.

Box, S.P. Robinson, J. Yarnold, and N. Somaiah. 2020. Intratumoral Hydrogen Peroxide With Radiation Therapy in Locally Advanced Breast Cancer: Results From a Phase 1 Clinical Trial. *Int. J. Radiat. Oncol.* 108:1019–1029.

Niu, B., K. Liao, Y. Zhou, T. Wen, G. Quan, X. Pan, and C. Wu. 2021. Application of glutathione depletion in cancer therapy: Enhanced ROS-based therapy, ferroptosis, and chemotherapy. *Biomaterials*. 277:121110.

Nolan, K.A., and R.H. Wenger. 2018. Source and microenvironmental regulation of erythropoietin in the kidney. *Curr. Opin. Nephrol. Hypertens*. 27:277–282.

Nordsmark, M., S.M. Bentzen, V. Rudat, D. Brizel, E. Lartigau, P. Stadler, A. Becker, M. Adam, M. Molls, J. Dunst, D.J. Terris, and J. Overgaard. 2005. Prognostic value of tumor oxygenation in 397 head and neck tumors after primary radiation therapy. An international multi-center study. *Radiother. Oncol.* 77:18–24.

Nordsmark, M., and J. Overgaard. 2000. A confirmatory prognostic study on oxygenation status and loco-regional control in advanced head and neck squamous cell carcinoma treated by radiation therapy. *Radiother. Oncol.* 57:39–43.

Nössing, C., and K.M. Ryan. 2022. 50 years on and still very much alive: 'Apoptosis: a basic biological phenomenon with wide-ranging implications in tissue kinetics.' *Br. J. Cancer 2022 1283*. 128:426–431.

Ntziachristos, V. 2010. Going deeper than microscopy: the optical imaging frontier in biology. *Nat. Methods*. 7:603–614.

Nytko, K.J., P. Spielmann, G. Camenisch, R.H. Wenger, and D.P. Stiehl. 2007. Regulated function of the prolyl-4-hydroxylase domain (PHD) oxygen sensor proteins. *Antioxid. Redox Signal.* 9:1329–1338.

O'Connor, J.P.B., J.K.R. Boult, Y. Jamin, M. Babur, K.G. Finegan, K.J. Williams, R.A. Little, A. Jackson, G.J.M. Parker, A.R. Reynolds, J.C. Waterton, and S.P. Robinson. 2016. Oxygen-Enhanced MRI Accurately Identifies, Quantifies, and Maps Tumor Hypoxia in Preclinical Cancer Models. *Cancer Res.* 76:787–795.

O'Connor, J.P.B., A. Jackson, G.J.M. Parker, C. Roberts, and G.C. Jayson. 2012. Dynamic contrast-enhanced MRI in clinical trials of antivascular therapies. *Nat. Rev. Clin. Oncol.* 9:167–177.

O'Connor, J.P.B., S.P. Robinson, and J.C. Waterton. 2019. Imaging tumour hypoxia with oxygen-enhanced MRI and BOLD MRI. *Br. J. Radiol.* 92.

O'Rourke, J.F., C.W. Pugh, S.M. Bartlett, and P.J. Ratcliffe. 1996. Identification of hypoxically inducible mRNAs in HeLa cells using differential-display PCR. Role of hypoxia-inducible factor-1. *Eur. J. Biochem.* 241:403–410.

Ogawa, S., R.S. Menon, D.W. Tank, S.G. Kim, H. Merkle, J.M. Ellermann, and K. Ugurbil. 1993. Functional brain mapping by blood oxygenation level-dependent contrast magnetic resonance imaging. A comparison of signal characteristics with a biophysical model. *Biophys. J.* 64:803.

Ogawa, Y. 2016. Paradigm Shift in Radiation Biology/Radiation Oncology—Exploitation of the "H2O2 Effect" for Radiotherapy Using Low-LET (Linear Energy Transfer) Radiation such as X-rays and High-Energy Electrons. *Cancers 2016, Vol. 8, Page 28*. 8:28.

Ogunrinu, T.A., and H. Sontheimer. 2010. Hypoxia increases the dependence of glioma cells on glutathione. *J. Biol. Chem.* 285:37716–37724.

Oh, E.T., J.W. Kim, J.M. Kim, S.J. Kim, J.S. Lee, S.S. Hong, J. Goodwin, R.J. Ruthenborg,

M.G. Jung, H.J. Lee, C.H. Lee, E.S. Park, C. Kim, and H.J. Park. 2016. NQO1 inhibits proteasome-mediated degradation of HIF-1α. *Nat. Commun. 2016 71*. 7:1–14.

Ohh, M., C.W. Park, M. Ivan, M.A. Hoffman, T.Y. Kim, L.E. Huang, N. Pavletich, V. Chau, and W.G. Kaelin. 2000. Ubiquitination of hypoxia-inducible factor requires direct binding to the beta-domain of the von Hippel-Lindau protein. *Nat. Cell Biol.* 2:423–427.

Okunieff, P., M. Hoeckel, E.P. Dunphy, K. Schlenger, C. Knoop, and P. Vaupel. 1993. Oxygen tension distributions are sufficient to explain the local response of human breast tumors treated with radiation alone. *Int. J. Radiat. Oncol. Biol. Phys.* 26:631–636.

Olcina, M., P.S. Lecane, and E.M. Hammond. 2010. Targeting hypoxic cells through the DNA damage response. *Clin. Cancer Res.* 16:5624–5629.

Olcina, M.M., I.P. Foskolou, S. Anbalagan, J.M. Senra, I.M. Pires, Y. Jiang, A.J. Ryan, and E.M. Hammond. 2013. Replication Stress and Chromatin Context Link ATM Activation to a Role in DNA Replication. *Mol. Cell*. 52:758.

Olive, P.L., and J.P. Banáth. 2004. Phosphorylation of histone H2AX as a measure of radiosensitivity. *Int. J. Radiat. Oncol. Biol. Phys.* 58:331–335.

Orino, K., L. Lehman, Y. Tsuji, H. Ayaki, S. V. Torti, and F.M. Torti. 2001. Ferritin and the response to oxidative stress. *Biochem. J.* 357:241.

Osler, W. 1893. The principles and practice of medicine. 708 pp.

Overgaard, J. 2011. Hypoxic modification of radiotherapy in squamous cell carcinoma of the head and neck--a systematic review and meta-analysis. *Radiother. Oncol.* 100:22–32.

Overgaard, J., H.S. Hansen, M. Overgaard, L. Bastholt, A. Berthelsen, L. Specht, B. Lindeløv, and K. Jørgensen. 1998. A randomized double-blind phase III study of nimorazole as a hypoxic radiosensitizer of primary radiotherapy in supraglottic larynx and pharynx carcinoma. Results of the Danish Head and Neck Cancer Study (DAHANCA) Protocol 5-85. *Radiother. Oncol.* 46:135–146.

Pagé, E.L., G.A. Robitaille, J. Pouysségur, and D.E. Richard. 2002. Induction of hypoxia-inducible factor-1alpha by transcriptional and translational mechanisms. *J. Biol. Chem.* 277:48403–48409.

Paget, S. 1889. THE DISTRIBUTION OF SECONDARY GROWTHS IN CANCER OF THE BREAST. *Lancet*. 133:571–573.

Paiji, C., and A. Sedarat. 2022. Endoscopic Management of Esophageal Cancer. *Cancers (Basel)*. 14.

Pan, Y., K.D. Mansfield, C.C. Bertozzi, V. Rudenko, D.A. Chan, A.J. Giaccia, and M.C. Simon. 2007. Multiple factors affecting cellular redox status and energy metabolism modulate hypoxia-inducible factor prolyl hydroxylase activity in vivo and in vitro. *Mol. Cell. Biol.* 27:912–925.

Papac, R.J. 2001. Origins of cancer therapy. *Yale J. Biol. Med.* 74:391.

Papandreou, I., R.A. Cairns, L. Fontana, A.L. Lim, and N.C. Denko. 2006. HIF-1 mediates adaptation to hypoxia by actively downregulating mitochondrial oxygen consumption. *Cell Metab.* 3:187–197.

Papandreou, I., C. Krishna, F. Kaper, D. Cai, A.J. Giaccia, and N.C. Denko. 2005. Anoxia is necessary for tumor cell toxicity caused by a low-oxygen environment. *Cancer Res.* 65:3171–3178.

Park, W., S. Wei, B.S. Kim, B. Kim, S.J. Bae, Y.C. Chae, D. Ryu, and K.T. Ha. 2023.

Diversity and complexity of cell death: a historical review. *Exp. Mol. Med. 2023 558*. 55:1573–1594.

Parvez, S., M.J.C. Long, J.R. Poganik, and Y. Aye. 2018. Redox signaling by reactive electrophiles and oxidants. *Chem. Rev.* 118:8798–8888.

Patel, M.S., and L.G. Korotchkina. 2001. Regulation of mammalian pyruvate dehydrogenase complex by phosphorylation: complexity of multiple phosphorylation sites and kinases. *Exp. Mol. Med.* 33:191–197.

Pepper, M.S., N. Ferrara, L. Orci, and R. Montesano. 1991. Vascular endothelial growth factor (VEGF) induces plasminogen activators and plasminogen activator inhibitor-1 in microvascular endothelial cells. *Biochem. Biophys. Res. Commun.* 181:902–906.

Pepper, M.S., J.D. Vassalli, L. Orci, and R. Montesano. 1992. Proteolytic balance and capillary morphogenesis in vitro. *EXS*. 61:137–145.

Perillo, B., M. Di Donato, A. Pezone, E. Di Zazzo, P. Giovannelli, G. Galasso, G. Castoria, and A. Migliaccio. 2020. ROS in cancer therapy: the bright side of the moon. *Exp. Mol. Med*. 52:192–203.

Perry, J.C. 1896. Roentgen Rays—Their Application to Medicine and Surgery. *Am. J. Dent. Sci.* 30:307.

Peters, L.J., B. O'Sullivan, J. Giralt, T.J. Fitzgerald, A. Trotti, J. Bernier, J. Bourhis, K. Yuen, R. Fisher, and D. Rischin. 2010. Critical impact of radiotherapy protocol compliance and quality in the treatment of advanced head and neck cancer: results from TROG 02.02. *J. Clin. Oncol.* 28:2996–3001.

Pham-Huy, L.A., H. He, and C. Pham-Huy. 2008. Free Radicals, Antioxidants in Disease and Health. *Int. J. Biomed. Sci.* 4:89.

Phillips, R.M., M.A. Nayl, W.D. Stephen, and S.A. Everett. 1999. Bioreductive Activation of a Series of Indolequinones by Human DT-Diaphorase: Structure-Activity Relationships. 4071–4080.

Pietrangelo, A. 2017. Ferroportin disease: pathogenesis, diagnosis and treatment. *Haematologica*. 102:1972–1984.

Pires, I.M., Z. Bencokova, M. Milani, L.K. Folkes, J.A. Li, M.R. Stratford, A.L. Harris, and E.M. Hammond. 2010. Effects of acute versus chronic hypoxia on DNA damage responses and genomic instability. *Cancer Res.* 70:925.

Piskounova, E., M. Agathocleous, M.M. Murphy, Z. Hu, S.E. Huddlestun, Z. Zhao, A.M. Leitch, T.M. Johnson, R.J. DeBerardinis, and S.J. Morrison. 2015. Oxidative stress inhibits distant metastasis by human melanoma cells. *Nat. 2015 5277577*. 527:186–191.

Porto, V., E. Borrajo, D. Buceta, C. Carneiro, S. Huseyinova, B. Domínguez, K.J.E. Borgman, M. Lakadamyali, M.F. Garcia-Parajo, J. Neissa, T. García-Caballero, G. Barone, M.C. Blanco, N. Busto, B. García, J.M. Leal, J. Blanco, J. Rivas, M.A. López-Quintela, and F. Domínguez. 2018. Silver Atomic Quantum Clusters of Three Atoms for Cancer Therapy: Targeting Chromatin Compaction to Increase the Therapeutic Index of Chemotherapy. *Adv. Mater.* 30:1801317.

Porto, V., D. Buceta, B. Domínguez, C. Carneiro, E. Borrajo, M. Fraile, N. Davila-Ferreira, I.R. Arias, J.M. Blanco, M.C. Blanco, J.M. Devida, L.J. Giovanetti, F.G. Requejo, J.C. Hernández-Garrido, J.J. Calvino, M. López-Haro, G. Barone, A.M. James, T. García-Caballero, D.M. González-Castaño, M. Treder, W. Huber, A. Vidal, M.P. Murphy, M.A. López-Quintela, and F. Domínguez. 2022. Silver Clusters of Five Atoms as

Highly Selective Antitumoral Agents Through Irreversible Oxidation of Thiols. *Adv. Funct. Mater.* 1–14.

Potteti, H.R., C.R. Tamatam, R. Marreddy, N.M. Reddy, S. Noel, H. Rabb, and S.P. Reddy. 2016. Nrf2-AKT interactions regulate heme oxygenase 1 expression in kidney epithelia during hypoxia and hypoxia-reoxygenation. *Am. J. Physiol. Renal Physiol.* 311:F1025–F1034.

Pouysségur, J., and F. Mechta-Grigoriou. 2006. Redox regulation of the hypoxia-inducible factor. *Biol. Chem.* 387:1337–1346.

Powis, G., and W.R. Montfort. 2001. Properties and biological activities of thioredoxins. *Annu. Rev. Biophys. Biomol. Struct.* 30:421–455.

Prabhakar, N.R. 2001. Oxygen sensing during intermittent hypoxia: cellular and molecular mechanisms. *J. Appl. Physiol.* 90:1986–1994.

Provot, S., and E. Schipani. 2007. Fetal Growth Plate. *Ann. N. Y. Acad. Sci.* 1117:26–39.

Pu, F., F. Chen, Z. Zhang, D. Shi, B. Zhong, X. Lv, A.B. Tucker, J. Fan, A.J. Li, K. Qin, D. Hu, C. Chen, H. Wang, F. He, N. Ni, L. Huang, Q. Liu, W. Wagstaff, H.H. Luu, R.C. Haydon, L. Shen, T.C. He, J. Liu, and Z. Shao. 2022. Ferroptosis as a novel form of regulated cell death: Implications in the pathogenesis, oncometabolism and treatment of human cancer. *Genes Dis.* 9:347.

Pugh, C.W., C.C. Tan, R.W. Jones, and P.J. Ratcliffe. 1991. Functional analysis of an oxygen-regulated transcriptional enhancer lying 3' to the mouse erythropoietin gene. *Proc. Natl. Acad. Sci. U. S. A.* 88:10553.

Qutub, A.A., and A.S. Popel. 2008. Reactive Oxygen Species Regulate Hypoxia-Inducible Factor 1α Differentially in Cancer and Ischemia. *Mol. Cell. Biol.* 28:5106.

Radi, R. 2018. Oxygen radicals, nitric oxide, and peroxynitrite: Redox pathways in molecular medicine. *Proc. Natl. Acad. Sci. U. S. A.* 115:5839–5848.

Ramachandran, S., T.S. Ma, J. Griffin, N. Ng, I.P. Foskolou, M.S. Hwang, P. Victori, W.C. Cheng, F.M. Buffa, K.B. Leszczynska, S.F. El-Khamisy, N. Gromak, and E.M. Hammond. 2021. Hypoxia-induced SETX links replication stress with the unfolded protein response. *Nat. Commun. 2021 121*. 12:1–14.

Ramanathan, R.K., J. Abbruzzese, T. Dragovich, L. Kirkpatrick, J.M. Guillen, A.F. Baker, L.A. Pestano, S. Green, and D.D. Von Hoff. 2011. A randomized phase II study of PX-12, an inhibitor of thioredoxin in patients with advanced cancer of the pancreas following progression after a gemcitabine-containing combination. *Cancer Chemother. Pharmacol.* 67:503–509.

Ramanathan, R.K., J.J. Stephenson, G.J. Weiss, L.A. Pestano, A. Lowe, A. Hiscox, R.A. Leos, J.C. Martin, L. Kirkpatrick, and D.A. Richards. 2012. A phase I trial of PX-12, a small-molecule inhibitor of thioredoxin-1, administered as a 72-hour infusion every 21 days in patients with advanced cancers refractory to standard therapy. *Invest. New Drugs*. 30:1591–1596.

Ramsey, M.R., and N.E. Sharpless. 2006. ROS as a tumour suppressor? *Nat. Cell Biol. 2006 811*. 8:1213–1215.

Ray, P.D., B.W. Huang, and Y. Tsuji. 2012. Reactive oxygen species (ROS) homeostasis and redox regulation in cellular signaling. *Cell. Signal.* 24:981.

Reczek, C.R., and N.S. Chandel. 2017. The two faces of reactive oxygen species in cancer. *Annu. Rev. Cancer Biol.* 1:79–98.

Reisz-Porszasz, S., M.R. Probst,', B.N. Fukunaga, and O. Hankinsonl12. 1994. Identification of functional domains of the aryl hydrocarbon receptor nuclear

translocator protein (ARNT). *Mol. Cell. Biol.* 14:6075.
Reyes, H., S. Reisz-Porszasz, and O. Hankinson. 1992. Identification of the Ah receptor nuclear translocator protein (Arnt) as a component of the DNA binding form of the Ah receptor. *Science*. 256:1193–1195.
Rhee, S.G. 2016. Overview on Peroxiredoxin. *Mol. Cells*. 39:1–5.
Rhee, S.G., and S.H. Bae. 2015. The antioxidant function of sestrins is mediated by promotion of autophagic degradation of Keap1 and Nrf2 activation and by inhibition of mTORC1. *Free Radic. Biol. Med.* 88:205–211.
Rischin, D., R.J. Hicks, R. Fisher, D. Binns, J. Corry, S. Porceddu, and L.J. Peters. 2006. Prognostic significance of [18F]-misonidazole positron emission tomography-detected tumor hypoxia in patients with advanced head and neck cancer randomly assigned to chemoradiation with or without tirapazamine: a substudy of Trans-Tasman Radiation Oncology Group Study 98.02. *J. Clin. Oncol.* 24:2098–2104.
Rischin, D., L.J. Peters, B. O'Sullivan, J. Giralt, R. Fisher, K. Yuen, A. Trotti, J. Bernier, J. Bourhis, J. Ringash, M. Henke, and L. Kenny. 2010. Tirapazamine, cisplatin, and radiation versus cisplatin and radiation for advanced squamous cell carcinoma of the head and neck (TROG 02.02, HeadSTART): a phase III trial of the Trans-Tasman Radiation Oncology Group. *J. Clin. Oncol.* 28:2989–2995.
Rivera, L., M. Puyol, S. Miltsov, and J. Alonso. 2007. New hexamethine-hemicyanine dyes for the development of integrated optochemical sensors. *Anal. Bioanal. Chem.* 387:2111–2119.
Robert Grimes, D., and M. Partridge. 2015. A mechanistic investigation of the oxygen fixation hypothesis and oxygen enhancement ratio. *Biomed. Phys. Eng. express*. 1:045209.
Rocha, C.R.R., C.C.M. Garcia, D.B. Vieira, A. Quinet, L.C. De Andrade-Lima, V. Munford, J.E. Belizário, and C.F.M. Menck. 2014. Glutathione depletion sensitizes cisplatin- and temozolomide-resistant glioma cells in vitro and in vivo. *Cell Death Dis. 2014 510*. 5:e1505–e1505.
Roche, T.E., J.C. Baker, X. Yan, Y. Hiromasa, X. Gong, T. Peng, J. Dong, A. Turkan, and S.A. Kasten. 2001. Distinct regulatory properties of pyruvate dehydrogenase kinase and phosphatase isoforms. *Prog. Nucleic Acid Res. Mol. Biol.* 70.
Rogers, J.L., L. Bayeh, T.H. Scheuermann, J. Longgood, J. Key, J. Naidoo, L. Melito, C. Shokri, D.E. Frantz, R.K. Bruick, K.H. Gardner, J.B. MacMillan, and U.K. Tambar. 2013. Development of Inhibitors of the PAS-B Domain of the HIF-2α Transcription Factor. *J. Med. Chem.* 56:1739.
Rohwer, N., and T. Cramer. 2011. Hypoxia-mediated drug resistance: novel insights on the functional interaction of HIFs and cell death pathways. *Drug Resist. Updat.* 14:191–201.
Roos, G., and J. Messens. 2011. Protein sulfenic acid formation: From cellular damage to redox regulation. *Free Radic. Biol. Med.* 51:314–326.
Rosenfeld, E., B. Beauvoit, M. Rigoulet, and J.M. Salmon. 2002. Non-respiratory oxygen consumption pathways in anaerobically-grown Saccharomyces cerevisiae: evidence and partial characterization. *Yeast*. 19:1299–1321.
Rouschop, K.M., L.J. Dubois, T.G. Keulers, T. Van Den Beucken, P. Lambin, J. Bussink, A.J. Van Der Kogel, M. Koritzinsky, and B.G. Wouters. 2013. PERK/eIF2α signaling protects therapy resistant hypoxic cells through induction of glutathione synthesis and protection against ROS. *Proc. Natl. Acad. Sci. U. S. A.* 110:4622–4627.

Rtishchev, N.I., D. V. Samoilov, V.P. Martynova, and A. V. El'tsov. 2001. Luminescence properties of nitro derivatives of fluorescein. *Russ. J. Gen. Chem.* 71:1467–1478.

Ryan, H.E., J. Lo, and R.S. Johnson. 1998. HIF-1 alpha is required for solid tumor formation and embryonic vascularization. *EMBO J.* 17:3005–3015.

Rzymski, T., and A.L. Harris. 2007. The unfolded protein response and integrated stress response to anoxia. *Clin. Cancer Res.* 13:2537–2540.

Sabharwal, S.S., and P.T. Schumacker. 2014. Mitochondrial ROS in cancer: initiators, amplifiers or an Achilles' heel? *Nat. Rev. Cancer 2014 1411*. 14:709–721.

Saghian, M., S. Dehghanpour, and Z. bayatani. 2023. A facile, rapid procedure for Knoevenagel condensation reaction catalyzed by efficient amino-bifunctional frameworks under mild conditions. *Sci. Rep.* 13:15563.

Sakagami, H., Y. Makino, K. Mizumoto, T. Isoe, Y. Takeda, J. Watanabe, Y. Fujita, Y. Takiyama, A. Abiko, and M. Haneda. 2014. Loss of HIF-1α impairs GLUT4 translocation and glucose uptake by the skeletal muscle cells. *Am. J. Physiol. Endocrinol. Metab.* 306.

Salem, A., R.A. Little, A. Latif, A.K. Featherstone, M. Babur, I. Peset, S. Cheung, Y. Watson, V. Tessyman, H. Mistry, G. Ashton, C. Behan, J.C. Matthews, M.C. Asselin, R.G. Bristow, A. Jackson, G.J.M. Parker, C. Faivre-Finn, K.J. Williams, and J.P.B. O'Connor. 2019. Oxygen-enhanced MRI Is Feasible, Repeatable, and Detects Radiotherapy-induced Change in Hypoxia in Xenograft Models and in Patients with Non-small Cell Lung Cancer. *Clin. Cancer Res.* 25:3818–3829.

Samanta, D., and G.L. Semenza. 2017. Maintenance of redox homeostasis by hypoxia-inducible factors. *Redox Biol.* 13:331–335.

Samanta, D., and G.L. Semenza. 2018. Metabolic adaptation of cancer and immune cells mediated by hypoxia-inducible factors. *Biochim. Biophys. acta. Rev. cancer.* 1870:15–22.

Sánchez-álvarez, M., R. Strippoli, M. Donadelli, A. V. Bazhin, and M. Cordani. 2019. Sestrins as a Therapeutic Bridge between ROS and Autophagy in Cancer. *Cancers (Basel).* 11.

Sandhu, S., L. Kydd, and J. Jaworski. 2017. Luminescent Probe Based Techniques for Hypoxia Imaging. *J. nanomedicine Res.* 6.

Sayin, V.I., M.X. Ibrahim, E. Larsson, J.A. Nilsson, P. Lindahl, and M.O. Bergo. 2014. Antioxidants accelerate lung cancer progression in mice. *Sci. Transl. Med.* 6.

Schieber, M., and N.S. Chandel. 2014. ROS Function in Redox Signaling and Oxidative Stress. *Curr. Biol.* 24:R453.

Schmidt, A., and O.F. Weber. 2006. In memoriam of Rudolf virchow: a historical retrospective including aspects of inflammation, infection and neoplasia. *Contrib. Microbiol.* 13:1–15.

Schödel, J., and P.J. Ratcliffe. 2019. Mechanisms of hypoxia signalling: new implications for nephrology. *Nat. Rev. Nephrol.* 15:641–659.

Scholz, H., F.J. Boivin, K.M. Schmidt-Ott, S. Bachmann, K.U. Eckardt, U.I. Scholl, and P.B. Persson. 2021. Kidney physiology and susceptibility to acute kidney injury: implications for renoprotection. *Nat. Rev. Nephrol.* 17:335–349.

Seagroves, T.N., H.E. Ryan, H. Lu, B.G. Wouters, M. Knapp, P. Thibault, K. Laderoute, and R.S. Johnson. 2001. Transcription Factor HIF-1 Is a Necessary Mediator of the Pasteur Effect in Mammalian Cells. *Mol. Cell. Biol.* 21:3436.

Secomb, T.W., R. Hsu, E.T. Ong, J.F. Gross, and M.W. Dewhirst. 1995. Analysis of the

Effects of Oxygen Supply and Demand on Hypoxic Fraction in Tumors. *Acta Oncol. (Madr)*. 34:313–316.
Semenza, G.L. 1999. Regulation of mammalian O2 homeostasis by hypoxia-inducible factor 1. *Annu. Rev. Cell Dev. Biol.* 15:551–578.
Semenza, G.L. 2001. Regulation of hypoxia-induced angiogenesis: a chaperone escorts VEGF to the dance. *J. Clin. Invest.* 108:39–40.
Semenza, G.L. 2008. Tumor metabolism: cancer cells give and take lactate. *J. Clin. Invest.* 118:3835–3837.
Semenza, G.L. 2011. Oxygen Sensing, Homeostasis, and Disease. *N Engl J Med*. 365:537–584.
Semenza, G.L. 2012a. Hypoxia-inducible factors in physiology and medicine. *Cell*. 148:399–408.
Semenza, G.L. 2012b. Hypoxia-inducible factors: Mediators of cancer progression and targets for cancer therapy. *Trends Pharmacol. Sci.* 33:207–214.
Semenza, G.L. 2014a. Oxygen sensing, hypoxia-inducible factors, and disease pathophysiology. *Annu. Rev. Pathol.* 9:47–71.
Semenza, G.L. 2014b. Hypoxia-inducible factor 1 and cardiovascular disease. *Annu. Rev. Physiol.* 76:39–56.
Semenza, G.L., B.H. Jiang, S.W. Leung, R. Passantino, J.P. Concordat, P. Maire, and A. Giallongo. 1996. Hypoxia response elements in the aldolase A, enolase 1, and lactate dehydrogenase A gene promoters contain essential binding sites for hypoxia-inducible factor 1. *J. Biol. Chem.* 271:32529–32537.
Semenza, G.L., M.K. Nejfelt, S.M. Chi, and S.E. Antonarakis. 1991. Hypoxia-inducible nuclear factors bind to an enhancer element located 3' to the human erythropoietin gene. *Proc. Natl. Acad. Sci. U. S. A.* 88:5680.
Semenza, G.L., and N.R. Prabhakar. 2018. The role of hypoxia-inducible factors in carotid body (patho) physiology. *J. Physiol.* 596:2977–2983.
Semenza, G.L., P.H. Roth, H.M. Fang, and G.L. Wang. 1994. Transcriptional regulation of genes encoding glycolytic enzymes by hypoxia-inducible factor 1. *J. Biol. Chem.* 269:23757–23763.
Semenza, G.L., and G.L. Wang. 1992. A nuclear factor induced by hypoxia via de novo protein synthesis binds to the human erythropoietin gene enhancer at a site required for transcriptional activation. *Mol. Cell. Biol.* 12:5447.
Sgarbi, G., G. Gorini, A. Costanzini, S. Barbato, G. Solaini, and A. Baracca. 2017. Hypoxia decreases ROS level in human fibroblasts. *Int. J. Biochem. Cell Biol.* 88:133–144.
Sgarbi, G., G. Gorini, F. Liuzzi, G. Solaini, and A. Baracca. 2018. Hypoxia and IF1 Expression Promote ROS Decrease in Cancer Cells. *Cells*. 7.
Shafirovich, V., and N.E. Geacintov. 2017. Removal of oxidatively generated DNA damage by overlapping repair pathways. *Free Radic. Biol. Med.* 107:53–61.
Shen, H., Y. Yang, S. Xia, B. Rao, J. Zhang, and J. Wang. 2014. Blockage of Nrf2 suppresses the migration and invasion of esophageal squamous cell carcinoma cells in hypoxic microenvironment. *Dis. esophagus Off. J. Int. Soc. Dis. Esophagus*. 27:685–692.
Shen, J., N. Khan, L.D. Lewis, R. Armand, O. Grinberg, E. Demidenko, and H. Swartz. 2003. Oxygen Consumption Rates and Oxygen Concentration in Molt-4 Cells and Their mtDNA Depleted (ρ0) Mutants. *Biophys. J.* 84:1291.

Shi, Y., F. Nikulenkov, J. Zawacka-Pankau, H. Li, R. Gabdoulline, J. Xu, S. Eriksson, E. Hedström, N. Issaeva, A. Kel, E.S.J. Arnér, and G. Selivanova. 2014. ROS-dependent activation of JNK converts p53 into an efficient inhibitor of oncogenes leading to robust apoptosis. *Cell Death Differ. 2014 214*. 21:612–623.

Shimoda, L.A., and G.L. Semenza. 2012. HIF and the Lung. *https://doi.org/10.1164/rccm.201009-1393PP*. 183:152–156.

Shin, S.Y., J.M. Lee, M.S. Lee, D. Koh, H. Jung, Y. Lim, and Y.H. Lee. 2014. Targeting cancer cells via the reactive oxygen species-mediated unfolded protein response with a novel synthetic polyphenol conjugate. *Clin. Cancer Res.* 20:4302–4313.

Siemann, D.W., and M.R. Horsman. 2015. Modulation of the tumor vasculature and oxygenation to improve therapy. *Pharmacol. Ther.* 153:107–124.

Sies, H. 2015. Oxidative stress: a concept in redox biology and medicine. *Redox Biol.* 4:180–183.

Sies, H., V. V. Belousov, N.S. Chandel, M.J. Davies, D.P. Jones, G.E. Mann, M.P. Murphy, M. Yamamoto, and C. Winterbourn. 2022. Defining roles of specific reactive oxygen species (ROS) in cell biology and physiology. *Nat. Rev. Mol. Cell Biol. 2022 237*. 23:499–515.

Silva, A., J.A. Yunes, B.A. Cardoso, L.R. Martins, P.Y. Jotta, M. Abecasis, A.E. Nowill, N.R. Leslie, A.A. Cardoso, and J.T. Barata. 2008. PTEN posttranslational inactivation and hyperactivation of the PI3K/Akt pathway sustain primary T cell leukemia viability. *J. Clin. Invest.* 118:3762–3774.

Sinbad, O.O., A.A. Folorunsho, O.L. Olabisi, O.A. Ayoola, and E.J. Temitope. 2019. Vitamins as Antioxidants. *J. Food Sci. Nutr. Res.* 2:214–235.

Singh, R., and P.P. Manna. 2022. Reactive oxygen species in cancer progression and its role in therapeutics. *Open Explor. 2019 31*. 3:43–57.

Singleton, D.C., A. Macann, and W.R. Wilson. 2021. Therapeutic targeting of the hypoxic tumour microenvironment. *Nat. Rev. Clin. Oncol. 2021 1812*. 18:751–772.

Skwarski, M., D.R. McGowan, E. Belcher, F. Di Chiara, D. Stavroulias, M. McCole, J.L. Derham, K.Y. Chu, E. Teoh, J. Chauhan, D. O'Reilly, B.H.L. Harris, P.S. Macklin, J.A. Bull, M. Green, G. Rodriguez-Berriguete, R. Prevo, L.K. Folkes, L. Campo, P. Ferencz, P.L. Croal, H. Flight, C. Qi, J. Holmes, J.P.B. O'Connor, F. V. Gleeson, W.G. McKenna, A.L. Harris, D. Bulte, F.M. Buffa, R.E. Macpherson, and G.S. Higgins. 2021. Mitochondrial Inhibitor Atovaquone Increases Tumor Oxygenation and Inhibits Hypoxic Gene Expression in Patients with Non-Small Cell Lung Cancer. *Clin. Cancer Res.* 27:2459–2469.

Song, I.S., H.K. Kim, S.H. Jeong, S.R. Lee, N. Kim, B.D. Rhee, K.S. Ko, and J. Han. 2011. Mitochondrial Peroxiredoxin III is a Potential Target for Cancer Therapy. *Int. J. Mol. Sci. 2011, Vol. 12, Pages 7163-7185*. 12:7163–7185.

Sørensen, B.S., and M.R. Horsman. 2020. Tumor Hypoxia: Impact on Radiation Therapy and Molecular Pathways. *Front. Oncol.* 10.

Sowter, H.M., P.J. Ratcliffe, P. Watson, A.H. Greenberg, and A.L. Harris. 2001. HIF-1-dependent regulation of hypoxic induction of the cell death factors BNIP3 and NIX in human tumors. *Cancer Res.* 61:6669–6673.

Spiegelberg, L., R. Houben, R. Niemans, D. de Ruysscher, A. Yaromina, J. Theys, C.P. Guise, J.B. Smaill, A. V. Patterson, P. Lambin, and L.J. Dubois. 2019. Hypoxia-activated prodrugs and (lack of) clinical progress: The need for hypoxia-based biomarker patient selection in phase III clinical trials. *Clin. Transl. Radiat. Oncol.*

15:62–69.
Spyrou, G., E. Enmark, A. Miranda-Vizuete, and J.Å. Gustafsson. 1997. Cloning and expression of a novel mammalian thioredoxin. *J. Biol. Chem.* 272:2936–2941.
Stöcker, S., K. Van Laer, A. Mijuskovic, and T.P. Dick. 2018. The Conundrum of Hydrogen Peroxide Signaling and the Emerging Role of Peroxiredoxins as Redox Relay Hubs. *Antioxid. Redox Signal.* 28:558–573.
Stone, W.L., H. Basit, and S.S. Mohiuddin. 2023. Biochemistry, Antioxidants. *StatPearls*.
Storz, P. 2005. Reactive oxygen species in tumor progression. *Front. Biosci.* 10:1881–1896.
Subburayan, K., F. Thayyullathil, S. Pallichankandy, A.R. Cheratta, and S. Galadari. 2020. Superoxide-mediated ferroptosis in human cancer cells induced by sodium selenite. *Transl. Oncol.* 13.
Suda, T., K. Takubo, and G.L. Semenza. 2011. Metabolic regulation of hematopoietic stem cells in the hypoxic niche. *Cell Stem Cell*. 9:298–310.
Sullivan, R., and C.H. Graham. 2007. Hypoxia-driven selection of the metastatic phenotype. *Cancer Metastasis Rev.* 26:319–331.
Sun, Q.A., D. Su, S. V. Novoselov, B.A. Carlson, D.L. Hatfield, and V.N. Gladyshev. 2005. Reaction mechanism and regulation of mammalian thioredoxin/glutathione reductase. *Biochemistry*. 44:14528–14537.
Sun, X., G. Niu, N. Chan, B. Shen, and X. Chen. 2011. Tumor hypoxia imaging. *Mol. imaging Biol.* 13:399–410.
Sunakawa, Y., T. Bekaii-Saab, and S. Stintzing. 2016. Reconsidering the benefit of intermittent versus continuous treatment in the maintenance treatment setting of metastatic colorectal cancer. *Cancer Treat. Rev.* 45:97–104.
Sundaresan, M., Z.-X. Yu, V.J. Ferrans, K. Irani, and T. Finkel. 1995. Requirement for generation of H2O2 for platelet-derived growth factor signal transduction. *Science*. 270:296–299.
Swinson, D.E.B., J.L. Jones, D. Richardson, C. Wykoff, H. Turley, J. Pastorek, N. Taub, A.L. Harris, and K.J. O'Byrne. 2003. Carbonic anhydrase IX expression, a novel surrogate marker of tumor hypoxia, is associated with a poor prognosis in non-small-cell lung cancer. *J. Clin. Oncol.* 21:473–482.
Szatrowski, T., and C. Nathan. 1991. Production of large amounts of hydrogen peroxide by human tumor cells. *Cancer Res.*
Tacar, O., P. Sriamornsak, and C.R. Dass. 2013. Doxorubicin: an update on anticancer molecular action, toxicity and novel drug delivery systems. *J. Pharm. Pharmacol.* 65:157–170.
Takahashi, A., N. Ohtani, K. Yamakoshi, S.I. Iida, H. Tahara, K. Nakayama, K.I. Nakayama, T. Ide, H. Saya, and E. Hara. 2006. Mitogenic signalling and the p16INK4a–Rb pathway cooperate to enforce irreversible cellular senescence. *Nat. Cell Biol. 2006 811*. 8:1291–1297.
Takahashi, S., W. Piao, Y. Matsumura, T. Komatsu, T. Ueno, T. Terai, T. Kamachi, M. Kohno, T. Nagano, and K. Hanaoka. 2012. Reversible off-on fluorescence probe for hypoxia and imaging of hypoxia-normoxia cycles in live cells. *J. Am. Chem. Soc*. 134:19588–19591.
Taniguchi, Y., Y. Taniguchi-Ueda, K. Mori, and J. Yodoi. 1996. A novel promoter sequence is involved in the oxidative stress-induced expression of the adult T-cell leukemia-derived factor (ADF)/human thioredoxin (Trx) gene. *Nucleic Acids Res.*

24:2746.
Tanimoto, K., Y. Makino, T. Pereira, and L. Poellinger. 2000. Mechanism of regulation of the hypoxia-inducible factor-1 alpha by the von Hippel-Lindau tumor suppressor protein. *EMBO J.* 19:4298–4309.
Tannock, I.F. 1968. The relation between cell proliferation and the vascular system in a transplanted mouse mammary tumour. *Br. J. Cancer*. 22:258.
Tannock, I.F. 1998. Conventional cancer therapy: Promise broken or promise delayed? *Lancet*. 351:SII9–SII16.
Tappel, A.L. 1962. Vitamin E as the Biological Lipid Antioxidant. *Vitam. Horm.* 20:493–510.
Taylor, C.T., and J.C. McElwain. 2010. Ancient atmospheres and the evolution of oxygen sensing via the hypoxia-inducible factor in metazoans. *Physiology (Bethesda)*. 25:272–279.
Taylor, C.T., and C.C. Scholz. 2022. The effect of HIF on metabolism and immunity. *Nat. Rev. Nephrol.* 18:573.
Taylor, J.N., H. Baddeley, K.A. Goodchild, M.E.B. Powell, M. Thoumine, L.A. Culver, J. James Stirling, M.I. Saunders, P.J. Hoskin, H. Phillips, A.R. Padhani, and J.R. Griffiths. 2001. BOLD MRI of human tumor oxygenation during carbogen breathing. *J. Magn. Reson. Imaging*. 14:156–163.
Teicher, B.A., J.S. Lazo, and A.C. Salterelli. 1981. Classification of Antineoplastic Agents by their Selective Toxicities toward Oxygenated and Hypoxie Tumor Cells1. *Cancer Res.* 41:73–81.
Tello, D., E. Balsa, B. Acosta-Iborra, E. Fuertes-Yebra, A. Elorza, Á. Ordóñez, M. Corral-Escariz, I. Soro, E. López-Bernardo, E. Perales-Clemente, A. Martínez-Ruiz, J.A. Enríquez, J. Aragonés, S. Cadenas, and M.O. Landázuri. 2011. Induction of the mitochondrial NDUFA4L2 protein by HIF-1α decreases oxygen consumption by inhibiting Complex I activity. *Cell Metab.* 14:768–779.
Terris, D.J., E.Y. Ho, H.Z. Ibrahim, M.J. Dorie, M.S. Kovacs, Q.T. Le, A.C. Koong, H.A. Pinto, and J. Martin Brown. 2002. Estimating DNA repair by sequential evaluation of head and neck tumor radiation sensitivity using the comet assay. *Arch. Otolaryngol. Head. Neck Surg.* 128:698–702.
Thermann, M., L. Jostarndt, F. Eberhard, H. Richter, and W. Saß. 1985. [Oxygen supply of the human small intestine in mechanical ileus]. *Langenbecks Arch. Chir.* 363:179–184.
Thimmulappa, R.K., K.H. Mai, S. Srisuma, T.W. Kensler, M. Yamamoto, and S. Biswal. 2002. Identification of Nrf2-regulated Genes Induced by the Chemopreventive Agent Sulforaphane by Oligonucleotide Microarray 1. *CANCER Res.* 62:5196–5203.
Thomlinson, R.H., and L.H. Gray. 1955. The Histological Structure of Some Human Lung Cancers and the Possible Implications for Radiotherapy. *Br. J. Cancer*. 9:539.
Tian, H., S.L. McKnight, and D.W. Russell. 1997. Endothelial PAS domain protein 1 (EPAS1), a transcription factor selectively expressed in endothelial cells. *Genes Dev.* 11:72–82.
Tosun, Ç., A.L.D. Wallabregue, M. Mallerman, S.E. Phillips, C.M. Edwards, S.J. Conway, and E.M. Hammond. 2023. Antibody-Based Imaging of Bioreductive Prodrug Release in Hypoxia. *JACS Au*. 3:3237–3246.
Toth, R.K., and N.A. Warfel. 2017. Strange Bedfellows: Nuclear Factor, Erythroid 2-Like 2 (Nrf2) and Hypoxia-Inducible Factor 1 (HIF-1) in Tumor Hypoxia. *Antioxidants*

(Basel, Switzerland). 6.

Traverso, N., R. Ricciarelli, M. Nitti, B. Marengo, A.L. Furfaro, M.A. Pronzato, U.M. Marinari, and C. Domenicotti. 2013. Role of Glutathione in Cancer Progression and Chemoresistance. *Oxid. Med. Cell. Longev.* 2013.

Tsuchiya, Y., S.Y. Peak-Chew, C. Newell, S. Miller-Aidoo, S. Mangal, A. Zhyvoloup, J. Baković, O. Malanchuk, G.C. Pereira, V. Kotiadis, G. Szabadkai, M.R. Duchen, M. Campbell, S.R. Cuenca, A. Vidal-Puig, A.M. James, M.P. Murphy, V. Filonenko, M. Skehel, and I. Gout. 2017. Protein CoAlation: a redox-regulated protein modification by coenzyme A in mammalian cells. *Biochem. J.* 474:2489.

Tsuchiya, Y., A. Zhyvoloup, J. Baković, N. Thomas, B.Y.K. Yu, S. Das, C. Orengo, C. Newell, J. Ward, G. Saladino, F. Comitani, F.L. Gervasio, O.M. Malanchuk, A.I. Khoruzhenko, V. Filonenko, S.Y. Peak-Chew, M. Skehel, and I. Gout. 2018. Protein CoAlation and antioxidant function of coenzyme A in prokaryotic cells. *Biochem. J.* 475:1909.

Tu, B.P., and J.S. Weissman. 2002. The FAD- and O(2)-dependent reaction cycle of Ero1-mediated oxidative protein folding in the endoplasmic reticulum. *Mol. Cell*. 10:983–994.

Tuttle, S.W., A. Maity, P.R. Oprysko, A. V. Kachur, I.S. Ayene, J.E. Biaglow, and C.J. Koch. 2007. Detection of Reactive Oxygen Species via Endogenous Oxidative Pentose Phosphate Cycle Activity in Response to Oxygen Concentration: IMPLICATIONS FOR THE MECHANISM OF HIF-1α STABILIZATION UNDER MODERATE HYPOXIA. *J. Biol. Chem.* 282:36790–36796.

Twigger, S.A., B. Dominguez, V. Porto, L. Hacker, A.J. Chalmers, R. Breckenridge, M. Treder, A.C. Sedgwick, F. Dominguez, and E.M. Hammond. 2024. The activity of therapeutic molecular cluster Ag5 is dependent on oxygen level and HIF-1 mediated signalling. *Redox Biol.* 76:103326.

Uchiyama, Y., S. Yamagishi, T. Yamaura, K. Kanazawa, and H. Maruyama. 2023. In Vivo Imaging of Tumor Hypoxia by Maintaining Green Fluorescence of 9-Aminoanthracene Under Hypoxic Conditions. *Bioorg. Med. Chem.* 91:117407.

Ullah, M.S., A.J. Davies, and A.P. Halestrap. 2006. The plasma membrane lactate transporter MCT4, but not MCT1, is up-regulated by hypoxia through a HIF-1alpha-dependent mechanism. *J. Biol. Chem.* 281:9030–9037.

Ursini, F., and M. Maiorino. 2020. Lipid peroxidation and ferroptosis: The role of GSH and GPx4. *Free Radic. Biol. Med.* 152:175–185.

Vafa, O., M. Wade, S. Kern, M. Beeche, T.K. Pandita, G.M. Hampton, and G.M. Wahl. 2002. c-Myc can induce DNA damage, increase reactive oxygen species, and mitigate p53 function: a mechanism for oncogene-induced genetic instability. *Mol. Cell*. 9:1031–1044.

Vahrmeijer, A.L., M. Hutteman, J.R. Van Der Vorst, C.J.H. Van De Velde, and J. V. Frangioni. 2013. Image-guided cancer surgery using near-infrared fluorescence. *Nat. Rev. Clin. Oncol.* 10:507–518.

Valko, M., C.J. Rhodes, J. Moncol, M. Izakovic, and M. Mazur. 2006. Free radicals, metals and antioxidants in oxidative stress-induced cancer. *Chem. Biol. Interact.* 160:1–40.

Vancura, A., P. Bu, M. Bhagwat, J. Zeng, and I. Vancurova. 2018. Metformin as an Anticancer Agent. *Trends Pharmacol. Sci.* 39:867.

Vasavda, C., R. Kothari, A.P. Malla, R. Tokhunts, A. Lin, M. Ji, C. Ricco, R. Xu, H.G.

Saavedra, J.I. Sbodio, A.M. Snowman, L. Albacarys, L. Hester, T.W. Sedlak, B.D. Paul, and S.H. Snyder. 2019. Bilirubin links heme metabolism to neuroprotection by scavenging superoxide. *Cell Chem. Biol.* 26:1450.

Vaupel, P., and L. Harrison. 2004. Tumor hypoxia: causative factors, compensatory mechanisms, and cellular response. *Oncologist*. 9 Suppl 5:4–9.

Vaupel, P., M. Höckel, and A. Mayer. 2007. Detection and characterization of tumor hypoxia using pO2 histography. *Antioxid. Redox Signal.* 9:1221–1235.

Vaupel, P., F. Kallinowski, and P. Okunieff. 1989. Blood flow, oxygen and nutrient supply, and metabolic microenvironment of human tumors: a review. *Cancer Res.* 49:6449–6465.

Vengellur, A., B.G. Woods, H.E. Ryan, R.S. Johnson, and J.J. Lapres. 2003. Gene expression profiling of the hypoxia signaling pathway in hypoxia-inducible factor 1alpha null mouse embryonic fibroblasts. *Gene Expr.* 11:181–197.

Wallabregue, A.L.D., H. Bolland, S. Faulkner, E.M. Hammond, and S.J. Conway. 2023. Two Color Imaging of Different Hypoxia Levels in Cancer Cells. *J. Am. Chem. Soc.* 145:2572–2583.

Wang, G.L., B.H. Jiang, E.A. Rue, and G.L. Semenza. 1995. Hypoxia-inducible factor 1 is a basic-helix-loop-helix-PAS heterodimer regulated by cellular O2 tension. *Proc. Natl. Acad. Sci. U. S. A.* 92:5510–5514.

Wang, G.L., and G.L. Semenza. 1993. General involvement of hypoxia-inducible factor 1 in transcriptional response to hypoxia. *Proc. Natl. Acad. Sci. U. S. A.* 90:4304–4308.

Wang, G.L., and G.L. Semenza. 1995. Purification and characterization of hypoxia-inducible factor 1. *J. Biol. Chem.* 270:1230–1237.

Wang, J., K.A. Biedermann, and J. Martin Brown. 1992. Repair of DNA and chromosome breaks in cells exposed to SR 4233 under hypoxia or to ionizing radiation. *Cancer Res.* 52:4473–4477.

Wang, L., W. Yang, Y. Song, Y. Gu, and Y. Hu. 2020a. A double-indole structure fluorescent probe for monitoring sulfur dioxide derivatives with distinct ratiometric fluorescence signals in mammalian cells. *Spectrochim. Acta - Part A Mol. Biomol. Spectrosc.* 225:2–8.

Wang, S., X.F. Zhang, H.S. Wang, J. Liu, S.L. Shen, and X.Q. Cao. 2023. A highly sensitive NIR fluorescence probe for hypoxia imaging in cells and ulcerative colitis. *Talanta*. 252:123834.

Wang, W., H. Fang, L. Groom, A. Cheng, W. Zhang, J. Liu, X. Wang, K. Li, P. Han, M. Zheng, J. Yin, W. Wang, M.P. Mattson, J.P.Y. Kao, E.G. Lakatta, S.S. Sheu, K. Ouyang, J. Chen, R.T. Dirksen, and H. Cheng. 2008. Superoxide flashes in single mitochondria. *Cell*. 134:279–290.

Wang, W., C.P. Winlove, and C.C. Michel. 2003. Oxygen partial pressure in outer layers of skin of human finger nail folds. *J. Physiol.* 549:855.

Wang, X., X. Shen, Y. Yan, and H. Li. 2021. Pyruvate dehydrogenase kinases (PDKs): an overview toward clinical applications. *Biosci. Rep.* 41:1–15.

Wang, Y., X. Han, X. Zhang, L. Zhang, and L. Chen. 2020b. A high-selectivity fluorescent probe for hypoxia imaging in cells and a tumor-bearing mouse model. *Analyst*. 145:1389–1395.

Wang, Y., Y. Liu, S.N. Malek, P. Zheng, and Y. Liu. 2011. Targeting HIF1α eliminates cancer stem cells in hematological malignancies. *Cell Stem Cell*. 8:399–411.

Warburg, O. 1924. Über den Stoffwechsel der Carcinomzelle. *NW*. 12:1131–1137.
Warburg, O. 1956. On Respiratory Impairment in Cancer Cells. *Science (80-.)*. 124:269–270.
Wardman, P. 2001. Electron transfer and oxidative stress as key factors in the design of drugs selectively active in hypoxia. *Curr. Med. Chem.* 8:739–761.
Wardman, P. 2007. Chemical radiosensitizers for use in radiotherapy. *Clin. Oncol. (R. Coll. Radiol)*. 19:397–417.
Wardman, P., M.F. Dennis, S.A. Everett, K.B. Patel, M.R. Stratford, and M. Tracy. 1995. Radicals from one-electron reduction of nitro compounds, aromatic N-oxides and quinones: the kinetic basis for hypoxia-selective, bioreductive drugs. *Biochem. Soc. Symp.* 61:171–194.
Wartenberg, M., F.C. Ling, M. Müschen, F. Klein, H. Acker, M. Gassmann, K. Petrat, V. Pütz, J. Hescheler, and H. Sauer. 2003. Regulation of the multidrug resistance transporter P-glycoprotein in multicellular tumor spheroids by hypoxia-inducible factor (HIF-1) and reactive oxygen species. *FASEB J.* 17:503–505.
Watanabe, Y., C.E. Murdoch, S. Sano, Y. Ido, M.M. Bachschmid, R.A. Cohen, and R. Matsui. 2016. Glutathione adducts induced by ischemia and deletion of glutaredoxin-1 stabilize HIF-1α and improve limb revascularization. *Proc. Natl. Acad. Sci. U. S. A.* 113:6011–6016.
Waypa, G.B., J.D. Marks, R. Guzy, P.T. Mungai, J. Schriewer, D. Dokic, and P.T. Schumacker. 2010. Hypoxia triggers subcellular compartmental redox signaling in vascular smooth muscle cells. *Circ. Res.* 106:526–535.
Webb, J.D., M.L. Coleman, and C.W. Pugh. 2009. Hypoxia, hypoxia-inducible factors (HIF), HIF hydroxylases and oxygen sensing. *Cell. Mol. Life Sci.* 66:3539–3554.
Weidemann, A., and R.S. Johnson. 2008. Biology of HIF-1α. *Cell Death Differ. 2008 154*. 15:621–627.
Weinberg, R.A. 2014. Coming full circle - From endless complexity to simplicity and back again. *Cell*. 157:267–271.
Wenger, R., V. Kurtcuoglu, C. Scholz, H. Marti, and D. Hoogewijs. 2015. Frequently asked questions in hypoxia research. *Hypoxia (Auckland, N.Z.)*. 3:35.
Wheaton, W.W., and N.S. Chandel. 2011. Hypoxia. 2. Hypoxia regulates cellular metabolism. *Am. J. Physiol. Cell Physiol.* 300.
Wheaton, W.W., S.E. Weinberg, R.B. Hamanaka, S. Soberanes, L.B. Sullivan, E. Anso, A. Glasauer, E. Dufour, G.M. Mutlu, G.R. Scott Budigner, and N.S. Chandel. 2014. Metformin inhibits mitochondrial complex I of cancer cells to reduce tumorigenesis. *Elife*. 3.
WHO. Cancer.
WHO. Global cancer burden growing, amidst mounting need for services.
Wiesener, M.S., J.S. Jürgensen, C. Rosenberger, C.K. Scholze, J.H. Hörstrup, C. Warnecke, S. Mandriota, I. Bechmann, U.A. Frei, C.W. Pugh, P.J. Ratcliffe, S. Bachmann, P.H. Maxwell, and K.U. Eckardt. 2003. Widespread hypoxia-inducible expression of HIF-2alpha in distinct cell populations of different organs. *FASEB J.* 17:271–273.
Wilson, D.F., W.L. Rumsey, T.J. Green, and J.M. Vanderkooi. 1988. The oxygen dependence of mitochondrial oxidative phosphorylation measured by a new optical method for measuring oxygen concentration. *J. Biol. Chem.* 263:2712–2718.

Wilson, W.R., and M.P. Hay. 2011. Targeting hypoxia in cancer therapy. *Nat. Rev. Cancer*. 11:393–410.

Winterbourn, C.C., and M.B. Hampton. 2008. Thiol chemistry and specificity in redox signaling. *Free Radic. Biol. Med.* 45:549–561.

Witz, I.P., and O. Levy-Nissenbaum. 2006. The tumor microenvironment in the post-PAGET era. *Cancer Lett.* 242:1–10.

Wong, C.C.L., D.M. Gilkes, H. Zhang, J. Chen, H. Wei, P. Chaturvedi, S.I. Fraley, C.M. Wong, U.S. Khoo, I.O.L. Ng, D. Wirtz, and G.L. Semenza. 2011. Hypoxia-inducible factor 1 is a master regulator of breast cancer metastatic niche formation. *Proc. Natl. Acad. Sci. U. S. A.* 108:16369–16374.

Woo, S.H., I.C. Park, M.J. Park, H.C. Lee, S.J. Lee, Y.J. Chun, S.H. Lee, S. Il Hong, and C.H. Rhee. 2002. Arsenic trioxide induces apoptosis through a reactive oxygen species-dependent pathway and loss of mitochondrial membrane potential in HeLa cells. *Int. J. Oncol.* 21:57–63.

Worth, K.R., I. Papandreou, and E.M. Hammond. 2022. How the histological structure of some lung cancers shaped almost 70 years of radiobiology. *Br. J. Cancer*. 128:407–412.

Wu, G., Y.Z. Fang, S. Yang, J.R. Lupton, and N.D. Turner. 2004. Glutathione Metabolism and Its Implications for Health. *J. Nutr.* 134:489–492.

Wu, K.C., J.Y. Cui, and C.D. Klaassen. 2011a. Beneficial role of Nrf2 in regulating NADPH generation and consumption. *Toxicol. Sci.* 123:590–600.

Wu, L., Y. Ishigaki, W. Zeng, T. Harimoto, B. Yin, Y. Chen, S. Liao, Y. Liu, Y. Sun, X. Zhang, Y. Liu, Y. Liang, P. Sun, T. Suzuki, G. Song, Q. Fan, and D. Ye. 2021. Generation of hydroxyl radical-activatable ratiometric near-infrared bimodal probes for early monitoring of tumor response to therapy. *Nat. Commun. 2021 121*. 12:1–13.

Wu, M.Z., Y.P. Tsai, M.H. Yang, C.H. Huang, S.Y. Chang, C.C. Chang, S.C. Teng, and K.J. Wu. 2011b. Interplay between HDAC3 and WDR5 is essential for hypoxia-induced epithelial-mesenchymal transition. *Mol. Cell*. 43:811–822.

Wu, Q., J. Deng, D. Fan, Z. Duan, C. Zhu, R. Fu, and S. Wang. 2018. Ginsenoside Rh4 induces apoptosis and autophagic cell death through activation of the ROS/JNK/p53 pathway in colorectal cancer cells. *Biochem. Pharmacol.* 148:64–74.

Xiao, G.G., M. Wang, N. Li, J.A. Loo, and A.E. Nel. 2003. Use of proteomics to demonstrate a hierarchical oxidative stress response to diesel exhaust particle chemicals in a macrophage cell line. *J. Biol. Chem.* 278:50781–50790.

Xin, X., Y. Li, and H. Liu. 2020. Hesperidin ameliorates hypobaric hypoxia-induced retinal impairment through activation of Nrf2/HO-1 pathway and inhibition of apoptosis. *Sci. Rep.* 10.

Yamamoto, M., T.W. Kensler, and H. Motohashi. 2018. The KEAP1-NRF2 System: a Thiol-Based Sensor-Effector Apparatus for Maintaining Redox Homeostasis. *Physiol. Rev.* 98:1169–1203.

Yang, X., J. Bai, and Y. Qian. 2020. The investigation of unique water-soluble heptamethine cyanine dye for use as NIR photosensitizer in photodynamic therapy of cancer cells. *Spectrochim. Acta - Part A Mol. Biomol. Spectrosc.* 228:1–7.

Yao, S., Z. Wu, Y. Zhang, T. Yang, H. Yuan, W. Ding, W. He, Z. Guo, and Y. Chen. 2024. Dual-Mode Reversible Imaging of the Hypoxia Status of Acute and Chronic Hepatic Injury. *CCS Chem.* 1–14.

Yohena, T., I. Yoshino, T. Takenaka, T. Kameyama, T. Ohba, Y. Kuniyoshi, and Y.

Maehara. 2009. Upregulation of hypoxia-inducible factor-1alpha mRNA and its clinical significance in non-small cell lung cancer. *J. Thorac. Oncol.* 4:284–290.
Yu, A.Y., M.G. Frid, L.A. Shimoda, C.M. Wiener, K. Stenmark, and G.L. Semenza. 1998. Temporal, spatial, and oxygen-regulated expression of hypoxia-inducible factor-1 in the lung. *Am. J. Physiol.* 275.
Yuan, J., and D. Ofengeim. 2024. A guide to cell death pathways. *Nat. Rev. Mol. Cell Biol.* 25:379–395.
Yuan, J., Y.Q. Xu, N.N. Zhou, R. Wang, X.H. Qian, and Y.F. Xu. 2014. A highly selective turn-on fluorescent probe based on semi-cyanine for the detection of nitroreductase and hypoxic tumor cell imaging. *RSC Adv.* 4:56207–56210.
Yun, Z., H.L. Maecker, R.S. Johnson, and A.J. Giaccia. 2002. Inhibition of PPAR gamma 2 gene expression by the HIF-1-regulated gene DEC1/Stra13: a mechanism for regulation of adipogenesis by hypoxia. *Dev. Cell*. 2:331–341.
van der Zanden, S.Y., X. Qiao, and J. Neefjes. 2021. New insights into the activities and toxicities of the old anticancer drug doxorubicin. *FEBS J.* 288:6095–6111.
Zannella, V.E., A.D. Pra, H. Muaddi, T.D. McKee, S. Stapleton, J. Sykes, R. Glicksman, S. Chaib, P. Zamiara, M. Milosevic, B.G. Wouters, R.G. Bristow, and M. Koritzinsky. 2013. Reprogramming metabolism with metformin improves tumor oxygenation and radiotherapy response. *Clin. Cancer Res.* 19:6741–6750.
Zelko, I.N., T.J. Mariani, and R.J. Folz. 2002. Superoxide dismutase multigene family: a comparison of the CuZn-SOD (SOD1), Mn-SOD (SOD2), and EC-SOD (SOD3) gene structures, evolution, and expression. *Free Radic. Biol. Med.* 33:337–349.
Zhang, H., and H.J. Forman. 2012. Glutathione synthesis and its role in redox signaling. *Semin. Cell Dev. Biol.* 23:722.
Zhang, H., P. Gao, R. Fukuda, G. Kumar, B. Krishnamachary, K.I. Zeller, C.V. V. Dang, and G.L. Semenza. 2007. HIF-1 inhibits mitochondrial biogenesis and cellular respiration in VHL-deficient renal cell carcinoma by repression of C-MYC activity. *Cancer Cell*. 11:407–420.
Zhang, H., C.J. Koch, C.A. Wallen, and K.T. Wheeler. 1995. Radiation-induced DNA damage in tumors and normal tissues. III. Oxygen dependence of the formation of strand breaks and DNA-protein crosslinks. *Radiat. Res.* 142:163–168.
Zhang, J., S. Torabi Kohlbouni, and B. Borhan. 2019a. Cu-Catalyzed Oxidation of C2 and C3 Alkyl-Substituted Indole via Acyl Nitroso Reagents. *Org. Lett.* 21:14–17.
Zhang, Q., Q. Yan, H. Yang, and W. Wei. 2019b. Oxygen sensing and adaptability won the 2019 Nobel Prize in Physiology or medicine. *Genes Dis.* 6:328.
Zhang, S., M. Hosaka, T. Yoshihara, K. Negishi, Y. Iida, S. Tobita, and T. Takeuchi. 2010. Phosphorescent light-emitting iridium complexes serve as a hypoxia-sensing probe for tumor imaging in living animals. *Cancer Res.* 70:4490–4498.
Zhang, Y., W. Zhao, Y. Chen, H. Yuan, H. Fang, S. Yao, C. Zhang, H. Xu, N. Li, Z. Liu, Z. Guo, Q. Zhao, Y. Liang, and W. He. 2021. Rational construction of a reversible arylazo-based NIR probe for cycling hypoxia imaging in vivo. *Nat. Commun.* 12:1–10.
Zhang, Z., Q. Wang, J. Ma, X. Yi, Y. Zhu, X. Xi, Y. Feng, and Z. Jin. 2013. Reactive oxygen species regulate FSH-induced expression of vascular endothelial growth factor via Nrf2 and HIF1α signaling in human epithelial ovarian cancer. *Oncol. Rep.* 29:1429–1434.
Zhao, W., P. Zhuang, Y. Chen, Y. Wu, M. Zhong, and Y. Lun. 2023. “Double-Edged

Sword" Effect of Reactive Oxygen Species (ROS) in Tumor Development and Carcinogenesis. *Physiol. Res*. 72:301.

Zheng, J., S.J. Kim, S. Saeidi, S.H. Kim, X. Fang, Y.H. Lee, Y.N. Guillen-Quispe, H.K.C. Ngo, D.H. Kim, D. Kim, and Y.J. Surh. 2023. Overactivated NRF2 induces pseudohypoxia in hepatocellular carcinoma by stabilizing HIF-1α. *Free Radic. Biol. Med*. 194:347–356.

Zimmer, H., D.C. Lankin, and S.W. Horgan. OXIDATIONS WITH POTASSIUM NITROSODISULFONATE (FREMY'S RADICAL). THE TEUBER REACTION.

Chapter 8: Appendix

8.1 Supplementary information

Table 8.1: **Redox targeting strategies.** Drugs and agents that target an aspect of redox along with the stage of development they are at, references detailed in (An et al., 2024; Porto et al., 2022; Nimalasena et al., 2020).

Compound	Target	Types of cell death	Stage of development
Sorafenib	SLC7A11	Ferroptosis	Approved anti-cancer drug
Sulfasalazine	SLC7A11	Ferroptosis	Approved antibiotics
Erastin	SLC7A11	Ferroptosis	Preclinical
IFNG	SLC7A11	Ferroptosis	Approved immunomodulatory drug
FIN56	GPX4	Ferroptosis	Preclinical
ML162	GPX4	Ferroptosis	Preclinical
ML210	GPX4	Ferroptosis	Preclinical
RSL3	GPX4	Ferroptosis	Preclinical
N6F11	GPX4	Ferroptosis	Preclinical
PdPT	GPX4	Apoptosis and ferroptosis	Preclinical
Plumbagin	GPX4	Apoptosis	Preclinical
Buthionine sulfoximine (BSO)	GCLC	Apoptosis and ferroptosis	Phase I
PX-12	Trx	Apoptosis	Phase II
PMX464	Trx	Apoptosis	Preclinical
Ferroptocide	Trx	Ferroptosis	Preclinical
Auranofin	TrxR	Apoptosis and paraptosis	Approved anti-rheumatoid arthritis drug
Piperlongumine	TrxR	Apoptosis	Preclinical
WZ26	TrxR	Apoptosis	Preclinical
Diffractaic acid	TrxR	Apoptosis	Preclinical
Thimerosal	TrxR	Apoptosis	Preclinical
Shikonin	TrxR	Apoptosis and necroptosis	Preclinical
B63	TrxR	Paraptosis	Preclinical

Jolkinolide B	TrxR	Paraptosis	Preclinical
Nitrovin	TrxR	Paraptosis	Preclinical
2-Methoxyestradiol	SOD1	Apoptosis	Phase II
ATN-224	SOD1	Apoptosis	Phase II
Arsenic trioxide (As_2O_3)	ROS	Apoptosis	Approved anti-cancer drug
Bortezomib	ROS	Apoptosis	Approved anti-cancer drug
Cisplatin	ROS	Apoptosis and ferroptosis	Approved anti-cancer drug
Disulfiram	ROS	Apoptosis	Approved anti-alcoholism drug
5-Fluorouracil (5-FU)	ROS	Apoptosis	Approved anti-cancer drug
Lanperisone	ROS	Non-apoptosis	Approved muscle relaxant
Imexon	ROS	Apoptosis	Phase II
Nelfinavir	ROS	Apoptosis	Approved anti-HIV drug
Withaferin A	ROS	Paraptosis	Phase II
Neobavaisoflavone	ROS	Pyroptosis	Preclinical
Oxaliplatin	ROS	Parthanatos	Approved anti-cancer drug
Sanguinarine	ROS	Oxeiptosis	Preclinical
Auriculasin	ROS	Apoptosis, ferroptosis and oxeiptosis	Preclinical
Ag5	GSH/Trx	Apoptosis	Preclinical
H_2O_2	ROS	/	Phase I

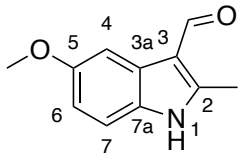
Table 8.2: **Mutational status of the cell lines used in this study.** Details of cell lines used in this study and their mutational status for key genes involved in tumorigenesis. Wild type is shown in green and mutations orange, with grey showing data not available on the DepMap database. OSCC=oesophageal squamous cell carcinoma, OAC=oesophageal adenocarcinoma, NSCLC=non-small cell lung cancer, CCC=clear cell carcinoma, CAC=colorectal adenocarcinoma. Data collected from DepMap (OmicsSomaticMutations database).

Cell line	Tumour type	p53	ARID1A	NFE2L2	KEAP1	K-Ras
OE21	OSCC	S90F and W91GfsTer32		G81S and D318H		
FLO1	OAC	C277F				
OE33	OAC	C135Y				
SKGT4	OAC	Q100Ter				G12A
A549	NSCLC				G333C	G12S
H460	NSCLC		I2135_L2136del		D236H	Q61H
RCC4	CCC					
RKO	CAC		D423TfsTer2, T939RfsTer2, D1850TfsTer33 and P1115QfsTer46		G350S	

8.2 Experimental

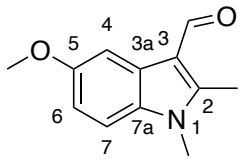
8.2.1 Indolequinone synthesis

Compound 1: 5-Methoxy-2-methyl-1*H*-indole (Huang et al., 2010; Phillips et al., 1999)



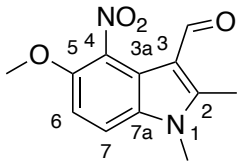
A solution of $POCl_3$ (4.13 mL, 44.4 mmol, 1.4 eq.) in ice water cooled DMF (12.0 mL) was stirred for 10 min at 0 °C to form the Vilsmeier reagent. This solution was then added to a solution of 5-methoxy-2-methyl-1*H*-indole (5.00 g, 31.0 mmol, 1.0 eq.) in anhydrous DMF (10.0 mL) cooled to −10 °C, over a period of 45 min. The reaction mixture was then stirred at 0 °C for a further 45 min and confirmed complete via TLC analysis. The reaction mixture was then added dropwise to an ice-cooled 2 M NaOH aqueous solution (200 mL) before extracting the aqueous phase with DCM (3 × 200 mL). The organic layers were combined, washed with brine (150 mL), 0.5 M LiCl aqueous solution (150 mL) and dried over Na_2SO_4 before filtering under gravity and concentrating *in vacuo*. The resulting brown solid residue was then washed with cooled (0 °C) ethyl acetate (2 × 100 mL) and suction filtered to yield the product as a beige solid (4.22 g, 22.3 mmol, 72 %). R_f 0.4 (6:4 PE/EtOAc); m.p. 178-181 °C (from EtOAc); ^{1}H NMR (400 MHz; $CDCl_3$) δ_H 10.12 (1H, s, H3, CHO), 8.60 (1H, s, NH), 7.76 (1H, d, *J*= 2.5 Hz, H4, Ar), 7.22 (1H, dd, *J*= 8.8, 0.6 Hz, H7, Ar), 6.87 (1H, dd, *J*= 8.8, 2.5 Hz, H6, Ar), 3.87 (3H, s, H5, OMe), 2.72 (3H, s, H2, Me); ESI-LRMS Calculated: 190 $[M + H]^+$ Observed: 190 $[M + H]^+$ (100 %). These data are in good agreement with the literature (Huang et al., 2010; Phillips et al., 1999).

Compound 2: 5-Methoxy-1,2-dimethyl-1*H*-indole-3-carbaldehyde (Huang et al., 2010; Phillips et al., 1999)



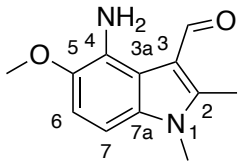
Under an argon atmosphere, a solution of 5-methoxy-2-methyl-1*H*-indole-3-carbaldehyde (1.20 g, 6.34 mmol, 1.0 eq.) in anhydrous DMF (8.00 mL) was gradually added to a suspension of sodium hydride (0.38 g of 60 % in mineral oil, 9.50 mmol, 1.5 eq.) in anhydrous DMF (7.50 mL) whilst stirring at rt. The reaction mixture was then stirred for 2 h at rt before being cooled to 0 °C. Iodomethane (0.47 mL, 7.61 mmol, 1.2 eq.) was then added dropwise to the reaction mixture before warming it back to rt and stirring for another 2 h upon which the reaction was complete, confirmed by TLC. The reaction was then quenched with the slow addition of distilled water (50.0 mL) before extracting the aqueous phase with DCM (3 × 50.0 mL). The consequent organic layers were combined, washed with distilled water (50.0 mL), 0.5 M LiCl aqueous solution (50.0 mL) and brine (50.0 mL) before being dried over Na_2SO_4, filtered under gravity and concentrated *in vacuo*. The resultant yellow solid was purified via silica gel column chromatography (20-40 % EtOAc/PE) to give the product as a pale-yellow solid (1.02 g, 5.02 mmol, 79 %). R_f 0.22 (6:4 PE/EtOAc); m.p. 125-128 °C (from $CHCl_3$); ^{1}H NMR (400 MHz; $CDCl_3$) δ_H 10.10 (1H, s, H3, CHO), 7.79 (1H, d, *J*= 2.6 Hz, H4, Ar), 7.16 (1H, dd, *J*= 8.8, 0.5 Hz, H7, Ar), 6.89 (1H, dd, *J*= 8.8, 2.6 Hz, H6, Ar), 3.89 (3H, s, N1, NMe), 3.65 (3H, s, H5, OMe), 2.63 (3H, s, H2, Me); ESI-MS Calculated 226 $[M + Na]^+$, 204 $[M + H]^+$ Observed 226 $[M + Na]^+$ (100 %), 204 $[M + H]^+$ (79 %). These data are in good agreement with the literature (Huang et al., 2010; Phillips et al., 1999).

Compound 3: 5-Methoxy-1,2-dimethyl-4-nitro-1*H*-indole-3-carbaldehyde (Huang et al., 2010; Phillips et al., 1999)



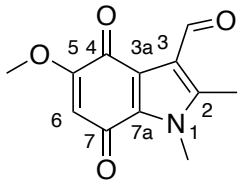
5-Methoxy-1,2-dimethyl-1*H*-indole-3-carbaldehyde (0.50 g, 2.46 mmol, 1.0 eq.) was dissolved in acetic acid (60.0 mL) and cooled to 0 °C. To this solution, a mixture of fuming nitric acid (2.31 mL, 55.4 mmol, 22.5 eq.) in acetic acid (9.00 mL) was added dropwise with stirring over 1 h. The reaction mixture was then stirred for another 3 h and confirmed complete by TLC. After this time, the reaction mixture was added to crushed ice water (100 g) and this suspension was stirred for 10 min. The resultant brown precipitate was collected by suction filtration, washed with distilled water (250 mL) and dried *in vacuo* to give the product as a light brown solid (0.46 g, 1.83 mmol, 74 %). R_f 0.25 (8:2 EtOAc/PE); m.p. 226-228 °C (from AcOH); ^{1}H NMR (400 MHz; $CDCl_3$) δ_H 9.97 (1H, s, H3, CHO), 7.37 (1H, d, *J*= 9.0 Hz, H7, Ar), 7.01 (1H, d, *J*= 9.0 Hz, H6, Ar), 3.94 (3H, s, N1, NMe), 3.73 (3H, s, H5, OMe), 2.74 (3H, s, H2, Me); ESI-MS Calculated 271 $[M + Na]^+$, 249 $[M + H]^+$ Observed 271 $[M + Na]^+$ (100 %), 249 $[M + H]^+$ (16 %). These data are in good agreement with the literature (Huang et al., 2010; Phillips et al., 1999).

Compound 4: 4-Amino-5-methoxy-1,2-dimethyl-1*H*-indole-3-carbaldehyde (Huang et al., 2010; Phillips et al., 1999)



Powdered tin (0.97 g, 8.18 mmol, 5.3 eq.) was added to a solution of 5-methoxy-1,2-dimethyl-4-nitro-1*H*-indole-3-carbaldehyde (0.44 g, 1.77 mmol, 1.1 eq.) in ethanol (30.0 mL). Aqueous 3 M HCl solution (12.0 mL, 36.0 mmol 23.2 eq.) was then added before heating the reaction mixture under reflux (80 °C) for 1 h and confirming completion by TLC. Distilled water (30.0 mL) was then added to the reaction mixture and the pH was adjusted to 8 using saturated sodium hydrogen carbonate solution. The aqueous phase was then extracted with chloroform (5 × 100 mL) and the combined organic layers were washed with brine (50.0 mL), dried over Na_2SO_4, filtered under gravity and concentrated *in vacuo*. The resulting yellow residue was then purified via silica gel column chromatography (50-80 % EtOAc/PE) to give the product as a yellow solid (0.32 g, 1.47 mmol, 94 %). R_f 0.29 (1:1 EtOAc/PE); m.p. 155-157 °C (from $CHCl_3$); ^{1}H NMR (400 MHz; $CDCl_3$) δ_H 9.82 (1H, s, H3, CHO), 6.86 (1H, d, *J*= 8.6 Hz, H7, Ar), 6.48 (1H, d, *J*= 8.6 Hz, H6, Ar), 3.87 (3H, s, N1, NMe), 3.61 (3H, s, H5, OMe), 2.63 (3H, s, H2, Me); ESI-MS Calculated 219 $[M + H]^+$ Observed 219 $[M + H]^+$ (100 %). These data are in good agreement with the literature (Huang et al., 2010; Phillips et al., 1999).

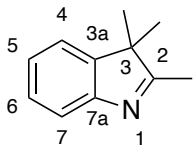
Compound 5: 5-Methoxy-1,2-dimethyl-4,7-dioxo-4,7-dihydro-1*H*-indole-3-carbaldehyde (Huang et al., 2010; Phillips et al., 1999)



A solution of Fremy's salt (0.620 g, 2.33 mmol, 5.0 eq.) in NaH_2PO_4/Na_2HPO_4 buffer (45.0 mL) was added to a solution of 4-amino-5-methoxy-1,2-dimethyl-1*H*-indole-3-carbaldehyde (0.108 g, 0.495 mmol, 1.1 eq.) in acetone (45.0 mL). The reaction mixture was stirred at rt for 1 h and confirmed complete by TLC before removing the acetone *in vacuo* and extracting the aqueous phase with EtOAc (4 × 100 mL). The organic layers were then combined, washed with brine, dried with Na_2SO_4 and filtered under gravity before concentrating *in vacuo*. The resulting orange solid was purified via silica gel column chromatography (3 % acetone in DCM) to give the product as an orange solid (0.0754 g, 0.323 mmol, 65 %). R_f 0.43 (3 % acetone in DCM); m.p. 163-165 °C (from $CHCl_3$); ^{1}H NMR (400 MHz; $CDCl_3$) δ_H 10.55 (1H, s, H3, CHO), 5.71 (1H, s, H6, Ar), 3.94 (3H, s, N1, NMe), 3.85 (3H, s, H5, OMe), 2.62 (3H, s, H2, Me); ESI-MS Calculated 256 $[M + Na]^+$, 234 $[M + H]^+$ Observed 256 $[M + Na]^+$ (100 %), 234 $[M + H]^+$ (40 %). These data are in good agreement with the literature (Huang et al., 2010; Phillips et al., 1999).

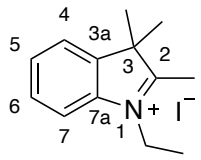
8.2.2 Hemicyanine synthesis:

Compound 6: 2,3,3-Trimethoxy-3*H*-indole (Yang et al., 2020)



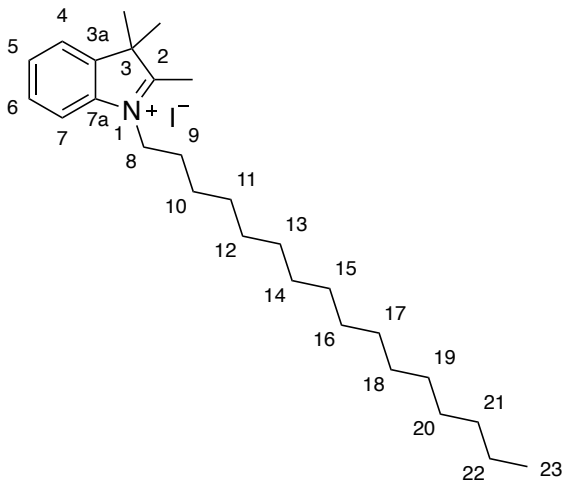
Phenylhydrazine (4.91 mL, 0.0500 mol, 1.0 eq.) and 3-methylbutan-2-one (6.00 mL, 0.0550 mol, 1.1 eq.) were added to ethanol (15.0 mL) along with acetic acid (2 drops). The reaction mixture was heated under reflux (80 °C) for 4 h and then concentrated *in vacuo*. Acetic acid (15.0 mL) was then added to the resultant residue, and it was heated under reflux (80 °C), under argon for 1 h with completion confirmed by TLC. The reaction mixture was then concentrated *in vacuo* and the resulting residue was neutralised with saturated sodium hydrogen carbonate solution (100 mL). The aqueous phase was extracted with DCM (3 × 100 mL) and the organic layers were combined, dried over Na_2SO_4, filtered under gravity and concentrated *in vacuo*. The resulting yellow residue was purified via silica gel column chromatography (7:3 PE/EtOAc) to give the pure product as a yellow oil (6.73 g, 42.3 mmol, 85 %). R_f 0.28 (6:4 PE/EtOAc); ^{1}H NMR (400 MHz; $CDCl_3$) δ_H 7.44 (1H, dt, *J*= 7.6, 1.0 Hz, H7, Ar), 7.21 (1H, dd, *J*= 7.4, 1.4 Hz, H6, Ar), 7.19-7.17 (1H, m, H4, Ar), 7.11 (1H, dd, *J*= 7.3, 1.1 Hz, H5, Ar), 2.18 (3H, s, H2, Me), 1.20 (6H, s, H3, 2 × Me); ESI-MS Calculated 160 $[M + H]^+$ Observed 160 $[M + H]^+$ (100 %). These data are in good agreement with the literature (Yang et al., 2020).

Compound 7: 1-Ethyl-2,3,3-trimethyl-3*H*-indol-1-ium (Wang et al., 2020a)



2,3,3-Trimethyl-3H-indole (1.00 g, 6.28 mmol, 1.0 eq.) was dissolved in a mixture of ethyl iodide (5.05 mL, 62.80 mmol, 10.0 eq.) and acetonitrile (12.0 mL). The reaction mixture was stirred under reflux (85 °C) for 24 h, under argon and confirmed complete by TLC analysis. It was then allowed to cool to rt and ice cooled Et_2O (100 mL) was added. The mixture was then cooled to 0 °C and left to allow the product to precipitate (15 min). Subsequent suction filtration and washing with ice cooled Et_2O (50.0 mL) allowed the product to be collected as a pink powder. This was dried *in vacuo* to yield the desired alkylated product (1.71 g, 5.43 mmol, 86 %). R_f 0.50 (1 % MeOH/DCM); m.p. 207-210 °C (from Et_2O); ^{1}H NMR (400 MHz; $CDCl_3$) δ_H 7.75-7.70 (1H, m, H7, Ar), 7.62-7.56 (3H, m, H4 – H6, Ar), 4.77 (2H, q, *J*= 7.5 Hz, N1, CH_2,), 3.15 (3H, s, H2, Me), 1.65 (6H, s, H3, 2 × Me), 1.62 (3H, t, *J*= 7.4 Hz, N1, Me); ESI-MS Calculated 188 $[M]^+$, 189 $[M + H]^+$ Observed 188 $[M]^+$ (100 %), 189 $[M + H]^+$ (15 %). These data are in good agreement with the literature (Wang et al., 2020a).

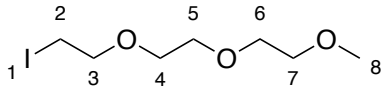
Compound 8: 1-Hexadecyl-2,3,3-trimethyl-3*H*-indol-1-ium (Connell et al., 2014)



2,3,3-Trimethyl-3H-indole (1.00 g, 6.28 mmol, 1.0 eq.) was dissolved in a mixture of iodohexadecane (5.92 mmol, 18.8 mmol, 3.0 eq.) and acetonitrile (15.0 mL). The reaction mixture was stirred under reflux (85 °C) for 24 h, under argon and confirmed complete by TLC analysis. It was then allowed to cool to rt before precipitating the product by the addition of ice cooled Et_2O (100 mL) and leaving at 0 °C for 15 min. Subsequent suction filtration was then used to collect the product as a light pink solid after washing with ice cooled Et_2O (20.0 mL). This was dried *in vacuo* to yield the desired alkylated product (1.86 g, 3.63 mmol, 58 %). R_f 0.16 (9:1 DCM/MeOH); m.p. 97-99 °C (from Et_2O); ^{1}H NMR (400 MHz; $CDCl_3$) δ_H 7.64-7.53 (4H, m, H4 - H7, Ar), 4.70 (2H, t, *J*= 7.8 Hz, H8, CH_2), 3.13 (3H, s, H2, Me), 1.93 (2H, p, *J*= 7.7 Hz, H9, CH_2), 1.66 (6H, s, H3, 2 × Me), 1.51-1.32 (26H, m, H10 - H22, CH_2), 0.87 (3H, t, *J*= 6.7 Hz, H23, Me); ESI-MS Calculated 384 $[M]^+$, 385 $[M + H]^+$ Observed 384 $[M]^+$ (100 %), 385 $[M + H]^+$ (29 %). These data are in good agreement with the literature (Connell et al., 2014).

8.2.3 PEG derivative synthesis:

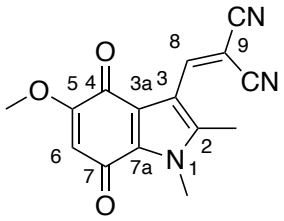
Compound 9: 1-Iodo-2-(2-(2-methoxyethoxy)ethoxy)ethane (Descotes and Pralyet, 1986)



2-(2-(2-Methoxyethoxy)ethoxy)ethan-1-ol (0.97 mL, 6.09 mmol, 1.0 eq.) was added to toluene (30.0 mL) along with PPh_3 (1.92 g, 7.31 mmol, 1.2 eq.), imidazole (1.24 g, 18.27 mmol, 3.0 eq.) and iodine (2.01 g, 7.92 mmol, 1.3 eq.). The reaction mixture was then stirred (90 °C) for 2 h, confirmed complete by TLC, before removing the solvent *in vacuo*. The resulting residue was dissolved in DCM and washed with saturated $Na_2S_2O_3$ solution (50.0 mL), distilled water (50.0 mL) and brine (50.0 mL). The combined organic layers were dried over Na_2SO_4, filtered under gravity and concentrated *in vacuo* to yield the product as a light brown oil (0.57 g, 2.09 mmol, 34 %). R_f 0.45 (5 % MeOH in DCM); ^1H NMR (400 MHz; $CDCl_3$) δ_H 3.79-3.55 (12H, m, H2 – H7, CH_2), 3.39 (3H, s, H8, Me); ESI-MS Calculated 297 $[M + Na]^+$ Observed 297 $[M + Na]^+$ (21 %). These data are in good agreement with the literature (Descotes and Pralyet, 1986).

8.2.4 Other Knoevenagel condensation syntheses:

Compound 10: 2-((5-Methoxy-1,2-dimethyl-4,7-dioxo-4,7-dihydro-1*H*-indol-3-yl)methylene)malononitrile



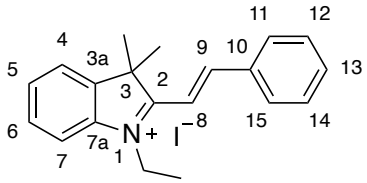
Toluene conditions: Piperidine (10 μL) and acetic acid (10 μL) were added to a mixture of 5-methoxy-1,2-dimethyl-4,7-dioxo-4,7-dihydro-1H-indole-3-carbaldehyde (50.0 mg, 0.214 mmol, 1.0 eq.) and malononitrile (15.0 mg, 0.235 mmol, 1.1 eq.) in toluene (5.00 mL). This reaction mixture was heated under reflux (110 °C) and checked by TLC for completion. After 24 h the reaction was complete and allowed to cool to rt before removing the solvent *in vacuo*. The resulting residue was dissolved in DCM (15.0 mL) and the organic layer was washed with distilled water (3 × 15.0 mL). The organic layers were then combined, washed with brine (50.0 mL), dried over Na_2SO_4, filtered under gravity and concentrated *in vacuo* before azeotroping with $CHCl_3$. The resulting residue was purified via silica gel column chromatography (0.5 - 5 % MeOH in DCM) to give the product.

Acetic anhydride conditions: 5-methoxy-1,2-dimethyl-4,7-dioxo-4,7-dihydro-1H-indole-3-carbaldehyde (50.0 mg, 0.214 mmol, 1.0 eq.) and malononitrile (0.14 g, 2.14 mmol, 10.0 eq.) were added to Ac_2O (3.00 mL) and the reaction mixture was heated under reflux (140 °C). The reaction mixture was checked for completion by TLC and was complete after 24 h. It was then cooled to 100 °C before adding distilled water (10.0 mL) and refluxing for 1 h. The reaction mixture was then allowed to cool to rt and the aqueous layer

was extracted with DCM (5 × 75.0 mL). The organic layers were combined and washed with brine (50.0 mL) before drying over Na_2SO_4, filtering under gravity, concentrating *in vacuo* and azeotroping with $CHCl_3$. The resulting residue was purified via silica gel column chromatography (1 - 5 % MeOH in DCM) to give the product.

R_f 0.43 (1 % MeOH in DCM); ^{1}H NMR (400 MHz; $CDCl_3$) δ_H 8.33 (1H, s, H8), 5.72 (1H, s, H6, Ar), 3.98 (3H, s, N1, NMe), 3.83 (3H, s, H5, OMe), 2.38 (3H, s, H2, Me); ^{13}C NMR (100 MHz; $CDCl_3$) δ_C 154.7 (C8), 107.0 (C6), 56.9 (C5, OMe), 33.2 (N1, NMe), 13.6 (C2, Me); ESI-MS Calculated 304 $[M + Na]^+$, 282 $[M + H]^+$ Observed 304 $[M + Na]^+$ (74 %), 282 $[M + H]^+$ (55 %). Characterisation incomplete as this compound was purely synthesised for a problem-solving purpose.

Compound 11: (*E*)-1-Ethyl-3,3-dimethyl-2-styryl-3*H*-indol-1-ium



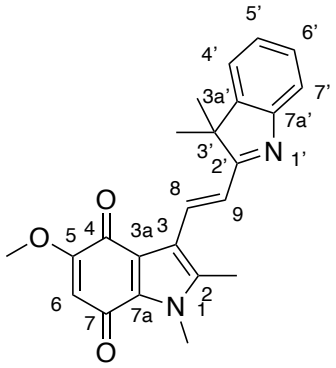
Toluene conditions: Piperidine (20.0 μL) and acetic acid (20.0 μL) were added to a mixture of 1-ethyl-2,3,3-trimethyl-3H-indol-1-ium (0.100 g, 0.317 mmol, 1.0 eq.) and benzaldehyde (0.0370 g, 0.349 mmol, 1.1 eq.). The reaction mixture was heated under reflux (110 °C) and checked for completion by TLC. After 21 h 15 min the reaction was complete and allowed to cool to RT. The solvent was then removed *in vacuo* and the resultant residue was dissolved in DCM (50.0 mL) before washing with distilled water (3 × 50.0 mL) and brine (50.0 mL), drying over Na_2SO_4, filtering under gravity and concentrating in vacuo.

Ethanol conditions: Piperidine (2 drops) was added to a mixture of 1-ethyl-2,3,3-trimethyl-3H-indol-1-ium (250 mg, 1.07 mmol, 1.0 eq.) and benzaldehyde (130 mg, 1.18 mmol, 1.1 eq.) in ethanol (5.00 mL). The reaction mixture was then heated under reflux (80 °C) and checked by TLC for completion. After 2 h 45 min the reaction was complete, and the reaction mixture was allowed to cool to rt before concentrating *in vacuo*. The resulting residue was then dissolved in water (50.0 mL) and extracted with DCM (7 × 50.0 mL). The organic layers were combined and washed with brine (50.0 mL) before drying over Na_2SO4, filtering under gravity and concentrating *in vacuo* prior to azeotroping with $CHCl_3$. The resultant brown residue was purified via silica gel column chromatography (20 % acetone: DCM) to give the product as a yellow solid (23.0 mg, 0.0570 mmol, 5 %).

R_f 0.13 (20 % acetone in DCM; ATR-IR υ max/cm^{-1}: 3054 (C=C), 2926, 2854, 2361, 1704, 1607, 1575, 1530, 1488, 1451; ^{1}H NMR (400 MHz; $CDCl_3$) δ_C 8.25 (1H, d, *J*= 16.3 Hz, H8), 8.21-8.18 (2H, m, H, Ar), 7.82 (1H, d, *J*= 16.3 Hz, H9), 7.72-7.68 (1H, m, H, Ar), 7.63-7.49 (6H, m, H, Ar), 5.05 (2H, q, *J*= 7.4 Hz, N1, CH_2), 1.87 (6H, s, H3, 2 × Me), 1.62 (3H, t, *J*= 7.4 Hz, N1, Me); ^{13}C NMR (100 MHz; $CDCl_3$) δ_H 181.7 (C), 155.2 (C8), 143.6 (C), 140.3 (C), 134.3 (C, Ar), 133.7 (C), 131.5 (C), 130.3, 129.9, 129.7, 123.0 (C, Ar), 115.2 (C), 112.8 (C9), 53.9 (C), 52.8 (C), 44.9 (N1, CH_2), 29.8 (C), 29.4 (C), 27.1 (C3), 14.5 (N1, CH3); ESI-MS Calculated 276 $[M]^+$, 277 $[M + H]^+$ Observed 276 $[M]^+$ (100 %), 277 $[M + H]^+$ (22 %). Characterisation incomplete as this compound was purely synthesised for a problem-solving purpose.

8.2.5 Initial probe synthesis:

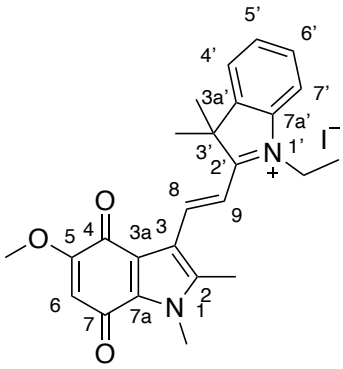
Compound 12 (**NA-HCIQ**): (*E*)-3-(2-(3,3-Dimethyl-3*H*-indol-2-yl)vinyl)-5-methoxy-1,2-dimethyl-1*H*-indole-4,7-dione



Piperidine (30.0 μL) and acetic acid (30.0 μL) were added to a solution of 2,3,3-trimethyl-3*H*-indole (67.5 mg, 0.424 mmol, 1.0 eq.) and 5-methoxy-1,2-dimethyl-4,7-dioxo-4,7-dihydro-1*H*-indole-3-carbaldehyde (98.9 mg, 0.424 mmol, 1.0 eq.) in toluene (3.00 mL) before heating under reflux (110 °C) for 22 h. Reaction completion was confirmed by TLC analysis and the reaction mixture was then left to cool to rt before being concentrated *in vacuo*. The resulting red residue was then azeotrope with $CHCl_3$ and purified via silica gel column chromatography (1 % MeOH in DCM) to give the product as a red solid (87.7 mg, 0.234 mmol, 55 %). R_f 0.5 (1 % MeOH in DCM); m.p. <300 °C (from $CHCl_3$); ATR-IR υ max/cm^{-1}: 2966, 2932, 2863, 2360, 1667, 1633, 1604, 1511, 1496, 1453, 1410; ^{1}H NMR (600 MHz; $CDCl_3$) δ_H 8.04 (1H, d, *J*= 16.7 Hz, H8), 7.63 (1H, d, *J*= 16.7 Hz, H9), 7.61-7.59 (1H, m, Ar), 7.36-7.29 (2H, m, Ar), 7.23 (1H, td, *J*= 7.3, 1.1 Hz, Ar), 5.70 (1H, s, H6), 3.99 (3H, s, N1, NMe), 3.86 (3H, s, H5, OMe), 2.50 (3H, s, H2, Me), 1.53 (6H, s, H3', 2 × Me), 1.65 (3H, t, *J*= 7.3 Hz, N1', CH_3); ^{13}C NMR (151 MHz; $CDCl_3$) δ_C 184.7 (C2'), 178.8 (C7), 177.8 (C4), 160.0 (C5), 147.1 (C2), 129.9 (C8), 127.8 (C, Ar), 125.7 (C, Ar), 123.1 (C9), 121.3 (C, Ar), 120.8 (C3a, C7a), 120.5 (C, Ar), 119.8 (C7a'), 106.7 (C6), 56.7 (C5, OMe), 53.0 (C3a'), 32.9 (N1, NMe), 24.2 (C3', 2×Me), 11.2 (C2, Me); ESI-HRMS Calculated

375.1709 [M + H]$^+$ Observed 375.1701 [M + H]$^+$; ESI-MS Calculated 375 [M + H]$^+$ Observed 375 [M + H]$^+$ (100 %); 98 % pure by HPLC analysis.

Compound 13 (**HClQ**): (*E*)-1-Ethyl-2-(2-(5-methoxy-1,2-dimethyl-4,7-dioxo-4,7-dihydro-1*H*-indpl-3-yl)vinyl)-3,3-dimethyl-3*H*-indol-1-ium

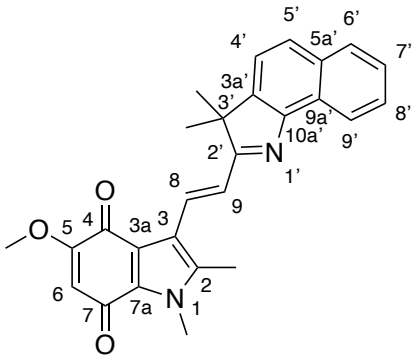


(*E*)-3-(2-(3,3-Dimethyl-3*H*-indol-2-yl)vinyl)-5-methoxy-1,2-dimethyl-1*H*-indole-4,7-dione (30.0 mg, 80.1 μmol, 1.0 eq.) was dissolved in MeCN (20 drops) and ethyl iodide (750 μL). The reaction mixture was heated (65 °C), under argon, in the dark and monitored using TLC analysis. After 18 h the reaction was confirmed to be complete by TLC, and the reaction mixture was cooled to rt, before the solvent was removed *in vacuo*. The resulting red residue was purified via silica gel column chromatography (1 – 5 % MeOH in DCM) to give the pure product as a red solid (31.2 mg, 58.8 μmol, 73 %). R_f 0.35 (5 % MeOH in DCM); m.p. >300 °C (from $CHCl_3$); ATR-IR υ max/cm^{-1}: 3468, 2980, 1635, 1601, 1590, 1540, 1504, 1461, 1403; ^{1}H NMR (600 MHz; $CDCl_3$) δ_H 8.81 (1H, d, *J*= 16.3 Hz, H8), 8.01 (1H, d, *J*= 16.3 Hz, H9), 7.62-7.53 (4H, m, H4' – H7'), 5.78 (1H, s, H6), 4.90 (2H, q, *J*= 7.3 Hz, N1', CH_2), 4.05 (3H, s, N1, NMe), 3.89 (3H, s, H5, OMe), 2.94 (3H, s, H2, Me), 1.89 (6H, s, H3', 2 × Me), 1.65 (3H, t, *J*= 7.3 Hz, N1', CH_3); ^{13}C NMR (151 MHz; $CDCl_3$) δ_C 182.1 (C2'), 178.5 (C4), 178.3 (C7), 159.6 (C5), 146.7 (C8), 145.8 (C2), 143.4 (C3a'), 140.3 (C7a'), 131.4 (C7a), 130.7 (C6'), 129.6 (C5'), 123.0 (C4'), 121.2 (C3a), 118.0 (C3), 114.2

(C7'), 112.6 (C9), 106.9 (C6), 56.91 (C5, OMe), 52.4 (C3'), 43.8 (N1', CH_2), 33.4 (N1, Me), 27.4 (C3', 2×Me), 14.2 (C2, Me), 13.7 (N1', CH_3); ESI-HRMS Calculated 403.2022 [M], 404.2100 $[M + H]^+$ Observed 403.2014 [M], 404.2050 $[M + H]^+$;ESI-MS Calculated 403 $[M]^+$, 404 $[M + H]^+$ Observed 403 $[M]^+$ (100 %), 404 $[M + H]^+$ (27 %) ; 98 % pure by HPLC analysis.

8.2.6 Fluorophore variation probe synthesis:

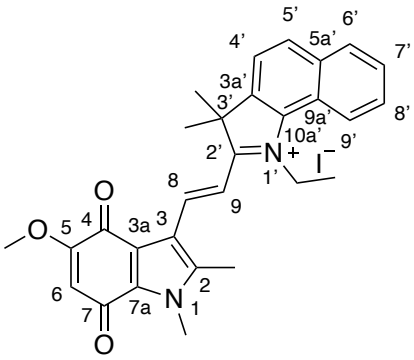
Compound 14: (*E*)-3-(2-(3,3-Dimethyl-3*H*-benzo[*g*]indol-2-yl)vinyl-5-methoxy-1,2-dimethyl-1*H*-indole-4,7-dione



Piperidine (20.0 μL) and acetic acid (20.0 μL) were added to a solution of 2,3,3-trimethyl-3*H*-benzo[*g*]indole (17.9 mg, 85.8 μmol, 1.0 eq.) and 5-methoxy-1,2-dimethyl-4,7-dioxo-4,7-dihydro-1*H*-indole-3-carbaldehyde (20.0 mg, 85.8 μmol, 1.0 eq.) in toluene (3.00 mL) before heating under reflux (110 °C) for 24 h. The reaction mixture was confirmed complete via TLC analysis and then left to cool to rt before removing the solvent *in vacuo*. The resulting residue was purified twice via silica gel column chromatography (50:50 PE/EtOAc and 1 % MeOH in DCM) to give the product as a red solid (20.8 mg, 49.0 μmol, 57 %). R_f 0.25 (1 % MeOH in DCM); m.p. 264-266 °C (from $CHCl_3$); ATR-IR υ max/cm^{-1}: 3055, 2925, 2864, 2361, 1634, 1613, 1497, 1459, 1411; ^{1}H NMR (600 MHz; $CDCl_3$) δ_H 8.68 (1H, d, *J*= 8.3 Hz, Ar), 8.22 (1H, d, *J*= 16.8 Hz, H8), 7.89 (1H, d, *J*= 8.2 Hz, Ar), 7.76 (1H, d, *J*= 8.2 Hz, Ar), 7.68 (1H, d, *J*= 16.8 Hz, H9), 7.59 (1H, ddd, *J*= 8.2, 6.8, 1.3 Hz, Ar), 7.52-7.47

(2H, m, Ar), 5.69 (1H, s, H6, Ar), 3.99 (3H, s, N1, NMe), 3.86 (3H, s, H5, OMe), 2.56 (3H, s, H2, Me), 1.61 (6H, s, H3', 2 × Me); ^{13}C NMR (151 MHz; $CDCl_3$) δ_C 184.9 (C2'), 178.8 (C7), 177.9 (C4), 160.0 (C5), 143.6 (C3a'), 133.9 (C, Ar), 129.7 (C8), 128.2 (C, Ar), 127.0 (C, Ar), 126.4 (C, Ar), 126.3 (C, Ar), 125.8 (C, Ar), 123.6 (C, Ar), 123.2 (C9), 120.8 (C3), 119.9 (C2), 119.4 (C3a, C7a), 106.7 (C6), 56.8 (C5, OMe), 53.9 (C3'), 32.9 (N1, NMe), 24.0 (C3', 2×Me), 11.5 (C2, Me); ESI-HRMS Calculated 425.1865 $[M + H]^+$ Observed 425.1856 $[M + H]^+$; Calculated 425 $[M + H]^+$ Observed 425 $[M + H]^+$ (100 %).

Compound 15: (*E*)-1-Ethyl-2-(2-(5-methoxy-1,2-dimethyl-4,7-dioxo-4,7-dihydro-1*H*-indol-3-yl)vinyl)-3,3-dimethyl-3*H*-benzo[*g*]indol-1-ium

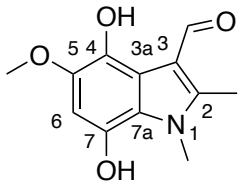


(*E*)-3-(2-(3,3-Dimethyl-3*H*-benzo[*g*]indol-2-yl)vinyl-5-methoxy-1,2-dimethyl-1*H*-indole-4,7-dione (15.0 mg, 35.3 μmol, 1.0 eq.) was dissolved in MeCN (20 drops) and ethyl iodide (500 μL). The reaction mixture was heated (65 °C), under argon, in the dark and monitored by TLC. After 12 h, the solvent was removed in vacuo and the resulting residue was transferred to a microwave vial with ethyl iodide (500 μL) and MeCN (10 drops). The reaction mixture was heated (65 °C), under argon, in the dark for 60 h. TLC analysis confirmed reaction completion and the reaction mixture was cooled to rt before removing the solvent *in vacuo*. The resultant red residue was purified via silica gel column chromatography (1 – 5 % MeOH in DCM) to give the pure product as a red solid (19.5 mg,

33.6 μmol, 95 %). R_f 0.25 (5 % MeOH in DCM); m.p. >300 °C (from $CHCl_3$); ATR-IR υ max/cm^{-1}: 3444, 2960, 2923, 2852, 2252, 1684, 1635, 1601, 1588, 1470, 1434, 1411; ^{1}H NMR (600 MHz; $CDCl_3$) δ_H 8.83 (1H, d, *J*= 16.2 Hz, H8), 8.39 (1H, d, *J*= 8.8 Hz, Ar), 8.15-8.04 (3H, m, H9 + Ar), 7.79 (1H, ddd, *J*= 8.7, 6.9, 1.4 Hz, Ar), 7.72-7.64 (2H, m, Ar), 5.78 (1H, s, H6, Ar), 5.35 (2H, q, *J*= 7.3 Hz, N1', CH_2), 4.06 (3H, s, N1, NMe), 3.89 (3H, s, H5, OMe), 2.98 (3H, s, H2, Me), 1.95 (6H, s, H3', 2 × Me), 1.91 (3H, t, *J*= 7.3 Hz, N1', CH_3) ; ^{13}C NMR (151 MHz; $CDCl_3$) δ_C 182.6 (C2'), 178.6 (C7), 178.5 (C4), 159.8 (C5), 146.3 (C8), 145.7 (C3), 143.9 (C3'), 135.2 (C10a'), 135.0 (C9a'), 133.4 (C2), 132.1 (C, Ar), 131.6 (C3a, C7a), 130.7 (C, Ar), 129.6 (C, Ar), 127.2 (C, Ar), 122.3 (C5a'), 120.6 (C, Ar), 119.2 (C, Ar), 118.4 (C3a'), 112.8 (C9), 107.1 (C6), 57.1 (C5, OMe), 47.3 (N1', CH_2), 33.6 (N1, NMe), 27.6 (C3', 2×Me), 14.6 (C2, Me), 14.5 (N1', CH_3); ESI-HRMS Calculated 453.2178 [M], 454.2256 $[M + H]^+$ Observed 453.2170 [M], 454.2204 $[M + H]^+$; Calculated 453 $[M]^+$, 454 $[M + H]^+$ Observed 453 $[M]^+$ (100 %), 454 $[M + H]^+$ (95 %).

8.2.7 Locked form probe synthesis:

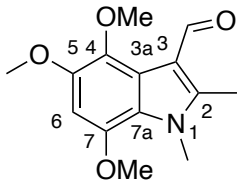
Compound 16: 4,7-Dihydroxy-5-methoxy-1,2-dimethyl-1*H*-indole-3-carbaldehyde



Sodium dithionite (374 mg, 4.29 mmol, 10.0 eq.) in distilled water (6.00 mL) was added to a suspension of 5-methoxy-1,2-dimethyl-4,7-dioxo-4,7-dihydro-1*H*-indole-3-carbaldehyde (50.0 mg, 0.429 mmol, 1.0 eq.) in ether (6.00 mL). This suspension was shaken for 10 min before separating the organic layer, extracting the aqueous layer with EtOAc (3 × 10.0 mL), washing with brine (3.00 mL), drying over Na_2SO_4 and concentrating

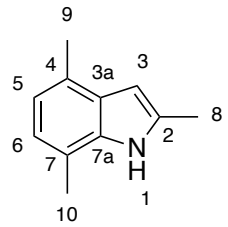
in vacuo. This product was taken onto the next step with no purification. R_f 0.16 (5 % acetone in DCM); ESI-MS Calculated 258 $[M + Na]^+$ Observed 258 $[M + Na]^+$ (100 %). Product was taken on without further characterisation due to its instability in oxygen rich conditions.

Compound 17: 4,5,7-Trimethoxy-1,2-dimethyl-1*H*-indole-3-carbaldehyde



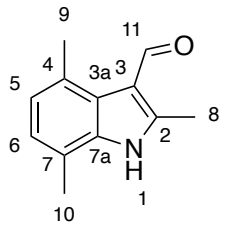
Me_2SO_4 (132 μL, 1.39 μmol, 6.5 $\times 10^{-3}$ eq.) and K_2CO_3 (0.325 g, 2.35 mmol, 11.1 eq.) were added to 4,7-dihydroxy-5-methoxy-1,2-dimethyl-1*H*-indole-3-carbaldehyde (50.0 mg, 0.213 mmol, 1.0 eq.) in acetone (5.00 mL) and the reaction mixture was heated (60 °C) for 12 h, until judged complete by TLC analysis. The reaction mixture was allowed to cool to rt before filtering through celite, then washing with 1 M HCl (5.00 mL), distilled water (5.00 mL) and brine (5.00 mL). The organic layer was then dried over Na_2SO_4, filtered under gravity and concentrated *in vacuo*. The resulting residue was purified via silica gel column chromatography (30 – 100 % EtOAc/PE with 0.1 % AcOH) to give the product as a yellow solid (16.6 mg, 63.0 μmol, 30 %). The product was then further purified via semi-preparative HPLC (5 – 95 % acetonitrile/H_2O) to afford the product as a yellow solid (1.1 mg, 4.18 μmol, 2 %). R_f 0.62 (8:2 EtOAc/PE with 0.1 % AcOH); m.p. >300 °C (from MeCN); ATR-IR υ max/cm^{-1}: 3659, 2981, 2886, 2823, 1903, 1474, 1462; ^1H NMR (400 MHz; $CDCl_3$) δ_H 10.44 (1H, s, H3, CHO), 6.43 (1H, s, H6, Ar), 3.95 (3H, s, N1, NMe), 3.93 (3H, s, H4/7, OMe), 3.92 (3H, s, H4/7, OMe), 3.88 (3H, s, H5, OMe), 2.76 (3H, s, H2, Me); ESI-MS Calculated 264 $[M + H]^+$ Observed 264 $[M + H]^+$ (84 %).

Compound 18: 2,4,7-Trimethyl-1*H*-indole (Zhang et al., 2019a)



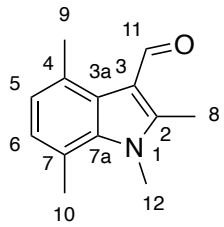
Under an argon atmosphere, isopropenyl magnesium bromide solution (1.0 M, 7.94 mL, 7.94 mmol, 3.0 eq.) was added in one portion to 1,4-dimethyl-2-nitrobenzene (400 mg, 2.65 mmol, 1.0 eq.) in anhydrous THF (8.84 mL) at −40 °C. The reaction was stirred at this temperature for 1 h and confirmed complete by TLC analysis. The reaction mixture was subsequently quenched with sat. NH_4Cl (8.84 mL) and extracted with EtOAc (3 × 10.0 mL) before washing with brine (10.0 mL), drying with Na_2SO_4, filtering under gravity and concentrating *in vacuo*. The crude brown product was purified via silica gel column chromatography (1 % EtOAc in PE) to yield the desired product as a light brown oil (101 mg, 0.63 mmol, 24 %). R_f 0.56 (9:1 PE/EtOAc); ^{1}H NMR (400 MHz; $CDCl_3$) δ_H 7.81 (1H, s, N1, NH), 6.89-6.82 (2H, m, H5+H6, Ar), 6.29-6.28 (1H, m, H3, Ar), 2.53 (3H, s, H9/10, Me), 2.50 (3H, s, H9/10, Me), 2.47 (3H, s, H8, Me); ESI-LRMS Calculated: 160 $[M + H]^+$ Observed: 160 $[M + H]^+$ (100 %). These data are in good agreement with the literature (Zhang et al., 2019a).

Compound 19: 2,4,7-Trimethyl-1*H*-indole-3-carbaldehyde (Zhang et al., 2019a)



A solution of $POCl_3$ (0.25 mL, 2.69 mmol, 1.4 eq.) in anhydrous DMF (0.73 mL) was stirred for 10 min at 0 °C to form the Vilsmeier reagent. This solution was then added to a solution of 2,4,7-trimethyl-1*H*-indole (300 mg, 1.88 mmol, 1.0 eq.) in anhydrous DMF (0.610 mL) cooled to −10 °C, over a period of 45 min. The reaction mixture was then stirred at 0 °C for a further 45 min and confirmed complete via TLC analysis. The reaction mixture was then added dropwise to an ice-cooled 2 M NaOH aqueous solution (10.0 mL) before extracting the aqueous phase with DCM (3 × 10.0 mL). The organic layers were combined, washed with brine (10.0 mL), 0.5 M LiCl aqueous solution (10.0 mL) and dried over Na_2SO_4 before filtering under gravity and concentrating *in vacuo* to give the product as a brown solid (272 mg, 1.45 mmol, 77 %). R_f 0.4 (6:4 PE/EtOAc); ^{1}H NMR (400 MHz; $CDCl_3$) δ_H 10.46 (1H, s, H11, CHO), 8.60 (1H, s, H1, NH), 6.96 – 6.91 (2H, m, H5+6, Ar), 2.81 (3H, s, H10, Me), 2.73 (1H, s, H9, Me), 2.47 (3H, s, H8, Me); ESI-LRMS Calculated: 188 $[M + H]^+$ Observed: 188 $[M + H]^+$ (100 %). These data are in good agreement with the literature (Zhang et al., 2019a).

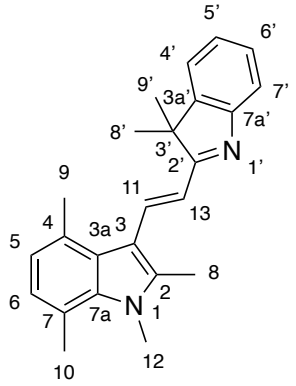
Compound 20: 1,2,4,7-Tetramethyl-1*H*-indole-3-carbaldehyde (Huang et al., 2010; Phillips et al., 1999)



Under an argon atmosphere, a solution of 2,4,7-trimethyl-1*H*-indole-3-carbaldehyde (226 mg, 1.20 mmol, 1.0 eq.) in anhydrous DMF (1.30 mL) was gradually added to a suspension of sodium hydride (82.0 mg of 60 % in mineral oil, 2.06 mmol, 2.0 eq.) in anhydrous DMF (1.22 mL) whilst stirring at rt. The reaction mixture was then stirred for 2 h at rt before being cooled to 0 °C. Iodomethane (77.2 μL, 1.24 mmol, 1.2 eq.) was then added dropwise to the reaction mixture before warming it back to rt and stirring for another 2 h upon which the reaction was complete, confirmed by TLC. The reaction was then quenched with the slow addition of distilled water (8.00 mL) before extracting the aqueous phase with DCM (3 × 8.00 mL). The consequent organic layers were combined, washed with distilled water (8.00 mL), 0.5 M LiCl aqueous solution (8.00 mL) and brine (8.00 mL) before being dried over Na_2SO_4, filtered under gravity and concentrated *in vacuo*. The resultant yellow solid was purified via silica gel column chromatography (8:2 PE/EtOAc) to give the product as a yellow solid (130 mg, 0.65 mmol, 54 %). R_f 0.43 (1:1 PE/EtOAc); m.p. 147-150 °C (from $CHCl_3$); ^{1}H NMR (600 MHz; $CDCl_3$) δ_H 10.49 (1H, s, H11, CHO), 6.92 – 6.84 (2H, m, H5+6, Ar), 3.96 (3H, s, H12, Me), 2.79 (3H, s, H9, Me), 2.76 (3H, s, H8, Me), 2.69 (3H, s, H10, Me); ^{13}C NMR (151 MHz; $CDCl_3$) δ_C 187.1 (C11), 145.4 (C2), 135.9 (C7a), 128.3 (C4), 126.7 (C6), 126.0 (C5), 124.5 (C3a), 119.1 (C7), 116.0 (C3), 32.5

(C12), 23.1 (C9), 20.7 (C10), 12.5 (C8); ESI-HRMS Calculated 202.1232 $[M + H]^+$ Observed 202.1226 $[M + H]^+$; ESI-MS Calculated 202 $[M + H]^+$ Observed 202 $[M + H]^+$ (100 %).

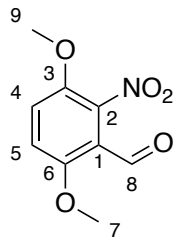
Compound 21: (*E*)-3-(2-(3,3-Dimethyl-3*H*-indol-2-yl)vinyl)-1,2,4,7-tetramethyl-1*H*-indole



Piperidine (30.0 μL) and acetic acid (30.0 μL) were added to a solution of 2,3,3-trimethyl-3*H*-indole (79.0 mg, 0.497 mmol, 1.0 eq.) and 1,2,4,7-tetramethyl-1*H*-indole-3-carbaldehyde (100 mg, 0.497 mmol, 1.0 eq.) in toluene (3.00 mL) before heating under reflux (110 °C) for 24 h. Reaction completion was confirmed by TLC analysis and the reaction mixture was then left to cool to rt before being concentrated *in vacuo*. The resulting red residue was then azeotrope with $CHCl_3$ and purified via silica gel column chromatography (7:3 PE/EtOAc) to give the product as a red solid (5.20 mg, 15.2 μmol, 3 %). R_f 0.5 (1:1 PE/EtOAc); m.p. 143-145 °C ($CHCl_3$); ^{1}H NMR (600 MHz; C_6D_6) δ_H 8.66 (1H, d, *J*= 16.2 Hz, H11, C=C), 7.89 (1H, d, *J*= 7.6 Hz, H7', Ar), 7.25-7.20 (1H, m, H4', Ar), 7.12-7.08 (2H, m, H5' + 6', Ar), 6.85 (2H, dd, *J*= 16, 4 Hz, H5 + 6, Ar), 6.76 (1H, d, *J*= 16.2 Hz, H13, C=C), 3.04 (3H, s, H12, NMe), 2.80 (3H, s, H9, Me), 2.41 (3H, s, H8, Me), 2.10 (3H, s, H10, Me), 1.33 (6H, s, H8' + H9', 2 × Me) ; ^{13}C NMR (151 MHz; C_6D_6) δ_C 183.6 (C2'), 155.6 (C7a'), 147.1 (C3a'), 136.7 (C7a), 136.3 (C2), 134.7 (C11), 128.5 (C4), 128.4 (C6'), 127.4 (C6), 125.4 (C5'), 125.1 (C3a), 123.0 (C5), 121.2 (C4'), 120.9 (C13), 120.6 (C7), 118.4

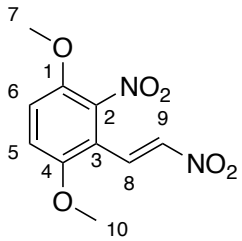
(C7'), 113.1 (C3), 52.4 (C3'), 32.3 (C12), 24.3 (C8',C9'), 22.2 (C9), 20.7 (C10), 12.3 (C8); ESI-HRMS Calculated 343.2174 $[M + H]^+$ Observed 343.2169 $[M + H]^+$; ESI-MS Calculated 343 $[M + H]^+$ Observed 343 $[M + H]^+$ (100 %).

Compound 22: 3,6-Dimethoxy-2-nitrobenzaldehyde (Kitahara et al., 1985)



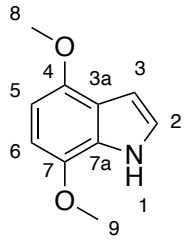
Conc. HNO_3 (9 mL) was added dropwise to a solution of 2,5-dimethoxybenzaldehyde (3.00 g, 18.05 mmol) in AcOH (30.0 mL) at 0 °C. The reaction mixture was then stirred for 1 h at rt before being confirmed complete by TLC analysis. Distilled water (150 mL) was added to the reaction mixture and the resulting yellow slurry was filtered *under vacuo* to give a fluffy yellow solid. The crude product was purified via silica gel column chromatography (10–50 % EtOAc/PE) to give the product as a yellow fluffy solid (3.41 g, 16.2 mmol, 89 %). R_f 0.81 (50:50 PE/EtOAc); m.p. 137-139 °C ($CHCl_3$); ^{1}H NMR (400 MHz; $CDCl_3$) δ_H 10.36 (1H, s, H8, CHO), 7.27 (1H, d, *J*= 9.3 Hz, H5, Ar), 7.10 (1H, d, *J*= 9.3 Hz, H4, Ar), 3.94 (3H, s, H9, OMe), 3.87 (3H, s, H7, OMe); ESI-LRMS Calculated: 212 $[M + H]^+$ Observed: 212 $[M + H]^+$ (100 %). These data are in good agreement with the literature (Kitahara et al., 1985).

Compound 23: (*E*)-1,4-Dimethoxy-2-nitro-3-(2-nitrovinyl)benzene (Kitahara et al., 1985)



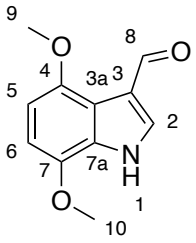
3,6-Dimethoxy-2-nitrobenzaldehyde (2.42 g, 11.46 mmol) and ammonium acetate (1.78 g) were added to nitromethane (22.3 mL) and the reaction was refluxed (100 °C) for 3 h. The reaction was confirmed complete by TLC analysis and cooled to rt. The reaction mixture was diluted with distilled water (50.0 mL) and then extracted with DCM (3 × 100 mL). The organic layers were combined and washed with brine (75.0 mL) before drying over Na_2SO_4, filtering under gravity and concentrating *in vacuo*. The product was purified via silica gel column chromatography (30-50 % EtOAc/PE) to give the product as a yellow solid (2.30 g, 9.05 mmol, 79 %). R_f 0.58 (1:1 PE/EtOAc); m.p. 138-140 °C ($CHCl_3$); ^{1}H NMR (400 MHz; $CDCl_3$) δ_H 7.96 (1H, d, *J*= 12 Hz, H8, C=C), 7.74 (1H, d, *J*= 12 Hz, H9, C=C), 7.15 (1H, d, *J*= 8 Hz, H5, Ar), 7.06 (1H, d, *J*= 8 Hz, H6, Ar), 3.97 (3H, s, H7, OMe), 3.89 (3H, s, H10, OMe); ESI-LRMS Calculated: 255 $[M + H]^+$ Observed: 255 $[M + H]^+$ (100 %). These data are in good agreement with the literature (Kitahara et al., 1985).

Compound 24: 4,7-Dimethoxy-1*H*-indole (Kitahara et al., 1985)



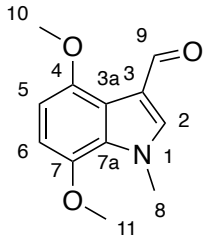
Iron powder (62.0 g, 1.11 mol, 240 eq.) was gradually added in portions to a boiling solution of (*E*)-1,4-dimethoxy-2-nitro-3-(2-nitrovinyl)benzene (0.98 g, 4.64 mmol, 1.0 eq.) in AcOH (180 mL). The reaction mixture was heated at reflux (118 °C) for 1 h and confirmed complete via TLC analysis. The reaction mixture was cooled to rt before being poured into a saturated aqueous solution of Na_2SO_3. The solid material was removed by filtering through celite and the celite pad was washed with DCM (3 × 100 mL). The filtrate was then extracted with DCM (3 × 50.0 mL) and the organic layers were combined and washed with distilled water before drying over Na_2SO_4, filtering under gravity and concentrating *in vacuo*. The product was purified via silica gel column chromatography (80:20 PE/EtOAc) to give the product as a yellow solid (315 mg, 1.78 mmol, 38 %). R_f 0.43 (8:2 PE/EtOAc); ^{1}H NMR (400 MHz; $CDCl_3$) δ_H 8.37 (1H, s, H1, NH), 7.12 (1H, dd, *J*= 3.2, 2.3 Hz, H2, CH), 6.63 (1H, dd, *J*= 3.2, 2.3 Hz, H3, CH), 6.52 (1H, d, *J*= 8 Hz, H6, Ar), 6.39 (1H, d, *J*= 8 Hz, H5, Ar), 3.93 – 3.92 (6H, m, H8+9, OMe); ESI-LRMS Calculated: 178 $[M + H]^+$ Observed: 178 $[M + H]^+$ (100 %). These data are in good agreement with the literature (Kitahara et al., 1985).

Compound 25: 4,7-Dimethoxy-1*H*-indole-3-carbaldehyde (Huang et al., 2010; Phillips et al., 1999)



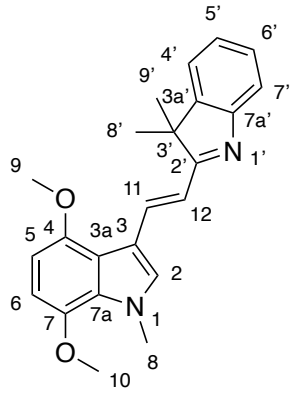
A solution of $POCl_3$ (0.30 mL, 3.23 mmol, 1.43 eq.) in ice water cooled DMF (0.870 mL) was stirred for 10 min at 0 °C to form the Vilsmeier reagent. This solution was then added to a solution of 4,7-dimethoxy1*H*-indole (400 mg, 2.26 mmol, 1.00 eq.) in anhydrous DMF (0.730 mL) cooled to −10 °C, over a period of 45 min. The reaction mixture was then stirred at 0 °C for a further 45 min and confirmed complete via TLC analysis. The reaction mixture was then added dropwise to an ice-cooled 2 M NaOH aqueous solution (14.0 mL) before extracting the aqueous phase with DCM (3 × 20 mL). The organic layers were combined, washed with brine (15.0 mL), 0.5 M lithium chloride aqueous solution (15.0 mL) and dried over Na_2SO_4 before filtering under gravity and concentrating *in vacuo*. The resulting brown solid residue was then washed with cooled (0 °C) ethyl acetate (2 × 10.0 mL) and filtered *under vacuo* before purifying via silica gel column chromatography (80:20 PE/EtOAc) to give the product as a beige solid (357 mg, 1.74 mmol, 77 %). R_f 0.50 (8:2 PE/EtOAc); ^{1}H NMR (400 MHz; $CDCl_3$) δ_H 10.48 (1H, s, H1, NH), 8.93 (1H, s, H8, CHO), 7.89 (1H, d, *J*= 3.2 Hz, H2, CH), 6.6.0 (1H, d, *J*= 8 Hz, H5/6, Ar), 6.56 (1H, d, *J*= 8 Hz, H5/6, Ar), 3.95 (3H, s, H10, OMe), 3.93 (3H, s, H9, OMe); ESI-LRMS Calculated: 206 $[M + H]^+$ Observed: 206 $[M + H]^+$ (100 %). These data are in good agreement with the literature (Huang et al., 2010; Phillips et al., 1999).

Compound 26: 4,7-Dimethoxy-1-methyl-1*H*-indole-3-caraldehyde (Huang et al., 2010; Phillips et al., 1999)



Under an argon atmosphere, a solution of 4,7-dimethoxy-2-methyl-indoline-3-carbaldehyde (357 mg, 1.74 mmol, 1.0 eq.) in anhydrous DMF (2.20 mL) was gradually added to a suspension of sodium hydride (0.14 g of 60 % in mineral oil, 3.48 mmol, 2.0 eq.) in anhydrous DMF (2.10 mL) whilst stirring at rt. The reaction mixture was then stirred for 2 h at rt before being cooled to 0 °C. Iodomethane (0.13 mL, 2.09 mmol, 1.2 eq.) was then added dropwise to the reaction mixture before warming it back to rt and stirring for another 2 h upon which the reaction was complete, confirmed by TLC. The reaction was then quenched with the slow addition of distilled water (10.0 mL) before extracting the aqueous phase with DCM (3 × 10.0 mL). The consequent organic layers were combined, washed with distilled water (10.0 mL), 0.5 M LiCl aqueous solution in distilled water (10.0 mL) and brine (10.0 mL) before being dried over Na_2SO_4, filtered under gravity and concentrated *in vacuo* to give the product as a beige solid (0.208 g, 0.95 mmol, 55 %). R_f 0.53 (1:1 PE/EtOAc); m.p. 139-141 °C (DCM) ^{1}H NMR (400 MHz; $CDCl_3$) δ_H 10.42 (1H, s, H9, CHO), 7.66 (1H, s, H2, CH), 6.57 (1H, d, *J*= 8 Hz, H5/6, Ar), 6.53 (1H, *J*= 8 Hz, H5/6, Ar), 4.07 (3H, s, H11, OMe), 3.93 (3H, s, H10, OMe), 3.89 (3H, s, H8, NMe); ESI-LRMS Calculated: 220 $[M + H]^+$ Observed: 220 $[M + H]^+$ (100 %). These data are in good agreement with the literature (Huang et al., 2010; Phillips et al., 1999).

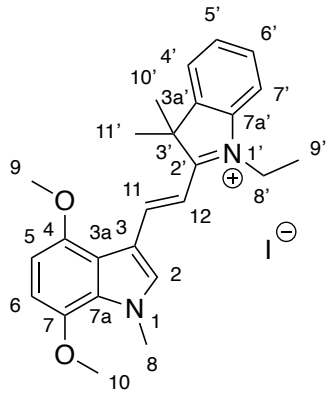
Compound 27: (*E*)-3-(2-(3,3-Dimethyl-3*H*-indol-2-yl)vinyl)4,7-dimethoxy-1-methyl-1*H*-indole



Piperidine (40.0 μL) and AcOH (40.0 μL) were added to a solution of 2,3,3-trimethyl-3*H*-indole (72.6 mg, 0.456 mmol, 1.0 eq.) and 4,7-dimethoxy-1-methyl-1*H*-indole-3-carbaldehyde (100 mg, 0.456 mmol, 1.0 eq.) in toluene (4.00 mL) before heating under reflux (110 °C) for 5 h. Reaction completion was confirmed by TLC analysis and the reaction mixture was then cooled to rt before being concentrated *in vacuo*. The resulting orange/red residue was purified via silica gel column chromatography (20–50 % EtOAc/PE) to give the product as an orange/red solid (133 mg, 0.370 mmol, 81 %). R_f 0.20 (1:1 PE/EtOAc); m.p. 184-187 °C (from EtOAc); ^{1}H NMR (600 MHz; $CDCl_3$) δ_H 8.32 (1H, d, *J*= 16.8 Hz, H11, C=C), 7.59 (1H, d, *J*= 7.6 Hz, H7', Ar), 7.35–7.28 (3H, m, H2+H4'+H6', CH+Ar), 7.21 – 7.17 (1H, m, H5', Ar), 6.98 (1H, d, *J*= 16.8 Hz, H12, C=C), 6.52 (1H, d, *J*= 8.4 Hz, H6, Ar), 6.44 (1H, d, *J*= 8.4 Hz, H5, Ar), 4.06 (3H, s, H8, NMe), 3.96 (3H, s, H9, OMe), 3.88 (3H, s, H10, OMe), 1.54 (6H, s, H8' + H9', Me); ^{13}C NMR (151 MHz; $CDCl_3$) δ_C 184.6 (C2'), 154.4 (C4), 149.3 (C7a'), 147.2 (C7), 142.9 (C3a'), 133.8 (C11), 128.4 (C7a), 128.0 (C2), 127.7 (C6'), 124.9 (C5'), 121.0 (C4'), 120.1 (C12), 119.1 (C7'), 116.9 (C3), 114.2 (C3a), 103.2 (C6), 100.5 (C5), 56.0 (C9), 55.8 (C10), 52.5 (C3'), 37.1 (C8), 25.0 (C8', C9');

ESI-HRMS 361.1916 $[M + H]^+$ Observed 361.1913 $[M + H]^+$; ESI-MS Calculated 361 $[M + H]^+$ Observed 361 $[M + H]^+$ (100 %).

Compound 28: (*E*)-2-(2-(4,7-Dimethoxy-1-methyl-1*H*-indol-3-yl)vinyl)-1-ethyl-3,3-dimethyl-3*H*-indol-1-ium

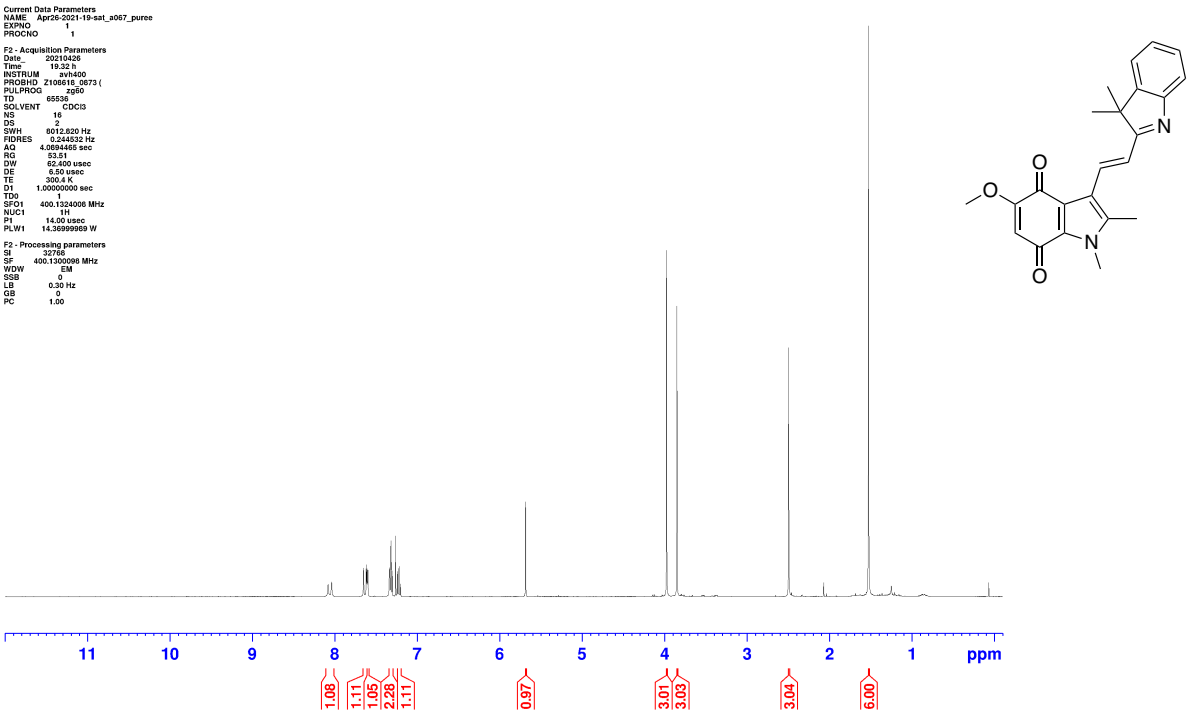


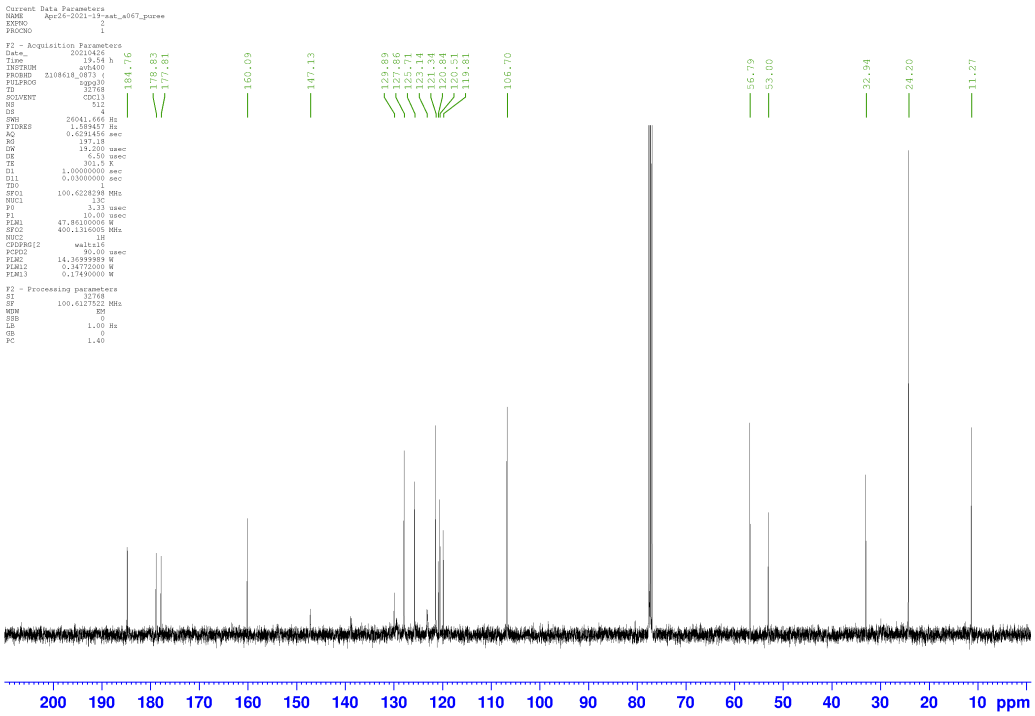
(*E*)-3-(2-(3,3-Dimethyl-3*H*-indol-2-yl)vinyl)-4,7-dimethoxy-1-methyl-1*H*-indole (50.0 mg, 0.138 mmol, 1.0 eq.) was dissolved in MeCN (20 drops) and ethyl iodide (500 μL). The reaction mixture was heated (65 °C), under argon, in the dark and monitored using TLC analysis. After 24 h the reaction was confirmed to be complete by TLC, and the reaction mixture was cooled to rt, before the solvent was removed *in vacuo*. The resulting red residue was purified via silica gel column chromatography (1 – 5 % MeOH in DCM) to give the product as a red solid (82.1 mg, 0.21 mmol, 109 %). R_f 0.50 (9:1 DCM/MeOH); m.p. 141-144 °C (from DCM); ^{1}H NMR (600 MHz; $CDCl_3$) δ_H 10.05 (1H, s, H2, CH), 9.13 (1H, d, *J*= 15.6 Hz, H11, C=C), 7.77 (1H, d, *J*= 15.5 Hz, H12, C=C), 7.51-7.27 (4H, m, H4'-7', Ar), 6.66 – 6.61 (2H, s, H5+6, Ar), 4.75 (2H, q, *J*= 7.2 Hz, H8', CH_2), 4.26 (3H, s, H10, OMe), 4.00 (3H, s, H9, OMe), 3.90 (3H, s, H8, NMe), 1.79 (6H, s, H10'+11', Me), 1.58 (3H, t, *J*= 7.2 Hz, H9', CH_3); ^{13}C NMR (151 MHz; $CDCl_3$) δ_C 178.3 (C2'), 151.8 (C4), 149.0 (C7a'), 143.6 (C7), 142.3 (C3a'), 141.4 (C11), 129.2 (C7a), 128.7 (C2), 127.0 (C6'), 122.5 (C5'), 118.9 (C4'), 115.9 (C12), 112.3 (C7'),105.7 (C3a'), 105.4 (C3a), 104.5 (C6), 56.1 (C5), 56.0 (C9), 50.5

(C10), 42.1 (C3'), 38.8 (C8'), 29.9 (C8), 27.9 (C10', C11'), 14.0 (C9'); ESI-HRMS Calculated 389.2229 $[M]^+$, 390.2307 $[M + H]^+$ Observed 389.2227 $[M]^+$, 390.2260 $[M + H]^+$; ESI-MS Calculated 389 $[M]^+$, 390 $[M + H]^+$ Observed 389 $[M]^+$, 390 $[M + H]^+$ (100 %).

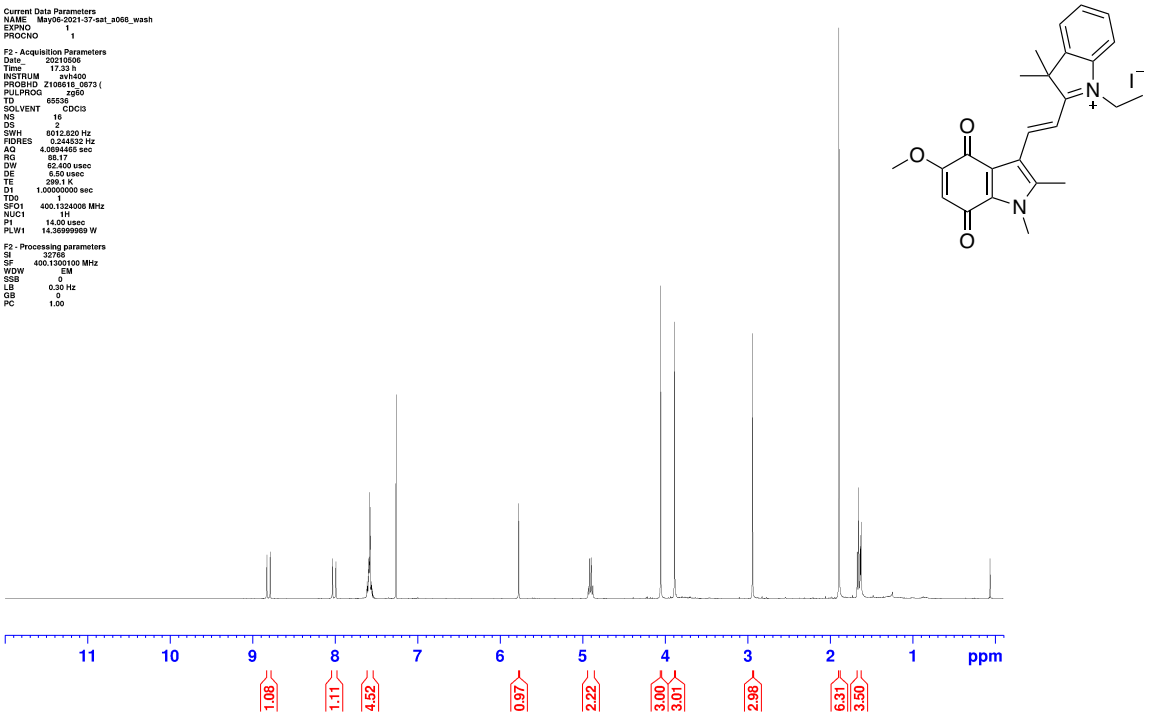
8.3 NMR Spectra

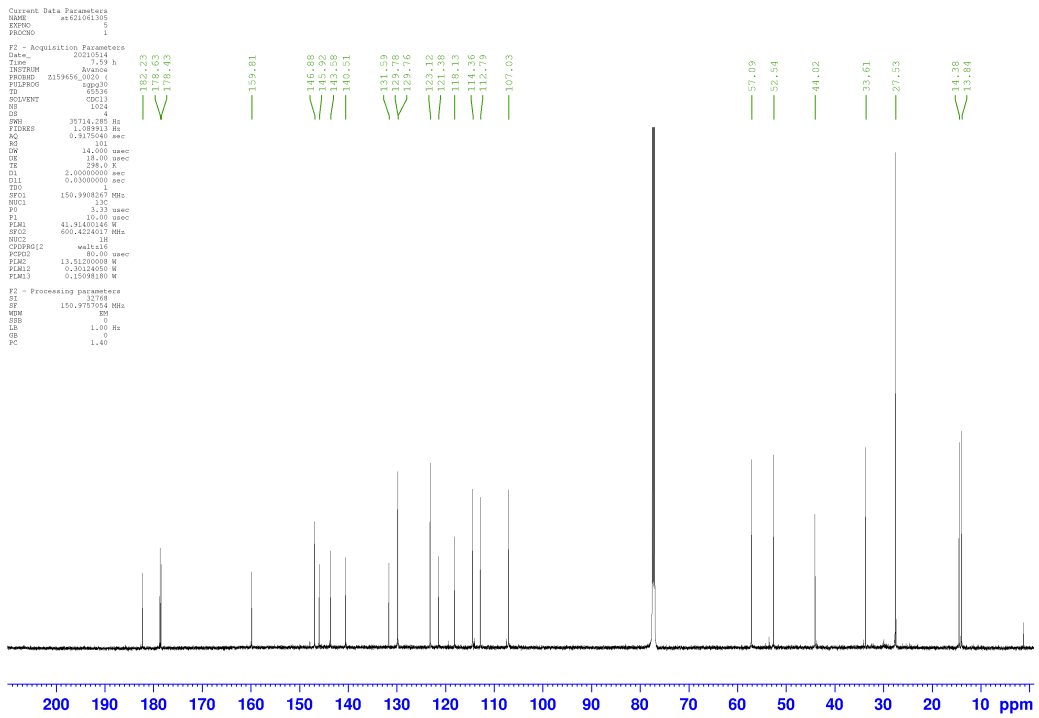
Compound 12 (**NA-HCIQ**): (*E*)-3-(2-(3,3-Dimethyl-3*H*-indol-2-yl)vinyl)-5-methoxy-1,2-dimethyl-1*H*-indole-4,7-dione



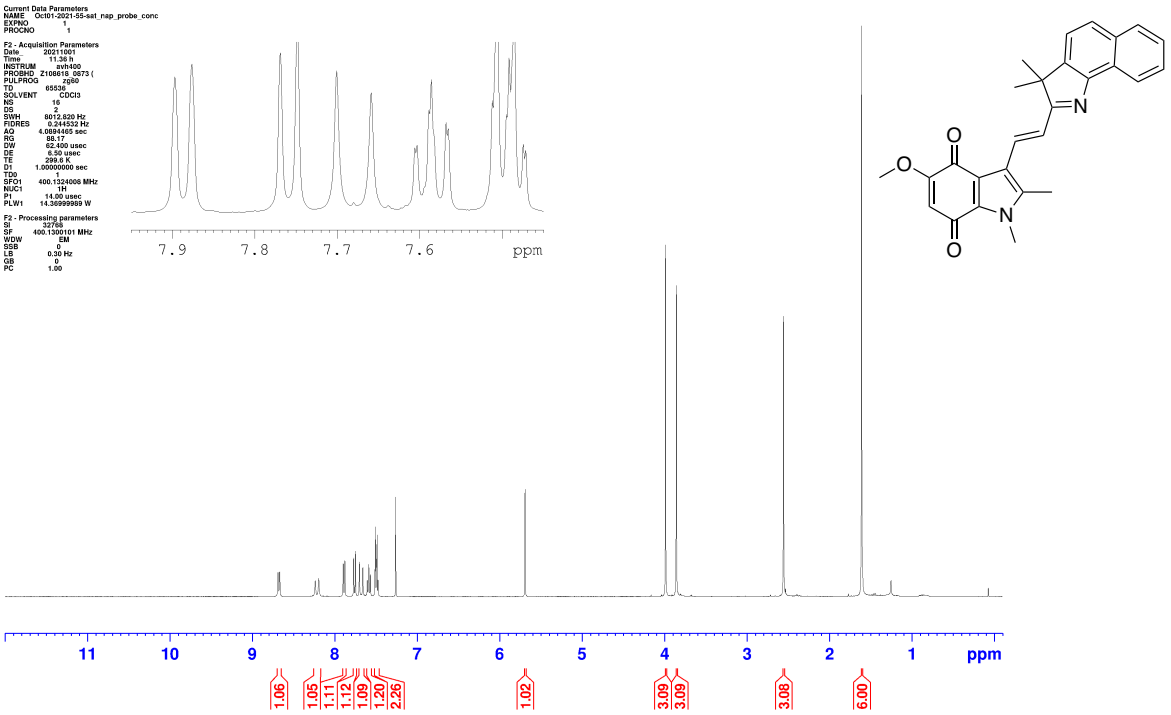


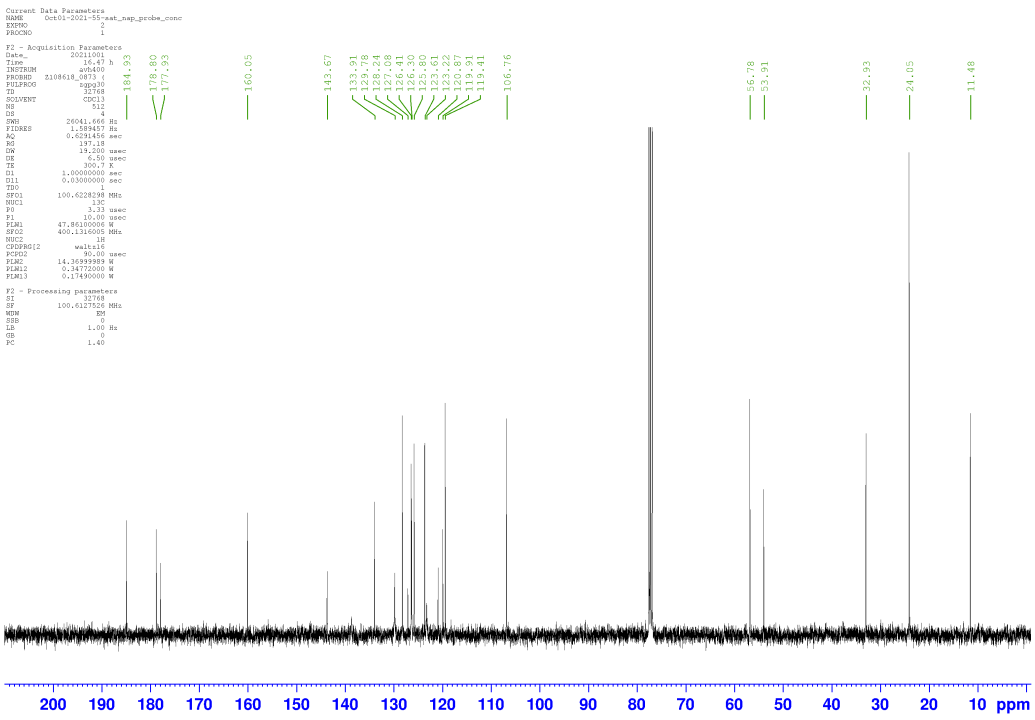
Compound 13 (**HClQ**): (*E*)-1-Ethyl-2-(2-(5-methoxy-1,2-dimethyl-4,7-dioxo-4,7-dihydro-1*H*-indpl-3-yl)vinyl)-3,3-dimethyl-3*H*-indol-1-ium



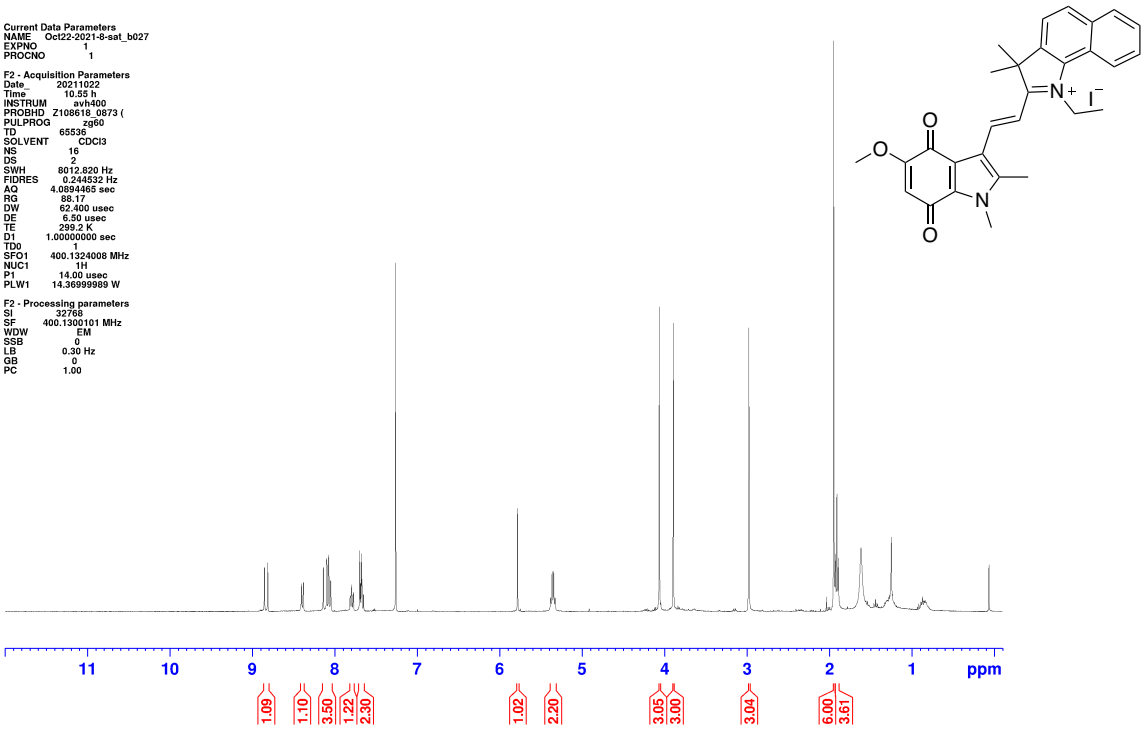


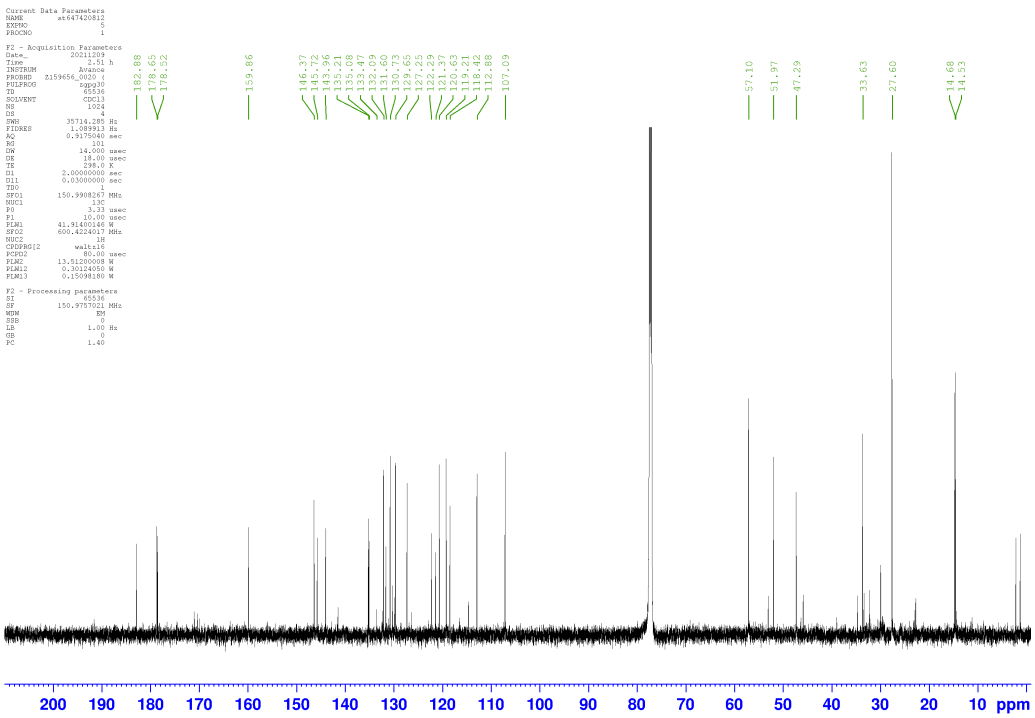
Compound 14: (*E*)-3-(2-(3,3-Dimethyl-3*H*-benzo[*g*]indol-2-yl)vinyl-5-methoxy-1,2-dimethyl-1*H*-indole-4,7-dione



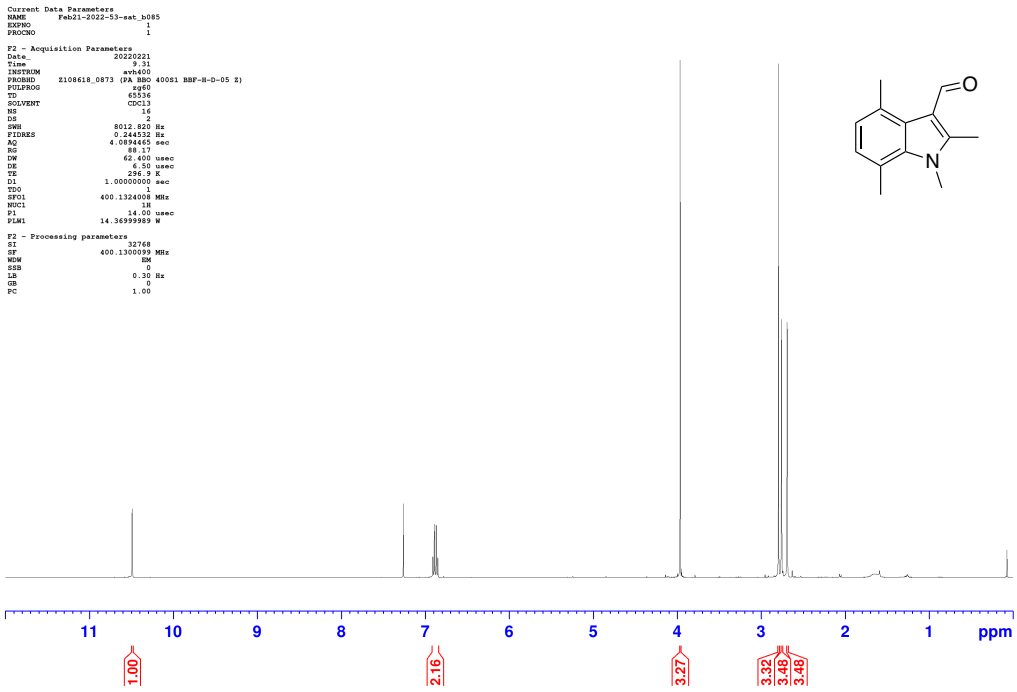


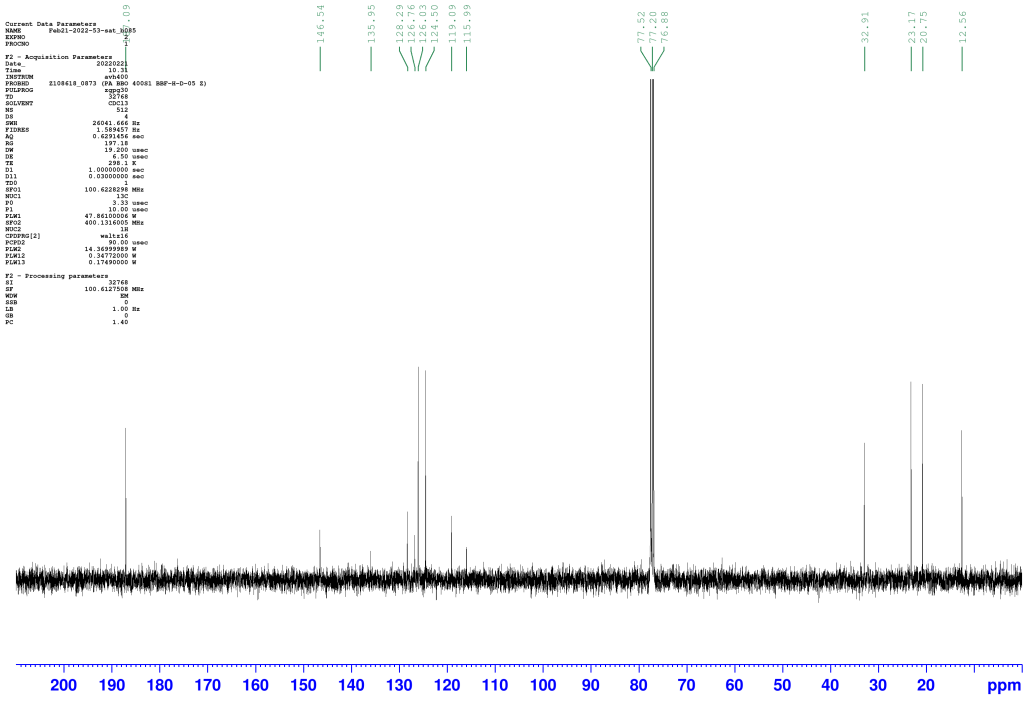
Compound 15: (*E*)-1-Ethyl-2-(2-(5-methoxy-1,2-dimethyl-4,7-dioxo-4,7-dihydro-1*H*-indol-3-yl)vinyl)-3,3-dimethyl-3*H*-benzo[*g*]indol-1-ium



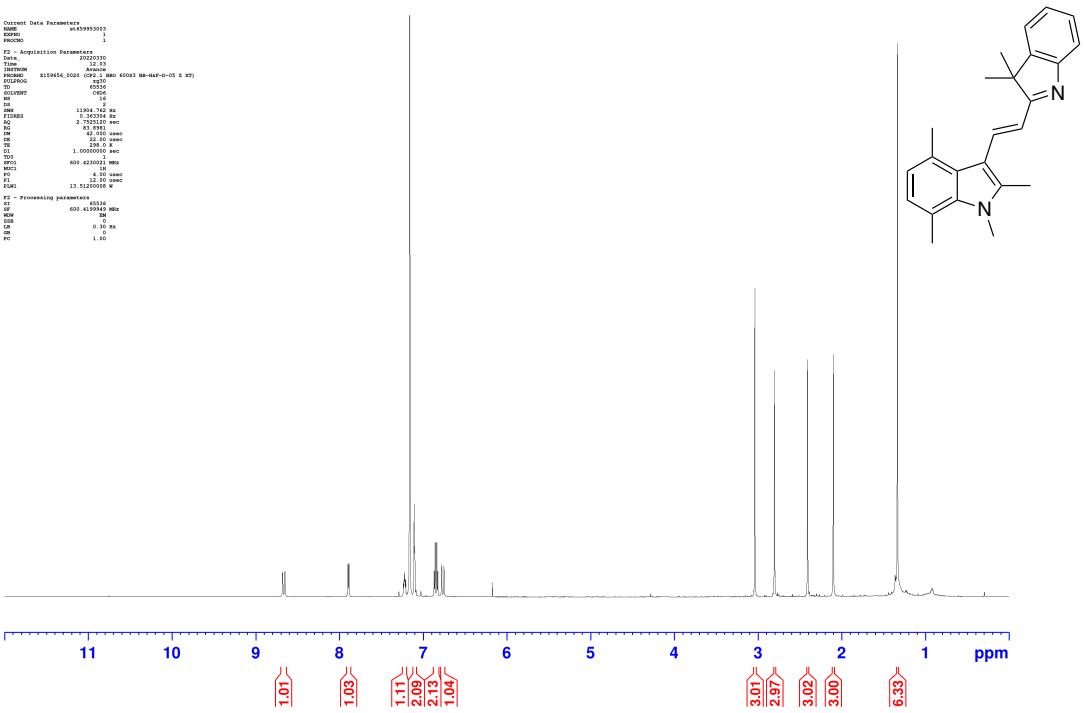


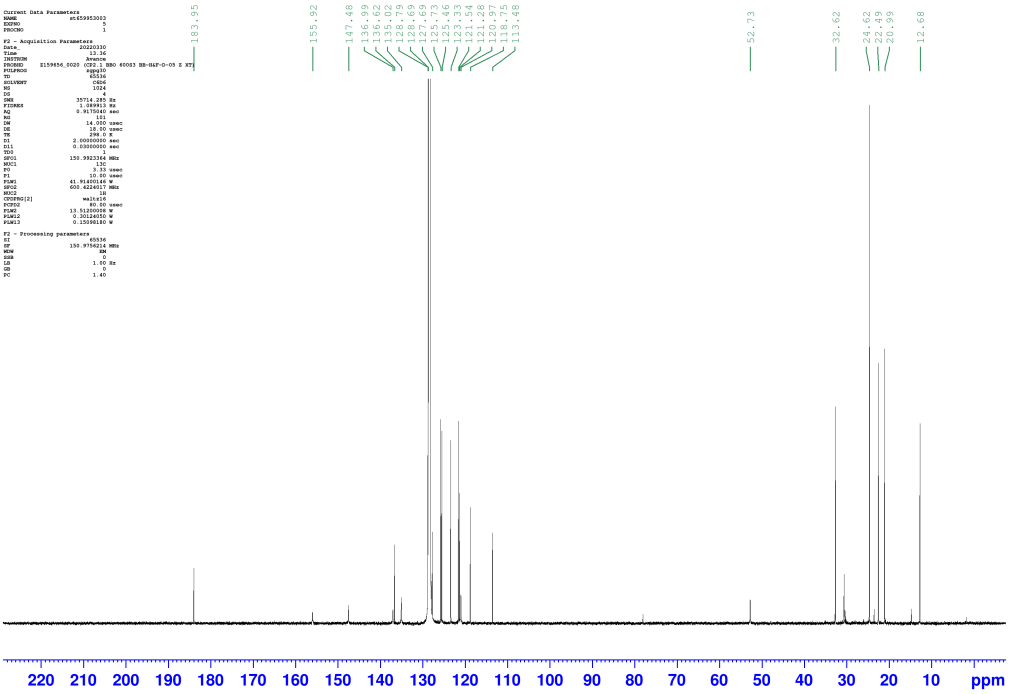
Compound 20: 1,2,4,7-Tetramethyl-1*H*-indole-3-carbaldehyde



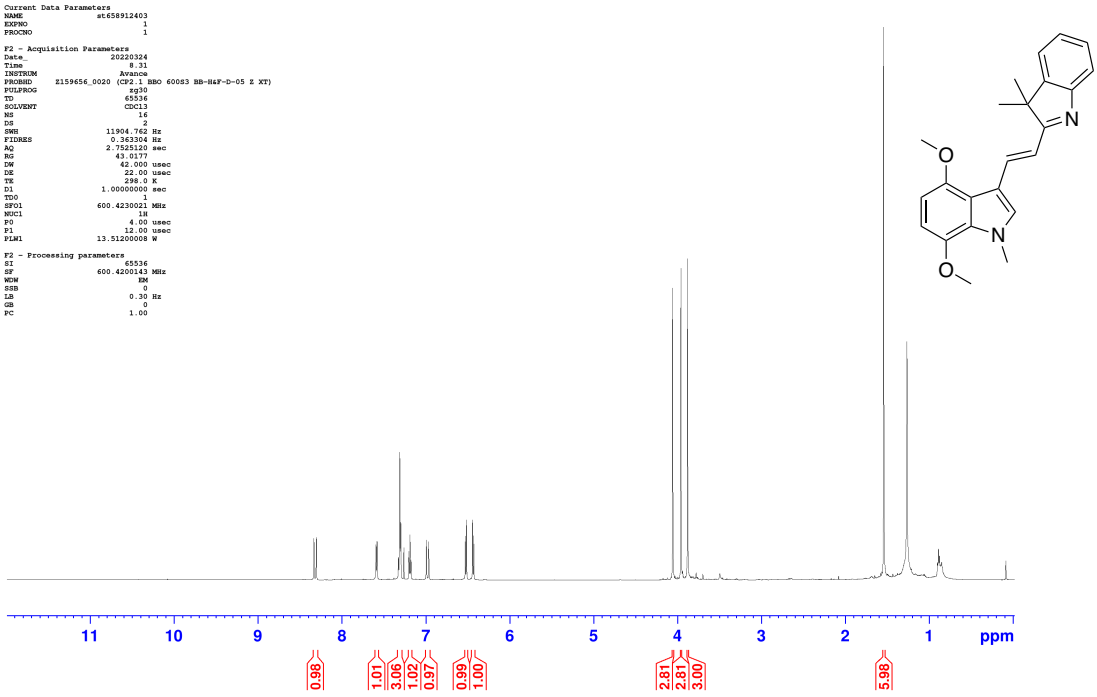


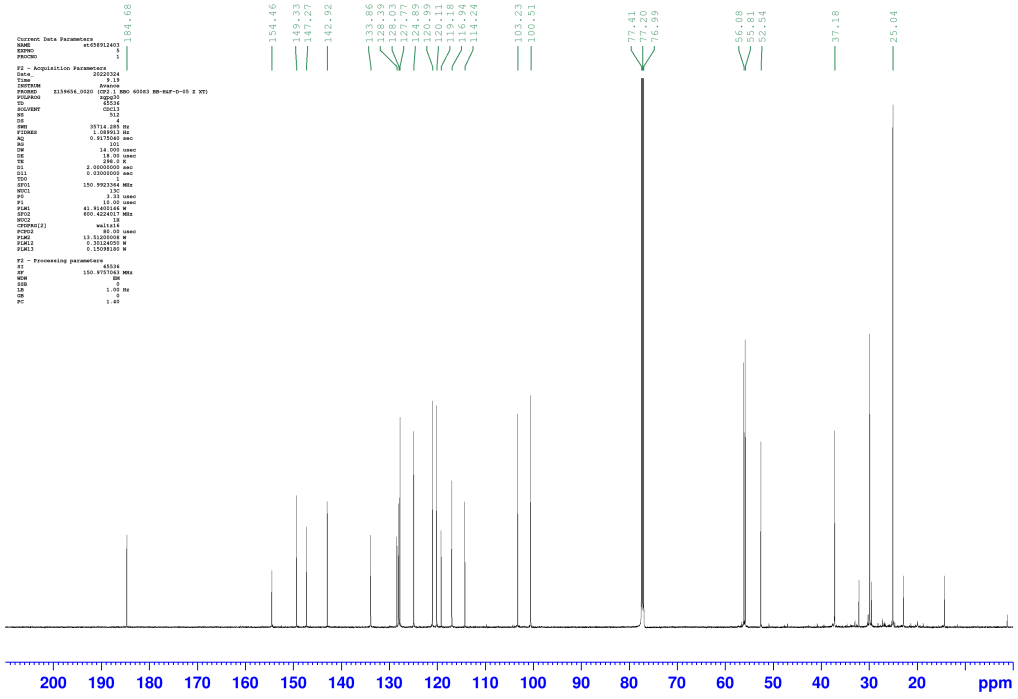
Compound 21: (*E*)-3-(2-(3,3-Dimethyl-3*H*-indol-2-yl)vinyl)-1,2,4,7-tetramethyl-1*H*-indole



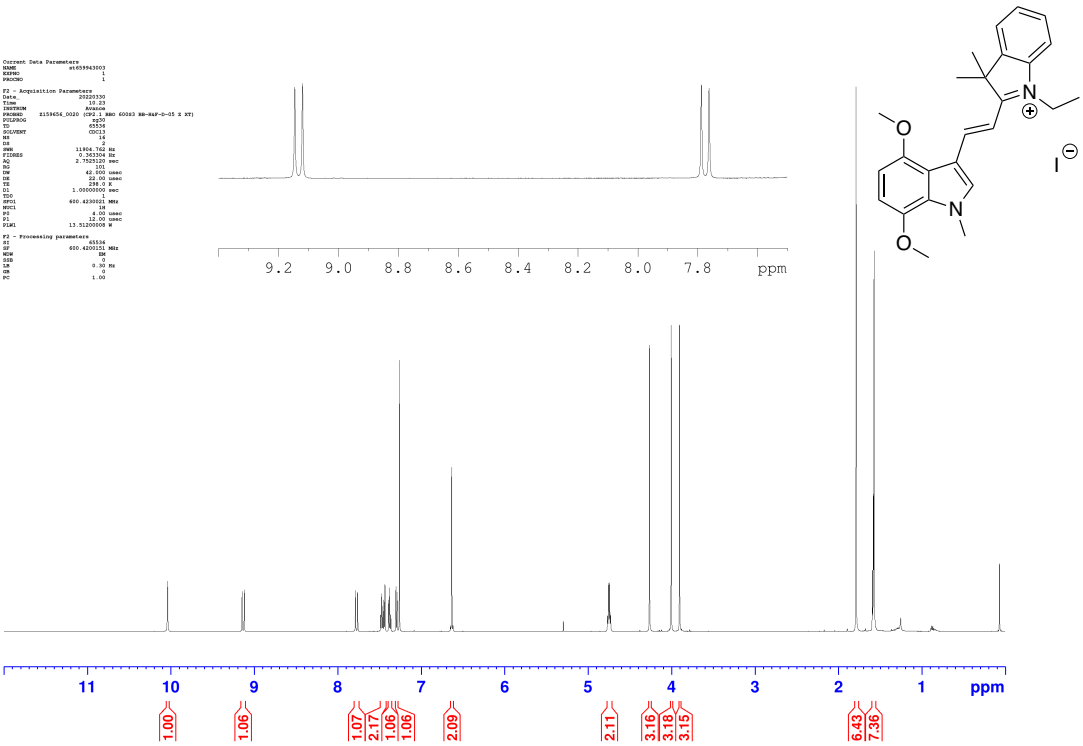


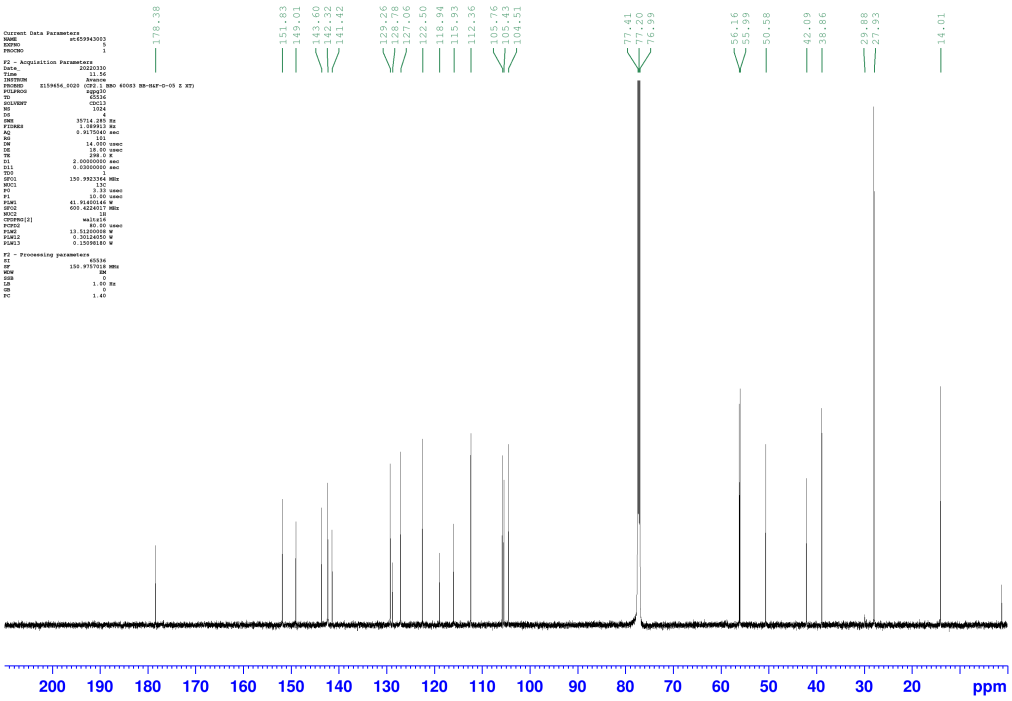
Compound 27: (*E*)-3-(2-(3,3-Dimethyl-3*H*-indol-2-yl)vinyl)4,7-dimethoxy-1-methyl-1*H*-indole





Compound 28: (*E*)-2-(2-(4,7-Dimethoxy-1-methyl-1*H*-indol-3-yl)vinyl)-1-ethyl-3,3-dimethyl-3*H*-indol-1-ium





8.4 Presentations, awards and manuscripts from this thesis

8.4.1 Poster and oral presentations

Investigating changes to the redox environment in hypoxic conditions: BACR Tumour Microenvironment Meeting, Nottingham, 2023 (poster)

Investigating the contribution of redox stress to the therapy resistance of cells experiencing hypoxia: Internal Seminar, Oncology Department, Oxford, 2023 (talk)

Targeting hypoxic tumours with silver molecular clusters: Annual MitOX Meeting, Oxford, 2023 (poster)

Targeting hypoxic tumours with silver molecular clusters: Annual Oxford Cancer Symposium, Oxford, 2023 (poster)

Targeting hypoxic tumours with silver molecular clusters: MRC DTP Student Symposium, University of Oxford, 2023 (talk)

Targeting radiation resistant tumours with silver molecular clusters: Poster Series, Oncology Department, University of Oxford, 2023 (poster)

Design, synthesis and validation of a reversible fluorescent probe for measuring hypoxia in real time: Student Symposium, Oncology Department, University of Oxford, 2022 (talk)

Design, synthesis, and validation of a reversible fluorescent probe for measuring real time hypoxia: MRC DTP Student Symposium, University of Oxford, 2022 (3 min flash talk)

Investigation of the contributions of redox stress to the therapy resistance of cells experiencing cycling oxygen levels: Student Symposium, Oncology Department, University of Oxford, 2021 (poster)

Investigation of the contributions of redox stress to the therapy resistance of cells experiencing cycling oxygen levels: MRC DTP Student Symposium, University of Oxford, 2021 (poster)

8.4.2 Prizes/Awards

2024 Best poster at RedOx-KCL/MITHRAS public engagement day, London

2023 Travel award from St Peters College, Oxford

2023 Supplementary funding from the Oxford-MRC Doctoral Training Partnership (DTP)

8.3.3 Manuscripts

A colorimetric approach for monitoring the reduction of platinum(iv) complexes in aqueous solution. Huang S, Marsh JW, White JRG, Ha TQ, **Twigger SA**, Diez-Perez I, Sedgwick AC. New J Chem. 2024 Apr 10;48(17):7548-7551.

The activity of therapeutic molecular cluster Ag5 is dependent on oxygen level and HIF-1 mediated signalling. **Twigger SA**, Dominguez B, Porto V, Hacker L, Chalmers AJ, Breckenridge R, Treder M, Sedgwick AC, Dominguez F, Hammond EM. Redox Biol. 2024 Aug 22;76:103326.

NJC

COMMUNICATION

View Article Online
View Journal | View Issue

Check for updates

Cite this: *New J. Chem.*, 2024, **48**, 7548

Received 23rd February 2024,
Accepted 9th April 2024

DOI: 10.1039/d4nj00859f

rsc.li/njc

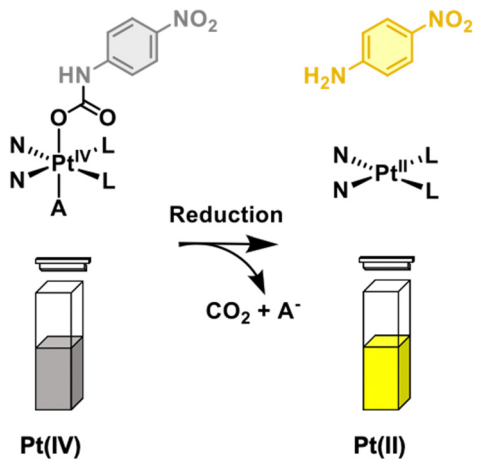
A colorimetric approach for monitoring the reduction of platinum(IV) complexes in aqueous solution†

Shitong Huang,[a] Jevon W. Marsh,[a] Jhanelle R. G. White,[c] Tracy Q. Ha,[c] Sophie A. Twigger,[b] Ismael Diez-Perez[c] and Adam C. Sedgwick *[ac]

We report the synthesis of 4-nitrophenyl (4-NP) functionalised Pt(IV) complexes as a colorimetric strategy for monitoring Pt(IV) reduction in aqueous solution. Treatment of each 4-NP functionalised Pt(IV) complex with the biological reductant sodium ascorbate led to a colour change from clear to yellow, which was attributed to the reduction of Pt(IV) to Pt(II) and simultaneous release of 4-nitroaniline. Trends in reduction profiles and a photocatalysed reduction for each Pt(IV) complex were observed.

Cisplatin, oxaliplatin, and carboplatin are amongst the most widely used chemotherapeutics in oncology.[1] Unfortunately, platinum(II) anticancer agents are plagued by severe toxicity issues, which ultimately impact treatment success rates.[2] In an attempt to address these limitations, efforts have been devoted to studying the Pt(IV) analogues of these FDA-approved chemotherapeutics.[3] The kinetic inertness of these low-spin, octahedral Pt(IV) complexes has the potential to reduce off-target toxicity and enhance drug bioavailability.[4,5] Our current understanding is that Pt(IV) complexes undergo cancer selective reduction and form a toxic Pt(II) product with the loss of two axial ligands.[1] Gibson and co-workers highlighted that we cannot eliminate the possibility of forming more than one Pt(II) species.[6,7] Although promise has been shown in preclinical studies, no Pt(IV) anticancer agent has been approved.[8,9] One of the biggest obstacles to Pt(IV) therapy is the need to improve our understanding of Pt(IV) reduction and identify how it correlates within a biological context.[10,11] Several research groups have developed diagnostic strategies to assist in these efforts.[12–14] Here, we present a simple colorimetric strategy that allows monitoring of the reduction of Pt(IV) to Pt(II) in aqueous solution to help identify factors that lead to reduction, Scheme 1.

The most routine method for studying both the stability and reduction of Pt(IV) complexes is through high-performance liquid chromatography (HPLC).[15] Although effective, most Pt-complexes are weakly absorbing, resulting in the need of millimolar concentrations for each complex to be seen on the HPLC chromatogram. In addition, the long wait times between HPLC experiments prevents the rapid screening of potential reductants. Optical techniques such as UV-Vis spectroscopy have found widespread use in assay development including high-throughput screening.[11–13] We rationalised by installing 4-nitroaniline onto the axial position of a Pt(IV) complex, we could access a general approach to screen reductants and study the reduction of Pt(IV) to Pt(II) by UV-Vis spectroscopy. With this design, Pt(IV) reduction results in the release of free strongly absorbing 4-nitroaniline (yellow colour, λ_{max} = 385 nm, see ESI,† Fig. S1) *via* rapid decarboxylation of an unstable carbamic



Scheme 1 The general design of the colorimetric strategy developed in this study for monitoring platinum(IV) reduction.

[a] *Chemistry Research Laboratory, University of Oxford, Mansfield Road, OX1 3TA, UK. E-mail: adam.sedgwick@kcl.ac.uk*
[b] *Department of Oncology, University of Oxford, Old Road Campus Research Building, Oxford, OX3 7DQ, UK*
[c] *Department of Chemistry, King's College London, 7 Trinity Street, London, SE1 1DB, UK*

† Electronic supplementary information (ESI) available. See DOI: https://doi.org/10.1039/d4nj00859f

Open Access Article. Published on 10 April 2024. Downloaded on 9/27/2024 3:34:14 PM.
This article is licensed under a Creative Commons Attribution-NonCommercial 3.0 Unported Licence.

 This journal is © The Royal Society of Chemistry and the Centre National de la Recherche Scientifique 2024

Open Access Article. Published on 10 April 2024. Downloaded on 9/27/2024 3:34:14 PM.
This article is licensed under a Creative Commons Attribution-NonCommercial 3.0 Unported Licence.

acid intermediate (Scheme 1).[15–17] We believe this strategy would help improve our efforts in identifying factors that lead to the reduction of Pt(IV) to Pt(II).

As a proof of concept, 4-nitrophenyl (4-NP) functionalised Pt(IV) complexes (**Cis-4NP**, **Oxali-4NP** and **Carbo-4NP**) were synthesised, derived from the classical platinum anticancer agents, cisplatin(II), oxaliplatin(II) and carboplatin(II) (Fig. 1). Each Pt(II) complex was first oxidised to the corresponding Pt(IV) hydroxo-aceto complex, CisPt(OH)(OAc) (**1**), OxPt(OH)(OAc) (**2**), and CbPt(OH)(OAc) (**3**) using hydrogen peroxide and acetic acid as a solvent (see ESI,† Scheme S1). Subsequent treatment of each Pt(IV) reagent (**1–3**) with 4-nitrophenylisocyanate in DMF afforded the desired 4-NP functionalised Pt(IV) complexes, **Cis-4NP**, **Oxali-4NP** and **Carbo-4NP** in yields of 30%, 44% and 46%, respectively (see ESI,† Scheme S2 and for the full experimental methods).[14]

With the 4-NP functionalised Pt(IV) complexes in hand, we turned our attention to evaluating the photophysical and stability properties of each complex in solution (PBS, pH = 7.40). All three Pt(IV) complexes displayed strong absorption bands centred at ~340 nm and were found stable over the course of 24 hours (see ESI,† Fig. S2–S4). HPLC analysis was used as complementary method to confirm the stability of each complex over a 24-hour period (see ESI,† Fig. S5–S7). The concentrations needed for UV-Vis spectroscopy was also shown suitable for HPLC analysis; no HPLC trace of **2** was observed at the same concentrations, highlighting our inability to often study Pt(IV) complexes at biologically relevant concentrations (see ESI,† Fig. S8). Sodium ascorbate (NaAsc) is a routinely used biological reductant for Pt(IV) chemistry.[1,15] Excitingly, the addition of NaAsc (100 equiv., 5 mM) to a solution of **Cis-4NP** (50 μM), led to a gradual change in UV-Vis absorption over the course of 7 hours with a decrease at 338 nm and increase at 404 nm (Fig. 2). Observable to the naked eye was a colour change from clear to a bright yellow solution indicative of the release of 4-nitroaniline (see ESI,† Fig. S9). The release of 4-nitroaniline was confirmed by HPLC (see ESI,† Fig. S10). Interestingly, when compared to **Oxali-4NP** and **Carbo-4NP**, and in line with previous reports,[15] a trend in NaAsc sensitivity was observed

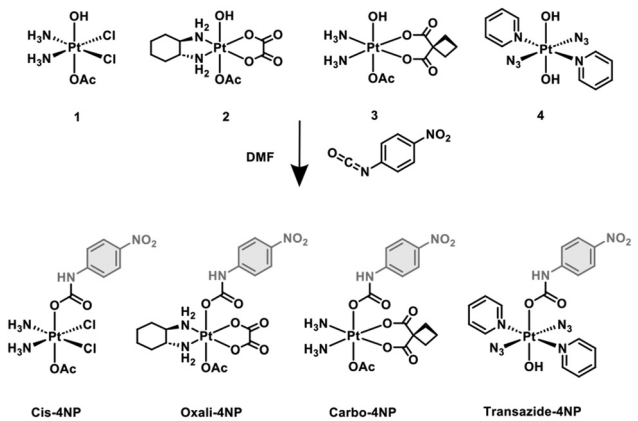


Fig. 1 Reaction scheme for the synthesis of 4-nitrophenyl functionalised Pt(IV) complexes used in this study (**Cis-4NP**, **Oxali-4NP**, **Carbo-4NP** and **Transazide-4NP**).

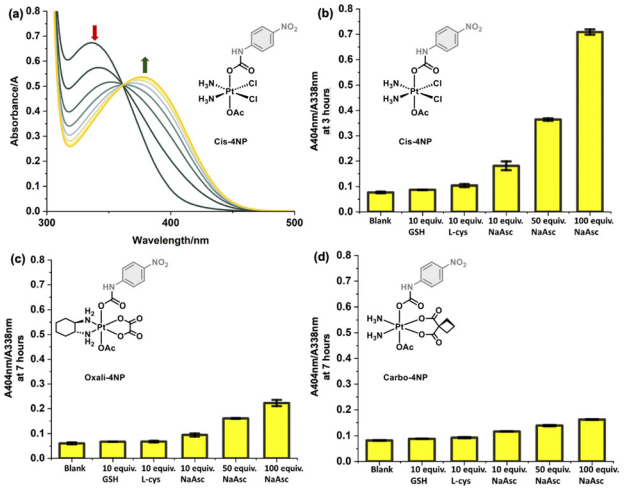


Fig. 2 (a) Absorption spectra of **Cis-4NP** (50 μM) in a PBS buffer solution (pH = 7.40, with 1% DMF) containing NaAsc (100 equiv., 5 mM). Measurements were taken over the course of 7 hours. (b) Bar chart of the change in absorption (404 nm/338 nm) of **Cis-4NP** (50 μM) treated with different reductants NaAsc (100/50/10 equiv., 5/2.5/0.5 mM), L-cys (10 equiv., 0.5 mM) and GSH (10 equiv., 0.5 mM) and measured after 3 hours incubation. (c) and (d) Bar charts of the changes in absorption (404 nm/338 nm) of **Oxali-4NP** and **Carbo-4NP** (50 μM) treated with different reductants; NaAsc (100/50/10 equiv., 5/2.5/0.5 mM); L-cys (10 equiv., 0.5 mM) and GSH (10 equiv. 0.5 mM) and measured after 7 hours incubation. Error bars represent SD.

(**Cis-4NP** > **Oxali-4NP** > **Carbo-4NP**). As seen in Fig. 2c and d, **Oxali-4NP** and **Carbo-4NP** treated with NaAsc (100 equiv. 5 mM) displayed smaller changes to the corresponding absorption spectra and HPLC traces when compared to the untreated controls (see ESI,† Fig. S11 and S12). Mass spectrometry confirmed the reduction of **Oxali-4NP** and **Carbo-4NP** to oxaliplatin and carboplatin, respectively. Whereas, **Cis-4NP** afforded a mixture of Pt(II) species (see ESI,† Fig. S13–S15). The response of each 4-NP complex was shown selective for NaAsc when compared to other biological reductants such as glutathione (GSH) and L-cysteine (L-Cys) (Fig. 2; see ESI† for spectra, Fig. S16–S18). Overall, the obtained data confirms the success of this colorimetric strategy.

To demonstrate the general utility of this approach, we wanted to apply this strategy to a non-classical Pt(IV) complex. *t,t,t*-[$Pt(N_3)_2(OH)_2(py)_2$] (transazide) was reported in 2010 as a photoactivatable chemotherapeutic (PACT), only displaying cytotoxicity upon light irradiation.[18,19] It is believed that Transazide forms reactive azide-based radicals under light irradiation, which leads to the formation of a mixture of cytotoxic Pt(IV) and Pt(II) species.[18,20] Using the same synthetic protocols, we isolated **Transazide-4NP** in 57% yield (see ESI,† Scheme S2). Determined by UV-Vis and HPLC, **Transazide-4NP** displayed excellent aqueous stability over the course of 24 hours (see ESI,† Fig. S19 and S20). Confirming the ability to use our colorimetric strategy for this light activatable Pt(IV) complex, **Transazide-4NP** was irradiated for 5 hours using a desktop lamp fitted with a Deltech LED bulb (wavelength: 350-400 nm, 80 Lumen, 1.2 W) (see ESI,† General information and methods section). As seen

Open Access Article. Published on 10 April 2024. Downloaded on 9/27/2024 3:34:14 PM.
This article is licensed under a Creative Commons Attribution-NonCommercial 3.0 Unported Licence.

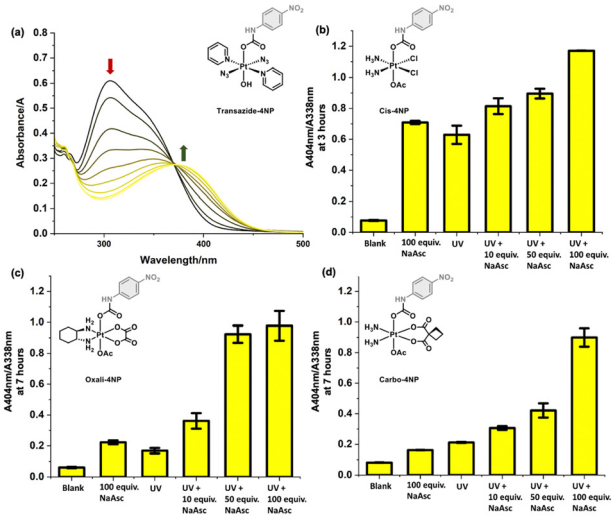


Fig. 3 (a) Absorption spectra of **Transazide-4NP** (25 μM) in PBS buffer solution (pH = 7.40, with 1% DMF) under light irradiation from 0–5 hours. (b) Bar chart of the change in absorption (A404 nm/A338 nm) of **Cis-4NP** with difference concentrations of NaAsc (100/50/10 equiv., 5/2.5/0.5 mM) under light irradiation (3 hours). (c) and (d) Bar chart of the change in absorption (A_{404nm}/A_{338nm}) of **Oxali-4NP**/**Carbo-4NP** (50 μM) with difference concentrations of NaAsc (NaAsc (100/50/10 equiv., 5/2.5/0.5 mM) under light irradiation (7 hours)). Error bars represent SD.

in Fig. 3a, under light irradiation, a gradual change in absorption spectra was observed with a decrease in 338 nm and increase in absorption at 404 nm. The release of 4-nitroaniline from **Transazide-4NP** was confirmed by HPLC and NMR analysis (see ESI,† Fig. S21 and S22). More than one peak was observed in the HPLC chromatogram post light irradiation, suggesting the formation of several Pt-based species as described in previous reports.[18] As a comparison, we wanted to test how each of the classical Pt(IV) complexes **Cis-4NP**, **Oxali-4NP** and **Carbo-4NP** behaved under the same light irradiation conditions to **Transazide-4NP**. Previous efforts by the groups of Ang and Zhu have reported the design of light responsive Pt(IV) complexes that are based on the FDA-approved scaffolds, thus warranting the exploration of our colorimetric systems.[21,22] To our surprise, the light irradiation of **Cis-4NP** resulted in a rapid change to its absorption spectra, which was at a similar rate to the light activation of **Transazide-4NP** (see ESI,† Fig. S23 and S24). In stark contrast, minimal changes to the absorption spectra of **Oxali-4NP** and **Carbo-4NP** was observed after 3 hours of light irradiation (see ESI,† Fig. S23 and S24). Previous reports have shown NaAsc as a potential catalyst for the photoreduction of Pt(IV) complexes,[18,19] we were therefore motivated to test the influence of NaAsc on the rate of the photo-mediated reduction of **Cis-4NP**, **Oxali-4NP** and **Carbo-4NP**. Remarkably, the presence of NaAsc during the light irradiation experiments resulted in significant increases in the rate of change of the absorption spectra of **Cis-4NP**, **Oxali-4NP** and **Carbo-4NP**, Fig. 3b–d. The influence of NaAsc and light proved greater than either NaAsc or light alone for each complex (see ESI,† Fig. S25–S230), which was also confirmed by HPLC analysis (see ESI,† Fig. S31–S33). Unexpectedly, the addition of NaAsc (100 equiv., 2.5 mM) to a solution of **Transazide-4NP** (25 μM) resulted in a change to the absorption spectra along with the observed release of 4-nitroaniline, which suggests the reduction of Pt(IV) to Pt(II) (see ESI,† Fig. S34–S36). To the best of our knowledge this is an observation not previously reported.

Throughout this study, we have observed a trend in the sensitivity of NaAsc (and photo-)mediated reduction for the classical platinum agents **Cis-4NP** > **Oxali-4NP** > **Carbo-4NP**. To rationalise this trend, we wanted to interpret the chemical environment of the Pt centre by ^{195}Pt NMR and cyclic voltammetry. Use of ^{195}Pt NMR revealed distinctly different chemical shifts between **Cis-4NP**, **Oxali-4NP** and **Carbo-4NP**, with values of 1253 ppm, 1632 ppm and 1971 ppm, respectively. The NMR information obtained suggests the strong influence of the equatorial ligands towards Pt(IV) reduction. Further supporting this observation, cyclic voltammetry shows increase (becoming more negative) in reduction potential from **Cis-4NP** to **Carbo-4NP** (−0.25/−0.30/−0.38 V *vs.* Ag/AgCl see ESI,† Fig. S37 and S38) indicating that carboplatin-based **Carbo-4NP** is least sensitive to reduction as also shown *via* our colorimetric strategy.

In summary, we report 4-nitrophenyl functionalised Pt(IV) complexes as a colorimetric strategy to provide an optical method for monitoring Pt(IV) reduction. 4-NP functionalised Pt(IV) complexes of the classical platinum anticancer agents, cisplatin(II), oxaliplatin(II) and carboplatin(II) were synthesised. NaAsc-mediated reduction was monitored *via* UV-Vis spectroscopy, which identified trends in NaAsc sensitivity between complexes. An unexpected photocatalysed reduction of Pt(IV) complexes was observed. We believe this simple colorimetric strategy has the potential to find future utility in other research labs for studying the reduction of Pt(IV) complexes without solely relying on HPLC instrumentation.

Conflicts of interest

There are no conflicts to declare.

Acknowledgements

ACS would like to thank the Glasstone Research fellowship (University of Oxford), Jesus College (Oxford), King's College London, and program grant (EP/X033015/1) for financial support. SAT was supported by an Oxford MRC DTP studentship (MR/N013468/1). We would also like to acknowledge Professor Ester Hammond (University of Oxford) for mentorship and support on background projects. ACS and SH would like to acknowledge Professor Stephen Faulkner's (University of Oxford) support, mentorship, and guidance within his lab space.

References

1 T. C. Johnstone, K. Suntharalingam and S. J. Lippard, *Chem. Rev.*, 2016, **116**, 3436–3486.
2 V. Stojanovska, S. Sakkal and K. Nurgali, *Am. J. Physiol.: Gastrointest. Liver Physiol.*, 2015, **308**, G223–G232.
3 Z. Xu, Z. Wang, Z. Deng and G. Zhu, *Coord. Chem. Rev.*, 2021, **442**, 213991.

 This journal is © The Royal Society of Chemistry and the Centre National de la Recherche Scientifique 2024

Open Access Article. Published on 10 April 2024. Downloaded on 9/27/2024 3:34:14 PM.
This article is licensed under a Creative Commons Attribution-NonCommercial 3.0 Unported Licence.

4 D. Gibson, *J. Inorg. Biochem.*, 2019, **191**, 77–84.
5 A. Najjar, N. Rajabi and R. Karaman, *Curr. Pharm. Des.*, 2017, **23**, 2366–2376.
6 E. Wexselblatt and D. Gibson, *J. Inorg. Biochem.*, 2012, **117**, 220–229.
7 A. Nemirovski, I. Vinograd, K. Takrouri, A. Mijovilovich, A. Rompel and D. Gibson, *Chem. Commun.*, 2010, **46**, 1842–1844.
8 G. Thiabaud, G. He, S. Sen, K. A. Shelton, W. B. Baze, L. Segura, J. Alaniz, R. Munoz Macias, G. Lyness, A. B. Watts, H. M. Kim, H. Lee, M. Y. Cho, K. S. Hong, R. Finch, Z. H. Siddik, J. F. Arambula and J. L. Sessler, *Proc. Natl. Acad. Sci. U. S. A.*, 2020, **117**, 7021–7029.
9 N. J. Wheate, S. Walker, G. E. Craig and R. Oun, *Dalton Trans.*, 2010, **39**, 8113–8127.
10 M. H. C. Boulet, H. R. Bolland, E. M. Hammond and A. C. Sedgwick, *J. Am. Chem. Soc.*, 2023, **145**, 12998–13002.
11 H. Yao and G. Zhu, *Dalton Trans.*, 2022, **51**, 5394–5398.
12 J. X. Ong, C. S. Q. Lim, H. V. Le and W. H. Ang, *Angew. Chem., Int. Ed.*, 2019, **58**, 164–167.
13 E. J. New, R. Duan, J. Z. Zhang and T. W. Hambley, *Dalton Trans.*, 2009, 3092–3101, DOI: **10.1039/B821603G**.
14 G. Liu, Y. Zhang, H. Yao, Z. Deng, S. Chen, Y. Wang, W. Peng, G. Sun, M.-K. Tse, X. Chen, J. Yue, Y.-K. Peng, L. Wang and G. Zhu, *Sci. Adv.*, 2023, **9**, eadg5964.
15 S. Chen, H. Yao, Q. Zhou, M. K. Tse, Y. F. Gunawan and G. Zhu, *Inorg. Chem.*, 2020, **59**, 11676–11687.
16 T. Babu, A. Sarkar, S. Karmakar, C. Schmidt and D. Gibson, *Inorg. Chem.*, 2020, **59**, 5182–5193.
17 P. L. Carl, P. K. Chakravarty and J. A. Katzenellenbogen, *J. Med. Chem.*, 1981, **24**, 479–480.
18 N. J. Farrer, J. A. Woods, L. Salassa, Y. Zhao, K. S. Robinson, G. Clarkson, F. S. Mackay and P. J. Sadler, *Angew. Chem., Int. Ed.*, 2010, **49**, 8905–8908.
19 N. J. Farrer, L. Salassa and P. J. Sadler, *Dalton Trans.*, 2009, 10690–10701, DOI: **10.1039/B917753A**.
20 E. M. Bolitho, C. Sanchez-Cano, H. Shi, P. D. Quinn, M. Harkiolaki, C. Imberti and P. J. Sadler, *J. Am. Chem. Soc.*, 2021, **143**, 20224–20240.
21 V. E. Y. Lee, C. F. Chin and W. H. Ang, *Dalton Trans.*, 2019, **48**, 7388–7393.
22 H. Yao, S. Chen, Z. Deng, M.-K. Tse, Y. Matsuda and G. Zhu, *Inorg. Chem.*, 2020, **59**, 11823–11833.

Redox Biology 76 (2024) 103326



Contents lists available at ScienceDirect

Redox Biology

journal homepage: www.elsevier.com/locate/redox



The activity of therapeutic molecular cluster Ag5 is dependent on oxygen level and HIF-1 mediated signalling

Sophie A. Twigger [a], Blanca Dominguez [b], Vanesa Porto [b], Lina Hacker [a], Anthony J. Chalmers [c], Ross Breckenridge [d], Martin Treder [d], Adam C. Sedgwick [e], Fernando Dominguez [b], Ester M. Hammond [a,*]

[a] Department of Oncology, University of Oxford, Oxford, OX3 7DQ, UK
[b] Department of physiology and CIMUS Universidade de Santiago de Compostela, Spain
[c] School of Cancer Sciences, University of Glasgow, UK
[d] Arjuna Therapeutics, Milladoiro, Spain
[e] Department of Chemistry, King's College London, London, SE1 1DB, UK

ARTICLE INFO

Keywords:
Hypoxia
Redox
Ag5
HIF-1
Radiation

ABSTRACT

Regions of hypoxia occur in most solid tumours and are known to significantly impact therapy response and patient prognosis. Ag5 is a recently reported silver molecular cluster which inhibits both glutathione and thioredoxin signalling therefore limiting cellular antioxidant capacity. Ag5 treatment significantly reduces cell viability in a range of cancer cell lines with little to no impact on non-transformed cells. Characterisation of redox homeostasis in hypoxia demonstrated an increase in reactive oxygen species and glutathione albeit with different kinetics. Significant Ag5-mediated loss of viability was observed in a range of hypoxic conditions which mimic the tumour microenvironment however, this effect was reduced compared to normoxic conditions. Reduced sensitivity to Ag5 in hypoxia was attributed to HIF-1 mediated signalling to reduce PDH via PDK1/3 activity and changes in mitochondrial oxygen availability. Importantly, the addition of Ag5 significantly increased radiation-induced cell death in hypoxic conditions associated with radioresistance. Together, these data demonstrate Ag5 is a potent and cancer specific agent which could be used effectively in combination with radiotherapy.

1. Introduction

Cancer cells can be characterised by an imbalance in reduction-oxidation (redox) homeostasis and specifically elevated levels of reactive oxygen species (ROS) [1]. High levels of free radical species have been attributed to increased metabolic activity, oncogene activation (e.g. K-Ras or c-Myc mutations) and disruption of key antioxidant signalling pathways [2,3]. The redox state provides a targetable difference between normal and cancer cells that can be therapeutically exploited.

Most solid tumours have some degree of hypoxia, due to abnormal vasculature and high metabolic demand [4,5]. The impact of hypoxia on ROS levels is controversial with some studies demonstrating increased ROS production in normal and malignant cells under hypoxia [6–9], whilst others reporting the opposite [10–13], suggesting a complex dependence on cell line, experimental conditions and specific ROS subtype. Where described, increased ROS levels under hypoxic conditions are thought to originate from complex I/III of the mitochondrial electron transport chain, the NADPH oxidase enzyme family and iron release from the Fenton reaction [14–16]. Hypoxia-induced ROS have been shown to contribute to the stabilisation of the hypoxia-inducible transcription factor, HIF-1, a heterodimeric protein complex composed of an oxygen-sensitive alpha subunit (HIF-1α) and a constitutively expressed HIF-1β subunit [17]. Activation of HIF-1 leads to numerous downstream responses including upregulation of anti-oxidant signalling [18,19]. More recently, ROS levels in hypoxia have been shown to contribute to transcriptional stress through the accumulation of DNA:RNA hybrids, R-loops [20].

The two main antioxidant mechanisms within the cell are the glutathione (GSH) and thioredoxin (Trx) pathways, both of which are regulated by the signalling molecule nicotinamide adenine dinucleotide (NADPH) which maintains them in a reduced state [21]. An upregulation of cellular GSH contributes to redox homeostasis in hypoxic

* Corresponding author.
E-mail address: ester.hammond@oncology.ox.ac.uk (E.M. Hammond).

https://doi.org/10.1016/j.redox.2024.103326
Received 29 July 2024; Received in revised form 17 August 2024; Accepted 21 August 2024
Available online 22 August 2024
2213-2317/© 2024 Published by Elsevier B.V. This is an open access article under the CC BY-NC-ND license (http://creativecommons.org/licenses/by-nc-nd/4.0/).

conditions, balancing out increases in both ROS and reactive nitrogen species (RNS) [7]. In addition, the uptake of L-cysteine, which is essential for GSH synthesis, is reported to increase in hypoxia via upregulation of dedicated transporter systems (X_c^- system) [7].

Redox-dependent agents such as doxorubicin have been described, where conversion to a semiquinone moiety by cellular reductases produces high levels of ROS in the cell [22]. Furthermore, a number of agents have been designed to target cellular antioxidant pathways. For example, buthionine sulfoximine (BSO), ebselen and auranofin, increase ROS levels beyond the threshold that cancer cells can tolerate, thereby inducing cell death [17,23,24]. As an example, BSO induces apoptosis by inhibiting γGCS, the first enzyme in GSH biosynthesis, decreasing the levels of intracellular GSH and leaving the cell susceptible to oxidative stress [23]. However, pre-clinical testing of these drugs revealed off target toxicity or limited efficacy which was attributed to a failure to inhibit all the antioxidant systems [25].

More recently, a therapeutic molecular cluster composed of five silver atoms (Ag5) was reported to inhibit both the GSH and Trx antioxidant pathways [26]. Using ROS species as substrates, Ag5 catalyses the irreversible oxidation of thiol groups present on cysteine residues within GSH/Trx, leaving them unable to reduce ROS/RNS and alleviate cellular stress. The Ag5-dependent accumulation of ROS in the cell leads to apoptosis [26]. In addition, the use of molecular clusters, such as Ag5, presents an attractive therapeutic strategy due to their small size, compared to most therapeutics, allowing the penetration of poorly vascularised regions such as those that lead to tumour hypoxia.

Therapy resistance in hypoxia is well-characterised, with many of the underpinning mechanisms known, however the response of hypoxic cells to ROS-dependent therapies remains unclear partly due to the incomplete understanding of how hypoxia affects redox homeostasis [5,27]. Here, we investigate the impact of oxygen levels on redox homeostasis and the efficacy of a ROS-dependent therapeutic, Ag5, in these physiological conditions.

2. Results

2.1. Ag5 leads to loss of viability in cancer but not normal cells

The response to Ag5 in the lung adenocarcinoma cell lines, A549 and H460 was compared to non-transformed cell lines, MRC5 and HFL-1 (both lung fibroblast). Using an MTT assay, a significant loss of viability was determined in response to Ag5 in both A549 and H460 cells in a dose dependent manner. In contrast, little to no effect on viability was observed in the normal cells (Fig. 1A). A549 cells were exposed to additional doses of Ag5 in order to calculate the IC50, which was found to be approximately 0.67 μM. In contrast it was not possible to determine the IC50 for Ag5 using the same doses in the non-transformed MRC5 cell line (Fig. 1B). To confirm that the observed toxicity was independent of the presence of silver ions, we used Ag + as a control compound. Cell survival was not impacted by exposure to Ag+ in A549 or H460 cells (Fig. 1C). As expected, the levels of ROS (mitochondrial) were found to be significantly higher in the A549 cells compared to the non-transformed MRC5 cells, supporting the reported mechanism of action for Ag5. (Fig. 1D and E). To demonstrate that Ag5 activity is not restricted to lung cancer cell lines, we tested a panel of oesophageal cancer cell lines. Here, we also observed a dose-dependent loss of viability in response to Ag5 (Fig. 1F). Notably, there did not appear to be a difference in sensitivity to Ag5 across the cell lines tested, suggesting sensitivity is not restricted to the presence of specific mutations (Table S1). As previously reported, Ag5-mediated cell death was found to be apoptotic (Fig. 1G) [26]. We hypothesised that other cell death pathways may also be involved. Specifically, we asked if Ag5 led to ferroptosis as this is a ROS-dependent form of cell death resulting from lipid peroxidation [28]. However, no significant increase in lipid peroxidation was found in response to Ag5 in the tested conditions, suggesting increased ferroptosis is not a relevant cell death mechanism (Fig. 1H). Overall, our results show a dose-dependent toxicity of Ag5, specifically in cancer cells.

2.2. Hypoxia leads to increases in ROS and GSH levels

The specific ratio of O_2/H_2O_2 has been described as critical for the action of Ag5. H_2O_2 binds to Ag5 with a lower adsorption energy than it binds to O_2, however, the catalytic activity of Ag5 is increased when bound to H_2O_2 in comparison to O_2 [26]. Therefore, before further testing of Ag5, we characterised the changes in redox in physiologically relevant conditions, using a combination of assays for ROS and the main cellular antioxidants, Trx and GSH. To begin, we measured oxidative stress using probes for both total cellular ROS (Fig. 2A and B) and mitochondrial ROS (superoxide, $O^{2\bullet-}$) (Fig. 2C and D). In both cases a significant increase in ROS was determined in the hypoxic conditions tested (2 or <0.1 % O_2). Next, we measured Trx levels and found no significant change in either of the hypoxic conditions tested (2 or <0.1 % O_2) (Fig. 2E). However, in agreement with previous reports, we found that GSH levels increased in response to hypoxia (Fig. 2F) [7,29–31]. N-Ethylmaleimide (NEM) was included as a negative control to confirm the cellular GSH level measurements, as NEM contains an alkene functional group that reacts with thiols present on the cysteines within GSH. To investigate GSH levels further, we synthesised a thiol responsive fluorescent probe (FL-1), that utilised the thiol reactive 2,4-DNB protecting group to mask the fluorophore 3-*O*-methylfluorescein and quench the fluorescence emission [25]. Thus, upon reaction with GSH, the 2,4-DNB unit is removed, and the highly fluorescent fluorescein moiety is released allowing the measurement of changes in GSH concentrations. GSH-mediated changes were confirmed in solution along with thiol selectivity and in cells using N-acetylcysteine (NAC) and NEM (Figs. S1A–E). Using FL-1, we again determined a significant increase in GSH in hypoxic conditions (2 and < 0.1 % O_2) (Fig. 2G). Importantly, all the assays carried out were carried out without including reoxygenation and therefore reflect redox status in the hypoxic conditions described at the time of testing. The increase of both ROS and GSH at the 6 h time point in hypoxic conditions prompted us to explore further the kinetics of these changes. A549 cells were exposed to hypoxia (2 % O_2) and mitochondrial ROS and GSH levels determined over a 12-h period. As previously, both ROS and GSH were significantly increased after exposure to 2 % O_2 for 6 h, however these data also demonstrated that ROS levels peaked after just 30 min (Fig. 2H). In contrast, GSH levels did not peak until 6 h exposure to hypoxia (Fig. 2I) confirming differential kinetics of GSH and ROS with the antioxidant response lagging behind the initial burst in oxidative stress (Fig. 2J). The observed changes in redox likely underpin differential sensitivities to cancer therapeutics including Ag5 in hypoxia. However, the exact impact of these changes specifically on Ag5 sensitivity remains unclear. If the increase in ROS was more biologically significant, the sensitivity to Ag5 would be predicted to increase, whilst if the increase in GSH was more relevant, the sensitivity would be expected to decrease.

2.3. Hypoxic cells are less sensitive to Ag5

Having demonstrated that redox homeostasis is changed by hypoxia and therefore likely to impact sensitivity to Ag5, we exposed A549 cells to hypoxia (<0.1–2 % O_2) followed by treatment with Ag5 (Fig. 3A). As expected, HIF-1α was stabilised in response to all the hypoxic conditions tested (2, 0.5 and < 0.1 % O_2) and this was not impacted by the addition of Ag5 (Fig. 3B). In each of the conditions, A549 cells were less sensitive to Ag5 in hypoxia compared to normoxia (Fig. 3C). Notably, despite no significant difference in the response to Ag5 in 2 and 0.5 % O_2, the cells treated at <0.1 % O_2 were more sensitive to Ag5 compared to the other hypoxic conditions. The biological response to hypoxia is oxygen dependent and it is likely that accumulation of replication stress and subsequent DNA damage response signalling specifically at <0.1 % O_2 may explain the sensitivity to Ag5 compared to milder levels of hypoxia

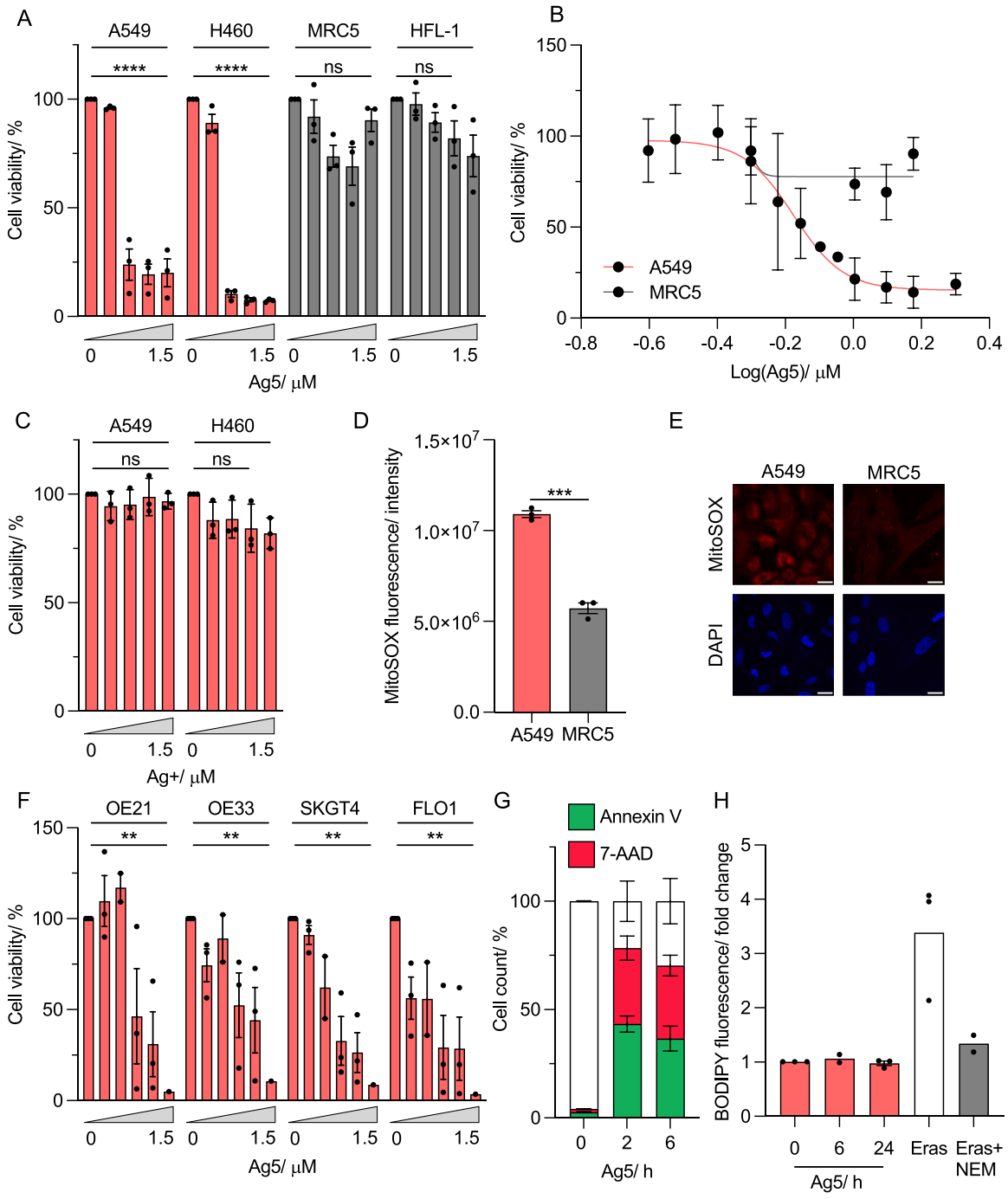


Fig. 1. Ag5 is toxic to cancer cells but not non-transformed cells.

A. Lung cancer lines (A549, H460) and non-transformed lung lines (MRC5, HFL-1) were treated with Ag5 (0, 0.5, 1, 1.25, 1.5 μM) for 1 h and analysed via MTT 20 h later.

B. A549 and MRC5 cells were treated with Ag5 (0, 0.25, 0.3, 0.4, 0.5, 0.6, 0.7, 0.8, 0.9, 1, 1.25, 1.5, 2 μM) for 1 h and analysed via MTT 20 h later.

C. A549 and H460 cells were treated with the control compound, Ag+ (0, 0.5, 1, 1.25, 1.5 μM) for 1 h, followed by an MTT assay 20 h later.

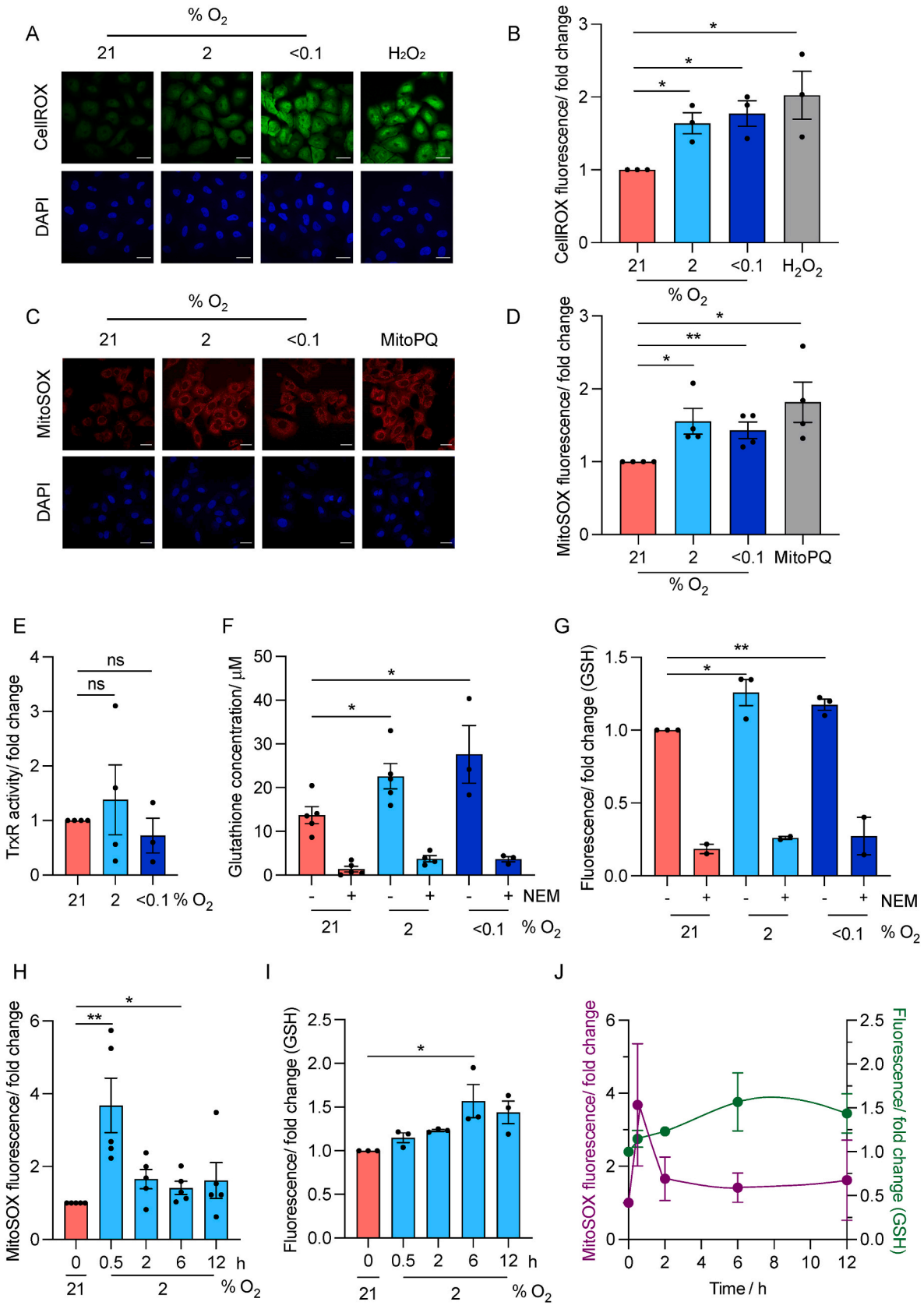
D. Levels of ROS (MitoSOX) were determined in untreated A549 and MRC5 cells.

E. Representative images from part D. Scale bar = 20 μm

F. A panel of oesophageal cancer cell lines (OE21, OE33, SKGT4, FLO1) were treated with Ag5 (0, 0.5, 1, 1.25, 1.5 μM) for 1 h and an MTT assay was carried out after 20 h

G. A549 cells were treated with Ag5 (1 μM) for 1 h followed by annexin-V and 7-AAD assay for apoptosis after 2 and 6 h

H. A549 cells were treated with Ag5 (1 μM) for 1 h, followed by a lipid peroxidation assay 6 and 24 h after drug treatment. Erastin (10 μM) was used as a positive control and NEM (200 μM) to verify that the fluorescence recorded was due to lipid peroxidation. Data shown in A, B, C, D, E, F and G are n = 3. Data shown in part H is n = 3 except for the Erastin + NEM condition which is n = 2. Black dots on the graphs shown represent biological repeats (each of which was carried out in triplicate, except for the IF). Data presented as mean + SEM. Statistical testing was done using a two-way ANOVA test for the cell viability assays or a *t*-test for the lipid peroxidation assay. **p < 0.01, ***p < 0.001, ****p < 0.0001, ns = non-significant.



(caption on next page)

Fig. 2. Changes to redox in hypoxic conditions.
A. A549 cells were exposed to 21, 2 and < 0.1 % O_2 (6 h) followed by staining for total ROS (CellROX). H_2O_2 (25 μM, 3 h) was used as a positive control to induce ROS. Representative images are shown. Scale bar = 12 μm
B., Quantification of total ROS fold change in A549 cells stained using the CellROX assay in 21, 2, <0.1 % O_2 (6 h). H_2O_2 (25 μM) was added as a control that induces ROS.
C. A549 cells were exposed to 21, 2 and < 0.1 % O_2 (6 h) followed by staining for mitochondrial ROS (MitoSOX). MitoPQ (10 μM, 6 h) was used as positive control. Representative images are shown. Scale bar = 12 μm.
D. Quantification of mitochondrial ROS fold change in A549 cells stained using the MitoSOX assay in 21, 2 and < 0.1 % O_2 (6 h). MitoPQ (10 μM) was added as a control that induces mitochondrial ROS.
E. The fold change in TrxR activity was determined in A549 cells exposed to 21, 2 or <0.1 % O_2 for 6 h
F. A549 cells were exposed to the O_2 levels shown (6 h) and GSH levels were determined (GSH GLO assay). In each case NEM (200 μM, 6 h) was included to verify that the luminescence recorded was due to GSH.
G. A549 cells were exposed to the O_2 levels shown (6 h) and GSH levels determined using FL-1. In each case NEM (200 μM, 6 h) was included to verify that the fluorescence recorded was due to GSH.
H. A549 cells were exposed to 2 % O_2 (0, 0.5, 2, 6, 12 h) followed by staining for mitochondrial ROS (MitoSOX).
I. A549 cells were exposed to 2 % O_2 (0, 0.5, 2, 6, 12 h) followed by determination of GSH levels using FL-1.
J. The data shown in parts H and I are plotted together to illustrate the differential kinetics of hypoxia induced mitochondrial ROS levels (MitoSOX) and GSH levels (FL-1) in A549 cells exposed to 2 % O_2 (0, 0.5, 2, 6, 12 h).
Data shown in A, B, C, D, E, F, G, H and I are n = 3/4. Black dots on the graphs shown represent biological repeats (each of which was carried out in triplicate, except for the IF). Data presented as mean + SEM. Statistical testing was done using an unpaired *t*-test. *p < 0.05, **p < 0.01, ns = non-significant.

(Fig. S2A) [20]. To further verify these findings, we carried out a colony survival assay in A549 cells treated with Ag5 in either normoxia or hypoxia (2 % O_2). Supporting our previous findings, cells treated in hypoxia were significantly less sensitive to Ag5 compared to those in normoxia (Fig. 3D and E). Importantly, this oxygen-dependent sensitivity to Ag5 was also observed in H460 cells demonstrating that it was not a cell line dependent effect (Figs. S2B and C).

Together, these data suggest that Ag5 is less active in hypoxic conditions. Ag5 has been shown to lead to increased ROS as a result of loss of GSH/Trx activity, therefore we measured ROS (mitochondrial) after exposure to Ag5 in both normoxic and hypoxic (2 % O_2) conditions. As expected, a significant increase in ROS were determined in normoxia after Ag5 treatment but not in hypoxia (Fig. 3F). The oxidation/reduction ratio of the mitochondrial antioxidant enzyme, thioredoxin-dependent peroxide reductase (PRDX3), has been shown previously to be a primary mediator of Ag5 action [26]. Therefore, we pre-exposed A549 and H460 cells to hypoxia (2 % O_2), followed by Ag5 treatment (as in Fig. 3A) and determined the oxidation status of PRDX3 (Fig. 3G, H, S2D, E). As expected, in normoxia, the level of oxidised PRDX3 increased and the level of reduced PRDX3 decreased in an Ag5-dependent manner, confirming that the reduction/oxidation ratio PRDX3 could be used as a marker of Ag5 activity. However, the ratio of oxidised/reduced PRDX3 was reduced in hypoxia compared to normoxia. These data indicate that Ag5 is less active in hypoxic conditions, correlating with the reduced toxicity observed.

To investigate further, we exposed cells treated with Ag5 to hypoxia, but without the pre-exposure to hypoxia (Fig. 3I). Our hypothesis was that due to the rapid increase in ROS observed previously and relatively slow increase in GSH activity (Fig. 2H and I), sensitivity to Ag5 could be unchanged using this scheduling. As expected, we saw no difference in sensitivity to Ag5 in either A549 or H460 cells in normoxia versus hypoxia (Fig. 3J, K, S2F, G). Together, these data suggest that the increase in GSH levels observed in hypoxia have more of an impact on sensitivity to Ag5 than the changes in ROS levels.

2.4. Sensitivity to Ag5 in hypoxia is rescued by loss of HIF-1α

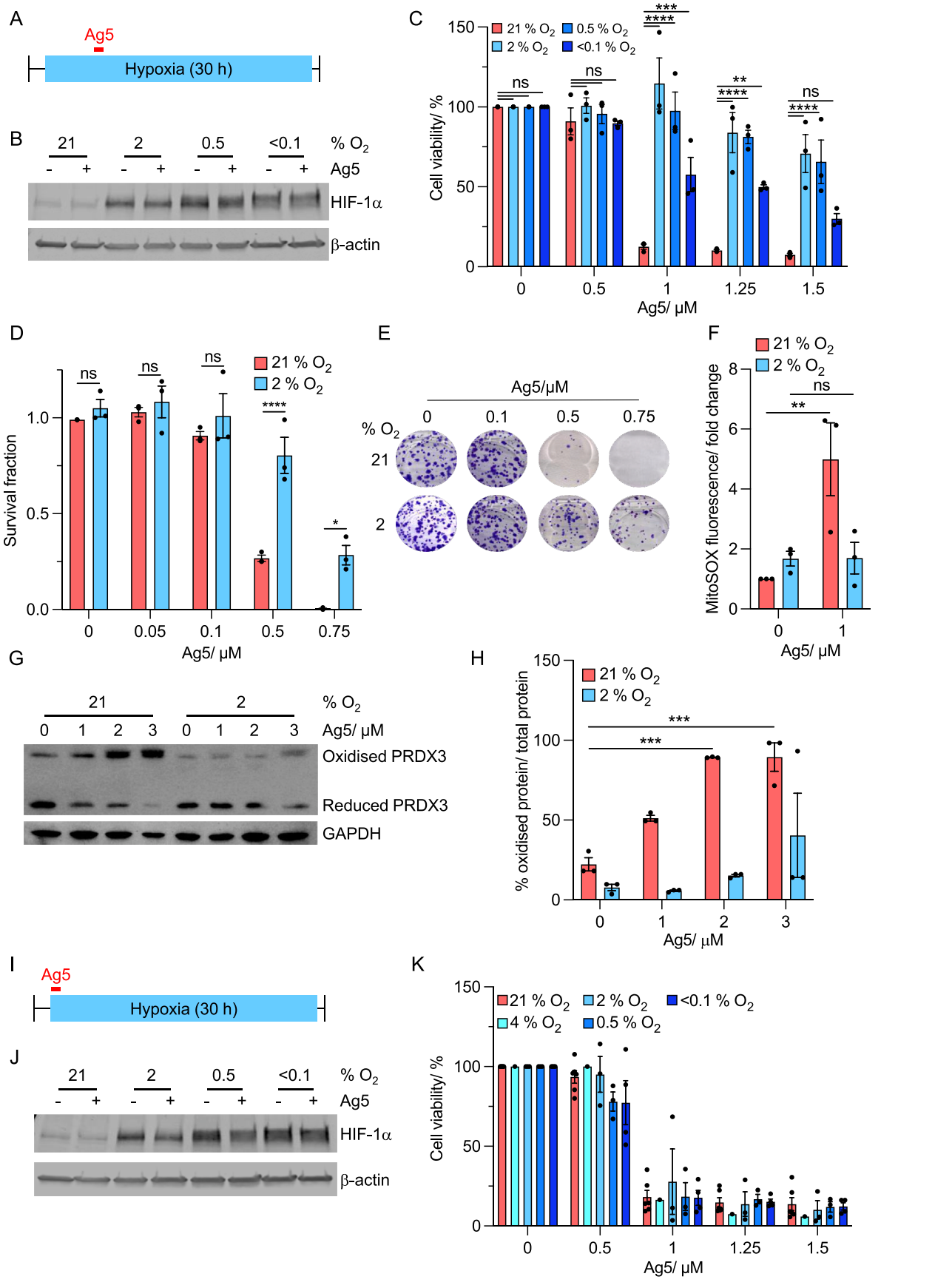
Given the necessity of pre-exposure to hypoxia to decrease response to Ag5, we hypothesised that HIF-1 could play a role in determining sensitivity to Ag5. We used two models to investigate the role of HIF-1 in the reduced sensitivity seen in hypoxia to Ag5. First, we used the genetically matched colorectal carcinoma cell lines ($RKO^{HIF-1\alpha+/+}$ and $RKO^{HIF-1\alpha-/-}$). In normoxia, no significant difference in sensitivity to Ag5 was found between the two cell lines and as expected neither stabilised HIF-1α (Fig. 4A and B). In contrast, when Ag5 was added in hypoxic conditions (2 % O_2), the $RKO^{HIF-1\alpha-/-}$ cells were significantly more sensitive compared to $RKO^{HIF-1\alpha+/+}$ and HIF-1α was stabilised (Fig. 4B and C). As expected, $RKO^{HIF-1a+/+}$ cells showed higher Ag5 sensitivity in normoxia compared to hypoxia (2 % O_2) (Fig. S3A). These data confirm that HIF-1α plays a role in sensitivity to Ag5. To further investigate, we employed the $RCC4^{VHL+/+}$ and $RCC4^{VHL-/-}$ cell lines as models of pseudo-hypoxia, as HIF-1α is stabilised in normoxic conditions in the VHL null cells (Fig. 4D) [32]. Cells lacking VHL were significantly less sensitive to Ag5 compared to the VHL proficient cells in normoxia (Fig. 4E), further supporting the role of HIF-1α in mediating Ag5 sensitivity.

2.5. Impact of HIF-1α signalling on redox

Next, as both ROS and GSH levels increased in hypoxic conditions, we investigated if this was a HIF-dependent effect. To explore the impact of HIF-1 on ROS levels, we exposed $RKO^{HIF-1\alpha+/+}$ and $RKO^{HIF-1\alpha-/-}$ cells to normoxia and hypoxia (2 % O_2) and measured total cellular and mitochondrial ROS levels. Supporting our earlier finding that ROS levels increase in hypoxia, we saw a significant increase in fluorescence associated with CellROX (total cellular ROS) when the cells were exposed to 2 % O_2. However, no significant difference was observed between the cell lines indicating that total ROS levels were not altered in a HIF-1 dependent manner (Fig. 5A and B). As previously, an increase in MitoSOX was observed in RKO cells however, the loss of HIF-1α was found to lead to a further increase (Fig. 5C and D). In order to test if HIF-1 played a significant role in the hypoxic increase of GSH, we measured GSH levels in the $RKO^{HIF-1\alpha+/+}$ and $RKO^{HIF-1\alpha-/-}$ cells in normoxic and hypoxic conditions (2 and < 0.1 % O_2). As previously and using both assays, GSH levels increased in hypoxia but, were not significantly altered by loss of HIF-1 α (Fig. 5 E–S 3B). Together, these data support the hypothesis that loss of HIF-1α restores sensitivity to Ag5 by increasing mitochondrial ROS, which is expected to enhance Ag5 activity, and likely by also reducing HIF-1-mediated signalling to genes with anti-oxidant functions [18,19].

2.6. Sensitivity to Ag5 is restored in hypoxia by loss of PDK1/3

To support our hypothesis that changes in mitochondrial ROS impact sensitivity to Ag5, we treated A549 cells with a combination of Ag5 and FCCP, which leads to an increase in ROS through uncoupling of mitochondrial oxidative phosphorylation [33]. As predicted the combination of Ag5 and FCCP had a greater impact on cell viability compared to either agent alone (Fig. 6A). In response to hypoxia, the glycolytic pathways are upregulated, due to increased expression of glucose transporters e.g. Glut1, which are HIF-1 targets [34–36]. In contrast, oxidative phosphorylation (OXPHOS) is inhibited in hypoxia via HIF-1



(caption on next page)

Fig. 3. Hypoxic cells are less sensitive to Ag5.
A. Schematic representation of cell viability assays with Ag5 with pre-exposure to hypoxic conditions. Cells were placed in hypoxia for 6 h and then treated with Ag5 for 1 h
B. A549 cells were exposed to 21, 2, 0.5 and < 0.1 % O_2 (6 h) before treatment with or without Ag5 (1 μM) for 1 h. After 20 h samples were harvested for western blotting of HIF-1α and β-actin as a loading control.
C. A549 cells were exposed to 21, 2, 0.5 and < 0.1 % O_2 (6 h) and then treated with Ag5 (0, 0.5, 1, 1.25, 1.5 μM) for 1 h, followed by an MTT assay 20 h later.
D. A549 cells were exposed to 21, 2, 0.5 and < 0.1 % O_2 (6 h) and then treated with Ag5 (0, 0.5, 1, 1.25, 1.5 μM) for 1 h, followed by a colony survival assay.
E. Representative images of the colonies formed in part D.
F. A549 cells were exposed to 21 or 2 % O2 (4 h) followed by Ag5 treatment (5 min) and staining for mitochondrial ROS (MitoSOX).
G. A549 cells were exposed to 21 and 2 % O_2 (4 h) and then treated with Ag5 (0, 1, 2, 3 μM) for 15 min, followed by western blotting for PRDX3, with GAPDH as a loading control.
H. Quantification of the percentage of oxidised/reduced PRDX3 in A549 cells after exposure to 21 and 2 % O_2 (4 h) followed by Ag5 treatment (15 min) and western blotting.
I. Schematic representation of cell viability assays with Ag5 with no pre-exposure to hypoxic conditions. Cells were exposed to Ag5 for 1 h
J. A549 cells were treated with Ag5 (1 μM) and then immediately exposed to 21, 2, 0.5 and < 0.1 % O_2. Media was changed after 1 h and western blotting was carried out 20 h later for HIF-1α with β-actin as a loading control.
K. A549 cells were treated with Ag5 (0, 0.5, 1, 1.25, 1.5 μM) and then immediately exposed to 21, 2, 0.5 and < 0.1 % O_2. Media was changed after 1 h and an MTT assay was carried out 20 h later.
Data shown in C, D, E, F, G, H and K are n = 3/4. Black dots on the graphs shown represent biological repeats (each of which was carried out in triplicate). Data presented as mean + SEM. Statistical testing was done using a two-way ANOVA test with each bar compared to the 21 % O_2 counterpart. *p ≤ 0.05, **p < 0.01, ***p < 0.001, ****p < 0.0001, ns = non-significant.

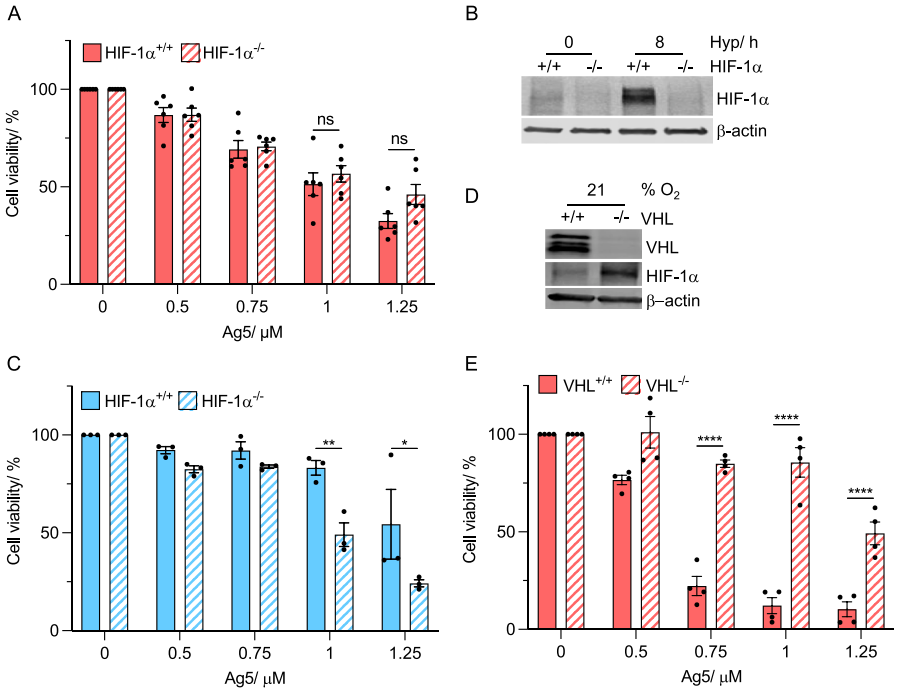


Fig. 4. Sensitivity to Ag5 is HIF-1α dependent.
A. RKO and $RKO^{HIF-1\alpha-/-}$ cells were treated with Ag5 (0, 0.5, 0.75, 1, 1.25 μM) for 1 h in 21 % O_2 followed by an MTT assay 20 h later.
B. RKO and $RKO^{Hif-1\alpha-/-}$ cells were exposed to 21 % and <0.1 % O_2 (8 h) followed by western blotting for HIF-1α, with β-actin as a loading control.
C. RKO and $RKO^{HIF-1\alpha-/-}$ cells were exposed to 2 % O_2 (6 h), followed by treatment with Ag5 (0, 0.5, 0.75, 1, 1.25 μM) for 1 h and then an MTT assay 20 h later
D. Untreated RCC4 and $RCC4^{VHL-/-}$ cells were western blotted for VHL, HIF-1α and a loading control (β-actin).
E. RCC4 and $RCC4^{VHL-/-}$ cells were treated with Ag5 (0, 0.5, 0.75, 1, 1.25 μM) for 1 h in 21 % O_2 followed by an MTT assay 20 h later.
Data shown in A, C and E are n = 3. Black dots on the graphs shown represent biological repeats (each of which was carried out in triplicate). Data presented as mean + SEM. Statistical testing was done using a two-way ANOVA test. *p < 0.05, **p < 0.01, ****p < 0.0001, ns = non-significant.

mediated increases in pyruvate dehydrogenase kinase (PDK) expression which prevents pyruvate dehydrogenase (PDH) fuelling the tricarboxylic acid (TCA) cycle with pyruvate (Fig. S3C) [32]. By blocking PDH, the amount of oxygen available in the mitochondria is increased, therefore altering the ratio of O_2/H_2O_2. Both PDK1/3 are well characterised targets of HIF-1α [37–39]. We predicted that in the absence of PDK1/3, the ratio of O_2/H_2O_2 in hypoxia would be more similar to that in normoxia and sensitivity to Ag5 would be restored. In order to test this hypothesis, we used RKO cells with reduced expression of PDK1 and PDK3 [32]. As expected, mitochondrial ROS levels increased more in response to hypoxia when PDK1/3 levels were depleted (Fig. 6B and C). We exposed RKO and $RKO^{shPDK1/3}$ cells to 21 or 2 % O_2, treated them with Ag5 (as in Fig. 3A) and determined cell viability via MTT assay. As expected, the RKO cells were less sensitive to Ag5 at 2 % O_2 compared to 21 % O_2. In normoxia, there was no significant difference in sensitivity to Ag5 between the two cell lines (Fig. 6D). However, the $RKO^{shPDK1/3}$ cells were significantly more sensitive to Ag5 in hypoxia (2 % O_2), compared to the wildtype RKO cells (Fig. 6E). These data demonstrate that sensitivity to Ag5 in hypoxia can be restored through loss of PDK1/3 and more broadly through combination with agents which lead to

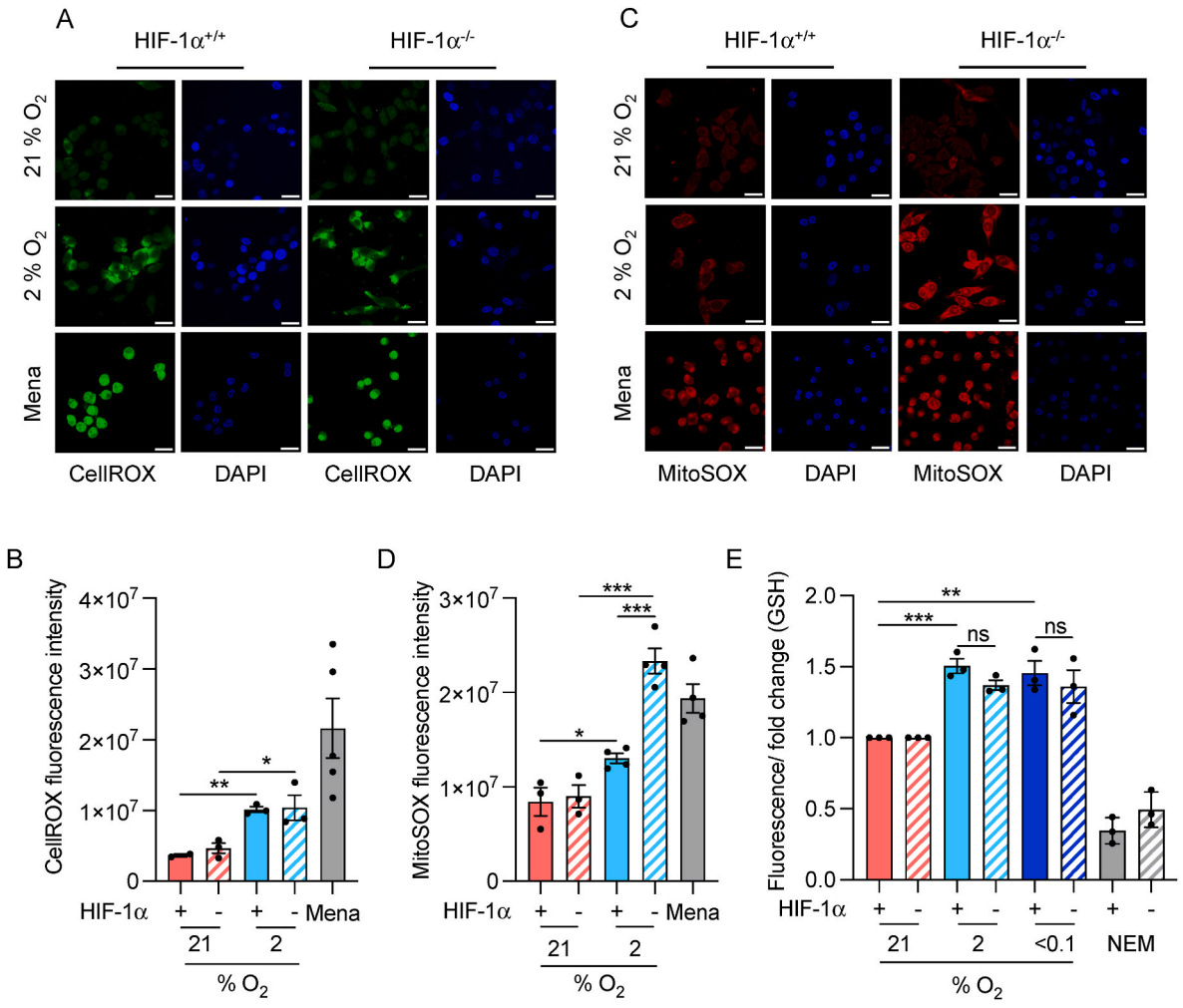


Fig. 5. The role of HIF-1 in redox.

A. RKO and RKO$^{HIF-1\alpha-/-}$ cells were exposed to 21 or 2 % O_2 (6 h) followed by staining for total ROS (CellROX). Menadione (100 μM, 6 h) was used as a positive control to induce ROS. Scale bar = 20 μm

B. Quantification of total ROS in RKO and RKO$^{HIF-1\alpha-/-}$ cells stained using the CellROX assay in 21 and 2 % O_2 (6 h). As a control, menadione (100 μM) was added to induce ROS.

C. RKO and RKO$^{HIF-1\alpha-/-}$ cells were exposed to 21 or 2 % O_2 (6 h) followed by staining for mitochondrial ROS (MitoSOX). Menadione (100 μM, 6 h) was used as a positive control to induce ROS. Scale bar = 20 μm.

D. Quantification of mitochondrial ROS in RKO and RKO$^{HIF-1\alpha-/-}$ cells stained using the MitoSOX assay in 21 and 2 % O_2 (6 h). As a control, menadione (100 μM) was added to induce ROS.

E. RKO and RKO$^{Hif-1\alpha-/-}$ cells were exposed to the O_2 levels shown (6 h) and GSH levels determined (FL-1). In each case NEM (200 μm, 6 h) was also included to verify that the fluorescence recorded was due to GSH.

Data shown in A, B, C, D and E are n = 3. Black dots on the graphs shown represent biological repeats (each of which was carried out in triplicate, except for the IF). Data presented as mean + SEM. Statistical testing was done using an unpaired *t*-test. *p < 0.05, **p < 0.01, ***p < 0.001 ns= non-significant.

increased mitochondrial ROS levels.

2.7. Ag5 increases the radiosensitivity of hypoxic cells

Despite the reduced sensitivity to Ag5 in hypoxia, or conditions where HIF-1 is expressed, Ag5 is a promising anti-cancer agent due to the lack of toxicity observed in non-transformed cells (Fig. 1A). Radiation in the form of radiotherapy leads to the generation of hydroxyl (•OH) radicals from the hydrolysis of water which cause DNA damage and cell death [40]. Therefore, we asked if the combination of Ag5 and radiation would be effective. Importantly, we investigated the impact of Ag5 on radiosensitivity in hypoxic conditions as hypoxia is a major mechanism of radiation resistance [41]. A549 cells were exposed to radiobiological hypoxia (<0.1 % O_2) and treated with both Ag5 and radiation (0, 2, 4 Gy) and a colony survival assay carried out (Fig. 6F). As expected, the cells irradiated in hypoxic (<0.1 % O_2) conditions were significantly more radioresistant compared to those treated in normoxic conditions (Fig. S3D) and HIF-1α was stabilised in all conditions (Fig. 6G). The combination of Ag5 and radiation had a greater effect on cell survival compared to either agent alone (Fig. 6H). Together, these data suggest that the combination of Ag5 and radiotherapy would be efficacious and does not increase hypoxia-induced radioresistance.

3. Discussion

The therapeutic molecular cluster Ag5 leads to significant loss of viability in a range of cancer cell lines but not non-transformed cells therefore making it an attractive anti-cancer agent. Here, we investigated how the activity of Ag5 was impacted by conditions which reflect the physiological levels of oxygen commonly found in solid tumours. In all of the hypoxic conditions tested, cells were less sensitive to Ag5 compared to normoxic (21 % O_2) conditions, but notably hypoxic cancer

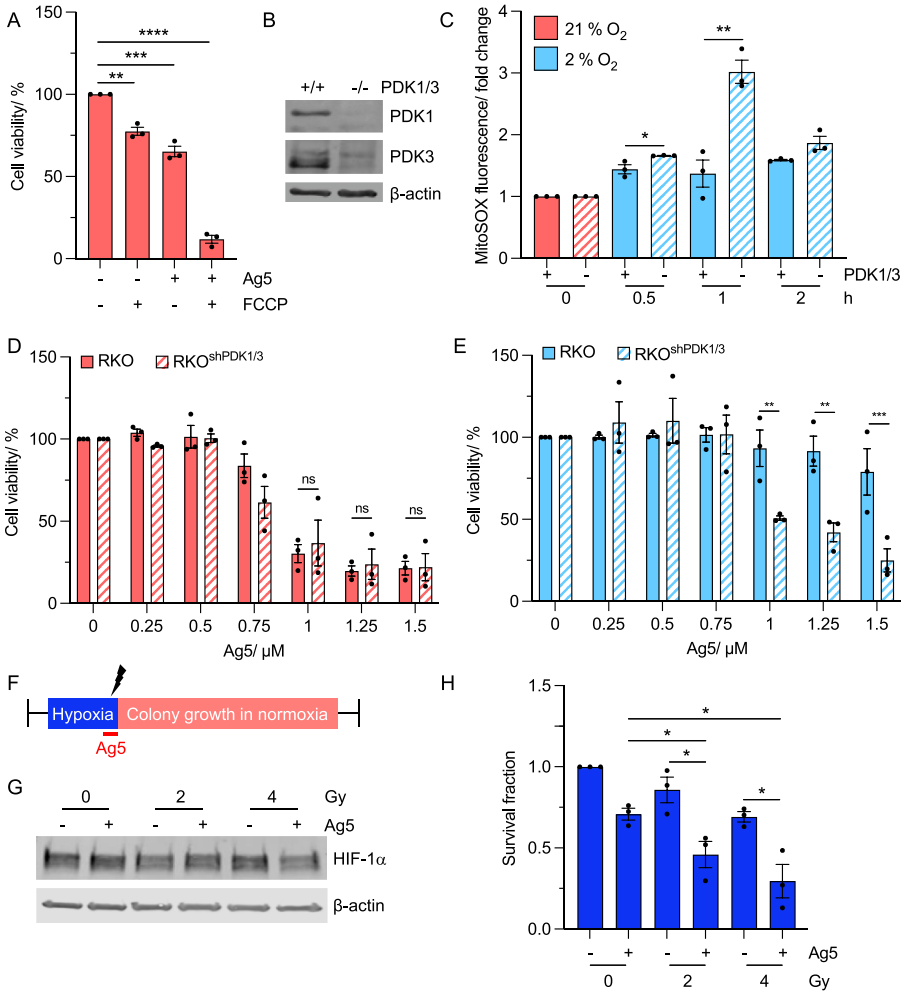


Fig. 6. Sensitivity to Ag5 in hypoxia can be restored by altering cellular redox.

A. A549 cells were either untreated or treated with FCCP (6 h), Ag5 (1 h) or both FCCP (6 h) and Ag5 (1 h) followed by an MTT assay 20 h later.

B. Levels of PDK1, PDK3 and a loading control (β-actin) are shown in untreated RKO and RKO$^{shPDK1/3}$ cells.

C. RKO and RKO$^{shPDK1/3}$ cells were exposed to 2 % O_2 (0, 0.5, 1, 2, 3, 6 h) followed by staining for mitochondrial ROS (MitoSOX).

D. RKO and RKO$^{shPDK1/3}$ cells were treated with Ag5 (0, 0.25, 0.5, 0.75, 1, 1.25 μM) for 1 h in normoxia (21 % O_2) followed by an MTT assay 20 h later.

E. RKO and RKO$^{shPDK1/3}$ cells were exposed to hypoxia (2 % O_2) (6 h), followed by treatment with Ag5 (0, 0.5, 0.75, 1, 1.25 μM) for 1 h followed by an MTT assay 20 h later.

F. Schematic representation of the experimental set up for combining Ag5 with radiation in hypoxia (not to scale). Importantly, radiation (indicated with black lightning strike) was delivered in hypoxic conditions i.e. without reoxygenation. Colonies were then allowed to form in normoxic (21 % O_2) conditions.

G. A549 cells were exposed to <0.1 % O_2 (4 h), followed by treatment with Ag5 (1 μM) for 1 h. During Ag5 treatment, cells were irradiated (0, 2, 4 Gy) in hypoxic conditions. Cells were harvested after the 1 h treatment and western blotted for HIF-1α, with β-actin as a loading control.

H. A549 cells were treated as in part E followed by return to normoxic conditions (21 % O_2), and colony survival assay.

Data shown in A, C, D, E and H are n = 3. Black dots on the graphs shown represent biological repeats (each of which was carried out in triplicate). Data presented as mean + SEM. Statistical testing was done using a two-way ANOVA test for cell viability and unpaired *t*-test for colony survival. *p < 0.05, **p < 0.01, ***p < 0.001, ****p < 0.0001 ns= non-significant.

cells were still more sensitive to Ag5 compared to the non-transformed cells. Normal cells experiencing the levels of hypoxia found in tumours and tested here are rare within the normal body providing an exploitable therapeutic window. Importantly, the combination of radiation and Ag5 significantly increased cell death in hypoxia compared to radiation alone. The decreased sensitivity to Ag5 observed in hypoxia was found to be HIF-1α dependent and more specifically dependent on the HIF-1 target genes PDK1/3. Our data supports the hypothesis that loss of PDK1/3 in hypoxic conditions relieves the inhibitory effect of PDH on oxygen consumption and therefore increases available oxygen and ROS in the mitochondria which is the site of Ag5 action. Ag5 is known to be exquisitely sensitive to the ratio of O_2/H_2O_2 [26].

As part of this study, we also provide a detailed characterisation of the redox environment in hypoxic conditions including changes in ROS (total and mitochondrial) and the major antioxidant systems. Our study demonstrates that, in the absence of reoxygenation, hypoxia leads to an increase in ROS and GSH levels, supported by previous literature [7,28,42,43]. Importantly, we demonstrate that the kinetics of the increase in ROS and GSH differ with ROS levels peaking quickly (30 min) and GSH lagging behind. The increase in mitochondrial ROS was found to be HIF-1α dependent. In contrast, total cellular ROS and GSH levels were not impacted by HIF-1α activity in our hands. Notably, a previous study found GSH synthesis to be induced by chemotherapy in a HIF-dependent manner in triple negative breast cancer (TNBC), indicating that there is likely a dependence on experimental conditions [44].

In summary, Ag5 is an exciting addition to the class of redox dependent agents with anti-cancer activity. The high potency of Ag5 in cancer cells is likely underpinned by targeting both GSH and Trx

pathways therefore preventing cancer cells circumventing reduced antioxidant capacity. Our study highlights the importance of testing anti-cancer agents in conditions which mimic the hypoxic tumour microenvironment as Ag5 is less toxic in these conditions. However, Ag5 remains a promising anti-cancer approach as it shows selective activity in cancer compared to normal cells and combines well with radiation.

4. Methods

4.1. Cells, cell culture and reagents

Human non-small cell lung carcinoma cells A549 (ATCC) and H460 (Prof. Geoff Higgins, University of Oxford) were grown in DMEM. Human oesophageal cancer OE21, OE33, FLO1 and SK-GT-4 cells (Dr Ricky Sharma, University of Oxford) were grown in DMEM (OE21 and FLO1) and RPMI (OE33 and SK-GT-4). Human colorectal RKO and $RKO^{HIF-1\alpha-/-}$ cancer cells were grown in DMEM [45]. $RKO^{shPDK1/3}$ cells (Prof. Nicholas Denko, The Ohio State University) were also grown in DMEM [37]. Human renal clear carcinoma RCC4 and $RCC4^{VHL-/-}$ cancer cell lines (Prof. Sir Peter Ratcliffe, University of Oxford) were grown in DMEM. Human foetal lung fibroblast cell lines MRC5 and HFL-1 (Prof. Geoff Higgins, University of Oxford), were grown in DMEM and nutrient mixture F12 HAM media, respectively. All media was supplemented with 10 % FBS and 1 % P/S and cells were cultured in humified incubators at 37 °C with 5 % CO_2. All cell lines were verified to be negative for mycoplasma using a Lonza MycoAlert® mycoplasma detection assay (LT07-318, Lonza). Ag5/Ag+ was provided by Arjuna Therapeutics. A stock solution of Ag5 was prepared in water and stored at room temperature, protected from light. The stock solution was sonicated for 30–60 min prior to every use and diluted in serum-free DMEM before adding to cells. Cells were exposed to Ag5/Ag + for 1 h in serum free media, which was then replaced with complete media.

4.2. Ag5 treatment

Cells were treated with Ag5 in FBS free media for 1 h, except for the PRDX3 assay in which treatment was 15 min, media was then changed to complete serum containing media. In hypoxic conditions, FBS free media and complete serum media were equilibrated to the desired O_2 concentration before use.

4.3. MTT assay

Cells were seeded in flat bottomed 96 well plates and allowed to adhere for 2–4 h (37 °C, 5 % CO_2), before being exposed to a range of O_2 conditions. Each treatment condition was carried out in triplicate. After 20 h, MTT reagent (0.5 mg/mL, Invitrogen) was added for 3 h (37 °C) with the plate protected from light. The plates were then removed from their respective oxygen environment and the MTT containing media was discarded. DMSO (100 μL) was added to each well and the plate was incubated in the dark for 15 min (37 °C) before measuring absorbance (570 nm) (POLARstar plate reader, BMG LabTech). Cell viability was calculated as a percentage in comparison to the untreated control. The IC50 was calculated using non-linear regression.

4.4. Annexin-V assay

After treatment, cells were washed twice with PBS and then stained with Annexin V-FITC (1:10, 15 min, BD biosciences, 550,911) and 7-AAD (5 μM, 15 min, BD biosciences, 555,816), following the manufacturer's instructions. Images were obtained using an Olympus IX51 microscope equipped with an Olympus DP72 camera and CellSens Imaging Software and processed with ImageJ.

4.5. Lipid peroxidation assay

After drug treatment, the media was removed and cells were incubated with BODIPY™ 581/591 lipid peroxidation sensor (2 μM, Invitrogen, D3861) in PBS for 30 min at 37 °C, away from light. Ferrostatin (5 μM) was used as a positive control and was added at the same time as seeding. Cells were then trypsinised in the dark and the pellet resuspended in FACs buffer (PBS, 2 % FBS, 0.5 mM EDTA). Samples were then analysed on a CytoFLEX flow cytometer (Beckman Coulter) using CytExpert software. Analysis was carried out for a cell count of 10,000 events for each treatment condition in triplicate. FloJo software (BD Biosciences) was used to analyse the data.

4.6. ROS assays

Intracellular and mitochondrial ROS levels were determined using the CellROX™ Green (Thermo Fisher Scientific, C10444) and MitoSOX™ Red (Thermo Fisher Scientific, M36008), respectively. After drug/hypoxia treatment cells were incubated with either 10 μM CellROX™ Green (30 min) or 5 μM MitoSOX™ Red (10 min) at 37 °C in the dark. H_2O_2 (25 μM, 3 h, Sigma-Aldrich), MitoPQ (10 μM, 6 h) and menadione (100 μM, 6 h, Merck) were used as controls. After staining, cells were fixed using 4 % PFA (10 min), washed three times with PBS and mounted with ProLong™ Diamond Antifade Mountant with DAPI (Invitrogen). Microscopy imaging was carried out using a Zeiss 780 or 710 confocal Microscope (Carl Zeiss Ag, Jena, Germany) at 60× magnification and at least 100 cells were counted per condition for quantification.

4.7. GSH assays

The GSH-Glo assay was carried out according to the manufacturer's instructions (Promega, V6911). Each treatment condition was performed in triplicate. Cells were seeded (4000/well) in white walled, flat bottomed 96 well plates and allowed to adhere overnight. Plates were then placed in the stated oxygen tension and were either untreated or pre-treated with NEM (200 μM) for 6 h. A standard curve was generated at 21 % O_2.

Synthesis of the novel GSH probe (FL-1) is described in the supplementary information. To assay GSH using FL-1, cells were seeded (4000/well) in flat bottomed 96 well plates and allowed to adhere overnight. Plates were then placed in the stated oxygen tensions and were either untreated or pre-treated with NEM (200 μM) for 6 h. FL-1 (10 μM) was then added to each well and the contents of the well was mixed. After 1 h, the fluorescence was measured (POLARstar plate reader, BMG LabTech).

4.8. Trx assay

The TrxR assay was carried out, to investigate Trx levels, according to the manufacturer's instructions (AbCam, ab83463). Each treatment condition was performed in triplicate. Cells were seeded in glass dishes and allowed to adhere overnight. Plates were then placed in the required oxygen tension for 6 h. Cells were then harvested and assayed for Trx using the TrxR assay kit, colorimetric (AbCam, ab83463).

4.9. Hypoxia treatment

Cells were exposed to hypoxia at the stated oxygen tensions using a Bactron II anaerobic chamber (Shel labs) for <0.1 % O_2 and an M35 hypoxia workstation (Don Whitley) for 0.5–4 % O_2. Glass dishes were used for hypoxia experiments, except when plastic plates were required (MTT, GSH or colony assays). Oxygen concentrations were periodically validated using anaerobic oxygen indicator strips (Thermo Fisher) and an OxyLite (Oxford Optronix).

4.10. Immunoblotting

Cells were harvested in UTB lysis buffer (9 M Urea, 75 mM Tris-HCl pH 7.5, 0.15 M β-mercaptoethanol) and briefly sonicated. Proteins were separated on a 4–20 % polyacrylamide gel (Bio-Rad) and transferred onto a nitrocellulose membrane (Bio-Rad). The Odyssey Infrared Imaging System (LI-COR Biosciences) was used. Antibodies used were HIF-1α (BDBiosciences, 610,959), β-Actin (Santa Cruz, 69,879), VHL (Cell Signalling, 68,547), Glut-1 (Abcam, ab14683), Gapdh (Protein tech, 60,004-1-1 g), PDK1 (AbCam, ab110025), PDK3 (AbCam, 154,549), p53-S15 (Cell Signalling, 92,845) and p53 (Santa Cruz, sc-126).

4.11. Colony survival assay

Cells were seeded at the appropriate density, depending on the treatment condition, in 6-well plates to give a total volume of 2 mL per well. Seeding was calculated to give a plating efficiency above 50 % for the untreated condition. Each treatment condition was performed in triplicate. After treatment (Ag5/IR/hypoxia) colonies were allowed to grow in a humified incubator (37 °C, 5 % CO_2) for 14 days. Once the colonies had formed a sufficient size (>50 cells), the media was removed and they were stained with crystal violet (0.5 % w/v in 50 % MeOH and 20 % EtOH) for 1 h, before washing with water. Colonies were counted using a manual cell counter (Stuart Scientific). The survival fraction was calculated by no. Of colonies counted/no. Of cells seeded × PE, where PE is the plating efficiency of the untreated control (no. Of colonies counted/no. Of cells seeded).

4.12. PRDX3 assay

Cells were seeded in plastic dishes and allowed to adhere overnight, prior to drug/hypoxia treatment. The media was then replaced with 80 mM methyl methanethiosulfonate (MMTS) (Sigma, 64,306) enriched media to prevent oxidation of reduced thiols. The dishes were washed 2 x ice cold PBS, followed by addition of 75 μL RIPA buffer (50 mM Tris, pH 7.5, 150 mM NaCl, 1 % (v/v) Triton-X100, 0.1 % (w/v) SDS, 0.5 % (w/v) sodium deoxycholate) supplemented with 1 mM sodium orthovanadate, 1 mM PMSF, 5 mM NaF, 1x Protease inhibitor cocktail and 80 mM MMTS. The cells were scraped into the buffer after 20 min incubation on ice. The samples were sonicated (30 % amplitude, 1 s on, 1 s off x 10) and then centrifuged (14,000 rpm, 20 min, 4 °C). Samples were mixed with loading buffer (250 mM Tris-Cl (pH 6.8), 8 % SDS, 0.1 % bromophenol blue, 40 % (v/v) glycerol, H_2O) (non-oxidising), heated (96 °C, 5 min) and electrophoresed on a 15 % acrylamide gel (250 V, 50 A). The gel was transferred (1 h) onto a PVDF membrane and blocked with milk powder (1 h), washed 3 x TNT (0.1 % TWEEN) and incubated with antibody (PRDX3, Abcam, ab129206) (4 °C, overnight). The membrane was then washed 3 x TNT (0.1 % TWEEN), incubated with 2° antibody (1 h, rt), followed by washing 3 x TNT (0.1 % TWEEN). ECL reagent was then added, and the gels were visualised using a ChemiDoc Imaging System (BioRad). The membranes were then blotted for GAPDH (Sigma, MAB374), followed by a HRP 2° antibody and then visualised using a ChemiDoc.

4.13. Radiation treatment

Irradiation was carried out using γ-rays from a Cs-137 irradiator (GSM: GSR D1) at a dose rate of 1.7 Gy/min, at rt. For irradiating experiments in hypoxia, cells were transferred to airtight Perspex plastic boxes to allow for transportation to and from the irradiator [32].

4.14. Statistical analysis

GraphPad Prism software (GraphPad software Inc.) was used to carry out all statistical analysis, including two-way ANOVA tests and unpaired t-tests. Data is presented as mean + SEM. Statistical testing is described in each figure legend. *$p < 0.05$, **$p < 0.01$, ***$p < 0.001$, ****$p < 0.0001$, ns = not significant.

CRediT authorship contribution statement

Sophie A. Twigger: Writing – review & editing, Validation, Methodology, Investigation, Formal analysis, Data curation. **Blanca Dominguez:** Methodology, Investigation, Formal analysis, Data curation. **Vanesa Porto:** Methodology, Investigation, Formal analysis, Data curation. **Lina Hacker:** Writing – review & editing, Formal analysis, Data curation. **Anthony J. Chalmers:** Conceptualization. **Ross Breckenridge:** Conceptualization. **Martin Treder:** Conceptualization. **Adam C. Sedgwick:** Methodology, Investigation, Formal analysis, Data curation. **Fernando Dominguez:** Writing – review & editing, Supervision, Funding acquisition, Formal analysis, Conceptualization. **Ester M. Hammond:** Writing – review & editing, Writing – original draft, Supervision, Project administration, Funding acquisition, Formal analysis, Conceptualization.

Declaration of competing interest

RB is the CEO and Board Director of Arjuna Therapeutics. MT is the CSO of Arjuna Therapeutics. FD is scientific advisor and shareholder of Arjuna Therapeutics and has patents on Ag5 synthesis and the therapeutic applications.

Data availability

No data was used for the research described in the article.

Acknowledgements

We would like to acknowledge Dr Ejung Moon and Dr Nuria Vilaplana Lopera for assistance with the lipid peroxidation assay. SAT was supported by an Oxford MRC DTP studentship (MR/N013468/1) and would also like to thank St Peter's college graduate award scheme. LH and EMH thank the EPSRC for the support of programme grant EP/S019901/1. ACS would like to thank King's College London for a generous start up package and the EPSRC programme grant (EP/X033015/1) for financial support. FD was partially supported by "la Caixa" Foundation (LCF/PR/PR12/11070003); Ministry of Science, Innovation and Universities (MAT2017-89678-R, AEI/FEDER, EU); Xunta de Galicia (Singular Research Center of Galicia accreditation 2019–2022 ref ED431G 2019/02) and the European Union (European Regional Development Fund – ERDF). Arjuna Therapeutics has received funding from MCIN/AEI/10.13039/501100011033 (Grant PLEC2022-009476) and by the "European Union NextGenerationEU/PRTR. Radiation facilities were supported by Cancer Research UK RadNet Centre Award C6078/A28736.

Appendix A. Supplementary data

Supplementary data to this article can be found online at https://doi.org/10.1016/j.redox.2024.103326.

References

[1] B. Perillo, et al., ROS in cancer therapy: the bright side of the moon, Exp. Mol. Med. 52 (2020) 192–203.
[2] O. Vafa, et al., c-Myc can induce DNA damage, increase reactive oxygen species, and mitigate p53 function: a mechanism for oncogene-induced genetic instability, Mol. Cell 9 (2002) 1031–1044.
[3] G.Y. Liou, P. Storz, Reactive oxygen species in cancer, Free Radic. Res. 44 (2010) 479–496.
[4] N. C. Hypoxia Denko, HIF1 and glucose metabolism in the solid tumour, Nat. Rev. Cancer 8 (2008) 705–713.
[5] E.M. Hammond, et al., The meaning, measurement and modification of hypoxia in the laboratory and the clinic, Clin. Oncol. 26 (2014) 277–288.

[6] N.S. Chandel, et al., Reactive oxygen species generated at mitochondrial complex III stabilize hypoxia-inducible factor-1α during hypoxia: a mechanism of O2 sensing, J. Biol. Chem. 275 (2000) 25130–25138.
[7] J. Duranteau, N.S. Chandel, A. Kulisz, Z. Shao, P.T. Schumacker, Intracellular signaling by reactive oxygen species during hypoxia in cardiomyocytes, J. Biol. Chem. 273 (1998) 11619–11624.
[8] E.C. Ferber, et al., FOXO3a regulates reactive oxygen metabolism by inhibiting mitochondrial gene expression, Cell Death Differ. 19 (2011) 968–979.
[9] T.A. Ogunrinu, H. Sontheimer, Hypoxia increases the dependence of glioma cells on glutathione, J. Biol. Chem. 285 (2010) 37716–37724.
[10] G. Sgarbi, et al., Hypoxia decreases ROS level in human fibroblasts, Int. J. Biochem. Cell Biol. 88 (2017) 133–144.
[11] S.W. Tuttle, et al., Detection of reactive oxygen species via endogenous oxidative pentose phosphate cycle activity in response to oxygen concentration: implications for the mechanism of HIF-1α stabilization under moderate hypoxia, J. Biol. Chem. 282 (2007) 36790–36796.
[12] W. Wang, et al., Superoxide flashes in single mitochondria, Cell 134 (2008) 279–290.
[13] G.B. Waypa, et al., Hypoxia triggers subcellular comparmental redox signaling in vascular smooth muscle cells, Circ. Res. 106 (2010) 526–535.
[14] D. Kung-Chun Chiu, et al., Hypoxia regulates the mitochondrial activity of hepatocellular carcinoma cells through HIF/HEY1/PINK1 pathway, Cell Death Dis. 10 (2019) 1–16.
[15] M. Tafani, et al., The interplay of reactive oxygen species, hypoxia, inflammation, and sirtuins in cancer initiation and progression, Oxid. Med. Cell. Longev. (2016) 1–18.
[16] C. Hei Antonio Cheung, et al., The Role of Ferroptosis in Cancer Development and Treatment Response, vol. 8, 2018, pp. 1–8.
[17] G.K. Azad, R.S. Tomar, Ebselen, a promising antioxidant drug: mechanisms of action and targets of biological pathways, Mol. Biol. Rep. 41 (2014) 4865–4879.
[18] A.A. Qutub, A.S. Popel, Reactive oxygen species regulate hypoxia-inducible factor 1α differentially in cancer and ischemia, Mol. Cell Biol. 28 (2008) 5106–5119.
[19] J. Pouysségur, F. Mechta-Grigoriou, Redox regulation of the hypoxia-inducible factor, Biol. Chem. 387 (2006) 1337–1346.
[20] T.S. Ma, et al., Hypoxia-induced transcriptional stress is mediated by ROS-induced R-loops, Nucleic Acids Res. 51 (2023) 11584–11599.
[21] H.Q. Ju, J.F. Lin, T. Tian, D. Xie, R.H. Xu, NADPH homeostasis in cancer: functions, mechanisms and therapeutic implications, Signal Transduct. Targeted Ther. 5 (2020) 1–12.
[22] K.J. Davies, J.H. Doroshow, The Journal of Biological Chemistry Redox Cycling of Anthracyclines by Cardiac Mitochondria, vol. 261, 1986, pp. 3060–3067.
[23] E. Desideri, F. Ciccarone, M.R. Ciriolo, Targeting glutathione metabolism: partner in crime in anticancer therapy, Nutrients 11 (2019) 1–12.
[24] F.H. Abdalbari, C.M. Telleria, The gold complex auranofin: new perspectives for cancer therapy, Discov. Oncol. 12 (2021) 1–18.
[25] J.A. Malla, et al., A glutathione activatable ion channel induces apoptosis in cancer cells by depleting intracellular glutathione levels, Angew. Chem., Int. Ed. 59 (2020) 7944–7952.
[26] V. Porto, et al., Silver clusters of five atoms as highly selective antitumoral agents through irreversible oxidation of thiols, Adv. Funct. Mater. 1–14 (2022).
[27] K.R. Worth, I. Papandreou, E.M. Hammond, How the histological structure of some lung cancers shaped almost 70 years of radiobiology, Br. J. Cancer 128 (2022) 407–412.
[28] B. Lu, et al., The role of ferroptosis in cancer development and treatment response, Front. Pharmacol. 8 (2017) 1–8.
[29] L. Kennedy, J.K. Sandhu, M.E. Harper, M. Cuperlovic-culf, Role of glutathione in cancer: from mechanisms to therapies, Biomolecules 10 (2020) 1–27.
[30] K.M. Rouschop, et al., PERK/eIF2α signaling protects therapy resistant hypoxic cells through induction of glutathione synthesis and protection against ROS, Proc. Natl. Acad. Sci. U.S.A. 110 (2013) 4622–4627.
[31] V.V. Khramtsov, R.J. Gillies, Janus-faced tumor microenvironment and redox, Antioxidants Redox Signal. 21 (2014) 723–729.
[32] S. Anbalagan, et al., Radiosensitization of renal cell carcinoma in vitro through the induction of autophagy, Radiother. Oncol. 103 (2012) 388–393.
[33] S. Demine, P. Renard, T. Arnould, Mitochondrial uncoupling: a key controller of biological processes in physiology and diseases, Cells 8 (2019).
[34] S.J. Kierans, C.T. Taylor, Regulation of glycolysis by the hypoxia-inducible factor (HIF): implications for cellular physiology, J. Physiol. 599 (2021) 23–37.
[35] G.L. Semenza, Tumor metabolism: cancer cells give and take lactate, J. Clin. Invest. 118 (2008) 3835–3837.
[36] R.E. Airley, et al., GLUT-1 and CAIX as intrinsic markers of hypoxia in carcinoma of the cervix: relationship to pimonidazole binding, Int. J. Cancer 104 (2003) 85–91.
[37] I. Papandreou, R.A. Cairns, L. Fontana, A.L. Lim, N.C. Denko, HIF-1 mediates adaptation to hypoxia by actively downregulating mitochondrial oxygen consumption, Cell Metabol. 3 (2006) 187–197.
[38] C.W. Lu, S.C. Lin, K.F. Chen, Y.Y. Lai, S.J. Tsai, Induction of pyruvate dehydrogenase kinase-3 by hypoxia-inducible factor-1 promotes metabolic switch and drug resistance, J. Biol. Chem. 283 (2008) 28106–28114.
[39] X. Wang, X. Shen, Y. Yan, H. Li, Pyruvate dehydrogenase kinases (PDKs): an overview toward clinical applications, Biosci. Rep. 41 (2021) 1–15.
[40] L. Wu, et al., Generation of hydroxyl radical-activatable ratiometric near-infrared bimodal probes for early monitoring of tumor response to therapy, Nat. Commun. 121 12 (2021) 1–13, 2021.
[41] R.G. Bristow, R.P. Hill, Hypoxia, DNA repair and genetic instability, Nat. Rev. Cancer 8 (2008) 180–192.
[42] I. Azimi, R.M. Petersen, E.W. Thompson, S.J. Roberts-Thomson, G.R. Monteith, Hypoxia-induced reactive oxygen species mediate N-cadherin and SERPINE1 expression, EGFR signalling and motility in MDA-MB-468 breast cancer cells, Sci. Rep. 7 (2017) 1–11.
[43] D.W. Killilea, R. Hester, R. Balczon, P. Babal, M.N. Gillespie, Free radical production in hypoxic pulmonary artery smooth muscle cells, Am. J. Physiol. Lung Cell Mol. Physiol. 279 (2000) L408–L412.
[44] H. Lu, et al., Chemotherapy triggers HIF-1-dependent glutathione synthesis and copper chelation that induces the breast cancer stem cell phenotype, Proc. Natl. Acad. Sci. U.S.A. 112 (2015) E4600–E4609.
[45] D.T. Dang, et al., Hypoxia-inducible factor-1α promotes nonhypoxia-mediated proliferation in colon cancer cells and xenografts, Cancer Res. 66 (2006) 1684–1693.